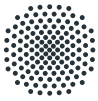

Universität Stuttgart

Metabolic compartmentalization in ^{13}C Metabolic Flux Analysis of Chinese Hamster Ovary cells

Von der Fakultät Energie-, Verfahrens-, und Biotechnik der Universität Stuttgart zur Erlangung der Würde eines Doktor-Ingenieurs (Dr.-Ing.) genehmigte Abhandlung

Vorgelegt von

Andy Wiranata Wijaya

aus Medan

Hauptberichter:	Prof. Dr.-Ing. Ralf Takors
Mitberichter:	Prof. Dipl.-Ing Dr.techn. Christoph Herwig

Tag der mündlichen Prüfung: 03.02.2023

Institut für Bioverfahrenstechnik

2023

This dissertation is dedicated to my wife, Fecianti, and my son, Evander.

Acknowledgements

I was and am still very grateful for being offered a PhD position in Germany, especially with a project relating Chinese Hamster Ovary cells. Therefore, I wish to express my sincere appreciation to my supervisor and academic mentor, Prof. Dr.-Ing Ralf Takors for his assistance and guidance throughout this work. One of the motto in your office "*There are no mistakes, only lesson*" always reminds me to put myself in the "learning mode". That was also why I was never afraid to bring a new idea to your office even if it was vague. Furthermore, I would like to thank Prof. Dr. Christoph Herwig and Prof. Dr. Roland Kontermann for their participation in the examination committee. I am indebted to Lisa Junghans for allowing me to access her invaluable first compartment-specific data set. It actually turns out to be the most important part of this theses. Without your kindly permission, I won't be able to finish this PhD theses.

I would like to pay my special regards to my project and research partners: Attila Teleki, Natascha Verhagen, Andreas Ulmer, and Lara Hundsdorfer. I thank you for the patience in dealing with someone impatient like me. Thank you for the endless effort in generating high quality data. Thank you for the

hardwork in generating our own ^{13}C code. Also, I wish to show my gratitude to the General Federal Ministry of Education and Research (BMBF) for the funding in DipImpact Project. I wish to thank our industrial project partners: Andreas Unsöld (Boehringer Ingelheim), Martin Schilling (Evonik Nutrition & Care), and Christoph Heinrich (Xell). Without the input and knowledge from our project partners, this project won't be as successful as it is now.

I also want to thank Insilico Biotechnology AG, especially Klaush Mauch, Waldemar Reusch, and Lothar Terfloth for giving me the chance to work with the internal code for Insilico Discovery. I identified the weakness of the tool, but at the end of the day, it was my incapability to establish a new Fortran-based solver to improve the existing Insilico Dicovery ^{13}C toolbox. Also, I am indebted to Richard Schäfer for helping me setting up Galaxy server with Insilico Discovery. I admit you spent more time than you need to and I am very thankful of that. Further, I wish to show my gratitude for my students: M. Fadhlullah and Haya Essa for their contribution to this work. I would also give my regards to the IBVT colleagues: Frau Reu, Max Becker, Vikas Patil, Andreas Ankenbauer, Maike Kuschel, Flora Siebler, Adrian Eilingsfeld, Carlos Castillo, Marius Brackmann, Christopher Sarkizi, Katharina Hofer, and Yannic Mast.

I wish to acknowledge the endless support and great love of my family: my wife, Fecianti; my son, Evander; my mother; and my father.

Contents

Decleration of Originality

I declare that the submitted work has been completed by me and that I have not used any other than permitted reference sources or materials. All references and other sources used by me have been appropriately acknowledged in the work.

Hiermit erkläre ich, dass ich die vorliegende Arbeit selbstständig angefertigt habe. Es wurden von mir nur die in der Arbeit ausdrücklich benannten Quellen und Hilfsmittel benutzt. Übernommenes Gedankengut wurde von mir als solches kenntlich gemacht.

Stuttgart, 15 May 2022

Andy Wiranata Wijaya

Papers

Paper I

Junghans, L., Teleki, A., **Wijaya, A. W.**, Becker, M., Schweikert, M., & Takors, R. (2019). From nutritional wealth to autophagy: *in vivo* metabolic dynamics in the cytosol, mitochondrion and shuttles of IgG producing CHO cells. *Metabolic engineering*, 54, 145-159.

Andy Wiranata Wijaya (AWW) performed metabolomics data analysis, simulation, and modelling using Isotopically Non-Stationary ^{13}C Metabolic Flux Analysis, graphical visualization of flux map, biological interpretation of the flux results, and write the manuscript

Paper II

Wijaya, A. W., & Takors, R. (2021). A transhydrogenase-like mechanism in CHO cells comprising concerted cytosolic reaction and mitochondrial shuttling activities. *Biochemical Engineering Journal*, 170, 107986.

Andy Wiranata Wijaya (AWW) conceptualize the study, performed data-analysis, flux visualization, and write the manuscript.

Paper III

Wijaya, A. W., Ulmer, A., Hundsdorfer, L., Verhagen, N., Teleki, A., & Takors, R. (2021). Compartment-specific metabolome labeling enables the identification of subcellular fluxes that may serve as promising metabolic engineering targets in CHO cells. *Bioprocess and biosystems engineering*, 44(12), 2567-2578.

Andy Wiranata Wijaya (AWW) conceptualize the study, performed data-analysis, metabolic flux analysis, flux visualization, and write the manuscript.

Paper IV

Wijaya, A. W., Verhagen, N., Teleki, A., & Takors, R. (2021). Compartment-specific ^{13}C metabolic flux analysis reveals boosted NADPH availability coinciding with increased cell-specific productivity for IgG1 producing CHO cells after MTA treatment. *Engineering in Life Sciences*, 21(12), 832-847.

Andy Wiranata Wijaya (AWW) conceptualize the study, performed data-analysis, metabolic flux analysis, flux visualization, and write the manuscript.

Paper V

Verhagen, N., **Wijaya, A. W.**,, Teleki, A., Fadhlullah, M., Unsoeld, A., Schilling, M., ... & Takors, R. (2020). Comparison of L-tyrosine containing dipeptides reveals maximum ATP availability for L-prolyl-L-tyrosine in CHO cells. *Engineering in life sciences*, 20(9-10), 384-394.

Andy Wiranata Wijaya (AWW) performed data-analysis, constrained-based analysis, flux visualization, and write the manuscript.

List of Figures

List of Tables

Zusammenfassung

Chinese Hamster Ovary Zellen sind derzeit im Fokus der mAb-Produktion und machen über 70% der gesamt zugelassenen Biopharmazeutika aus. Die bevorstehende Patentfreigabe von Blockbuster-Medikamenten öffnet den Markt für alternative Biosimilars. Diese Alternativen schaffen Preiswettbewerb, daher wurde die Entwicklung von Biosimilars durch die Notwendigkeit vorangetrieben, die Herstellungskosten zu senken.

Die Senkung der Herstellungskosten könnte durch die Optimierung der Zelllinien oder Zellkulturmedien erreicht werden. Dabei spielt OMICS eine wichtige Rolle, insbesondere beim Verständnis von Zellstoffwechsel. OMICS-Technologien liefern Einblicke in die zellulären Fähigkeiten (Baupläne) zu den tatsächlichen Aktivitäten (Metabolom/Fluxom).

Diese Arbeit nutzte die Flussanalyse, um den Metabolismus von CHO-Zellen zu untersuchen, insbesondere unter Verwendung von Kohlenstoff-13 (^{13}C Stoffflussanalyse). Die Kombination aus isotopischem nichtstationärem ^{13}C Stoffflussanalyse, kompartimentiertem Stoffwechselmodell und dem subzellulären Metabolomprofil ermöglicht die Quantifizierung der *in vivo* mitochondrialen Shuttles sowie die Identifizierung der subzellulären Flüsse

(z. B. Isoenzyme). Letzteres wurde als Limitierung für die Verbesserung der IgG1-Produktion identifiziert.

Abstract

Chinese hamster ovary cells is currently a prime focus in mAb production, comprising over 70% of the total approved biologics. The coming patent expiration of blockbuster drugs triggers new market competition for alternative biosimilars. These alternatives create price competition, hence, biosimilar development has been driven by the need to reduce the manufacturing cost.

Reducing the manufacturing cost could be achieved by the optimization of the cell lines or cell culture media. For this purpose, OMICS plays an important role, especially to understand cellular metabolism. OMICS technologies provide insights into the cellular capabilities (blueprint) to the actual activities (metabolome/fluxome).

This thesis utilized flux analysis to study the metabolism of CHO cells, especially with the use of Carbon-13 (^{13}C Metabolic Flux Analysis). The combination of isotopic non-stationary ^{13}C MFA, compartmented metabolic model, and the sub-cellular metabolome profile allow the quantification of the *in vivo* mitochondrial shuttles and identification of the sub-cellular fluxes (e.g. isoenzymes). The latter was identified as the bottleneck for improving IgG1 production.

Chapter 1

Introduction

1.1. History of the Chinese hamster ovary cells

More than 60 years ago, Dr. Theodore Puck ("the father of CHO cells") received a female Chinese hamster in his laboratory at the Boston Cancer Research Foundation. Accordingly, he isolated and immortalised the hamster's ovary cells [TP58]. These immortalised cells are well-known as Chinese Hamster Ovary cells (CHO cells). Since then, these cells have been transferred from laboratory-to-laboratory and used as the model organism of mammalian cells (the *Escherichia coli* of mammalian cells) [WW17].

Before the era of CHO cells, *E. coli* and baker yeast (*Saccharomyces cerevisiae*) were used in the production of various biologics, for example, insulin and growth hormones [Wal14]. Later in 1986, Genentech marked the first production of therapeutics protein with mammalian cells (the tissue plasminogen activator, tPA). At that time, Genentech scientist tried to produce

tPA with *E. coli* as the host. All in all, the productivity using *E. coli* was half of the CHO cells', the protein was not properly folded, and another step of post-translational modification was required [DEM+16]. Since then, mammalian cells have been the majority production host for therapeutic proteins. Nowadays, production with CHO cells accounts for more than 70% of the total approved biologics[JWHY+07]. Notably, in 2018, 57 out of the 68 mAb products approved are produced using CHO cells as host [Wal18].

1.2. Improving the cell-specific productivity (CSP)

In the coming years, most of the blockbuster biologics' patents will reach the expiry. Thus, this opens up new opportunities and competitions as the biosimilars enter the market. Consequently, bio-manufacturing paradigm is currently shifting based on these three criteria: (1) speed-to-market; (2) cost-efficiency; and (3) manufacturing flexibility. Therefore, process intensification as an effort to increase the volumetric productivity (product mass per bioreactor volume per time unit), is a topic of interest [CWG18]. Traditionally, cells were cultivated in $7-14$ days fed-batch processes to produce the recombinant protein. This yields approximately a titer of $1-5\ \mathrm{g\,L^{-1}}$, which corresponds to a volumetric productivity of $0.1-0.7\ \mathrm{g\,L^{-1}\,d^{-1}}$ [Kel09; XGJC17; YMK+16]. In recent development using an intensified/concentrated fed-batch processes, the volumetric productivity could be increased to $1-2\ \mathrm{g\,L^{-1}\,d^{-1}}$ [XGJC17; YMK+16]. To achieve a similar or better volumetric productivity using a smaller facility footprint, continuous processes are required, for instance, the perfusion process. Furthermore, cell-specific productivity (CSP), Viable Cell Density (VCD), and the culture length are the key parameters to achieve a success process intensification [CWG18].

Over the past decades, there have been many efforts to improve the CSP, for

example, generating more efficient and stable cell-lines [HGY+13; MBHW11; WW17]; switching to chemically-defined media [KKK+15a; PSD+17]; and bioprocess development [KOT+05; MKK+17], which resulted in the improvement of cell viability and stability during the production processes. Consequently, a 100-fold production titer increase was recorded when comparing the process in the 1980s and early 2000s. The production process in the 1980s typically lasted for seven days with no more than 2×10^6 cells ml^{-1} VCD; productivity slightly below 10 pg $cell^{-1}$ d^{-1} and 50 mg L^{-1} product titer. Advancing to the late 2000s, the production process can be maintained for almost three weeks with final VCD of 10×10^{10} cells ml^{-1} and product titer of almost 5 g L^{-1}. However, the titer increase did not follow by the CSP increase (from approximately 10 pg $cell^{-1}$ d^{-1} to below 40 pg $cell^{-1}$ d^{-1}) [DW11; KR16; LSA10; Wur04]. Hence, study of CHO cells should focus on the CSP improvement.

Having said that, the CSP could be enhanced by two means: (1) cell line development/cellular engineering; or (2) media optimization. In both cases, the use of systems biology tool (-OMICS) to study the metabolism alteration would be advantageous [KBLB13; Kit02; SSB+18]. Eventually, metabolism study might shed a light to the new metabolic engineering target and/or new novel ingredients for the cell culture media. Since the first industrial application, there have been many efforts to study and characterize CHO cells with systems biology approaches. Table 1.1 summarized the milestones of CHO cells studies since the first establishment in 1957.

Table 1.1.: Some of the most important milestones in CHO studies

YEAR	-omics studies	Milestones	Cell line
1957	–	Establishment of CHO cells [TP58]	CHO-ori
1987	–	Mitochondria isolation from CHO cells [MS87]	CHO-S

Table 1.1.: Some of the most important milestones in CHO studies (continued)

YEAR	-omics studies	Milestones	Cell line
	–	Lysosome protein isolation from CHO cells [MWS87]	
1999	Fluxomics	**First CHO metabolic model** • Metabolic flux analysis to study protein metabolism [NBF+99]	γ-CHO
2010	Fluxomics	**Two of the very first ^{13}C MFA applied in CHO cells** Study of perfusion cultures [GBB+10b]	N.A.
		Study of CHO's stationary phase [SRM11]	CHO-GS SF18
2011	Genomics	CHO-K1 genome sequence was published [XNL+11]	CHO-K1
	Transcriptomics	Transcript analysis using NGS [BHR+11]	CHO-K1
	Fluxomics	^{13}C MFA of CHO cells during growth and stationary phase [AA11]	CHO-K1
	Metabolomics	CHO cells metabolic profiling [SCM+11]	CHO-GS LB01
2012	Proteomics	LC-MS/MS based proteomic analysis [BTC+12]	CHO-K1
2013	Fluxomics	^{13}C MFA of CHO cells in fed-batch cultivation [TDRY13]	N.A.
	Fluxomics	CHO study using metabolic and kinetic model [GHJ13]	CRL9606

Table 1.1.: Some of the most important milestones in CHO studies (continued)

YEAR	-omics studies	Milestones	Cell line
2015	Metabolomics	Sub-cellular metabolomics technique enables metabolite profiling in mitochondria [MTPT15]	CHO-DP12
	Fluxomics	Using elementary flux modes to characterize isolated mitochondrial using selective pemeabilized CHO cells [NWN+15]	CHO-K1
2016	Genomics	First genome-scale CHO metabolic model was reconstructed [HAH+16]	–
2017	Fluxomics	^{13}C MFA was used to characterize different industrial cell lines [TSM+17]	CHOK1-SV
2019	Fluxomics	**First compartment-specific ^{13}C MFA** [JTW+19] • Characterize mitochondrial shuttle activities under different nutrient condition • New cellular NADPH source identified • Metabolic engineering target for improving IgG productivity was identified	CHO-DP12

1.3. Unravelling the mechanistic and physiological function of media additives

Animal-cell culture media development has been an attractive topic even since before the establishment of CHO cells (e.g. Eagle media in 1955 [Eag55]). Cell culture media, which was initially comprised of animal-derived serum (e.g. Fetal Bovine Serum; FBS or Fetal Calf Serum; FCS), was no longer attractive due to the prone risk of contamination and process variability. Accordingly, chemically-defined media was introduced and became the standard industrial-practise in therapeutic protein production.

Besides the cell line development and engineering, the optimization of cell culture media is the key to improve the CSP. One example is the optimization of amino acids composition to minimize metabolic waste [MWHY18]. Besides, the addition of different additives (e.g. growth factors or peptides) to the basal and feed media has been a common industrial practice to improve the process [BKP21; BVM+03; FTC+06]. Nonetheless, the related studies were carried out based on laboratory screening and without a deep mechanistic understanding of the impact of such compounds on cellular metabolism. Consequently, the mechanistic functionality of these compounds remains unknown, which could prevent the identification of novel compounds for cell culture media.

To study the impact of media additives, fluxomics is the suitable tool to unravel the mechanistic functioning of these additives to the cellular metabolism. The fate of these additives, when function as carbon sources, could be tracked inside the metabolism pathway. Meanwhile, those with stimulus properties will impact the carbon flow in the cellular metabolism. Thus, the phenotypic changes in term of metabolic flux discrepancy should be observed (Figure 1.1).

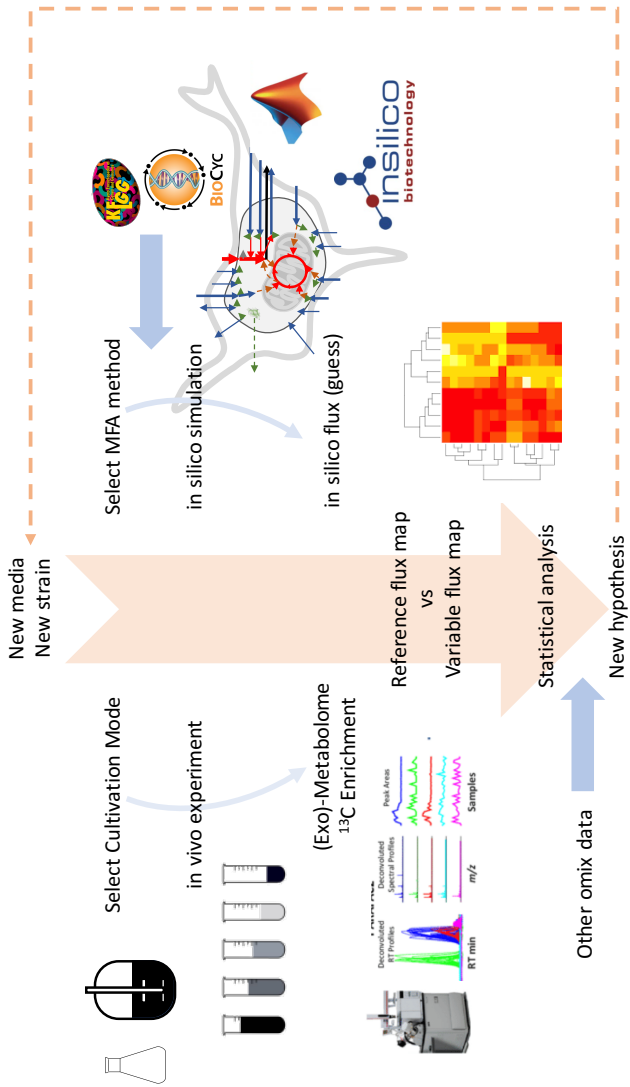

Figure 1.1.: Optimizing new cell line or new media using metabolic flux analysis

1.4. Metabolic compartmentalization in CHO cells metabolism

CHO cells are eukaryotic cells. Hence, it is a complex biological system, consisting of structural organization and spatial compartmentalization. In principle, cellular compartmentalization aims to restrict similar metabolic activities, in which different environments could be established (metabolome pool, enzyme concentration, or pH). Each organelle's membrane is very selectively permeable and the metabolite/protein inter-compartment transport is highly regulated and facilitated by a protein carrier [Pal04].

Spatial compartmentalization enables one enzyme type to operate in two different environmental conditions (isoenzyme), resulting in different metabolic behaviour (see Table 1.2). To date, these inter-compartment isoenzymes are poorly characterized for their *in vivo* activities. Furthermore, different isoform of the enzymes might possess different cofactors specificity in different compartment, serving a completely different metabolic purposes [HAH+16].

In the context of CHO cells as production host, the understanding of metabolism in different compartment could potentially optimize the protein production. One example is to decipher the glucose fate inside the cells which is highly

Table 1.2.: Genome-annotated isoenzymes (cytosol-mitochondria) of Chinese Hamster Ovary Cells in the central carbon metabolism pathway [HAH+16]

Enzyme	Compartment	
	Cytosol	Mitochondria
Aspartate transaminase	Got1, Got1l1	Got2
Malate dehydrogenase	Mdh1, Mdh1b	Mdh2
Malic enzyme	Me1	Me2, Me3
PEP Carboxykinase	Pck1	Pck2

regulated and interconnected with energy generation. Glucose is metabolized via glycolysis, producing pyruvate. In CHO cells, a portion of pyruvate was channelled into mitochondria, while, the rest is converted into lactate to reinstall the NAD^+ required in glycolysis. In this case, mitochondrion is the organelle responsible for generating most of the energy in the form of ATP [PHB22]. Maximizing pyruvate channelling to mitochondria (improved ATP production) could potentially lead to the antibody CSP improvement.

1.5. Mitochondrial shuttles

The mitochondrial membrane is selectively permeable, consisting of metabolite/solute carriers. In CHO cells, the majority of these carriers are annotated in the solute carrier family 25 (SLC25) and mitochondrial pyruvate carrier proteins (MPC) [HAH+16]. There are approximately 51 genes belonging to SLC25 that are annotated in the latest genome. These carriers play an essential role for maintaining a balanced resource between cytosol and mitochondria.

Regarding the glucose/energy metabolism, mitochondrial carrier certainly plays an essential role, especially the Mitochondrial Pyruvate Carrier (MPC). The overexpression of MPC in CHO cells has been reported to reduce lactate secretion [BPP+20]. Therefore, the alteration of MPC improves ATP production.

Besides its metabolite transport role, the synergy of multiple carriers also formed a complex shuttle system, possessing a distinct metabolic function. For example, the Malate-Aspartate Shuttle (MAS) for cytosolic NADH translocation to enzyme complex I in the inner mitochondrial membrane; and Malate-Pyruvate Shuttle (MPS) for NADPH generation [Pal04; Pal13]. MAS is an integral part of the cellular energy metabolism since NAD^+/NADH could

not be transported directly through the mitochondrial membrane. MAS has been extensively studied in mouse liver and other cell types, resulting in a general consensus that MAS is crucial for mammalian cells [Bor20; Mac82]. The activity of MAS was hypothesized to be the critical factor in beta-cells metabolism [SAB+00]. Very little is currently known about the existence and activity of such shuttle systems in CHO cells. Another similar shuttle, Citrate-Malate Shuttle (CMS), is also known to serve a similar purpose as MAS [Pal04]. Research to date has not yet determined the *in vivo* activity of these shuttles, which could be a crucial metabolic engineering target for improving CSP.

1.6. Fluxomics

The CSPs are cellular intrinsic parameters, which could be optimized by understanding the cellular metabolism. In this study, fluxomics was applied to study cellular metabolism since metabolic flux is the downstream and outcome of multiple cellular regulatory mechanisms at different level as depicted in Figure 1.2.

Fluxomics has been a leading -omics tool, especially in the field of microbial metabolic engineering [CN00; DEM+03; PM85; VP94; Wie01]. The tools has been used to assess the metabolism of a cell factory, identifying metabolic bottleneck, and adjusting the metabolism by the means of cellular engineering. In CHO cells, this tool has recently gained an interest, in particular to assist the process and media development activities [KBLB13].

The first flux analysis study in CHO cells was reported back in 1999 [NBF+99]. This study focused on the understanding of protein metabolism in γ-CHO cells. That study also featured the very first published metabolic model of CHO cells. Subsequently, it opened further flux analysis studies on CHO

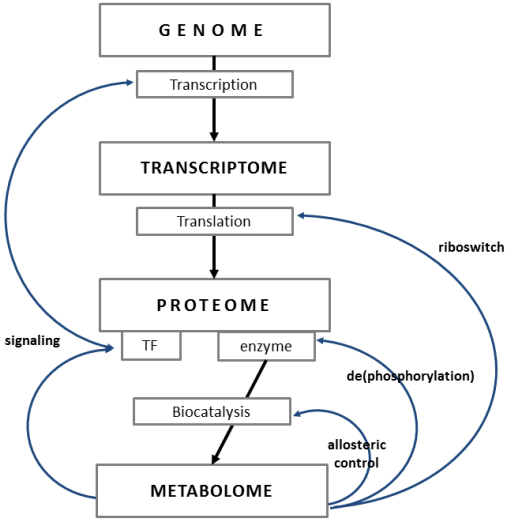

Figure 1.2.: Complex biological systems: interactions between different cellular -omics level from genome to metabolome [Kre07]

cells, from traditional metabolite-balancing based MFA to the application of carbon tracer (^{13}C MFA).

Even though metabolite balancing has been the fundamental characteristic of MFA [VP94], the utilization of stable isotopic compounds (e.g. ^{13}C, ^{15}N, or ^{2}H) for flux analysis has proven to significantly improve the flux quantification [Wie01]. The classical MFA/FBA relies on the balancing of every intracellular metabolites, including cofactors and electrons. Thus, it is less suitable to be applied for unraveling the compartment-specific metabolism in CHO cells due to the high cofactors specificity unknown. Moreover, FBA often misinterprets the futile cycles and pathway branching. This includes the fluxes of non-calculatable and non-identifiable pathway, e.g. the glycolytic-PPP splitting [AA11; SMR08; TDRY13]; anaplerotic reactions; and even the mitochondrial shuttle activities [JTW+19].

^{13}C metabolic flux analysis is also based on the same principle as the traditional counter-part (metabolite balancing). On top of that, the application of carbon-13 enabled the tracking of the carbon isotope fate inside the cellular metabolism. Hence, the additional information generated from the carbon-13 tracking surpass the use of cofactors and electron balancing. Thus, cofactors and electron balancing are not required in ^{13}C MFA, enabling a more accurate flux estimation. The tracking of carbon-13 inside the metabolism pathway could be performed by two means: isotopomer or isotopologue analysis. The identification and measurement of metabolites isotopomer is carried out by Nuclear Magnetic Resonance (NMR). A preferred option is the measurement of mass-isotopomer (isotopologue) with the Mass Spectrometer (MS) devices due to the cost constraint.

Mammalian cell metabolism is generally slower than microbes. Thus, the incorporation of carbon-13 into each metabolite requires more time to reach the isotopic steady state. Furthermore, it is extremely challenging to maintain nutrient homeostasis in the *in vitro* culture of these cells. Thus, the isotopic steady-state ^{13}C MFA could not be applied in the relatively short time frame. The labeling dynamics must be monitored and considered in the mathematical computation. Therefore, the isotopic non-stationary ^{13}C MFA is the appropriate tool for characterizing the CHO cells metabolism.

1.7. Compartment-specific ^{13}C Metabolic Flux Analysis

Flux analysis studies in CHO cells were initially performed with one-compartment model ([NBF+99]). However, recent studies showed that metabolic model compartmentalization must be considered when performing flux analysis studies in CHO cells ([NWB+14; PT17]). In principle, there are two levels of complexity: on the one hand, subcellular metabolic models should be

used to enable proper *in silico* predictions [NWB+14; PT17]; on the other hand, *in vivo* compartment-specific metabolome data should be accessible to allow data-driven studies [JTW+19; WUH+21].

The lack of compartment-specificity in the existing CHO cells ^{13}C MFA studies [AA11; TDRY13; TSM+17] was the result of the technology challenges in sub-cellular metabolomics [AA12], hindering the physiological understanding of the *in vivo* compartment-specific metabolism, in particular the *in vivo* metabolic physiology of CHO's mitochondria. To overcome the technology shortage, Nicolae and coworkers [NWN+15] introduced systems biology approaches (elementary node analysis) to study the isolated active CHO's mitochondria. Such approaches, however, are unsatisfactory because it was still uncertain whether the observation reflected the *in vivo* metabolism.

Subsequently, Matuszczyk and coworkers [MTPT15] developed the very first sub-cellular metabolomics technique, enabling access to the cytosol-free metabolome profile in CHO cells (Figure 1.3). This technology extends the flux quantification to another level, allowing the quantification of the inter-compartment isoenzymes, for example, malic enzyme and malate dehydrogenase [JTW+19; WUH+21].

The utilization of compartment-specific carbon-13 data and the non-stationary ^{13}C MFA allow the tools to resolve the sub-cellular metabolism even further [WUH+21]. Besides quantifying the sub-cellular fluxes and isoenzymes activities, compartment-specific ^{13}C MFA is also expected to resolve the mitochondrial solute carriers. Mitochondrial solute carriers are responsible for transporting various metabolites to/from mitochondria hence dictating the metabolic activity in both compartments.

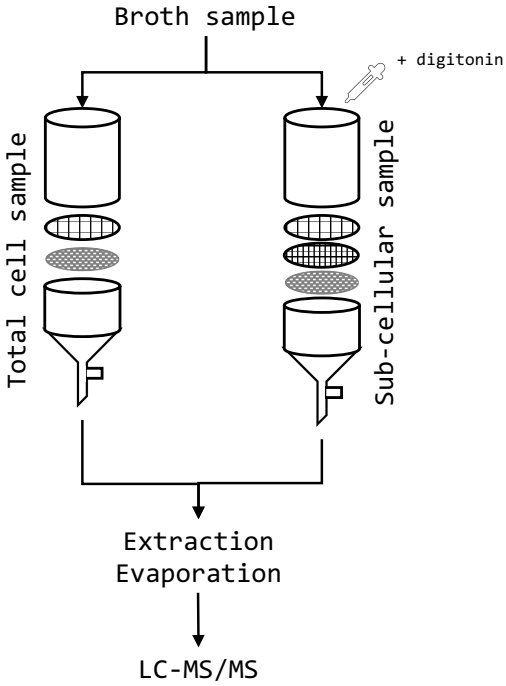

Figure 1.3.: Compartment-specific metabolomics developed by Matusczcyk and coworkers (2015) [MTPT15]

1.8. Scope of thesis

This thesis contributes to the paucity of the existing ^{13}C MFA studies in CHO cells, especially regarding the subcellular metabolism. A comprehensive insight into CHO-DP12 cell metabolism is provided, including the isoenzymes, sub-cellular, and mitochondrial shuttles' activities. Hence, this work focuses on the application of compartment-specific metabolomics (Matusczcyk and coworkers, 2015) to the non-stationary ^{13}C MFA. Therefore, this thesis is composed of a literature review (**chapter 2**) and 4 studies/chapters.

In **chapter 3**, the compartment-specific ^{13}C MFA was applied to study the metabolism of CHO-DP12 under different culture condition: nutrient in excess, L-glutamine limited, nitrogen starvation, and autophagy. In this study, the method was capable of estimating the fluxes of the central carbon metabolism including isoenzymes, subcellular fluxes, and mitochondrial shuttles. The metabolic phenotypes were eventually linked to the antibody CSP, which led to the identification of the metabolic engineering target.

NADH and NADPH are pivotal in cellular metabolism. Balancing the cellular NADH and NADPH are essential to support cellular growth, counter oxidative stress, and synthesize recombinant protein. Following the study in **chapter 3**, cellular NADH and NADPH was calculated using the metabolic flux distribution obtained from ^{13}C MFA. After balancing the cellular NADH and NADPH production-consumption, an interesting yet crucial mechanism was observed. Thus, **chapter 4** aimed to describe a special mechanism that has similar objective as the transhydrogenase enzyme (the conversion of NADH to NADPH or vice versa).

In **chapter 5**, the utilization of subcellular metabolomics was challenged by the means of computational modeling. The same metabolic model was used to estimate the metabolic fluxes using: (1) whole-cell metabolome information and (2) sub-cellular metabolome information. The estimated fluxes were analyzed and qualified whether the subcellular metabolome information must be used to obtain reliable flux estimation.

Eventually, the compartment-specific ^{13}C MFA was applied in studying the impact of cell culture media additives. In **chapter 6**, the metabolic impact of supplementing 5'-methylthioadenosine (MFA) in CHO-DP12 was studied. Flux analysis demonstrated that the cell underwent metabolic reprogramming when MTA was fed to the culture. Hence, the metabolic reprogramming led to an increase in antibody CSP.

Chapter 2

Theoretical Background

2.1. Chinese Hamster Ovary Cells

Chinese hamster (*Cricetulus griseus*) cells are epithelial cells derived from the ovary of a Chinese hamster in the laboratory of Dr. Theodore Puck. Since the process was badly documented, cell-culture experts decided to name the very first reported cell as CHO-ori [WW17]. These days, the offspring of CHO-ori [Puc85; TP58] are widely used in industrial scale for therapeutic protein production. Some of the most widely used cell lines in industrial and research settings are CHO-K1, CHO-DXB11, CHO-S, or CHO-DG44 [WW17]. CHO-DBX11 and CHO-DG44 are two cell lines with dihydrofolate reductase (DHFR) deficient [HM90].

2.2. Cell culture media development

2.2.1. History of cell culture media development

Scientists have been working on media development for cell culture application even before the establishment of CHO cells [Eag55; FPS59]. The use of animal-derived compounds in the traditional cell culture media is prone to the risk of contamination [WL99]. Therefore, the very first motive of cell culture media development is to substitute the animal-derived serum (e.g. Fetal Bovine Serum; FBS) in cell culture media. Besides, the inconsistent chemical composition of the FBS often caused performance variability and poor reproducibility [VBD+10]. Hence, FBS is no longer favourable, especially for industrial application [But05].

Various scientific reports indicate that initially, FBS was substituted with non-animal components, for example, hormones and latter vegetable hydrolysates. Nevertheless, these adjustments were still not adequate to solve the problem of process variability. Therefore, chemically-defined media, consisting of amino acids, sugar and trace mineral elements, was developed [GMG85; Ham65; HH77; HTY+92; MEO+09]. Table 2.1 summarized the cell culture media development.

Table 2.1.: Cell culture media development timeline

Year	Summary of cell culture media developed	References
1955	Eagle's media: Limited chemical defined media with 0.5 to 2% dialyzed horse serum; 12 essential L- amino acids were identified	[Eag55]
1959	The use of purified fetuin and albumin protein to replace serum for chemically defined media; experiment conducted only by platting	[FPS59]

Table 2.1.: Cell culture media development timeline (continued)

Year	Summary of cell culture media developed	References
1965*	Chemically defined media (F12) was formulated; suitable only for plating (not liquid fermentation)	[Ham65]
1976, 1979	The utilization of hormone to replace serum	[BS79; HS76]
1977*	Modification of F12 media, by introducing the addition of trace elements.	[HH77]
1985*	New synthetic media (GC3) was formulated. GC3 is composed of 1:1 mixture of F12[Ham65] and modified Eagle's media[Eag55] and supplemented with transferrin, insulin and selenium.	[GMG85]
1992*	The development of serum-free chemical defined media for the production of recombinant protein (hGH)	[HTY+92]
1995*	WCM5 serum-free media was tested for the production of IgG. WCM5 contains insulin as protein, ferric citrate to replace transferrin and choline chloride to replace lipid	[KR95]
2000	The use of vegetarian hydrolyzed peptones for the production of recombinant protein. Comparable quality and glycosylation pattern were observed. Furthermore, there were indications that amino acids could be used to replace peptones.	[HZQ+00]
2005	The substitution of insulin with amino acids and zinc compound.	[ZR05]
2007*	Protein-free chemical defined media was developed and tested for EH1 production using CHO as cell host	[HMG07]
2009*	Replacement of hydrolysate containing media with chemically defined media (consisting of amino acids)	[MEO+09]
2010*	The evaluation of dipeptides (AlaGln and AlaTyr) towards CHO growth and recombinant protein production	[ITT+10]
2010*	The substitution of glutamine by glutamate to prevent ammonium accumulation	[HCY10]

Table 2.1.: Cell culture media development timeline (continued)

Year	Summary of cell culture media developed	References
2012*	The utilization of Tyrosine- and Histidine-containing dipeptides enhance culture viability and recombinant protein production	[KMMD12]
2014*	CHO media optimization by altering the supplementation of amino acids; dipeptides and tripeptides (for low soluble amino acid)	[KKK+15b]

* CHO cell culture media development

2.2.2. Cell culture media additives

For the past decades, there have been efforts to improve the cell-specific antibody productivity by altering the cell culture media. One of the examples is the amino acids re-balancing [MWHY18; XKK+11]. On the other hand, novel media ingredients were supplemented to the medium, such as growth factors [GM76] and dipeptides [ASR98; KMMD12; ROH+88; SBP+16], to boost the cellular performance. Nevertheless, the mechanistic and physiological understanding of these compounds' role in cellular metabolism is still very limited. For example, the study of peptide feeding on the central carbon metabolism pathway, Nyberg and coworkers [NBF+99] concluded that the peptide was hydrolyzed into amino acids before being metabolized and was significantly assimilated into central carbon metabolism pathway.

Among the cell culture media additives, dipeptides are famous as the amino acids' substitute. Dipeptides have been used in cell culture media as the answer for amino acids' physio-chemicals limitation, such as stability (e.g. L-glutamine based dipeptides) or solubility (e.g. L-tyrosine based dipeptides). Thus, enhancing the amino acids availability in the media [ASR98; Für98;

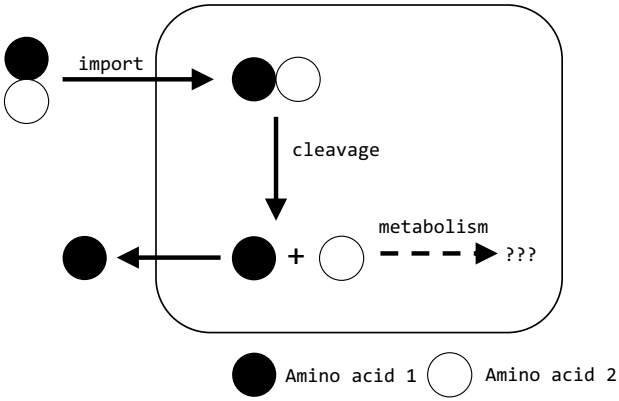

Figure 2.1.: Dipeptide consumption model proposed by Sanchez-Kopper and coworkers (2016) [SBP+16]

KMMD12]. There were various reports that the addition of dipeptides to cell culture media could enhance the cell culture bioprocesses, especially the recombinant antibody productivity [CB94; EP93; KMMD12]. Nevertheless, the basic understanding of dipeptide metabolism in CHO cells was not apparent until Sánchez-Kopper and coworkers [SBP+16] propose the dipeptide hydrolysis model when studying the dipeptide uptake kinetics in CHO cells (Figure 2.1).

2.3. Chinese hamster ovary cell metabolic model

CHO cell metabolism can be grouped into several classes according to the function, as depicted in Figure 2.2. These include catabolism, anabolism and biosynthetic reactions for growth and recombinant protein. The model consists of carbon catabolism (e.g. D-glucose and L-glutamine) to produce ATP and NADPH required for cellular anabolism. Additionally, precursors

required for cellular anabolism are also generated, such as Ru5P, DHAP, AcCoA, GAP, Pyr, and α-KG. The precursors generated in the first part are used in the cellular anabolism to synthesize endogenous carbon storage (presumably glycogen), nucleotides, glycerophospholipid, fatty acids and non-essential amino acids. CHO cells are not able to synthesize all the essential amino acids. Thus, these amino acids must be supplemented in the growth media.

Generally, a metabolic model should comprise the uptake of all the major nutrients in the media (typically carbon and nitrogen sources), the release/sink of major (by)-products, central carbon metabolism pathway and lumped anabolic reactions of its macromolecules biosynthesis (e.g. biomass and IgG). The metabolic model could be extended in the case of special studies involving special compounds that directly contributes to the carbon flow. For example, the study of dipeptide benefits in cell culture media must include the dipeptide cleavage model [SBP+16]. Conversely, the metabolic pathway of compounds that exclusively alter cellular regulatory mechanism is not necessary to be included in the metabolic model.

The selection of flux analysis technique also dictates the size of the metabolic model applied. For stoichiometric flux analysis (or classical MFA), a metabolic model must represent the criteria as mentioned earlier. Furthermore, a set of linear biochemical reactions/pathway could be lumped into one reaction. When using only the stoichiometric flux analysis or constrained-based analysis, it is almost impossible to solve the inter-compartments isoenzymes fluxes (e.g. malic enzyme). Hence, one of the isoenzymes could be assumed inactive. In the application of ^{13}C MFA, the detail of the metabolic model used usually depends on the labelled substrate of choice and the metabolome data availability [Ant15; WUH+21].

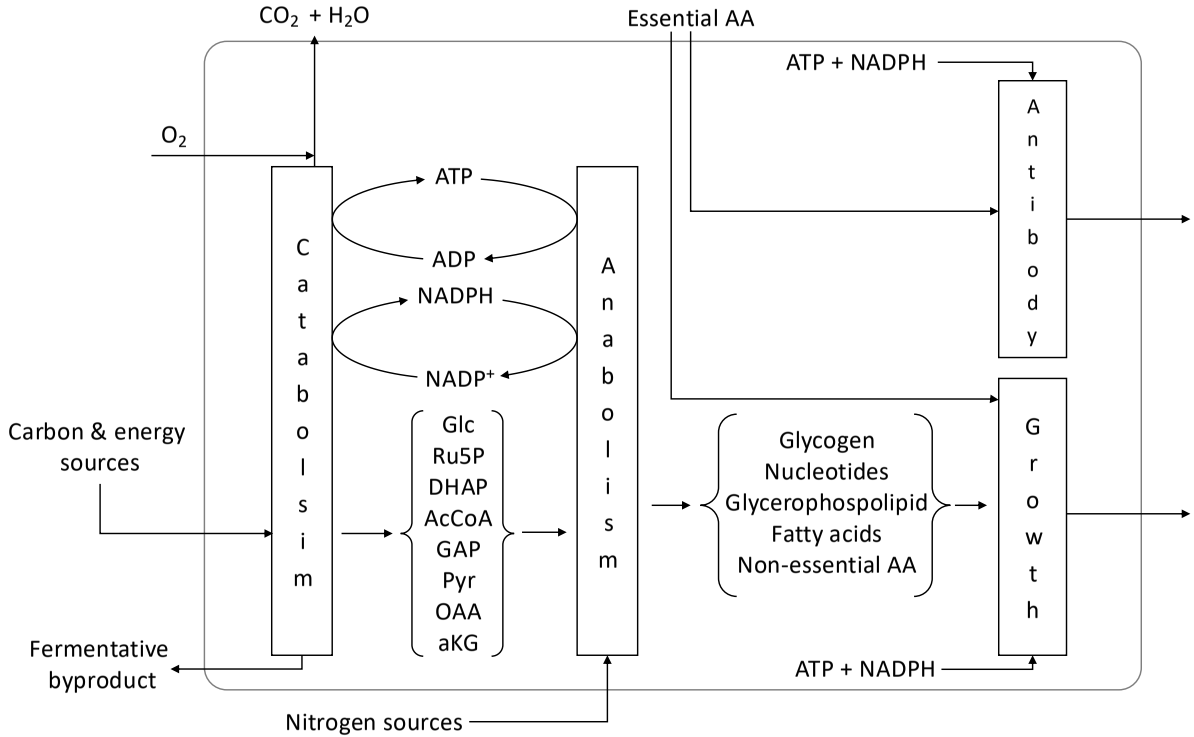

Figure 2.2.: Major parts of CHO metabolism. Figure was adapted from "Systems Biology - Properties of Reconstructed Networks" by Bernhard Ø Palsson, 2006, *Cambridge University Press* [Pal06]

2.3.1. Metabolic compartmentalization

Eukaryotes (e.g. mammalian cells) are multi-compartment biological systems, comprising cytosol, mitochondria, nucleus, endoplasmic reticulum (ER), peroxisome, golgi-apparatus (GA), lysosome and nucleus [MBB+18]. Metabolic compartmentalization is an important part to study eukaryotic cells [AA12]. Several studies have reported the importance of metabolic compartmentalization in CHO cells: (1) Pfizenmaier and Takors (2017) reported an overestimation of ATP in stoichiometric MFA studies with a non-compartmented model [PT17]; and (2) Nicolae and coworkers [NWB+14] encountered a sparse data fitting on single-compartment model when performing ^{13}C MFA and on contrary, multi-compartment model performed very well.

When performing metabolic modelling of CHO's central carbon metabolism pathway, at least two compartments are required: cytosol and mitochondria [AA12; NWB+14]. Initial processing of the nutrients occurs in the cytosol where the catabolism of sugars and amino acids took place. Subsequently, the intermediates metabolites were transferred into mitochondria to be fully catabolized and generated energy [MBB+18].

The other organelles, except cytosol and mitochondria, are usually not essential for this purpose because of the very low carbon flux in the respective organelles. Besides, often, these organelles are not the main interest of the study. Several exceptions are, for example, the study of *de novo* lipid biosynthesis pathway in CHO cells and antibody glycosylation must include ER and GA since both processes occur in the respective organelles.

2.3.2. Cellular catabolism

Catabolism is an essential process in a proliferating cell as it provides energy and precursors for the anabolic processes (Table 2.2). D-glucose consuming CHO cells require EMP (glycolysis), PPP, TCA cycle and anaplerotic reactions in the catabolism processes. D-glucose is initially processed in glycolysis, yielding 2 moles of NADH and 4 moles of ATP per mole of D-glucose. Also, several precursors required for cellular anabolism were generated, such as DHAP, 3PG and Pyr [LV11].

A fraction of the glycolytic carbon is typically channelled to the Pentose-Phosphate Pathway (PPP). The PPP supplies Ribose-5-phosphate (R5P), which is a precursor for nucleotide biosynthesis. In addition, the oxidative branch of the PPP also provides 2 moles of NADPH per mole of G6P. The latter is an essential electron carrier for cellular anabolic processes [HV18; LV11].

The final product of glycolysis, pyruvate, is then processed into the Citric Acid Cycle (CAC). CAC plays a vital role in mammalian cells' metabolism, like CHO cells. This metabolic pathway produces reducing equivalents to fuel the oxidative phosphorylation. One full cycle of CAC yields 1 mole FADH2, 3 moles NADH and 1 mole ATP equivalent. Besides, CAC also supplies essential precursors for cellular anabolism, such as citrate for *de novo* lipid biosynthesis, α-KG and OAA for glutamate and asparate formation respectively [LV11].

The latest CHO's genome revealed that CHO cells possess the gene for cataplerotic and anaplerotic reactions, for example, cytosolic PEP carboxykinase (*PEPCk*), mitochondrial pyruvate carboxylase (*pc*), and malic enzymes [HAH+16]. Also, previous studies on CHO's metabolism pin-pointed malic enzyme as the dominant NADPH cellular source [AA11; TDRY13].

Table 2.2.: Stoichiometric precursor(s) and cofactor(s) requirement for endogenous carbon storage and lipid biosynthesis [LV11]

Metabolite	Precursor(s)	NH_3[a]	ATP	NADPH	NADH[b]	O_2
	Polysaccharide					
Glycogen (monomer)	G6P	–	1	–	–	–
	Lipid					
Cholesterol	18×AcCoA	–	18	31	–	11
Phosphatidylcholine	DHAP + 17.43×AcCoA	–	22.43	32.38	–1	1.52
Phosphatidylethanolamine	DHAP + 17.43×AcCoA	–	22.43	32.38	–1	1.52
Phosphatidylinositol	DHAP + 17.43×AcCoA	–	22.43	32.38	–1	1.52
Phosphatidylserine	DHAP + 17.43×AcCoA + 3PG	1	22.43	32.38	–	1.52
Phosphatidylglycerol	2×DHAP + 17.43×AcCoA	–	21.43	32.38	–2	1.52
Cardiolipin	3×DHAP + 34.86×AcCoA	–	42.86	64.76	–3	3.04
Sphingomyelin	3PG + 16.72×AcCoA	1	21.72	32.19	–	1.76
	Nucleotides					
ATP	R5P + 3PG	5	9	–	1	–
GTP	R5P + 3PG + 2×C	5	10	–	2	–
CTP	R5P + OAA	3	6	–	1	–
UTP	R5P + OAA	2	5	–	1	–
dATP	R5P + 3PG + 2×C	5	9	1	1	–
dGTP	R5P + 3PG + 2×C	5	10	1	2	–
dCTP	R5P + OAA	3	6	1	1	–
dTTP	R5P + OAA + 1×C	2	7	2	1	–
	Non-essential amino acids					
L-alanine	Pyr	1	–	–	–	–
L-aspartate	OAA	1	–	–	–	–
L-glutamate	α-KG	1	–	–	–	–
Glycine	3PG	1	–	–	1	–
L-proline	α-KG	1	1	2	–	–
L-serine	3PG	1	–	–	1	–

[a] amino group requirement from nitrogen sources
[b] minus value means NADH production

2.3.3. Anabolic requirement

The cellular anabolic requirement for the protein, lipids, RNA, DNA, carbohydrates synthesize, and ATP demand follows the biomass composition proposed by Sheikh and coworkers [SFN05] (Table 2.3). Additional to Table 2.3, a cell density of 122 pg/cell was assumed. This biomass density was assumed to correlate with cellular volumetric density linearly.

Table 2.3.: Biomass composition and energy (ATP) requirement for growth [SFN05]

Metabolite	mmol/g_{DW}	Metabolite	mmol/g_{DW}
Amino acids		**Carbon storage**	
L-alanine	0.600	Glycogen	0.279
L-arginine	0.377	**Nucleotides**	
L-aspartate	0.359	dAMP	0.0148
L-cysteine	0.145	dCMP	0.0099
L-glutamine	0.322	dGMP	0.0099
L-glutamate	0.386	dTMP	0.0148
Glycine	0.538	AMP	0.0330
L-histidine	0.143	CMP	0.0551
L-isoleucine	0.324	GMP	0.0624
L-leucine	0.564	UMP	0.0330
L-lysine	0.570	**Lipid**	
L-methionine	0.138	Cholesterol	0.018
L-phenylalanine	0.219	Phosphatidylcholine	0.010
L-proline	0.313	Phosphatidylethanolamine	0.026
L-serine	0.430	Phosphatidylinositol	0.010
L-threonine	0.386	Phosphatidylserine	0.003
L-tryptophan	0.044	Phosphatidylglycerol	0.001
L-tyrosine	0.182	Diphosphatidylglycerol	0.003
L-valine	0.416	Sphingomyelin	0.008
Energy (ATP) requirement			
protein synthesis & processing			29.04
RNA synthesis & processing			0.07
DNA synthesis & processing			0.07

2.3.4. Mitochondrial carriers

Mitochondrial carriers are membrane-embedded proteins that are localized in the inner membrane of a mitochondrion. All of these carriers, except the Mitochondrial Pyruvate Carrier (MPC), are encoded by the SLC25 (Solute Carrier Family 25) genes. These carriers aim to facilitate the transport of solutes through the permeability barrier of the inner membrane of a mitochondrion [Pal04].

The latest CHO's genome published by Xu and coworkers [XNL+11] indicates that CHO cells possess these mitochondrial carriers as well as the MPC. Table 2.4 summarized the mitochondrial carriers encoded in CHO-K1 gene. Besides, several studies [JTW+19] and the recent CHO genome-scale metabolic model reconstruction also indicated that the putative alanine and asparagine carriers are also the two essential carriers [HAH+16].

Table 2.4.: Mitochondrial carriers encoded in CHO gene: Mitochondrial Pyruvate Carrier and Solute Carrier Family 25 (SLC25) and carriers based on reconstruction of genome scale model [HAH+16]

Gene name	Protein name	Solute(s)*	NCBI Gene ID
		Encoded in CHO's genome	
MPC	MPC1 MPC2	[S]: Pyruvate-H^+	100756279 100766986
SLC25A1	CIC	[A]: Citrate-H^+/Malate	100751442
SLC25A3	PHC	[A]: Pi-H^+/Pi-OH^-	100758020
SLC25A4 SLC25A5	ANT1 ANT2	[A]: ADP/ATP	100751779 100769087
SLC25A10	DIC	[A]: Malate/Pi	100766192

Table 2.4.: Mitochondrial carriers encoded in CHO gene: Mitochondrial Pyruvate Carrier and Solute Carrier Family 25 (SLC25) and carriers based on reconstruction of genome scale model (continued)

Gene name	Protein name	Solute(s)*	NCBI Gene ID
SLC25A11	OGC	[A]: Oxoglutarate/Malate	100770598
SLC25A12	AGC1	[A]: Aspartate/Glutamate-H^+	100768097
SLC25A13	AGC2		100766212
SLC25A15	ORC1	[A]: Ornithine/Citruline-H^+	100773024
SLC25A18	GC2	[S]: Glutamate-H^+ OR	100756941
SLC25A22	GC1	[A]: Glutamate/OH^-	100752846
SLC25A21	ODC	[A]: Oxoadipate/Oxoglutarate	100756680
		Putative carriers	
–	mAla	[U]: Ala	–
–	mAsn	[U]: Asn	–

* [A]: antiporter; [S]: symporter; [U]: unknown

2.3.5. Mitochondrial shuttle systems

In the mammalian cells' metabolism, these carriers form the shuttle systems to serve different purposes. For example, one of the most well-known mitochondrial shuttles is Malate-Aspartate Shuttle (MAS), that serves as NADH shuttle into mitochondria [Mac82]. Other putative shuttles systems are depicted in Figure 2.3.

Pyruvate-Citrate Shuttle (Figure 2.3 A), comprising of MPC, CIC (Citrate

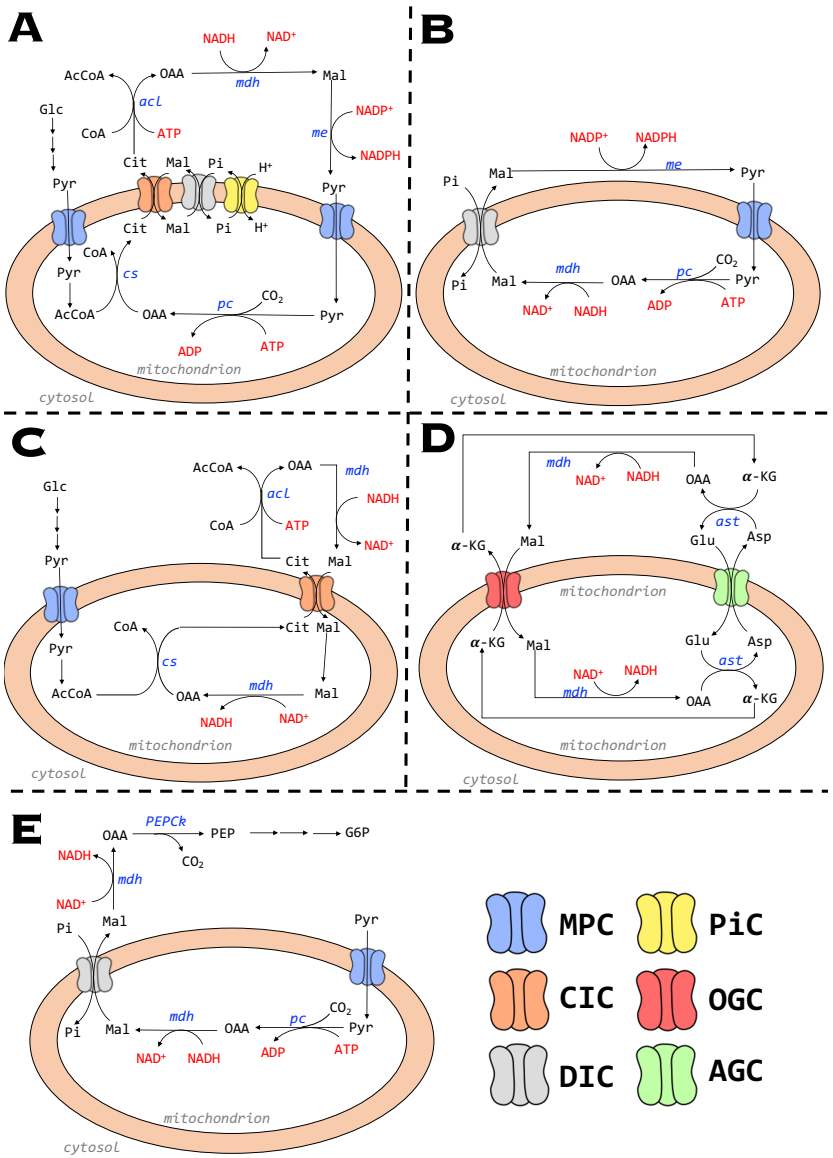

Figure 2.3.: Putative physiological role of mitochondrial shuttles in CHO cells: A. Pyruvate-Citrate Shuttle (PCS); B. Pyruvate-Malate Shuttle (PMS); C. Citrate-Malate Shuttle (CMS); D. Malate-Aspartate Shuttle (MAS); and E. Gluconeogenesis from Pyruvate. Figures were adapted from Palmieri (2003) [Pal04]

Carrier), DIC (Dicarboxylic acid carrier) and PiC (Phosphate/Pi Carrier), aims to convert the excess NADH in the cytosol into NADPH via cytosolic malate dehydrogenase and malic enzyme where malate served as the electron carrier. Several studies have indicated that PCS must be active in Pancreatic β-cells [FSCP00; GMA+07]. Even, the PCS is assumed to be crucial in the insulin secretion regulation. Nevertheless, there is no direct indication on the *in vivo* activity of PCS in CHO cells.

The existence of Pyruvate-Malate Shuttle (Figure 2.3 B)) has been hypothesized for more than two decades ago [Mac95]. MacDonald (1995) observed an increase in the enzyme content of MPC and DIC during the glucose-induced insulin secretion in pancreatic islets. Again, the main objective of PMS shuttle system is to convert mitochondrial-excess NADH to cytosolic NADPH indirectly. Again, similar to PCS, the *in vivo* activity has not yet been reported so far.

The goal of PCS and PMS are to produce cytosolic NADPH from either cytosolic or mitochondrial NADH resource. On the other hand, the Citrate-Malate Shuttle (Figure 2.3 C) and Malate-Aspartate-Shuttle (Figure 2.3 E) aim to transport NADH from the cytosol into mitochondria indirectly. Although both shuttle systems possess the same goal, the carriers involved in the systems are different. CMS composes of MPC and CIC; while MAS composes of OGC and AGC.

2.3.6. Metabolic network

A metabolic network model was formulated for the labelling study using ^{13}C glucose using the essential cellular catabolism and anabolism information based on the latest genomics and model reconstruction [HAH+16]. Several reactions were simplified to account for the metabolomics capability. For

example, Ribulose-5-P, Ribose-5-P, and Xylulose-5-P could not be adequately separated using our in-house chromatography methodology. Thus, P5P was formulated to account for the three pentose-5 phosphate metabolites. The model only comprises of 6 amino acids: L-Glutamine, L-Asparagine, L-Serine, L-Alanine, L-Aspartate, and L-Glutamate since these amino acids are the ones significantly affecting the central carbon metabolism.

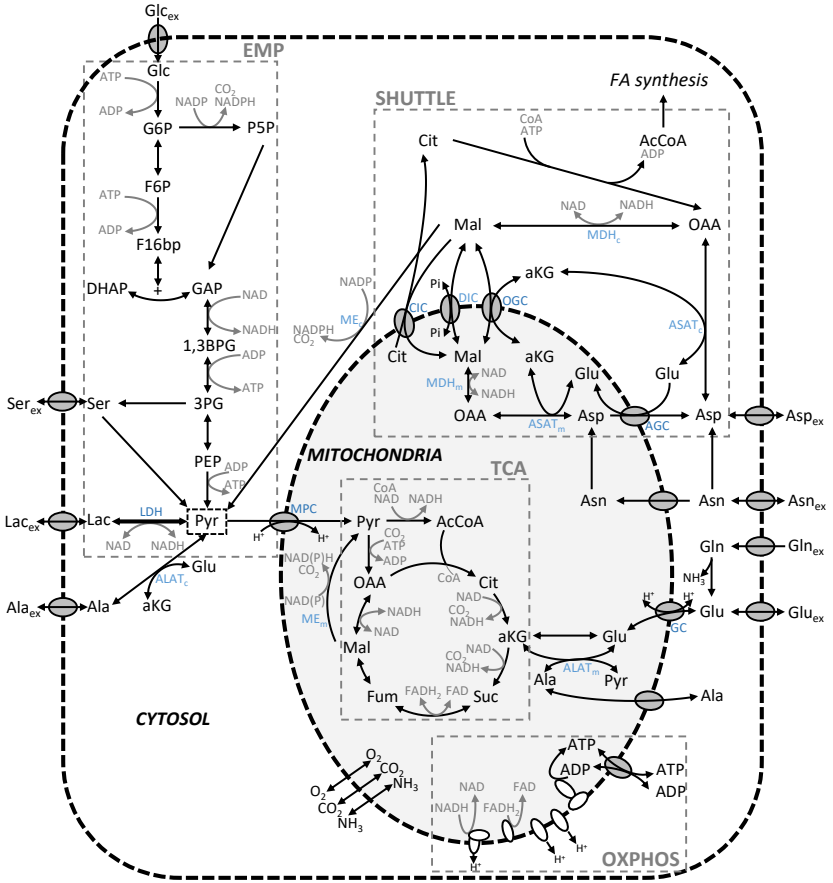

Figure 2.4.: Metabolic network model used in the ^{13}C MFA according to Junghans and coworkers [JTW+19]

2.4. Modelling of biological netowrk

2.4.1. Stoichiometric of a metabolic network

One of the prerequisites of metabolic modelling is the stoichiometry of the metabolic model. The information of intracellular biochemical reactions, intermediate metabolite compounds are included in the metabolic stoichiometry. Figure 2.5 (left) displays the upper part of glycolysis. By using the network information, stoichiometric matrix **S** could be formulated (Figure 2.5 (right)).

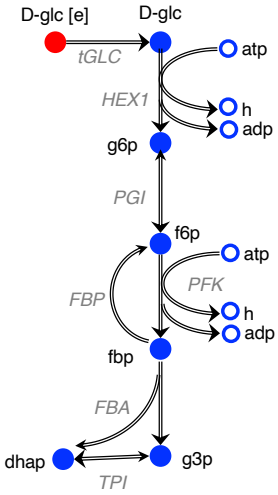

$$
\begin{array}{c}
 \\
\text{D-glc[e]} \\
\text{D-glc} \\
\text{atp} \\
\text{h} \\
\text{adp} \\
\text{g6p} \\
\text{f6p} \\
\text{fbp} \\
\text{g3p} \\
\text{dhap}
\end{array}
\begin{array}{c}
\begin{array}{ccccccc}
\text{tGLC} & \text{HEX1} & \text{PGI} & \text{PFK} & \text{FBP} & \text{FBA} & \text{TPI}
\end{array} \\
\begin{pmatrix}
-1 & 0 & 0 & 0 & 0 & 0 & 0 \\
1 & -1 & 0 & 0 & 0 & 0 & 0 \\
0 & -1 & 0 & -1 & 0 & 0 & 0 \\
0 & 1 & 0 & 1 & 0 & 0 & 0 \\
0 & 1 & 0 & 1 & 0 & 0 & 0 \\
0 & 1 & -1 & 0 & 0 & 0 & 0 \\
0 & 0 & 1 & -1 & 1 & 0 & 0 \\
0 & 0 & 0 & 1 & -1 & -1 & 0 \\
0 & 0 & 0 & 0 & 0 & 1 & 1 \\
0 & 0 & 0 & 0 & 0 & 1 & -1
\end{pmatrix}
\end{array}
= \text{N}
$$

Figure 2.5.: Upper glycolysis metabolic network (left) and stoichiomatric matrix representation of the network (right). Figure was adapted from "Systems Biology - Properties of Reconstructed Networks" by Bernhard Ø Palsson, 2006, *Cambridge University Press* [Pal06]

2.4.2. Metabolite balancing

Metabolite balancing is the foundation of all flux analysis techniques, which was first introduced by Varma & Palsson (1994) [VP94]. This method heavily relies on the stoichiometric information of the metabolic network (Figure 2.5). The basic assumption when utilizing this method is that the biological is in (pseudo)-steady-state (Equation 2.1).

$$\begin{aligned} \frac{d\mathbf{x}}{dt} = \mathbf{S} \cdot r + \Gamma \cdot u = \mathbf{N} \cdot v = 0 \\ \mathbf{v} = (v_1, v_2, ..., v_n) \\ \mathbf{x} = (x_1, x_2, ..., v_m) \end{aligned} \tag{2.1}$$

where:

- **S**: internal network matrix;
- Γ: membrane transport vector;
- **N**: entire network matrix comprising of **S** and Γ;
- **r**: internal flux vector;
- **u**: transport flux vector; and
- **v**: flux vector

2.4.3. Determinancy and calculability analysis

Van der Heijden and coworkers [VHH+94] proposed a calculability analysis to determine the network determinancy and calculability. The first step is to

calculate the null space (kernel) of matrix $\mathbf{N}$, where:

$$0 = \mathbf{N} \cdot \mathbf{K} \tag{2.2}$$

The number of columns in $\mathbf{K}$ is the network degree of freedom, which can also be calculated using Equation 2.3.

$$n_{dof} = \dim(\mathrm{kern}(\mathbf{N})) = \dim(\mathbf{v}) - \mathrm{rank}(\mathbf{N}) \tag{2.3}$$

To further analyze the determinancy and calculability, network information can be splitted into the known part and unknown part. The known part is the information obtained from measurement (extracellular rates $\mathbf{q}$) and from ^{13}C MFA optimizer (optimized flux parameter $\mathbf{p}$).

$$\begin{aligned}
\mathbf{v} = \begin{pmatrix} \mathbf{v}_k \\ \mathbf{v}_u \end{pmatrix}, \qquad \mathbf{v}_k = \begin{bmatrix} \mathbf{q} & \mathbf{p} \end{bmatrix} \qquad \mathbf{N} = \begin{pmatrix} \mathbf{N}_k & \mathbf{N}_u \end{pmatrix} \\
0 = \mathbf{N} \cdot \mathbf{v} \\
0 = \begin{pmatrix} \mathbf{N}_k & \mathbf{N}_u \end{pmatrix} \cdot \begin{pmatrix} \mathbf{v}_k \\ \mathbf{v}_u \end{pmatrix} \\
0 = \mathbf{N}_k \mathbf{v}_k + \mathbf{N}_u \mathbf{v}_u \\
\mathbf{v}_u = -\mathbf{N}_u^{-1} \mathbf{N}_k \mathbf{v}_k
\end{aligned} \tag{2.4}$$

Klamt and coworkers [KSG02] introduced a systems classification for network determinancy, redundancy, and calculability based on Equation 2.4:

- *Underdetermined*: $\mathrm{N}_u < \mathbf{v}_u$
- *Determined*: $\mathrm{N}_u = \mathbf{v}_u$
- *Redundant*: $\mathrm{N}_u < m$

- *Not redundant*: $N_u = m$
- A flux is *calculable* if it can be uniquely computed using Equation 2.4
- A flux is *non-calculable* if it cannot be uniquely computed using Equation 2.4

2.4.4. Intracellular flux estimation

For a determined case, the solution of intracellular flux distribution is unique and can be calculated as described in Equation 2.5.

$$\mathbf{v} = \begin{pmatrix} \mathbf{N} \\ \mathbf{N}_k \end{pmatrix}^{-1} \begin{pmatrix} 0 \\ \begin{bmatrix} \mathbf{q} & \mathbf{p} \end{bmatrix} \end{pmatrix} \tag{2.5}$$

Meanwhile, an over-determined case will yield more than one solutions due to the additional information available. These information (rates) are error-prone. Thus, the intracellular flux distribution can be estimated by minimizing the Sum of Square Residual of these information (Equation 2.6).

$$\mathrm{SSR} = \chi^2 = \sum \left(\frac{q_i - q_{m,i}}{\sigma_i} \right)^2 \tag{2.6}$$

2.5. ^{13}C Non-stationary metabolic flux analysis

Due to the varying ^{13}C enrichment rate in glycolysis and the rest of the central carbon metabolism, it is important to use the ^{13}C Non-Stationary Metabolic Flux Analysis to estimate the intracellular fluxes [AA11; JTW+19].

2.5.1. Carbon atom transition network

Besides the stoichiometric metabolic model (Section 2.3.6), a carbon atom transition model is also required to simulate the carbon labelling experiment. A carbon atom transition model provides the information of carbon atom fate in a biochemical reaction inside a metabolic network ([WNN15]). A simple carbon atom transition model is illustrated in Figure 2.6.

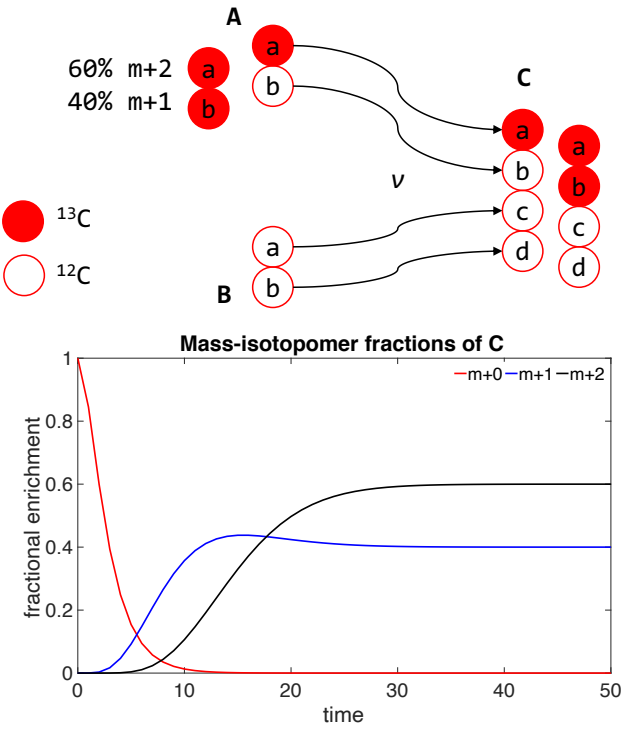

Figure 2.6.: Illustration of carbon atom transition of biochemical reaction v (top) and the respective labelling profile over time (bottom). The red-filled circles indicate the labelled carbon atom.

The carbon atom transition of biochemical reaction v (Figure 2.6) could be

expressed as Equation 2.7.

$$v : \mathrm{A}[(1,2)] + \mathrm{B}[(3.4)] \rightarrow \mathrm{C}[(1,2,3,4)] \tag{2.7}$$

The carbon atom transition network of CHO cells were obtained from previous studies [AA11; TDRY13] and is provided in Table 2.5.

2.5.2. Bidirectional reactions

The utilization of ^{13}C carbon enables the quantification of bidirectional fluxes in a metabolic model. The term "bidirectional" was described by Wiechert and de Graaf (1996) as biochemical reactions with a low $\triangle G$, which is the case for the majority of the cellular biochemical reactions [WG97]. The impact of bidirectional reaction compared to unidirectional reaction is depicted in Figure 2.7.

In this thesis, bidirectional fluxes (reactions reversibility) were defined according to Schaub and coworkers [SMR08] and Maierand coworkers [MHRM08] as described in Equation 2.8.

$$\begin{aligned} v_j &: A + B \rightleftharpoons C + D \\ \overrightarrow{v}_j &= \beta_j \times v_j^{nett} \\ \overleftarrow{v}_j &= \overrightarrow{v}_j - v_j^{nett} \end{aligned} \tag{2.8}$$

2.5.3. Isotopomer balancing

The mass balance principle also applies for each isotopomer in the carbon atom transition network. In general, the mass balances of each isotopomer

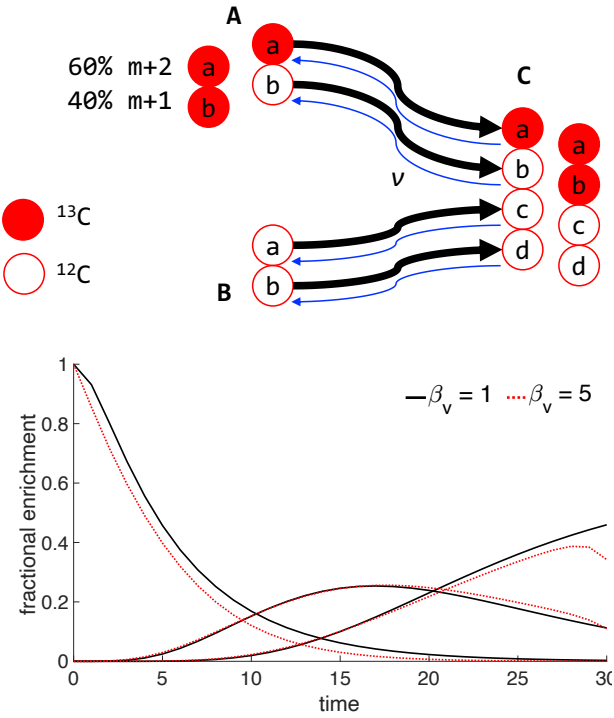

Figure 2.7.: The impact of reversibility to the labelling profile

can be expressed as Equation 2.9 [WNN15].

$$V_i \cdot \dot{x}_i = \dot{v}_i^{influx} - \dot{v}_i^{efflux} \tag{2.9}$$

where V_i denotes for intracellular metabolite concentration of i; $\dot{x}_i$ is the isotopomer fraction of i; and $\dot{v}_i^{influx}$, $\dot{v}_i^{influx}$ are labelling influx and efflux rate of isotopomer i respectively.

To model transient carbon-13 enrichments, the isotopomers of each metabo-

lite were balanced by Equation 2.10.

$$\frac{d(C_i I_i)}{dt} = \sum_{j=1}^{\mathrm{N}} \left[\alpha \left(\bigotimes_{k=1}^{0} \left(\sum_{m=1}^{n} \mathrm{IMM}_{k\to m} \right) \mathrm{I}_k \right) r_j + (1-\alpha)(\nu_{ij} r_j \mathrm{I}_j) \right] \tag{2.10}$$

with

$$\alpha = \begin{cases} 1, \text{ if } \nu_{ij} > 0 \\ 0, \text{ else} \end{cases}$$

where c_i, I_i ,and I_k denote vectors of intracellular concentrations of metabolites i and isotopomer distribution vectors, containing molar ratios that correspond to the fractional amounts of the individual isotopologues for metabolites i and k, respectively. The isotopomer mapping matrix $\mathrm{IMM}_{k\to m}$ describes the isotopomer transition from reactant k (with n number of reactants) to product m [SCNV97]. ν_{ij} equals the stoichiometric coefficient of metabolite i in reaction j, whose molar rate is r_j. The operator $\bigotimes$ denotes element-by-element vector multiplication.

2.5.4. Dilution by endo- and exo-metabolome pool

The presence of unlabelled endo- and exo- metabolome pools could dilute the ^{13}C enrichment. In CHO cells, the example of endo- metabolome is the endogenous carbon storage as described by Junghans and coworkers [JTW+19]. Whereas, the example of exogenous metabolome pool is the non-essential amino acids and lactate. The impact of this dilution is illustrated in Figure 2.8.

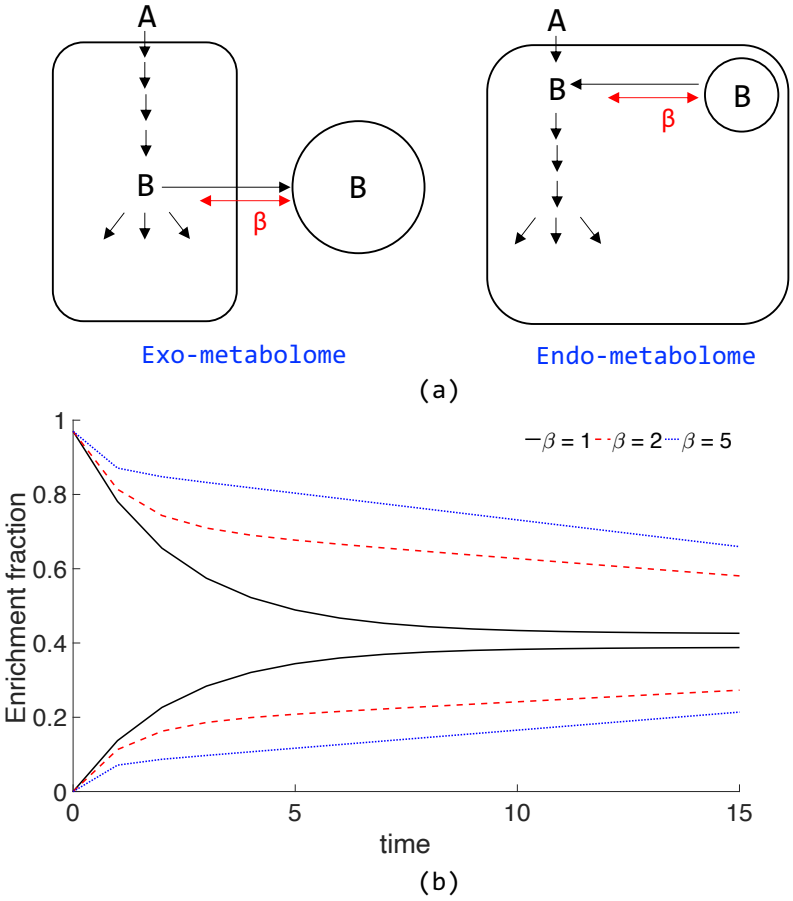

Figure 2.8.: (a) ^{13}C dillution by exo- (left) and endo- (right) metabolome pool. (b) The implication of the exchange fluxes to ^{13}C enrichment

The isotopomer dilution by the exogenous non-labelled source must be simulated to get a proper fitting of the mass-isotopomer profile. The isotopomer balances of the exogenous metabolome could be formulated using Equation

2.11.

$$\frac{d(\mathrm{I}_{i,ex})}{dt} = \frac{1}{C_{i,ex}}\left[\overline{C_X}(\overrightarrow{q}_{i,ex}\mathrm{I}_{i,in} - \overleftarrow{q}_{i,ex}\mathrm{I}_{i,ex}) - \frac{dC_{i,ex}}{dt}\mathrm{I}_{i.ex}\right] \quad \text{with} \quad \overrightarrow{q}_{i,ex} = \beta_i q^{net}_{i,ex} \quad \overleftarrow{q}_{i,ex} = \overrightarrow{q}_{i,ex} - q^{net}_{i,ex} \tag{2.11}$$

2.5.5. Carbon labelling simulation

Carbon labelling simulation was performed using MATLAB release 2018a (The MathWorks, Inc., Natick, MA, USA) environment. The Ordinary Differential Equations (ODEs) generated from intra- and extracellular isotopomers balancing were simulated using MATLAB based *ode15s* solver (Appendix A).

2.5.6. Parameter estimation

Parameter estimation was performed in the same environment as the carbon labelling simulation (MATLAB 2018a). The metabolic and carbon atom transition network contains 972 ODEs and 43 parameters (8 intracellular flux and 35 reversibility constants). These parameters were estimated by fitting the simulated mass isotopomers and the measured mass isotopomer. MATLAB 2018a based *fmincon* and *GlobalSearch* were applied to find the global minima of the Sum of Squared Residual (SSR) as defined in Equation 2.12. Parameter estimation solver fmincon inside GlobalSearch were

repeated at least 100 times from randomized initial guess.

$$\min f(\Phi) = \sum_{n=1}^{n} \left(\frac{\mathrm{MID}_i^{exp} - \mathrm{MID}_i^{sim}}{\sigma_i} \right)^2 \qquad \Phi \geq 0 \tag{2.12}$$

2.5.7. Goodness of Fit

Pearson-Fischer chi-square test was used to assess the model goodness of fit [BJS+11] as described in Equation 2.13.

$$\begin{aligned} \chi^2 &= \sum \frac{(O-E)^2}{E} = \frac{\left(\mathrm{MID}_i^{sim} - \mathrm{MID}_i^{exp}\right)^2}{\mathrm{MID}_i^{exp}} \\ df &= (n-p) \\ \chi^2 &\leq \chi^2_{(1-\alpha),df} \end{aligned} \tag{2.13}$$

2.5.8. Parameter confidence interval

Parameter uncertainty was assessed using a non-linear algorithm [AKS06]. The method assumes that the sum of squared residual is χ^2 distributed. Thus, the uncertainty of parameter was determined when optimizing the said systems with one degree of freedom (χ^2 distributed).

2.6. Metabolic and atom carbon transition model

Table 2.5.: Metabolic and atom carbon transition model used in this study

ID	Reaction name	Biochem. reaction and carbon atom transition
tGln	Glutamine importer	Gln_ex[(1,2,3,4,5)] => Gln[(1,2,3,4,5)]
gs	Glutaminase	Gln[(1,2,3,4,5)] => Glu[(1,2,3,4,5)]
tGlu	Glutamate transporter	Glu[(1,2,3,4,5)] = Glu_ex[(1,2,3,4,5)]
gdh	Glutamate dehydrogenase	aKG_m[(1,2,3,4,5)] = Glu_m[(1,2,3,4,5)]
tGlc	Glucose importer	Glc_ex[(1,2,3,4,5,6)] => G6P[(1,2,3,4,5,6)]
fGlyco	Carbon storage (glycogen) degradation	Glyco_ex[(1,2,3,4,5,6)] => G6P[(1,2,3,4,5,6)]
pgi	Phosphoglucose-isomerase	G6P[(1,2,3,4,5,6)] = F6P[(1,2,3,4,5,6)]
pfk	Phosphofructokinase + fructose-1,6-bisphosphatase	F6P[(1,2,3,4,5,6)] = FBP[(1,2,3,4,5,6)]
fbpa	Fructose-bisphosphate aldolase	FBP[(1,2,3,4,5,6)] = DHAP[(3,2,1)] + GAP[(4,5,6)]
tpi	Triophosphate isomerase	DHAP[(1,2,3)] = GAP[(1,2,3)]

ID	Reaction name	Biochem. reaction and carbon atom transition
gapdh	GAP dehydrogenase + biphosphoglycerate mutase	GAP[(1,2,3)] = 3PG[(1,2,3)]
eno	Phosphoglycerate hydratase	3PG[(1,2,3)] = PEP[(1,2,3)]
pkm	Pyruvate kinase	PEP[(1,2,3)] => Pyr[(1,2,3)]
ldh	Lactate dehydrogenase	Pyr[(1,2,3)] = Lac[(1,2,3)]
tLac	Lactate transporter	Lac[(1,2,3)] = Lac_ex[(1,2,3)]
G6Pdh	Glucose-6-phosphate dehydrogenase	G6P[(1,2,3,4,5,6)] => P5P [(2,3,4,5,6)] + CO2[(1)]
tkt1	Transketolase 1	P5P[(1,2,3,4,5)(6,7,8,9,10)] = S7P[(6,7,1,2,3,4,5)] + GAP[(8,9,10)]
tald	Transaldolase	E4P[(1,2,3,4)] + P5P[(5,6,7,8,9)] = F6P[(5,6,1,2,3,4)] + GAP[(7,8,9)]
tkt2	Transketolase 2	S7P[(1,2,3,4,5,6,7)] + GAP[(8,9,10)] = E4P[(4,5,6,7)] + F6P[(1,2,3,8,9,10)]
tCO2	CO2 evolution	CO2[(1)] => CO2_ex[(1)]
MPC	Pyruvate/H^+ symporter	Pyr[(1,2,3)] => Pyr_m[(1,2,3)]

ID	Reaction name	Biochem. reaction and carbon atom transition
CIC	Citrate/Malate antiporter	Cit_m[(1,2,3,4,5,6)] + Mal[(7,8,9,10)] => Cit[(1,2,3,4,5,6)] + Mal_m[(7,8,9,10)]
DIC	$PO34^{-}$/Malate antiporter	Mal_m[(1,2,3,4)] = Mal[(1,2,3,4)]
GC	Glutamate/H^{+} symporter	Glu_m[(1,2,3,4,5)] = Glu[(1,2,3,4,5)]
OGC	Malate/aKG antiporter	Mal[(1,2,3,4)] + aKG_m[(5,6,7,8,9)] = Mal_m[(1,2,3,4)] + aKG[(5,6,7,8,9)]
AGC	Aspartate/glutamate antiporter	Glu[(1,2,3,4,5)] + Asp_m[(6,7,8,9)] => Glu_m[(1,2,3,4,5)] + Asp[(6,7,8,9)]
mAla	Putative alanine transporter	Ala[(1,2,3)] = Ala_m[(1,2,3)]
mAsn	Putative asparagine transporter	Asn[(1,2,3,4)] = Asn_m[(1,2,3,4)]
pdh	Pyruvate dehydrogenase	Pyr_m[(1,2,3)] => AcCoA_m[(2,3)] + CO2[(1)]
cs	Citrate synthase	OAA_m[(1,2,3,4)] + AcCoA_m[(5,6)] => Cit_m[(4,3,2,6,5,1)]
idh	Iso-citrate dehydrogenase	Cit_m[(1,2,3,4,5,6)] = aKG_m[(1,2,3,4,5)] + CO2[(6)]
adh	aKG dehydrogenase + succinyl-CoA ligase + succinate dehydrogenase + fumarase	aKG_m[(1,2,3,4,5)(6,7,8,9,10)] = $Mal_m[(2,3,4,5)(10,9,8,7)] + CO2[(1)(6)]$

ID	Reaction name	Biochem. reaction and carbon atom transition
mdh	Malate dehydrogenase	Mal_m[(1,2,3,4)(5,6,7,8)] = OAA_m[(1,2,3,4)(8,7,6,5)]
pepck	Phosphoenolpyruvate carboxykinase	OAA[(1,2,3,4)] = PEP[(1,2,3)] + CO2[(4)]
me_c	Cytosolic malic enzyme	Mal[(1,2,3,4)] = Pyr[(1,2,3)] + CO2[(4)]
me_m	Mitochondrial malic enzyme	Mal_m[(1,2,3,4)] = Pyr_m[(1,2,3)] + CO2[(4)]
pc	Pyruvate carboxylase	Pyr_m[(1,2,3)] + CO2[(4)] = OAA_m[(1,2,3,4)]
mdh_c	Cytosolic malate dehydrogenase	OAA[(1,2,3,4)(5,6,7,8)] = Mal[(1,2,3,4)(8,7,6,5)]
tSer	Serine importer	Ser_ex[(1,2,3)] => Ser[(1,2,3)]
phdgh	Phosphoglycerate dehydrogenase + phosphoserine phosphatase	3PG[(1,2,3)] => Ser[(1,2,3)]
sds	Serine dehydratase	Ser[(1,2,3)] => Pyr[(1,2,3)]
tAla	Alanine transporter	Ala[(1,2,3)] = Ala_ex[(1,2,3)]
alt_c	Cytosolic alanine aminotransferase	Pyr[(1,2,3)] + Glu[(4,5,6,7,8)] = Ala[(1,2,3)] + aKG[(4,5,6,7,8)]
alt_m	Mitochondrial alanine aminotransferase	Ala_m[(1,2,3)] + aKG_m[(4,5,6,7,8)] = Pyr_m[(1,2,3)] + Glu_m[(4,5,6,7,8)]

ID	Reaction name	Biochem. reaction and carbon atom transition
tAsp	Aspartate transporter	Asp_ex[(1,2,3,4)] = Asp[(1,2,3,4)]
tAsn	Asparagine importer	Asn_ex[(1,2,3,4)] => Asn[(1,2,3,4)]
ast_c	Cytosolic aspartate aminotransferase	Asp[(1,2,3,4)] + aKG[(5,6,7,8,9)] = OAA[(1,2,3,4)] + Glu[(5,6,7,8,9)]
ast_m	Mitochondrial aspartate aminotransferase	Asp_m[(1,2,3,4)] + aKG_m[(5,6,7,8,9)] = OAA_m[(1,2,3,4)] + Glu_m[(5,6,7,8,9)]
asns	Asparaginase	Asn_m[(1,2,3,4)] = Asp_m[(1,2,3,4)]
muG6P	Biomass formation from G6P	G6P[(1,2,3,4,5,6)] => $G6P_{Xe}x[(1,2,3,4,5,6)]$
muGAP	Biomass formation from GAP	GAP[(1,2,3)] => GAP_X_ex[(1,2,3)]
muP5P	Biomass formation from P5P	P5P[(1,2,3,4,5)] => P5P_X_ex[(1,2,3,4,5)]
acl	Acetyl-CoA lyase	Cit[(1,2,3,4,5,6)] => OAA[(6,3,2,1)] + AcCoA[(5,4)]
muAcCoA	Biomass formation from AcCoA	AcCoA[(1,2)] => AcCoA_X_ex[(1,2)]
muSer	Biomass formation from serine	Ser[(1,2,3)] => Ser_X_ex[(1,2,3)]
muAla	Biomass formation from alanine	Ala[(1,2,3)] => Ala_X_ex[(1,2,3)]
muAsp	Biomass formation from aspartate	Asp[(1,2,3,4)] => Asp_X_ex[(1,2,3,4)]

ID	Reaction name	Biochem. reaction and carbon atom transition
muAsn	Biomass formation from asparagine	Asn[(1,2,3,4)] => Asn_X_ex[(1,2,3,4)]
muGln	Biomass formation from glutamine	Gln[(1,2,3,4,5)] => Gln_X_ex[(1,2,3,4,5)]
muGlu	Biomass formation from glutamate	Glu[(1,2,3,4,5)] => Glu_X_ex[(1,2,3,4,5)]

Chapter 3

From nutritional wealth to autophagy: *In vivo* metabolic dynamics in the cytosol, mitochondrion and shuttles of IgG producing CHO cells [1]

Abstract

To fulfil the optimization needs of current biopharmaceutical processes the knowledge how to improve cell specific productivities is of outmost importance. This requires a detailed understanding of cellular metabolism on a subcellular level inside compartments such as cytosol and mitochondrion. Using IgG1 producing Chinese hamster ovary (CHO) cells, a pioneering

[1] This chapter was published as: Junghans, L., Teleki, A., **Wijaya, A.W.**, Becker, M., Schweikert, M., & Takors, R. (2019). From nutritional wealth to autophagy: *In vivo* metabolic dynamics in the cytosol, mitochondrion and shuttles of IgG producing CHO cells. *Metabolic engineering*, **54**, 145-159. All experimental work described herein was carried out by Lisa Junghans and Max Becker. The analytical measurements (metabolomics and 13C profiling) were carried out by Lisa Junghans and Attila Teleki

protocol for compartment-specific metabolome analysis was applied. Various production-like growth conditions ranging from ample glucose and amino acid supply via moderate to severe nitrogen limitation were investigated in batch cultures. The combined application of quantitative metabolite pool analysis, ^{13}C tracer studies and non-stationary flux calculations revealed that Pyr/H^+ symport (MPC) bore the bulk of the mitochondrial transport under ample nutrient supply. Glutamine limitation induced the concerted adaptation of the bidirectional Mal/aKG (OGC) and the Mal/HPO_4^{2-} antiporter (DIC), even installing completely reversed shuttle fluxes. As a result, NADPH and ATP formation were adjusted to cellular needs unraveling the key role of cytosolic malic enzyme for NADPH production. Highest cell specific IgG1 productivities were closely correlated to a strong mitochondrial malate export according to the anabolic demands. The requirement to install proper NADPH supply for optimizing the production of monoclonal antibodies is clearly outlined. Interestingly, it was observed that mitochondrial citric acid cycle activity was always maintained enabling constant cytosolic adenylate energy charges at physiological levels, even under autophagy conditions.

3.1. Introduction

The production of biopharmaceuticals such as antibodies is steadily rising [ML17; Wal14] often using Chinese hamster ovary (CHO) cells as producers [BR06; EJL15; Wur04]. Currently, research activities are not only driven by increasing market demands but also by the growing number of expiring patents opening the door for cost-minimized production of biosimilars [Gau16; Mul12]. Product titers have increased substantially over the past years [KR16] predominately reflecting improvements of increasing viable cell densities in fed-batch processes. Interestingly, cell specific productivities did not rise equally still showing typical values of $20-40$ pg·cell^{-1}·day^{-1} in

industrial producers. This observation is particularly important as it mirrors the problem that viable cell densities can be improved by smart process engineering, whereas improvements of cell-specific productivities typically require detailed knowledge of intracellular metabolic control mechanisms. The need of understanding may even increase with the envisaged development of continuous production processes [HTS+14] that demand for optimized operating set points. It has been shown that ATP availabilities positively correlate with cell specific production rates of monoclonal antibodies [PMT15]. However, surprisingly few is known about the in vivo interaction of mitochondria, the key spot of respiratory ATP generation, and the cellular metabolism located in the cytosol. Accordingly, this study focuses on the compartment-specific analysis of metabolic fluxes and shuttle transporter activities of IgG1 producing CHO cells under *in vivo* conditions.

Mammalian mitochondria are membrane-bound organelles providing ATP via oxidative reactions linked to chemiosmosis, performing crucial metabolic conversions [DS03; KVG+08; Sch01], and are equipped with a conserved set of 37 genes which are involved in various mitochondrial functions, including respiratory chain, transcription and translation [GBL99; LHF83; Log06; UMBB97]. They are suspected of playing a key role in apoptotic cell death, which is triggered by the cell's energetic state [NF03]. Accordingly, the activity of mitochondria is tightly coupled to host cell needs. Transports of metabolites, nucleotides, and cofactors via the inner selective mitochondrial membrane (IMM) are tightly controlled via a set of carrier proteins and ion exchange channels [Pal04] finally to install proper bioenergetic conditions and redox states [KM09; LW71; Pal13]. Individual facets of the complex shuttle system such as the pyruvate carrier [VDG+14], respiration [KVG+08], or particular nucleotides [INT+09] have been studied. Isolated mitochondria [NQG15; NWN+15] or derived metabolic flux maps from whole-cell metabolic measurements that did not experimentally distinguish

between cellular compartments have been investigated through alternative approaches [AA11; AA13; GBB+10a; SRM11]. However, data from compartment resolved *in vivo* metabolomics are key to elucidate real mitochondrial shuttle activities in mammalian cells [INT+09; MTPT15; NSH11; WNH14].

This contribution builds on recent developments in compartment-specific metabolome quantification [MTPT15], extends the approach for ^{13}C labeling analysis, and exploits measurements for ^{13}C metabolic flux analysis (^{13}C MFA) [MHRM08; WW01]. Accordingly, cytosolic/mitochondrial shuttle activities are quantified *in vivo* investigating different production conditions. As such, the study significantly expands current state-of-the-art technologies by providing *in vivo* time-variant metabolic flux maps based on a broad spectrum of compartment-specific metabolite patterns.

3.2. Carbon labelling experiment

Bioreactor cultivations with CHO DP-12 cells were performed to enable the analysis of shuttle activities under three distinct growth scenarios (Figure 3.1a): (I) exponential growth with nutrients saturation (D-glucose and amino acids); (II) moderate nitrogen limitation by L-glutamine depletion; and (III) strong nitrogen limitation without L-glutamine and L-asparagine but with D-glucose saturation. As such, metabolic measurements mirrored the cellular response in the feast-to-famine transition with respect to nitrogen limitation.

Therefore, isotopic tracer studies were performed with biological duplicates (n = 2) by adding uniformly labeled [U-^{13}C]-D-glucose to reach an extracellular isotopic molar ratio of 25% [U-^{12}C]- and 75% [U-^{13}C]-D-glucose on day 2.5 (phase I) as illustrated in Figure 3.1a. Simultaneously, parallel cultivations for absolute quantification of intracellular pools (n = 2) were supplemented with non-labeled [U-^{12}C]-D-glucose to reach equal concentrations.

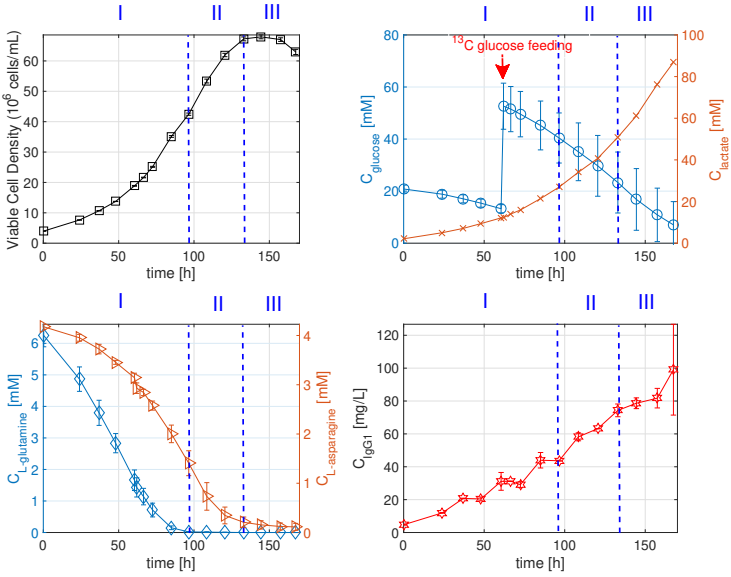

(a)

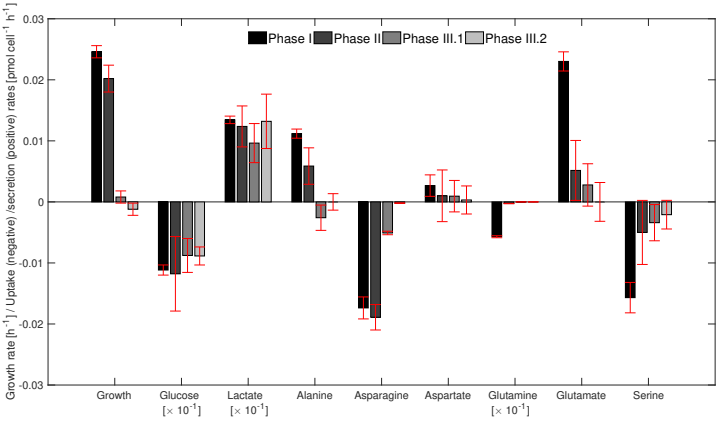

(b)

Figure 3.1.: Extracellular phenotypes (a) Dynamics of D-glucose, L-glutamine, and L-asparagine over time during the batch cultivation of CHO-DP12; (b) Input growth rate and extracellular rates for ^{13}C-Metabolic Flux Analysis presented as barplot. The negative rates indicate consumption, while the positive rates indicate secretion [JTW+19]

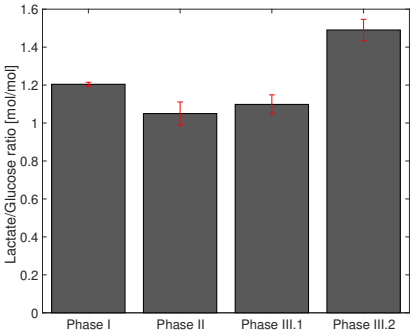

(c)

Figure 3.1.: Extracellular phenotypes (c) L-lactate/D-glucose ratio in different cultivation phases [JTW+19]

The cultivations were sampled twice per day (from day 1.5 to day 7), and subcellular metabolome analyses were achieved following the differential analysis protocol depicted in Figure 1.3 [MTPT15]. The method separates the cytosolic fraction from physically intact mitochondria. Furthermore, cytosolic depletion and mitochondrial membrane integrity were quantified using G6P, F6P, and cisAco as compartment-specific internal standards.

In phase I, the cells grew with a high specific growth rate of 0.0246 ± 0.001 h^{-1} while substantial amounts of D-glucose, L-glutamine, and L-asparagine were constantly consumed (Figure 3.1b). Consequently, secretions of overflow-metabolism products such as L-lactate, L-alanine L-glutamate, and L-aspartate; was observed. L-lactate was mostly generated from D-glucose, which is well known as Warburg effect [War56]. In this study, the L-lactate/D-Glucose ratio was in the range of 1.2 ± 0.011 mol/mol during the growth phase/. On the other hand, L-alanine, L-glutamate, and L-aspartate were produced as the consequence of L-glutamine catabolism.

Phase II marked the start of L-glutamine limitation and the cells grew with

a reduced growth rate of 0.0202 ± 0.0022 h^{-1}. Therefore, the net export of some overflow amino acids was also reduced (L-alanine, L-aspartate, and L-glutamate). The L-lactate/D-glucose ratio was slightly reduced compared to the previous phase (1.05 ± 0.06 mol/mol), indicating the increasingly importance of D-glucose for the citric acid (TCA) cycle activity. Accordingly, L-asparagine also became increasingly important for supporting cellular energetics.

Afterwards, the cells entered the stationary and autophagy phase (Phase III.1 and III.2). Phase III marked the start of nitrogen starvation phase, in which several amino acids were limited, for example, L-glutamine, L-asparagine, and L-serine. In phase III.1, the cells grew with a significantly reduced growth rate of 0.0008 ± 0.001 h^{-1}. While, in phase III.2, the cells were dying with a death rate of 0.0012 ± 0.001 h^{-1}. The L-lactate/D-Glucose ratio in this phase kept increasing to 1.1 ± 0.05 mol/mol in phase III.1 and 1.49 ± 0.056 mol/mol in phase III.2 (Figure 3.1c). The byproduct amino acids (L-alanine, L-aspartate,and L-glutamate) resulted from overflow metabolism previously were consumed to cope with the nitrogen limitation.

3.3. Isotopic labeling dynamics

Glycolytic intermediates reached isotopic steady state already by 6 h (first sampling, Figure 3.2), revealing the expected 25% non-labeled fraction (m+0) for all intermediates except for F16bp. During phase II and III, all intermediates showed either a small or large (F16bp) rise in the size of labeling fractions, which hints at changes in metabolic activity as a consequence of nitrogen limitation.

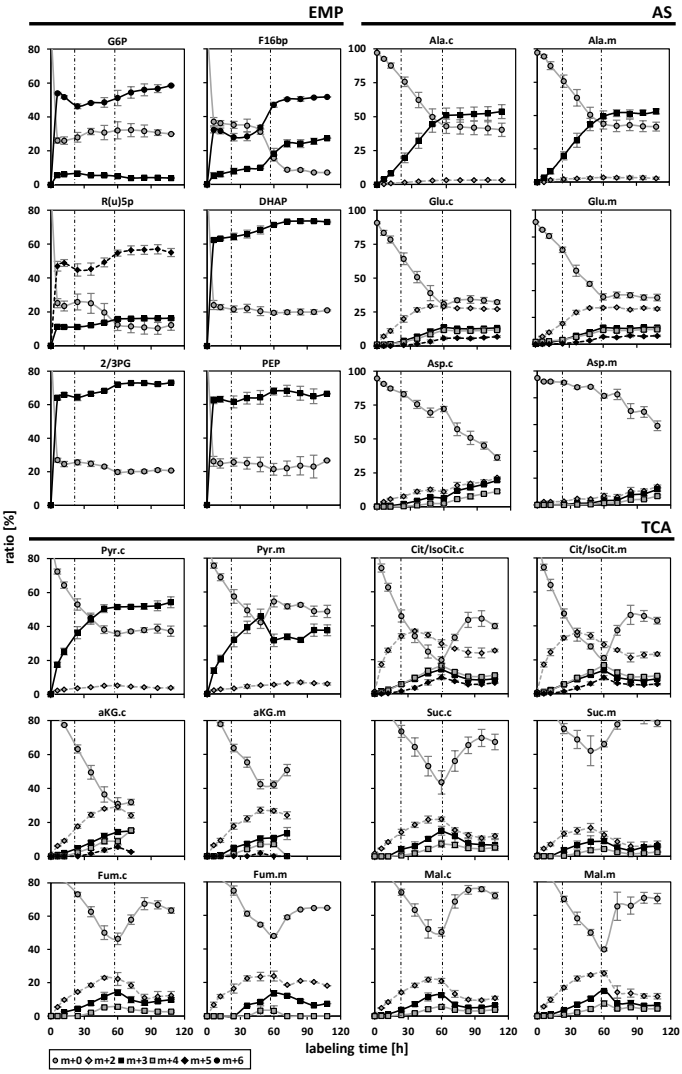

Figure 3.2.: Subcellular isotopic labeling dynamics of metabolites during different cultivation phases (I–III). Tracer experiments were performed as biological duplicates (n = 2) by the addition of uniformly labeled [U-^{13}C]-D-glucose, reaching an extracellular composition of 25% [U-^{12}C]- and 75% [U-^{13}C]-D-glucose. Mitochondrial (m) and cytosolic (c) isotopologue fractions (m + x) are listed separately as required. Mean values are based on at least two filter replicates of both [U-^{13}C] supplemented bioreactor cultivations. Errors were calculated using standard deviations. [JTW+19]

The compartment-specific labeling analysis revealed similar trends for Cit/iCit, aKG, Suc, Fum, and Mal. Most strikingly, the expected 25% non-labeled fraction (m+0), indicating a labeling steady state, was never achieved, neither in phase I nor in phase II. However, phase III apparently induced the inverse effects by equally fueling sources of non-labeled compounds into cytosol and mitochondria. In contrast, cytosolic Pyr pools reached a significantly time-delayed labeling steady state (approximately 60 h after labeling start) but remained in this labeling state even in phase III. Moreover, the labeling dynamics of subcellular Pyr pools differed significantly (Figure 3.2).

Figure 3.2 illustrates the compartment-specific labeling courses of Ala, Glu, and Asp. Whereas the latter showed a steady reduction in non-labeled Asp fractions, with notable different kinetics in the cytosol and mitochondria. Ala and Glu demonstrated very similar labeling trends in both compartments, characterized by continuous labeling during phases I and II and arrested labeling during phase III. Only Glu reached the expected labeling fraction with the labeled substrate. Additionally, labeling kinetics of mitochondrial Asp and significant amounts of mitochondrial Asn (Figure 3.2) indicated the presence of an unknown transporter system (mAsn).

3.4. Metabolic phenotypes of CHO-DP12 growing on TC-42 media

Figure 3.3 displays the intracellular flux distribution in four distinct phases during batch cultivation of CHO-DP12.

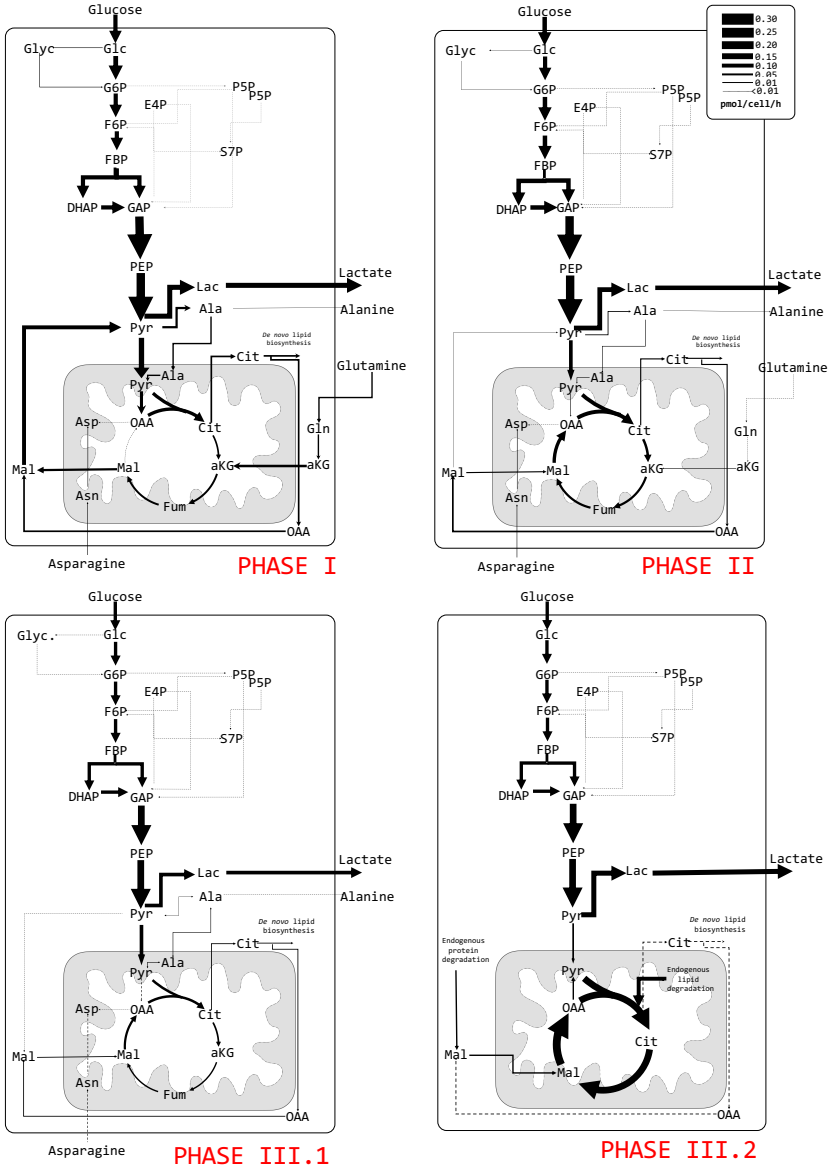

(a)

Figure 3.3.: Metabolic flux distribution of CHO-DP12 in various cultivation phases: (a) Central carbon metabolism presented as metabolic flux map during exponential growth phase (top left); L-glutamine limited phase (top right); stationary phase (bottom left); and autophagy (bottom right). The arrows' thickness indicate the flux level. [JTW+19]

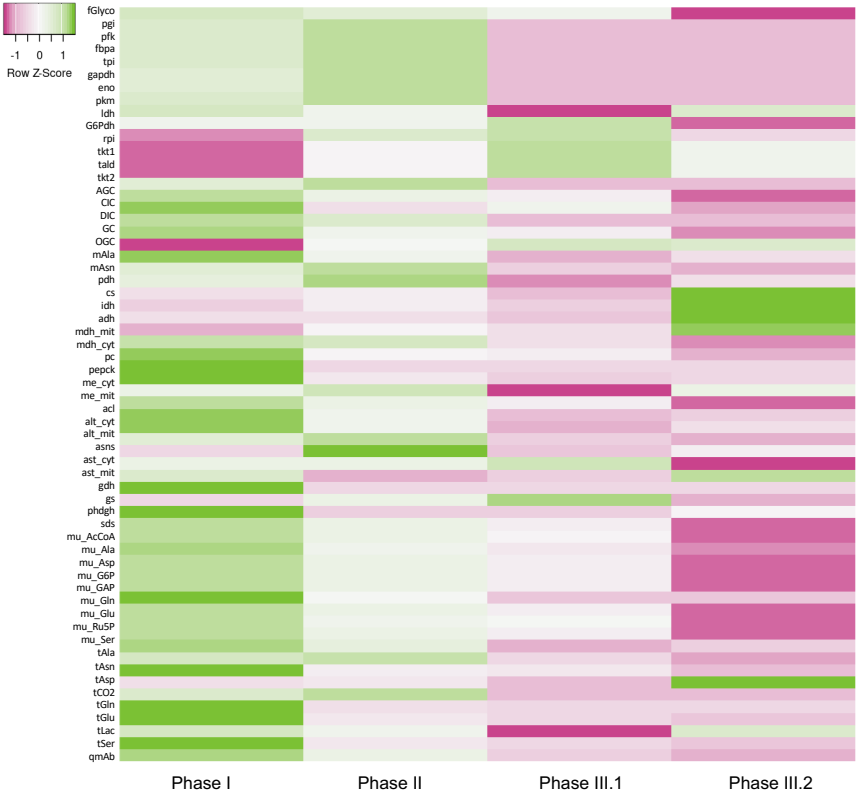

(b)

Figure 3.3.: Metabolic flux distribution of CHO-DP12 in various cultivation phases: (b) Activity of each biochemical reactions and transport processes in Phase I—Phase III.2 presented as a heatmap. The value was normalized for each reactions and the Z-score was presented in the heatmap.

Carbon labelling experiments were performed using uniformly labelled [U-^{13}C]-D-glucose in a biological duplicates culture (n = 2). The final glucose composition in the media was approximately 25% [U-^{12}C]-D-glucose and 75% [U-^{13}C]-D-glucose after the carbon-13 exposure. The results (intracellular flux distribution) were presented as four central carbon metabolic flux

maps (Figure 3.3a) and a heatmap indicating the relative activity of each metabolic reactions (Figure 3.3b).

Proliferating mammalian cells are characterized by high D-glucose uptake rate: 0.11 ± 0.0171 pmol·cell^{-1}·h^{-1} in phase I and 0.12 ± 0.06 pmol·cell^{-1}·h^{-1} in phase II. These results are consistent with those of previous studies [AA11; TDRY13]. As nitrogen became limited, D-glucose uptake and L-lactate secretion rates decreased equally by approximately 25% during phase III.1 and III.2. Furthermore, nearly 8% (0.01 ± 0.0014 pmol·cell^{-1}·h^{-1}) of total D-glucose was continuously in exchange with non-labelled endogenous carbon storage pool, presumably glycogen (*fGlyco*). The assumption of *fGlyco* enabled a proper fitting of intracellular G6P and P5P mass-isotopomer distribution (MID) profile. The *fGlyco* was gradually decreasing throughout the cultivation (0.009 ± 0.0012 and 0.007 ± 0.001 pmol·cell^{-1}·h^{-1} in phase II and phase III.1 respectively), before eventually vanished during the autophagy (Figure 3.3a). It is hypothesized that during nitrogen starvation, CHO cell focused its' remaining resources to survive, rather than creating intracellular carbon storage.

In proliferating cells, cellular demand of NADPH is high since NADPH plays a crucial role as reducing agent for cellular anabolic processes [HV18]. In CHO cells, oxidative PPP and cytosolic malic enzyme are the major NADPH sources. In this study, ^{13}C MFA indicated that only a small fraction of D-glucose entered the oxidative PPP: about 4%, resulting in about 0.0044 ± 0.0003 pmol·cell^{-1}·h^{-1} and 0.0046 ± 0.0003 pmol·cell^{-1}·h^{-1} of G6P dehydrogenase activities in phase I and III respectively. Furthermore, the oxidative PPP:glycolysis split ratio increased to about 25% in phase III.1; to about 0.0058 ± 0.0004 pmol·cell^{-1}·h^{-1} of G6P dehydrogenase flux before vanished in phase III.2. These findings support the previous studies that reported a remarkably low activity of oxidative PPP [AA11; TDRY13].

Furthermore, this study confirmed the finding from previous studies that malic enzyme is the primary source of NADPH in proliferating CHO cells [AA11; TDRY13]. Interestingly, the metabolic compartmentalization assisted ^{13}C MFA also specified the compartment of the malic enzyme (cytosolic malic enzyme), which was lacked during previous studies [AA11; TDRY13]. This study idenfitied cytosolic malic enzyme as the vital NADPH source during growth phase (0.1018 ± 0.0112 pmol·cell^{-1}·h^{-1}), which comprised of about 96% of the total cytosolic NADPH produced in phase I. During the L-glutamine limitation, the activity of cytosolic malic enzyme was significantly reduced to about 0.0099 ± 0.0011 pmol·cell^{-1}·h^{-1}. Hence, the role of oxidative PPP became more essential in supplying cytosolic NADPH ($\sim$ 30%). Interestingly in phase III, cytosolic NADPH was only produced via the oxidative PPP, and not the cytosolic malic enzyme.

Turning to the next part of the central carbon metabolism, the TCA cycle, represented by citrate synthase (*cs*), demonstrated different activities throughout the cultivation (Figure 3.3b). TCA activities were comparable in phase I and phase II (0.09 to 0.1 pmol·cell^{-1}·h^{-1}), which is the equivalent of about 40% of the consumed D-glucose. At the same time, L-lactate formation occurred at about 0.13 pmol·cell^{-1}·h^{-1}), indicating that recognized overflow metabolism (the 'Warburg effect') reduced the incoming glycolytic and anaplerotic fluxes of the cytosolic pyruvate pool by about 29% and 33% during phases I and II.

Observations under the ample nutrient conditions of phase I agree well with previous finding [SJH13], which indicated that the majority of pyruvate is derived from glycolysis (about 69%), and the remaining from cytosolic malic enzyme. The mitochondrial pyruvate pool fueled the TCA cycle via the pyruvate dehydrogenase (*pdh*) producing AcCoA and pyruvate carboxylase (*pc*) producing OAA in approximately equal proportions. Notably, the latter fraction was severely reduced with L-glutamine limitations and even inverse

with continued L-asparagine depletion during phase III.2. While in phase III.1, the TCA cycle activity was reduced to 0.069 ± 0.033 pmol·cell^{-1}·h^{-1}.

Another interesting observation during the extreme nitrogen starvation was that cells initiated autophagy as a survival strategy. Autophagy was identified by the de-enrichment of intracellular ^{13}C fractions, primarily those of the TCA cycle metabolites (Cit, α-KG, Fum, and Mal). Interestingly, the data fitting of 13C MFA could be achieved only by assuming additional two intracellular non-labeled pools: cytosolic malate (degradation product of non-labeled proteinogenic resources) and mitochondrial Acetyl-CoA (the degradation product of non-labeled lipid resources). This phenomenon suggested that intracellular non-labeled proteinogenic and lipid resources must have been accessed, fueling the oxidation products into the TCA cycle in mitochondria. Hence, the model predicted that the TCA cycle activity was increased about three-fold to 0.18 ± 0.086 pmol·cell^{-1}·h^{-1} in the autophagy phase (Figure 3.3a).

The high TCA cycle activity during autophagy also suggests that ATP generation was essential for cellular survival. At this time of the cultivation, the glycolytic activity was significantly reduced. Thus, the high TCA cycle activity was essential to provide more energy (ATP). Besides, we also observed that the TCA cycle activity was influenced by three factors: the glycolytic carbon fuel ($\sim$ 22%), intracellular lipid resources ($\sim$ 47%), and proteinogenic resources ($\sim$ 31%). Thus, this indicates that the cell minimized the utilization of glycolytic carbon to fuel the TCA cycle. One hypothesis is that aerobic glycolysis produces ATP faster. Besides, the re-oxidation of cytosolic NADH in the complex I enzyme requires a complex shuttle system for importing NADH into the mitochondrion, which would cost significant cellular resources. Hence, aerobic glycolysis was preferred during autophagy.

3.5. Mitochondrial carriers

The mitochondrial-bound carriers shuttle various metabolites across the mitochondrial membrane. Thus, the carriers play a vital role in the cellular metabolism, ensuring the continuity of various cellular activities, for example, the TCA cycle (ATP generation). Therefore, the main interest of this study is to characterize the mitochondrial-bound carriers in CHO cells (Table 2.4). Most research on the mitochondrial transporters has been carried out (*in vitro*) [MS87; NWN+15]. This research contributed to the first *in vivo* quantification the carriers' activities, especially the pyr/H^+ symporter (MPC), the cit/mal antiporter (CIC), the mal/phosphate dicarboxylate transporter (DIC), the mal/α-KG antiporter (OGC), the asp/glu antiporter (AGC), and the glu/H^+ symporter (GC). Additionally, ^{13}C MFA demonstrated that additional putative transporters are required to fit the model with the isotopologue data: putative Alanine transporter (mAla) and Asparagine importer to mitochondria (mAsn). This assumption was also supported by the latest genome-scale metabolic model reconstruction [HAH+16].

The activities of mitochondrial carriers and TCA cycle are depicted in Figure 3.4. As can be seen in Figure 3.4a and 3.4c, compartment-specific ^{13}C MFA reveals the highest shuttles activitiy occurred in phase I; approximately 0.4 ± 0.2 pmol cell^{-1} h^{-1} of the total metabolites transported. Furthermore, the amount of metabolites transported was gradually decreasing throughout the course of cultivation (0.24 ± 0.12 to 0.08 ± 0.04 pmol cell^{-1} h^{-1} of metabolites in Phase II to Phase III.2).

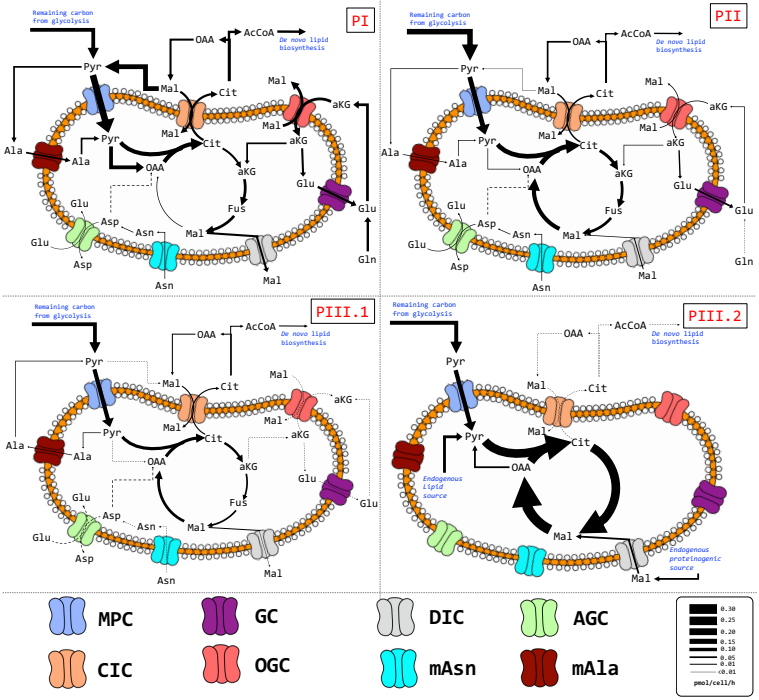

(a)

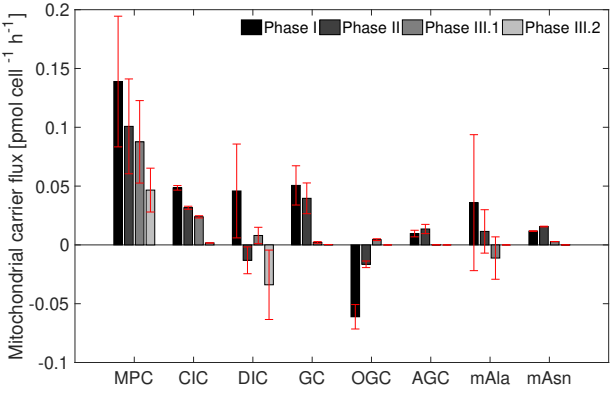

(b)

Figure 3.4.: ***In vivo* mitochondrial shuttles and TCA cycle activities** (a) mitochondrial shuttles and TCA cycle activity presented as metabolic flux map during exponential growth phase (top left); L-glutamine limited phase (top right); stationary phase (bottom left); and autophagy (bottom right); (b) mitochondrial carriers activity presented as barplot. The arrows' thickness in (a) indicate the flux level. [JTW+19]

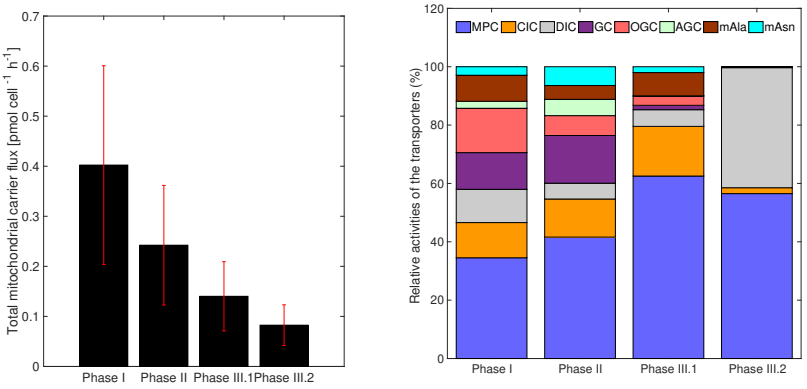

(c) (d)

Figure 3.4.: ***In vivo*** **mitochondrial shuttles and TCA cycle activities** (c) total absolute flux of mitochondrial carriers; and (d) relative activities of mitochondrial carriers [JTW+19]

Under ample D-glucose and nutrients conditions (phase I), mitochondrial carriers served as the carbon and precursor transporters for predominantly energy generation. Among all the mitochondrial carriers, the pyr/H^+ symporter (MPC) had the highest activity, which comprised about 35% of the total activities (Figure 3.4d). In CHO cells, the MPC served as one of the glycolytic carbon shuttles into the cellular powerhouse (mitochondrion). Besides, this study also indicated that a small portion of glycolytic carbon was shuttled using an alternative transporter, the alanine carrier (mAla), and the alanine aminotransferases. During the exponential growth phase, mAla contributed to the transport of about 21% of glycolytic carbon entering mitochondrion.

On the other hand, malate transport processes exhibited the second most active ones (15.19% in OGC; 12.06% in CIC; and 11.4% in DIC respectively) after the pyruvate carrier, MPC (Figure 3.4d). Overall, about 0.058 pmol cell^{-1} h^{-1} of malate was net exported to cytosol in phase I, fueling carbon

into cytosolic malic enzyme for NADPH production. Thus, the mitochondrial shuttles also indirectly regulated the NADPH production via cytosolic malic enzyme. If we now turn to the malate/α-KG carrier (OGC), when L-glutamine was in excess, the OGC served as the carrier of L-glutamine precursor (α-KG) into the TCA cycle while at the same time, exporting malate to the cytosol (Figure 3.4a).

Another carrier that might play a role in L-glutamine metabolism is the GC. In this study, GC activity was fairly similar to the OGC, which comprises 14.26% of the total transport flux in Phase I. Comparing the two results (OGC and GC), GC was functioned as L-glutamate exporter to cytosol, which was the amino acids' catabolism byproduct (amino group receiptor). Meanwhile, the activity of AGC , which is part of Malata-Aspartate Shuttle (MAS), was low (2.4%) compared to other carriers during the batch cultivation.

When L-glutamine was limited, less amount of carbon entered the mitochondria. Thus, the total mitochondrial carriers activity was decreased by approximately 40% compared to the glutaminolysis phase (Figure 3.4c). The overall activity reduction indicated that L-glutamine catabolism occurred in mitochondrion and was mediated by the mitochondrial carriers. For example, the activity of OGC was significantly reduced from 0.061 ± 0.0104 pmol cell^{-1} h^{-1} (15.19%) to 0.017 ± 0.0029 pmol cell^{-1} h^{-1} (6.8%). If we now turn to the GC activity, there was no significant compared to the previous phase.

Turning now to the experimental evidence on the MPC's activity. When L-glutamine was limited, the MPC became a more vital carrier, comprising of approximately 41.6% of the total transport activities. Nevertheless, the L-glutamine limitation reduced the total carbon entering the TCA cycle. Hence, shuttles rewiring was required to maintain the ATP supply from mitochondria. One key adaptation was the rewiring of malate metabolism.

Previously, malate was net exported to generate enough cytosolic malate to fuel the cytosolic malic enzyme. Assessing the mitochondrial malate shuttles during the L-glutamine limitation, it can be seen from Figure 3.4b that CIC was slightly reduced, DIC was reversed, and OGC was significantly reduced. Consequently, in this phase, malate was net imported (0.0285 pmol $cell^{-1}$ h^{-1}), which significantly reduced the activity of cytosolic malic enzyme in contrast to the previous phase.

Besides, the malate net import also indicated that one of the NADH indirect shuttle systems was active (Citrate-Malate Shuttle or Malate-Aspartate Shuttle). One possible explanation for these results may be the changes in cellular needs (NADPH vs ATP). When nutrient was in excess, the cells were focusing on synthesizing biomolecules for anabolism, which was NADPH demanding. The cellular needs were shifted when the cells sensed nutrient limitation. Hence, in this case, ATP production was preferred as a survival strategy.

L-glutamine limitation also led to an increase in the L-asparagine catabolism (mitochondrial asparaginase). Consequently, the activity of putative asparagine carrier (mAsn) increased by about 33%. Nevertheless, the ^{13}C MFA showed that the influence of L-asparagine catabolism to the TCA cycle activity was negligible ($< 2\%$).

When the culture entered nitrogen starvation phase (Phase III.1, stationary; and Phase III.2, autophagy), the overall shuttle activities were reduced further by approximately 42.16%. In these two phases, the majority of transport processes were associated with glycolytic carbon import via the MPC (62.54% in Phase III.1 and 56.52% in Phase III.2). In the stationary phase, all of the malate carriers (the CIC, OGC and DIC) were still active with CIC as the highest one. Concomitantly, a net malate import of 0.0204 pmol $cell^{-1}$ h^{-1} was observed, similar to the previous phase. During autophagy

(Phase III.2), the activity of DIC was surprisingly became dominant besides the MPC, comprising of 41.14% of the total activity. This is due to the assumption of cytosolic malate formation due to the self-cannibalism process. In this study, the DIC was the only independent malate transporter.

3.6. Mitochondrial shuttle systems

Mitochondrial shuttle systems are vital in proliferating and resting cells as they provide a unique funtionality in supporting cellular metabolism. In this study, two *in vivo* shuttle functions were investigated: (i) the NADPH-production shuttles and (ii) the NADH shuttles. There are four distinct shuttle systems that could achieve the two functionalities as depicted in Figure 3.5a: Pyruvate-Citrate Shuttle (PCS), Pyruvate-Malate Shuttle (PMS), Citrate-Malate Shuttle (CMS), and Malate-Asparate Shuttle (MAS). Flux estimation based on [U-$^{13}C_6$]-D-glucose and metabolic compartmentalization were used to unravel the *in vivo* shuttles activity.

The compartment-specific ^{13}C MFA revealed that only NADPH-production shuttles: PCS and PMS, were active during exponential growth phase (phase I) as depicted in Figure 3.5b. As described previously, the activity of oxidative PPP was low in this phase. Thus, an alternative NADPH producing route was needed to fulfill the cellular requirement, namely cytosolic malic enzyme. Interestingly, in this study, two out of four shuttle systems were active: the PCS and PMS, to provide sufficient cytosolic malate for the malic enzyme. PCS provide cytosolic malate via the reversed cytosolic malate dehydrogenase, using the acetyl-CoA lyase byproduct (OAA) as the precursor. Hence, the indirect convertion of cytosolic NADH into NADPH was occurred. The latter is known as transhydrogenase-like mechanism and will be discussed in the next section (Section 4). In addition, the cytosolic malate was provided

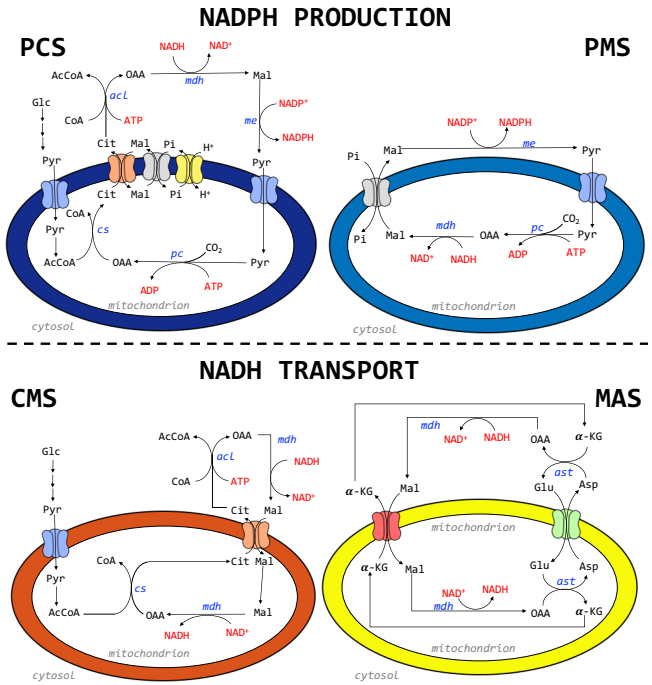

(a)

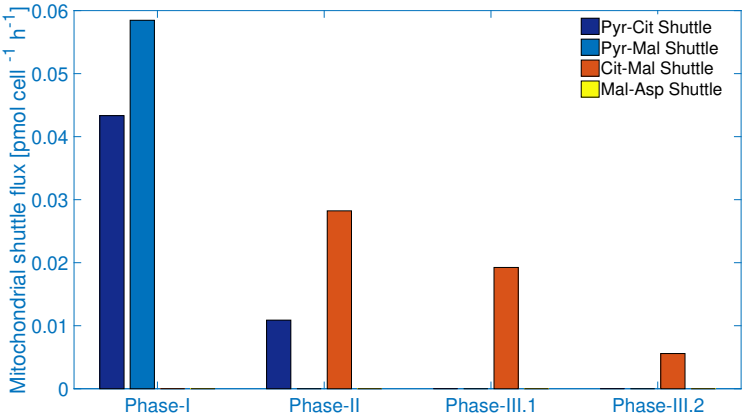

(b)

Figure 3.5.: The mitochondrial shuttle systems (a) Illustration of NADPH production shuttles: Pyruvate-Citrate Shuttle (PCS) and Pyruvate-Malate Shuttle (PMS); and NADH shuttles: Citrate-Malate Shuttle (CMS) and Malate-Aspartate Shuttle (MAS) (b) *In vivo* activity of different shuttle systems in CHO-DP12 [JTW+19]

via malate export using the DIC. In CHO-DP12, approximately 42% of the cytosolic malate was provided via the PCS and the rest via PMS (Figure 3.5b). Further analysis showed that the NADH shuttle systems (CMS or MAS) were not active at all. This indicates that aerobic glycolysis was preferred and the NADH generated in the TCA cycle was sufficient in generating the cellular ATP demand.

During the transition from exponential growth to stationary phase (L-glutamine limitation phase), the activity of shuttle systems changed dramatically. As shown in Figure 3.5b, the NADPH-production shuttles were decreased. This finding is in agreement with the previous result which indicated the reduction of cytosolic malic enzyme activity. Furthermore, flux analysis revealed that the activity of PCS was reduced by about 77%. Interestingly, the PMS was not active anymore when the L-glutamine was limited. Instead, the NADH-shuttle system, CMS, was active with an activity of about 0.03 $pmol \cdot cell^{-1} \cdot h^{-1}$. The CMS activity corresponds to about 13% of the total cytosolic NADH production.

When nitrogen was limited, the activity of NADPH-production shuttle was completely vanished. This result matches those observed earlier, especially regarding the NADPH production via cytosolic malic enzyme. Moreover, the NADH-shuttling system was still active, namely the CMS. However, the CMS's activity was reduced from 0.03 $pmol \cdot cell^{-1} \cdot h^{-1}$ to about 0.024 $pmol \cdot cell^{-1} \cdot h^{-1}$ in Phase III.1 and 0.002 $pmol \cdot cell^{-1} \cdot h^{-1}$ in Phase III.2.

The most interesting finding was that the well-known NADH-shuttle system, the MSA, was not active in CHO-DP12. A possible explanation for this might be due to how the cells metabolized L-glutamine. In L-glutamine catabolism, the Mal/α-KG antiporter (OGC) served as the of α-KG mitochondrial import. Besides, the activity of AGC was relatively low throughout the course of cultivation, with a maximum of 0.013 $pmol \cdot cell^{-1} \cdot h^{-1}$ in phase II before

vanished in phase III.1 and III.2.

3.7. Identifying metabolic engineering targets for optimizing IgG1 production

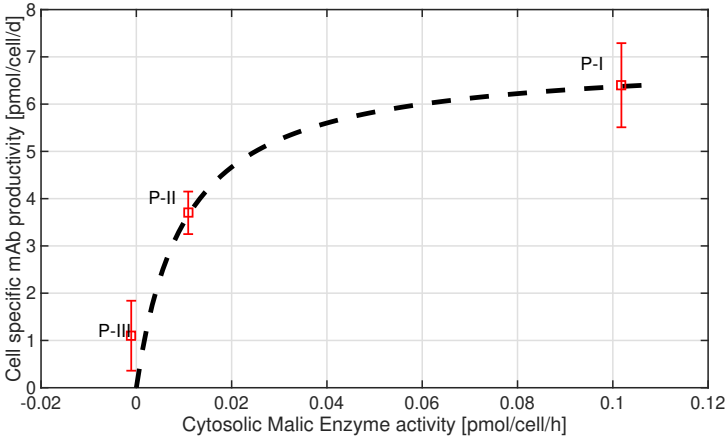

Figure 3.6.: Comparison of cell specific IgG1 productivities vs. cytosolic malic enzyme activities (fluxes) during different cultivation phases (I–III) [JTW+19]

Figure 3.6 displays the positive correlation between cell-specific mab productivity and the me_{cyt}, identified as the primary source of NADPH. Maximum cell-specific productivity was achieved under ample carbon and nutrient supply (phase I), allowing the maximum NADPH production via PCS and PMS (Figure 3.5b). Any reduction of nitrogen and/or carbon supply deteriorated the mAB productivity, which unravels the apparent demand to install proper substrate supply for achieving maximum product formation rates. Further limitations of L-glutamine (phase II) and L-asparagine (phase III) altered the mitochondrial shuttles from the full NADPH production scenario to the

full NADH shuttle, which strongly highlights the role of L-glutamine and L-asparagine in cellular energetics.

Figure 3.6 also suggests that $(\partial q_{m_{AB}})/(\partial v_{me_{cyt}})$, is the highest under limited nitrogen supply reflecting low undersaturated conditions (phase II). Apparently, non-metabolic regulation regimes gain importance the better the metabolic precursor, ATP and NADPH supply are. Consequently, research studies should focus on additional impact factors such as protein folding, translocation and secretion once sufficient metabolic precursor supply is ensured.

3.8. Conclusion

The experimental and analytical approach allowed a time-resolved compartment-specific study of metabolism and shuttle dynamics of CHO cells. Subcellular investigations revealed cellular survival strategies to adapt the cellular metabolism to severely changing nitrogen and carbon availability. Under ample D-glucose and amino acid supply, L-lactate secretion was maximal, as well as activities of the citrate-pyruvate (MPC, DIC, CIC) and malate-aspartate shuttles (OGC, AGC). As a consequence, a well-balanced cytosolic NADH, NADPH, and AcCoA supply, coinciding with high mitochondrial TCA activity, was established. Because most shuttling activities are concentration driven, said activities decreased with limited L-glutamine. However, adaptations were coordinated tightly, as indicated by the interplay between OGC and DIC to ensure a proper supply of malate, also comprising inverted DIC shuttling. Even when the cellular autophagy program was initiated, mitochondrial ATP levels persisted, and Mal exchange and Pyr import into mitochondria continued which assigns key roles of mitochondrial/cytosolic interaction to these metabolites.

In terms of metabolic engineering the findings disclose novel strain engineering perspectives putting proper L-glutamine supply in the focus: the switch from mitochondrial malate net-export to malate net-import coincided with diminishing L-glutamine supply and reduced NADPH formation – and, maybe most important, with a severe reduction of cell specific IgG1 productivities. Given that L-glutamine auxotrophic cells (this study) and cell lines with active glutamine synthase are alternatively used as production hosts, proper L-glutamine supply becomes an optimization goal. This question is further intertwined with product formation kinetics which may show growth coupled or non-growth coupled properties thereby requiring more or less NADPH for growth. In this study, net malate export from mitochondria to the cytosol, reflecting proper L-glutamine supply, was essential to achieve highest cell specific productivities. Additionally, sufficient respiratory ATP formation should be installed to ensure high cell specific productivities. As a result, L-glutamine supply, NADPH and ATP availability and growth capacities are tightly coupled and affect the product formation kinetics. Additionally, the results show that total productivity control shifts to metabolic engineering targets 'downstream' of precursor supply the better the substrate availability is. Given that current production cells are typically optimized with respect to protein processing the question occurs whether such strains need revisiting of central metabolism to fully exploit the inherent potential. Consequently, detailed systems metabolic engineering studies are needed to enable model-based cell engineering.

Chapter 4

A transhydrogenase-like mechanism in CHO cells comprising concerted cytosolic reaction and mitochondrial shuttling activities. [1]

Abstract

The proper supply and regeneration of reduction equivalents such as NADH and NADPH is of pivotal importance for living cells. Although both, NADH and NADPH, are electron carriers, they serve for different, complementing needs and require well balanced exchange. In Chinese hamster ovary (CHO) cells, the proton translocator 'Nicotinamide Nucleotide Transhydrogenase' (NNT) was annotated recently, but no *in vivo* operational evidence was given, yet. Here, we present another transhydrogenase-like mechanism building

[1] This chapter was published as: **Wijaya, A.W.** & Takors, R. (2021). A transhydrogenase-like mechanism in CHO cells comprising concerted cytosolic reaction and mitochondrial shuttling activities. *Biochemical Engineering Journal*, **170**, 107986

on the adaptive interplay of cytosolic malate dehydrogenase (mdh_{cyt}) and cytosolic malic enzyme (me_{cyt}) with the mitochondrial shuttles citrate carrier (CIC), dicarboxylate carrier (DIC), and mitochondrial pyruvate carrier (MPC). The system is highly flexible using malate and pyruvate as intermediary electron carriers and quickly adapts to current needs. Indications for the existence of the mechanism are found in different monoclonal antibody producing CHO cell lines and under growing and stationary conditions.

4.1. Introduction

The proper supply and regeneration of reducing equivalents such as NADH and NADPH is pivotal for living cells. Under aerobic conditions, oxidation of NADH is the dominant source of free Gibbs energy. 220 $kJ/mole_{NADH}$ are provided oxidizing NADH to create the thermodynamic driving force for anabolism. Basically, the latter is stored in ATP. On contrary, NADPH serves as an electron donor in anabolic reduction steps. Hence, NADH and NADPH are crucial pyridine nucleotide electron carriers in cellular metabolism, serving completely different; but complementary needs [HV18].

In mammalian cells, such as CHO cells, the primary NADH sources are found in cytosolic glycolysis and the mitochondrial citric acid cycle. Regeneration of NAD^+ from NADH predominantly occurs via two mechanisms: the cytosolic reduction of pyruvate to lactate via the lactate dehydrogenase (*ldh*) and the fueling of NADH electrons into the electron transport chain of the inner mitochondrial membrane-bound oxidative phosphorylation. Besides, NADPH is oxidized in multiple biosynthetic steps, including the formation of recombinant proteins. The proper supply of NADPH in IgG1 producing cells has been identified as a key metabolic engineering target for optimizing, e.g., monoclonal antibodies production [JTW+19]. Anabolic reactions are

predominately located outside the mitochondria.

Proliferating cells tend to maintain low NADH/NAD^+ ratios to ensure high glycolytic fluxes [SPJP74; ZWZ+16]. Conversely, NADPH/$NADP^+$ ratio remains relatively high to provide sufficient electrons for biosynthetic pathways [PDZ07; VEK69]. Mammalian cells may maintain preferred NADH/NAD^+ ratios by controlling the *ldh* activity. By analogy, cytosolic NADPH/$NADP^+$ ratios could be regulated by finetuning activities of the cytosolic, $NADP^+$ dependent enzymes Glucose-6-phosphate dehydrogenase, 6-phosphogluconate dehydrogenase, and malic enzyme [AA11; FYK+14; JTW+19; LSF+16].

The proper installation of NADH/NAD^+ and NADPH/$NADP^+$ ratios is crucial for achieving metabolic homeostasis [LV11]. Whereas the measures mentioned above focus on individual NADH/NAD^+ and NADPH/$NADP^+$ ratios, pro- and eukaryotic cells may use an additional tool: the so-called transhydrogenase enzyme. In essence, cytosolic and membrane-bound enzymatic activities often catalyze the reaction from NADH + $NADP^+$ to NAD^+ + NADPH and vice versa, respectively. Recently, Nesci and coworkers [NTP20] reported the enzyme structure of mitochondrial nicotinamide nucleotide transhydrogenase (NNT) in mammalian cells. Moreover, a similar proton-translocator encoding cytosolic NNT was annotated in the CHO genome [HAH+16]. However, experimental *in vivo* evidences of NNT operations in cytosol and mitochondrion are missing, still.

The examples have in common that redox reaction pairs are located in a single compartment. However, eukaryotes offer the possibility to perform oxidation/reduction reactions involving several reaction steps, even crossing membrane barriers, as depicted in Figure 4.1. One example may be the so-called pyruvate-citrate shuttle (PCS) comprising the mitochondrial pyruvate carrier (MPC) and the citrate/malate antiporter (CIC). PCS was anticipated to convert NADH into NADPH, utilizing malate as an electron

carrier during insulin production [Pal04]. Figure 4.1 elucidates that said system might be extended to a trans-compartment transhydrogenase-like function by integrating the pyruvate-malate shuttle (PMS). However, further experimental evidence is missing, still.

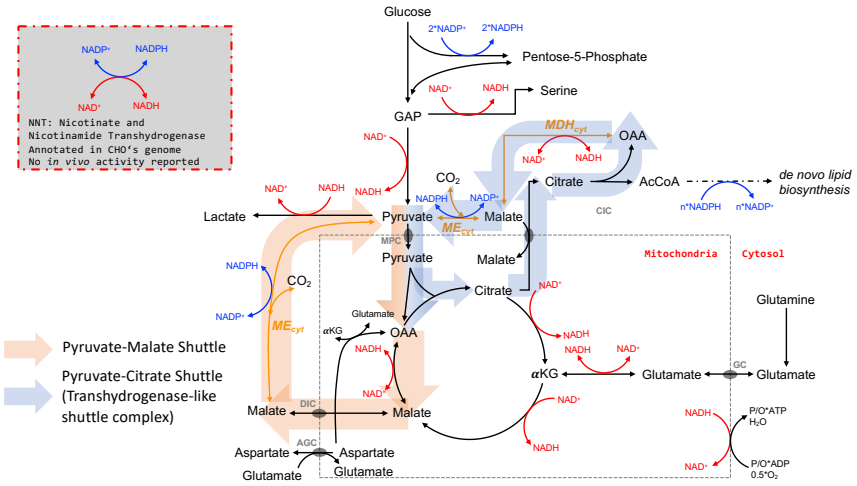

Figure 4.1.: Primary sources and sinks of NAD(H) and NADP(H) in CHO cells' central carbon metabolism. Orange (Pyruvate-Malate Shuttle): Mitochondrial electrons from oxaloacetate (OAA) and NADH are transferred to cytosolic NADPH via cytosolic malic enzyme (me_{cyt}). Blue (Pyruvate-Citrate Shuttle): Cytosolic electrons from OAA and NADH are charged on malate via cytosolic malate dehydrogenase (mdh_{cyt}) and translocated to cytosolic NADPH via cytosolic malic enzyme (me_{cyt}). Consequently, orange Pyruvate-Malate-Shuttle provides trans-compartment transhydrogenase activity. The blue Pyruvate-Citrate- Shuttle provides cytosolic transhydrogenase activity. [WT21]

Here, we give evidence to another multi-compartment, transhydrogenase-like mechanism building on the adaptive interplay of cytosolic malate dehydrogenase (mdh_{cyt}), cytosolic malic enzyme (me_{cyt}), and the intermediate electron carriers malate and pyruvate. Whereas pyruvate is always imported into mitochondrion, malate will be shown to be im- or exported depending on the cytosolic needs. Noteworthy, the existence was confirmed under in vivo conditions. Conclusions were based on intracellular flux distributions al-

ready provided in Junghans and coworkers [JTW+19] and in Verhagen and coworkers [VWT+20]. Said independent studies focused on the two CHO cell lines DP12 and BIBH1 under similar cultivation conditions, supporting the existence of the transhydrogenase-like mechanism in CHO.

4.2. Results

Results base on already published data of Junghans and coworkers [JTW+19] and Verhagen and coworkers [VWT+20] which were reconsidered for further evaluation (see Table 4.1 for complete intracellular flux distribution). Notably, Junghans and coworkers performed compartment-specific metabolomics and ^{13}C MFA, which allowed to elucidate mitochondrial shuttle activities *in vivo* via data-driven metabolic flux analysis. The pioneering data are compared with the results of Verhagen and coworkers, who studied the impact of L-Prolyl-L-Tyrosine (PY) addition on the metabolism of CHO BIBH1. PY amplified the cell-specific glucose uptake rate in the BIBH1 cell line while maintaining the lactate secretion rate. Thus, more carbon was fueled into mitochondria finally yielding different citric acid cycle activities. BIBH1 is an industry based IgG1-producer which demonstrated higher glucose uptake rates and IgG1 cell specific productivity compared to the CHO-DP12 cell line. Accordingly, the two independent data sets reflect similar cultivation conditions but different glycolytic and mitochondrial activities in CHO cells. In this sense, they serve as independent measurements challenging the hypothesis that the interplay of selected mitochondrial shuttle activities provides transhydrogenase-like mechanisms in CHO.

4.2.1. CHO cells' transhydrogenase-like mechanism

One of the central findings of Junghans and coworkers [JTW+19] was the identification of the cytosolic malic enzyme (me_{cyt}) as the primary source of cytosolic NADPH. Notably, related NADPH formation was 12.5-fold higher than NADPH production via the oxidative pentose phosphate pathway (PPP) in exponentially growing cells. The observation confirmed former hypothesis of Ahn & Antoniewicz [AA11] and Templeton and coworkers [TDRY13], who anticipated that Glucose-6-phosphate dehydrogenase is not the only and dominating source of NADPH.

Recently, the use of deuterated glucose tracers disclosed the conversion of serine to glycine inside mitochondria by methylene tetrahydrofolate dehydrogenase (MTHFD2/MTHFD2L) as an important mitochondrial source of NADPH [LPF+14]. Further evidences for transhydrogenase-like mechanisms were not found although recent findings indicated the existence of active mitochondrial nicotinamide nucleotide transhydrogenase (NNT) [NTP20].

As a further step of data evaluation, we now wondered which electron donors are used to fuel cytosolic NADPH formation via the me_{cyt}. We compared flux patterns of CHO-DP12 and BIBH1 being aware of the different modelling approaches for flux map identification but still wondering about the occurrence of common flux schemes. Interestingly, we found indications for common transhydrogenase-like activities as shown in Figure 4.2. Reevaluating the measured fluxes, we identified the NADH + $NADP^+$ → NAD^+ + NADPH regeneration scheme depicted in Figure 4.2. Fluxes varied within the observed range as depicted in Figure 4.2d. Interesting enough, we observed transhydrogenase-like activity without requiring any distinct transhydrogenase gene such as the annotated NNT.

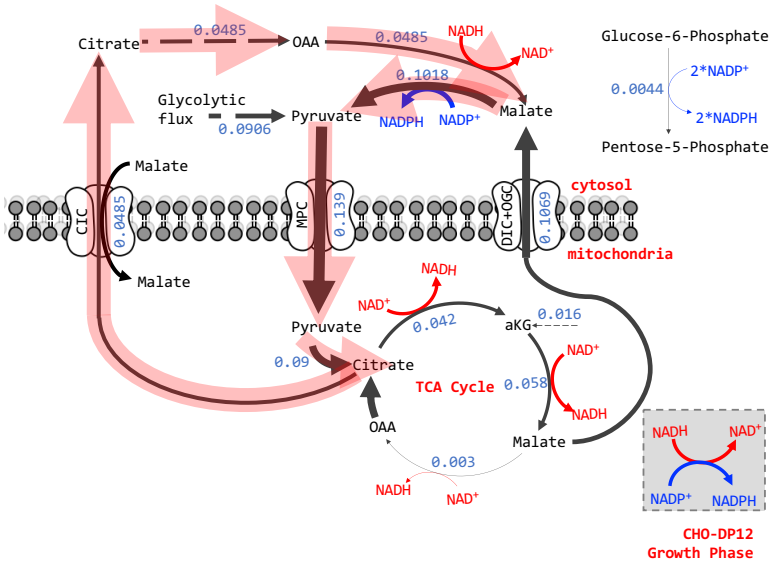

(a)

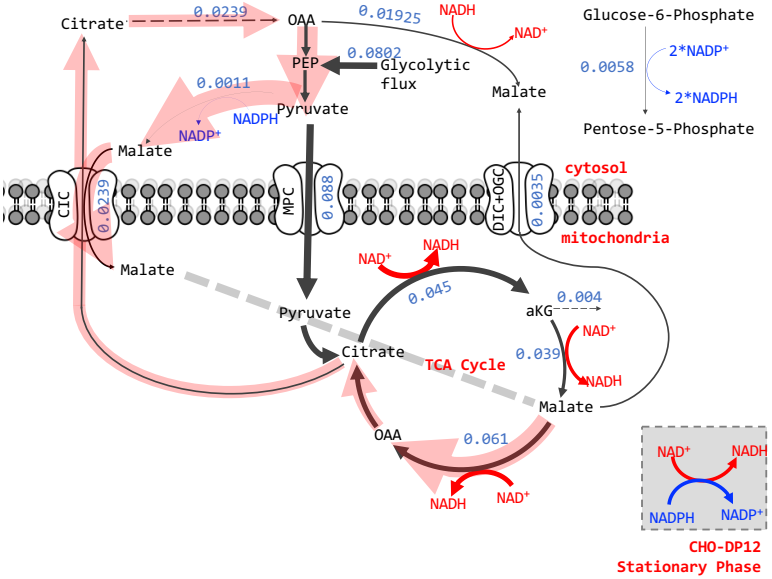

(b)

Figure 4.2.: Transhydrogenase-like mechanism in CHO cells (highlighted with reddish background): (a) observed in growth phase of CHO-DP12; (b) observed in stationary phase of CHO-DP12. Flux estimates (in pmol cell^{-1} h^{-1}) were derived from experimental duplicates. [WT21]

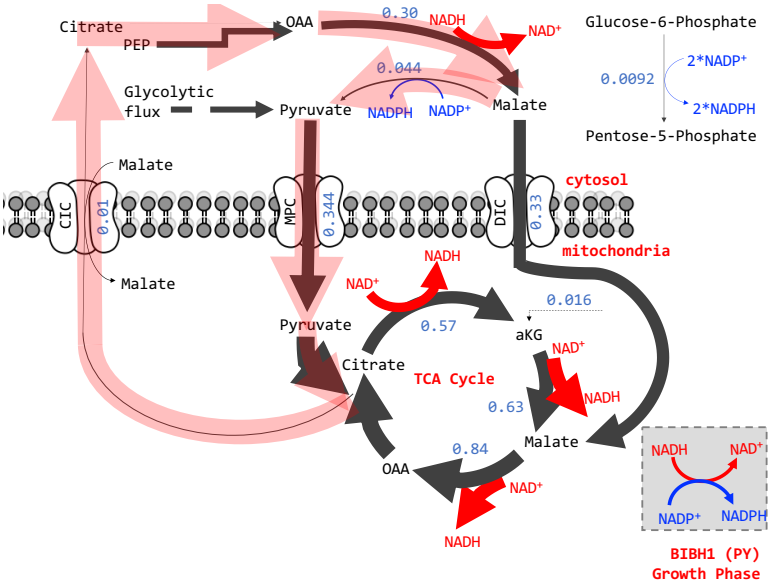

(c)

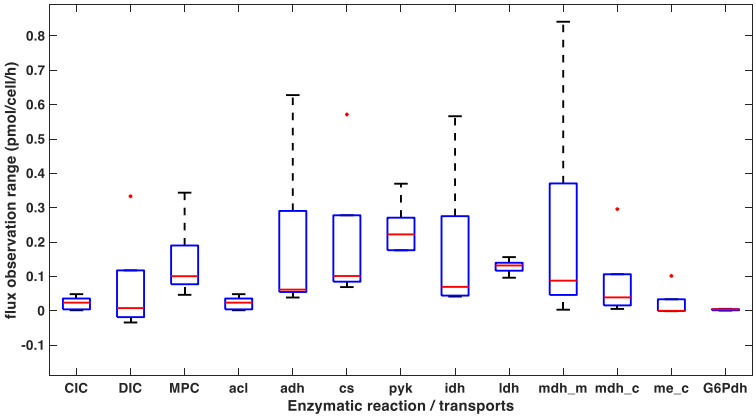

(d)

Figure 4.2.: Transhydrogenase-like mechanism in CHO cells (highlighted with reddish background): (c) observed in growth phase of CHO BIBH1; and (d) observed flux ranges derived from different data sets still supporting the transhydrogenase-like mechanism in two different CHO cell lines (CHO-DP12 and BIBH1). Flux estimates (in pmol cell^{-1} h^{-1}) were derived from experimental duplicates. [WT21]

The two enzymatic protagonists of the transhydrogenase-like mechanism in CHO cells are the mdh_{cyt} and the me_{cyt}. In brief, mdh_{cyt} catalyzes electron donation by oxidizing NADH to provide the electrons for the reduction of $NADP^+$ in me_{cyt}. The scenario in Figure 4.2a investigating CHO DP12 cells unravels that the majority of NADPH is provided by said mechanism identifying 0.0433 $pmol_{NADPH} \cdot cell^{-1} \cdot h^{-1}$ via $me_{cyt}$and only 0.0044 $pmol_{NADPH} \cdot cell^{-1} \cdot h^{-1}$ via the oxidative PPP. The intermediate electron carrier of cytosolic NADPH formation is malate. Malate was already identified as a key shuttling metabolite during the exponential growth of CHO tightly linking mitochondrial and cytosolic activities via the Malate/Aspartate shuttle [JTW+19]. As indicated in Figure 4.2a, pyruvate and malate enter the mitochondrion, the first via the mitochondrial pyruvate carrier (MPC) and the second via net interaction of the exporting dicarboxylate shuttle (DIC) and the importing citrate/malate antiporter (CIC). Note that DIC's direction may shift serving as mitochondrial malate exporter in Figure 4.2a and as malate importer in Figure 4.2c. This underlines the flexibility of the DIC shuttle emphasizing the dual function of malate: Malate export from mitochondrion supports NADPH demands under growth conditions whereas malate import into mitochondrion finally fuels the citric acid cycle. CIC and MPC always function in the same direction importing malate and pyruvate into mitochondrion. Once taken up, both metabolites enter the citric acid cycle, are oxidized to produce NADH which is finally respired to gain ATP. Although malate is net exported into cytosol in Figure 4.2a and net imported into mitochondrion in Figure 4.2c, predominant cytosolic NADPH formation still happens via me_{cyt}. Malate and pyruvate serve as intermediate electron carriers in both cases, net importing electrons into mitochondrion predominately via pyruvate using MPC.

Revisiting the study of Verhagen and coworkers [VWT+20], a similar transhydrogenase-mechanism observed in CHO-DP12 gets obvious. Now, the interplay of mdhcyt with me_{cyt} consumed NADPH which has been produced

in the PPP. Consequently, malate could be net imported into mitochondrion. CIC mediated malate import outcompeted DIC export. Apparently, the nutrient limiting conditions of scenario in Figure 4.2c did not require extraordinary amounts of NADPH for anabolic demands. Instead, there was a higher need for ATP which was fulfilled by oxidizing NADH generated from citric acid cycle activity.

Summarizing, each of the scenarios in Figure 4.2 gives evidence for the existence of a two-compartments transhydrogenase-like mechanism. The interplay comprises cytosolic mdh_{cyt}; me_{cyt}, the trans-compartment electron carriers: pyruvate and malate; and the mitochondrial citric acid cycle producing NADH. Reaction and shuttle activities adapt to the current needs of NADPH and NADH which are showcased by the flux maps in Figure 4.2. Interesting enough, the common scheme occurs in different cell lines and under different growth conditions covering wide ranges of flux distributions (Figure 4.2d). Notably, the wide range of the most flux distribution indicated in Figure 4.2d was mainly due to the different experimental setups (bioreactor vs shaking flask), cell lines, conditions, and metabolic states. As an example, high variability of citric acid cycle activities was caused by the PY boost in BIBH1 cell line compared to the reference state of DP12 cell line.

4.2.2. Transhydrogenase-like activity in CHO cells

Figure 4.3 summarizes compartment-specific production and consumption of NADH and NADPH for the flux scenarios depicted in Figure 4.2. To be precise: the NADPH producing fluxes via the oxidative pentose phosphate pathway, cytosolic malic enzyme (me_{cyt}), and the transhydrogenase-like mechanism are balanced with estimated cellular anabolic demands. Cytosolic and mitochondrial NADH formation and consumption are balanced by analogy considering respiration as gap filling sink. During exponential growth, me_{cyt}

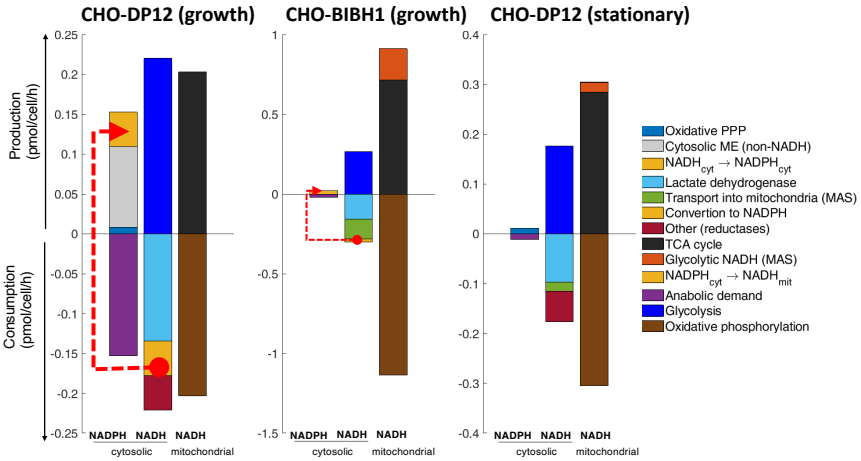

Figure 4.3.: Production (upper part) and consumption (lower part) of NADPH and NADH assigned to cytosol and mitochondrion and calculated for different cells: CHO-DP12 (left: growing; right: stationary) and CHO-BIBH1 (middle: growing). Different origins and sinks for NADH and NADPH are color encoded as listed in the legend. The dashed red line indicates the electron flows in the transhydrogenase-like mechanism. Fluxes are calculated from independent 13C studies already published as indicated in the text. [WT21]

fluxes of CHO-DP12 were approximately 0.1 $pmol_{malate} \cdot cell^{-1} \cdot h^{-1}$. 43% of the produced NADPH originated from the interaction with mdh_{cyt}, i.e., from cytosolic NADH. Considering the entire NADPH formation, including the oxidative pentose phosphate pathway, about 41% of total cytosolic NADPH was derived from cytosolic NADH. In the case of BIBH1, the trend was even more pronounced unravelling almost all of the NADPH was supplied from 'transhydrogenase-based' activity. As already outlined in Figure 4.2b, no NADPH was formed via me_{cyt} under severe nutrient limitation. The related support to NADH formation via reversed me_{cyt} accounted for less than 1% of total NADH (value too small for indication in Figure 4.3).

4.3. Concluding remarks

Transhydrogenase activity is often found in pro- and eukaryotic cells to quickly react on changing needs of NADH and NADPH. Genome annotation already anticipates the existence of a said enzyme called NNT in CHO. However, independent ^{13}C flux studies clearly pinpoint to the existence of an additional transhydrogenase-like mechanism comprising the tight interaction of MDH_{cyt} and ME_{cyt} together with the mitochondrial pyruvate carrier (MPC) and malate-dicarboxylate carrier (DIC). The malate carrier (DIC) has shown its high flexibility to adapt to changing needs by even inverting shuttle directions. Accordingly, one may fairly anticipate that the said transhydrogenase mechanism serves as a quick, tactical measure of CHO cells to adapt NADPH needs. It remains somewhat open whether and how NNT further supports electron equilibration for the reduction equivalents. Based on our estimations, NNT is likely to support NADPH formation only. Nevertheless, the question deserves further research activities as proper NADPH may be crucial for maximizing the therapeutic proteins' anabolic formation.

4.4. Supplementary Material

Table 4.1.: Summary of metabolic fluxes in different scenarios

ID	Reaction	Fluxes (pmol/cell/h)		
		Scenario a	Scenario b	Scenario c
AGC	Glu + Asp_m =>Glu_m + Asp	0.00965031	0.26986861	7.44E-05
CIC	Cit_m + Mal =>Cit + Mal_m	0.04850983	0.00515419	0.02385687
DIC	Mal_m = Mal	0.04585948	-0.3333595	0.00800755
GC	Glu_m = Glu	0.05058626	0.24281449	0.0021063
MPC	Pyr =>Pyr_m	0.13891239	0.34389077	0.08763999
OGC	Mal + aKG_m = Mal_m + aKG	-0.0611179	0.0000000	0.00446713
acl	Cit =>OAA + AcCoA	0.04850983	0.00515419	0.02385687
adh	aKG_m = Fum_m + CO2_m	0.06177246	0.62792404	0.03877627
alt_c	Pyr + Glu = Ala + aKG	0.05885351	0.0200000	-0.008
alt_m	Ala_m + aKG_m = Pyr_m + Glu_m	0.03590917	0.0000000	-0.0111928
asns_m	Asn_m = Asp_m	0.01172453	0.02247954	0.00279884
ast_c	Asp + aKG = OAA + Glu	-0.0022644	-0.2908103	-0.0035329

ID	Reaction	Fluxes (pmol/cell/h)		
		Scenario a	Scenario b	Scenario c
ast_m	Asp_m + aKG_m = OAA_m + Glu_m	0.00207422	0.26986861	0.00272441
csyn	AcCoA + OAA =>Cit	0.09010035	0.57154173	0.06913213
pgi	G6P = F6P	0.11154558	0.18489949	0.08637453
pfk	F6P = FbP	0.11143443	0.18503698	0.08847596
fbpa	FbP = GAP + DHAP	0.11143443	0.18503698	0.08847596
tpi	DHAP = GAP	0.11143443	0.18489427	0.08847596
gapdh	GAP = 3PG	0.22042218	0.37	0.17682671
eno	3PG = PEP	0.21959151	0.37	0.17544465
pkm	PEP =>Pyr	0.2225045	0.37	0.17652354
gdh	aKG_m = Glu_m	-0.0029526	-0.1357664	-0.0105003
gs	Gln =>Glu	0.05076881	0.03469011	4.89E-06
idh	Cit_m = aKG_m + CO2_m	0.04159052	0.56638755	0.04527526
ldh	Pyr = Lac	0.1344024	0.15636	0.09634277
mAla	Ala = Ala_m	0.03590917	0.0000000	-0.0111928
mAsn	Asn = Asn_m	0.01172453	0.02247954	0.00279884

ID	Reaction	Fluxes (pmol/cell/h)		
		Scenario a	Scenario b	Scenario c
mdh	Mal_m = OAA_m	0.00330492	0.84141034	0.06057692
mdh_c	OAA = Mal	0.04333246	0.29596448	0.01924511
me_c	Mal = Pyr + CO2	0.1018	0.04367589	-0.0010713
me_m	Mal_m = Pyr_m + CO2_m	0	0.12502738	-0.0014842
pc	Pyr_m = OAA_m	0.08472121	0.0000000	0.0058308
pdh	Pyr_m =>AcCoA_m	0.09010035	0.46891815	0.06913213
pepck	OAA = PEP + CO2	0.00291299	0.0000000	0.00107889
G6Pdh	G6P =>P5P + CO2	0.0044	8.82E-04	0.00582504

Chapter 5

Compartment-specific metabolome labeling enables the identification of subcellular fluxes that may serve as promising metabolic engineering targets in CHO cells [1]

Abstract

^{13}C labeling data are used to calculate quantitative intracellular flux patterns reflecting *in vivo* conditions. Given that approaches for compartment-specific metabolomics exist, the benefits they offer compared to conventional non-compartmented ^{13}C flux studies remain to be determined. Using compartment-specific labeling information of IgG1-producing Chinese ham-

[1] This chapter was published as: **Wijaya, A.W.**, Ulmer, A., Hundorsfer, L., Verhagen, N., Teleki, A., & Takors, R. (2021). Compartment-specific metabolome labeling enables the identification of subcellular fluxes that may serve as promising metabolic engineering targets in CHO cells. *Bioprocess and Biosystems Engineering*, **44**(12), 2467-2578

ster ovary cells, this study investigated differences of flux patterns exploiting and ignoring metabolic labeling data of cytosol and mitochondria. Although cellular analysis provided good estimates for the majority of intracellular fluxes, half of the mitochondrial transporters, and NADH and ATP balances, severe differences were found for some reactions. Accurate flux estimations of almost all isoenzymes heavily depended on the sub-cellular labelling information. Furthermore, key discrepancies were found for the mitochondrial carriers v_{AGC1} (aspartate/glutamate antiporter), v_{DIC} (malate/H^+ symporter), and v_{OGC} (α-ketoglutarate/malate antiporter). Special emphasis is given to the flux of cytosolic malic enzyme (v_{me}): it could not be estimated without the compartment-specific malate labelling information. Interesting enough, cytosolic malic enzyme is an important metabolic engineering target for improving cell-specific IgG1 productivity. Hence, compartment-specific 13C labeling analysis serves as prerequisite for related metabolic engineering studies.

5.1. Introduction

^{13}C metabolic flux analysis (^{13}C MFA) is a key tool for quantitative analysis in systems metabolic engineering. First, applications dealt with prokaryotic cells [Wie01] but the technique was also applied for eukaryotes, such as yeast [FW05; WDR+05], fungi [ZKR+08], mammalian [AA11], templeton2013peak, junghans2019nutritional, and plant [ASO07] cells. Among others, prokaryotes and eukaryotes differ in cellular compartmentalization, which is particularly important when using ^{13}C MFA. In eukaryotes, compartmentalization is essential since each cellular compartment fulfils different functions [AA12]. Even multi-compartment isozymes exist that serve different purposes. For example, Chinese hamster ovary (CHO) cells comprise cytosolic and mitochondrial malic enzymes (MEs) with different NAD^+ and

$NADP^+$ regeneration capacities, thereby fulfilling diverse catabolic and anabolic needs [JTW+19].

Metabolic compartmentalization must be considered when performing ^{13}C MFA [AA12]. There are two levels of complexity; on the one hand, subcellular metabolic models should be used to enable proper *in silico* predictions. On the other hand, *in vivo* compartment-specific metabolome data should be available to allow data-driven studies. Nicolae and coworkers [NWB+14] and Pfizenmaier & Takors [PT17] provided evidence for the importance of subcellular stoichiometric models for estimating fluxes in CHO cells. Regarding the latter, Matuszczyk and coworkers [MTPT15] applied compartment-specific metabolomics in CHO outlining that cytosolic ATP pools are considerably larger than their mitochondrial counterparts. Later, Junghans and coworkers [JTW+19] continued investigating mitochondrial and cytosolic metabolic patterns under different cultivation conditions. They found that pool sizes differed between cytosol and mitochondria for all conditions.

Given that subcellular metabolomics are very laborious [MTPT15], junghans2019nutritional, the question arises what differences may occur if ^{13}C flux analysis is based on whole-cell metabolomics instead of compartment-specific measurements. In other words, whether the additional lab-efforts justify the information gain of subcellular studies. Alternative approaches such as superimposing the patterns of two independent ^{13}C experiments using labelled glucose and labeled glutamine also aim to decipher subcellular flux distributions [AA13]. However, they rely on glutamine synthase deficient cells whereas the suggested subcellular metabolomics approach may be universally applicable.

Given that labeling dynamics in metabolite pools expressed by the ^{13}C labelling turn-over (τ_{13C}) are a key information for quantifying fluxes, influ-

encing factors may be considered. Two factors, pool size of metabolite i and net labelling flux j through this pool [BAB+15], exist. Either factor may change when a system's analysis shifts from simplifying single to realistic multi-compartment analysis. Differences in τ_{13C} may occur originating from individual pool sizes and fluxes inside the compartments. In theory, the same metabolite in different compartment might present a different labeling dynamic providing that the metabolite turn-over time is different. Thus, resulting on a different labeling dynamics (τ_{13C}).

Exploiting the unique subcellular labelling dataset of Junghans and coworkers [JTW+19], this study investigated whether subcellular labelling information is crucial to obtain the correct compartment-specific flux patterns. Flux distributions considering and ignoring subcellular metabolite labelling were performed using CHO as the showcase (metabolic model is displayed in Figure 5.1). This study investigated whether significant differences exist using whole-cell and compartment-specific metabolic information.

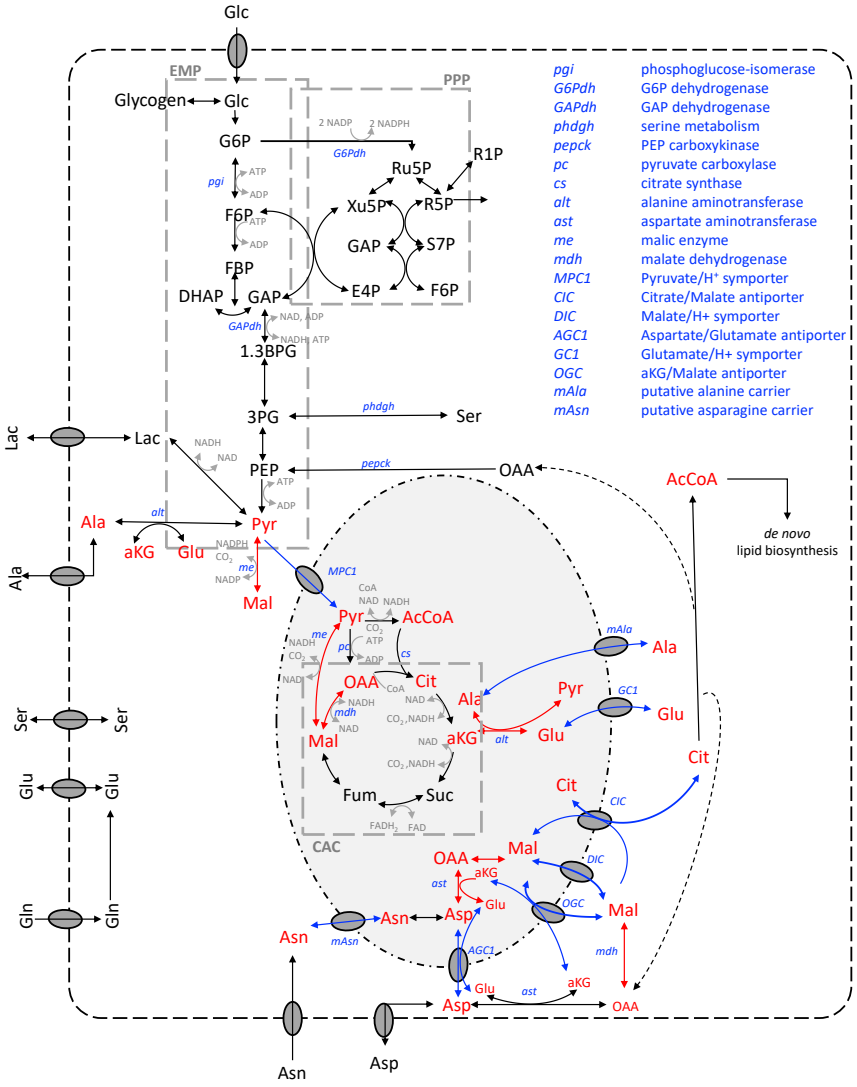

Figure 5.1.: Classification of enzymatic reaction used in the analysis. [Black arrow]: biochemical reactions belong to single compartment; [Red arrow]: biochemical reactions belong to multiple-compartment; [Blue arrow]: Intercompartment connector. Single compartment metabolites were labelled with black and multi-compartment metabolites were labelled with red. [WUH+21]

5.2. Result

Prior to the ^{13}C MFA studies, a metabolic network model was formulated (see Table 2.5). First the structural identifiability and calculability of the network was assessed applying well established methodologies (see Section 5.5.1). Next, the identifiability of distinct fluxes was checked by simulating intracellular ^{13}C labeling patterns assuming pool sizes measured by Junghans and coworkers [JTW+19]. Results presented in the appendix (Section 5.5.5) indicate the good identifiability of intracellular fluxes which motivated us to continue the study by analyzing real labeling patterns and flux distributions.

In a study by Junghans and coworkers, CHO-DP12 cells were cultivated in a bioreactor to investigate three distinct growth scenarios; (I) exponential growth with no (carbon and nitrogen) limitation; (II) moderate growth with L-glutamine depletion and L-asparagine saturation; and (III) stationary phase with severe nitrogen limitation. However, the current study regarding the impact of subcellular ^{13}C data only covers the exponential growth phase during the first 24 h. This period is typically investigated *in vitro* because labeling and cultivation conditions can be controlled easily, giving accurate results regarding flux distributions and cell-specific productivity [AA11; TDRY13]. The summary of all estimated intracellular fluxes is provided in Section 5.5.6

5.2.1. Cell growth and carbon labeling studies

During the exponential growth phase, cells grew with $0.02524 \pm 0.0009\ h^{-1}$. Carbon and nitrogen sources were constantly consumed, and metabolic byproducts were steadily released with constant specific rates. D-glucose was consumed as a major carbon source while L-glutamine and L-asparagine

served as primary nitrogen sources. Additionally, the Warburg effect was observed [War56], showing a glucose-to-lactate ratio of 0.93 $mol_{D\text{-glucose}}/mol_{L\text{-lactate}}$. ^{13}C carbon labelling was introduced by the addition of 75% [U-^{13}C]-D-glucose after 2.5 days, revealing no phenotypic changes, i.e., no alterations of cellular metabolism.

5.2.2. ^{13}C metabolic flux analysis using compartment-specific metabolome data

^{13}C MFA was performed using compartment-specific metabolome data reflecting subcellular pools of cytosol and mitochondria together with isotopomer profiles of the said compartments. Flux estimations were performed at least 100 times with randomized input values and rational boundary values for each parameter. Finally, the χ^2 tests achieved 228.87, which served the statistical constraint of 232.92 on a 95% significance level.

5.2.2.1. Glycolysis and PPP

High glycolytic (0.112 ± 0.0171 pmol·cell^{-1}·h^{-1} of hexokinase) and extremely low PPP fluxes (0.008 ± 0.001 pmol·cell^{-1}·h^{-1} of G6P dehydrogenase) were found. The latter accounted for 6.68% of the D-glucose consumed. These observations are in agreement with the findings of Ahn and Antoniewicz [AA11], who performed ^{13}C MFA in adherent CHO-K1 cells. Additionally, approximately 15% (0.016 ± 0.002 pmol·cell^{-1}·h^{-1}) of intracellular G6P was continuously in exchange with endogenous glycogen.

5.2.2.2. *In vivo* mitochondrial shuttle

Glycolytic carbon fueled into mitochondria via two transport mechanisms; 77% entered via the mitochondrial pyruvate carrier (MPC1/2) and 23% via a putative L-alanine transporter. MPC1/2 showed the highest mitochondrial transport activities while other transporters exchanged compounds for different purposes; (i) mitochondrial citrate carrier (citrate/malate antiporter; 0.049 ± 0.002 pmol·cell^{-1}·h^{-1}) served as a citrate exporter to provide cytosolic acetyl-CoA for the *de novo* lipid biosynthesis pathway; (ii) the malate-aspartate shuttle comprising 2-oxoglutarate carrier (α-ketoglutarate/malate antiporter) and aspartate-glutamate carrier (aspartate/glutamate antiporter), which is often described as an indirect NADH shuttle because imported malate is oxidized to oxaloacetate, releasing NADH, fulfilled a different function; malate was net exported from mitochondria to fuel ME_{cyt}.

5.2.2.3. Cytosolic malic enzyme and NADPH production

NADPH is a key electron donator for anabolic pathways and is essential for monoclonal antibody biosynthesis. Templeton and coworkers [AA11] and Ahn & Antoniewicz [TDRY13] suggested MEs as key NADPH producers in CHO cells. This hypothesis was further confirmed via compartment-specific flux analysis [JTW+19]. Cytosolic ME (ME_{cyt}) was identified as the primary provider serving NADPH needs. Compartment-specific ^{13}C MFA estimated that about 86% of the NADPH requirement was fulfilled by ME_{cyt} (0.09 ± 0.01 pmol·cell^{-1}·h^{-1}).

5.2.3. ^{13}C Metabolic flux analysis using non-compartmented metabolome data

An additional ^{13}C MFA was performed to investigate the importance of distinct sub-cellular information to elucidate proper *in vivo* subcellular flux patterns. Non-compartmented analysis considered that no subcellular measurements were available. Instead, only entire cell labeling patterns should exist. Consequently, compartment-specific information was merged again, applying Equation 5.1.

$$\mathrm{MID}_i^{comb} = \mathrm{MID}_i^{cyt} \cdot f + \mathrm{MID}_i^{mit} \cdot (1 - f) \tag{5.1}$$

Where f denotes the molar fraction of metabolite i in the cytosol. During simulations, f was treated as an optimization parameter for those metabolites presented in both compartments: pyruvate, citrate, α-ketoglutarate, malate, alanine, aspartate, asparagine, and glutamine. Accordingly, f serves as an alternate indicator for the importance of considering compartments properly. Furthermore, flux estimation was achieved by fitting the measured non-compartment metabolome data with calculated MID using Equation 5.2.

$$min\ f(\phi) = \sum \left(\frac{\mathrm{MID}_i^{comb} - \mathrm{MID}_i^{exp}}{\sigma_i} \right)^2 \tag{5.2}$$

This study was performed using the same model consisting of 42 intracellular biochemical reactions (Figure 5.1). Analyzing the merged data via ^{13}C MFA yielded a χ^2 value of 140.127 on the 95% confidence level, which was accepted as a good fit (with 154.30 as the χ^2 statistical threshold on 95% confidence interval). Figure 5.2 provides the comparison of intracellular flux distributions estimated with (left) and without (right) sub-cellular

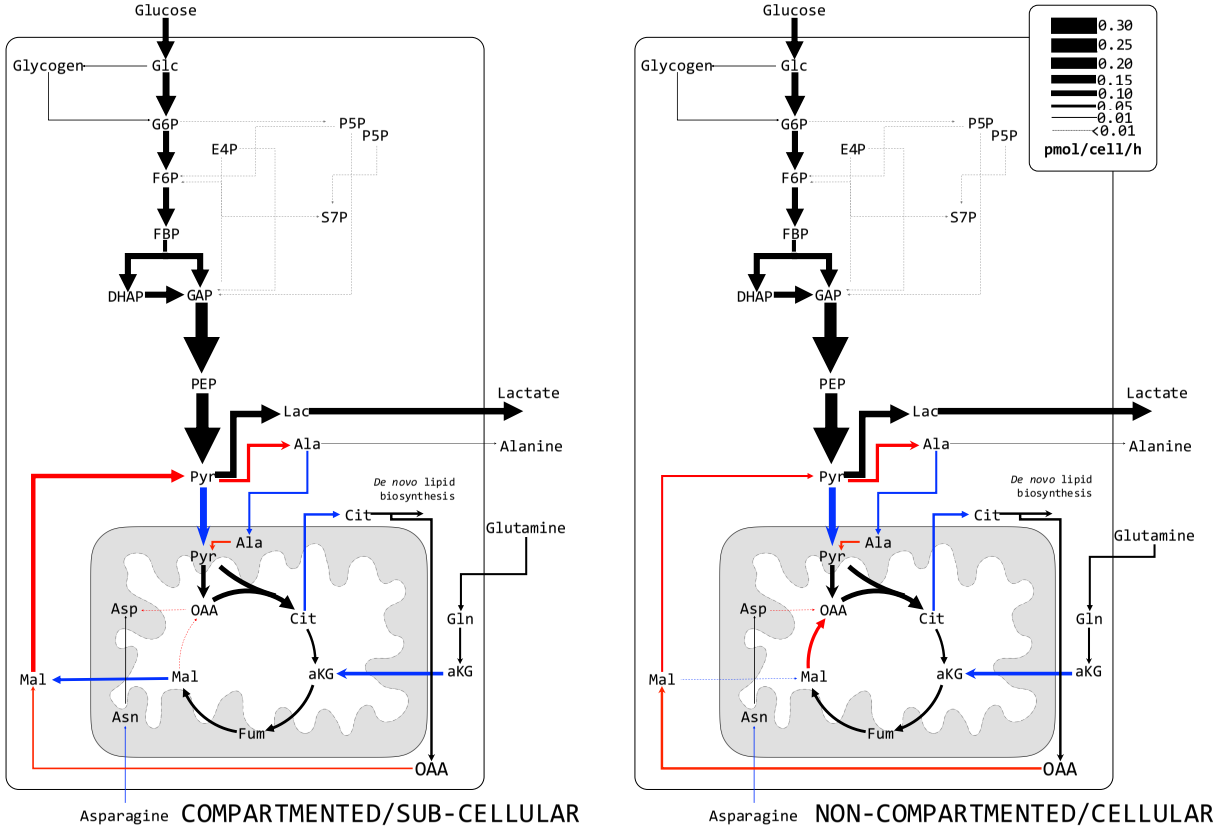

Figure 5.2.: ^{13}C MFA study with and without compartment-specific metabolome data: Intracellular flux distribution estimated using compartment-specific (left) and non-compartmented data (right) [WUH+21]

information. The related single-compartment key fluxes and iso-enzymatic rates are depicted as bar plots in Figure 5.3a and 5.3b. Notably, the term 'iso enzymes' encodes fluxes connecting the same substrates and products but localized in different compartments.

5.2.3.1. Biochemical reactions localized in a single compartment

Figure 5.3a and 5.3b (left) shows fluxes of biochemical reactions that exist in one compartment (cytosol or mitochondria) only. Most of them revealed similar results irrespective of whether compartment-specific information was used (black) or not (grey). Figure 5.3a demonstrates the case the metabolome pools and the respective fluxes were the same for both studies, yielding a similar τ_{13C}. This is also true for citrate synthase v_{cs}, although identifiability was poor. Similar results were observed for cytosolic-based reactions: pyruvate carboxylase (v_{pc}) and PEP carboxykinase (v_{pepck}) (Figure 5.3b). These single-compartment reactions possessed the particularity of utilizing the same metabolites but in different compartments. In this particular case, no statistically sound difference between v_{pc} and v_{pepck} was found, most likely because compartment-specific OAA values lacked.

5.2.3.2. Iso-enzymatic reactions localized in different compartments

Special emphasis is laid on the so-called iso-enzymatic reactions of Figure 5.3b (right), which catalyze similar conversions in different compartments. The fluxes of malate dehydrogenase (v_{mdh}), ME (v_{me}), aspartate amino-transferases (v_{ast}), and alanine amino-transferases (v_{alt}) are localized in cytosol and mitochondria, respectively. Of the eight isoenzymes analyzed, almost all of the conversion rates were significantly different. The only exception is the mitochondrial malate dehydrogenase ($v_{mdh,mit}$) which revealed

statistical similarity although fluxes even reversed. On contrary, the cytosolic malate dehydrogenase ($v_{mdh,cyt}$) also disclosed flux reversion but with a sound statistical identifiability.

Non-compartmented data were not able to properly reflect real fluxes of the amino-transferases, namely alanine amino-transferases (v_{alt}) and aspartate amino transferases (v_{ast}). The analysis of whole-cell data caused an overestimation of the flux magnitude compared to compartment-specific analysis. Notably, the substrate aspartate occurred in cytosol and mitochondria and is a key player of the aspartate-malate shuttle. Moreover, alanine was involved in the co-transport of glycolytic carbon into mitochondria with the MPC1/2. In this case, proper localization and labeling information of the compound is key to estimate fluxes correctly.

Additionally, severe bias was observed for fluxes of both malic enzymes (v_{me}) as displayed in Figure 5.3b (right). By trend, ^{13}C flux estimations using non-compartmented data identified significantly lower (about 30%) cytosolic $v_{me,cyt}$ than the non-compartmented data. Regarding mitochondria, the opposite was found. The finding for v_{me} using non-compartmented data is consistent with the observations of Ahn & Antoniewicz [AA11] and Templeton and coworkers [TDRY13] who also performed ^{13}C MFA with cellular data. Importantly, cytosolic ME activity via $v_{me,cyt}$ was identified as a key supplier for NADPH needed for IgG production in CHO cells [JTW+19].

5.2.3.3. Mitochondrial metabolite carriers

Comparing shuttle activities using sub-cellular and cellular labeling information reveals significant differences for half of the inter-compartment transporters, namely the aspartate/glutamate antiporter (v_{AGC1}), malate carrier (v_{DIC}), α-ketoglutarate/malate antiporter (v_{OGC}), and the putative

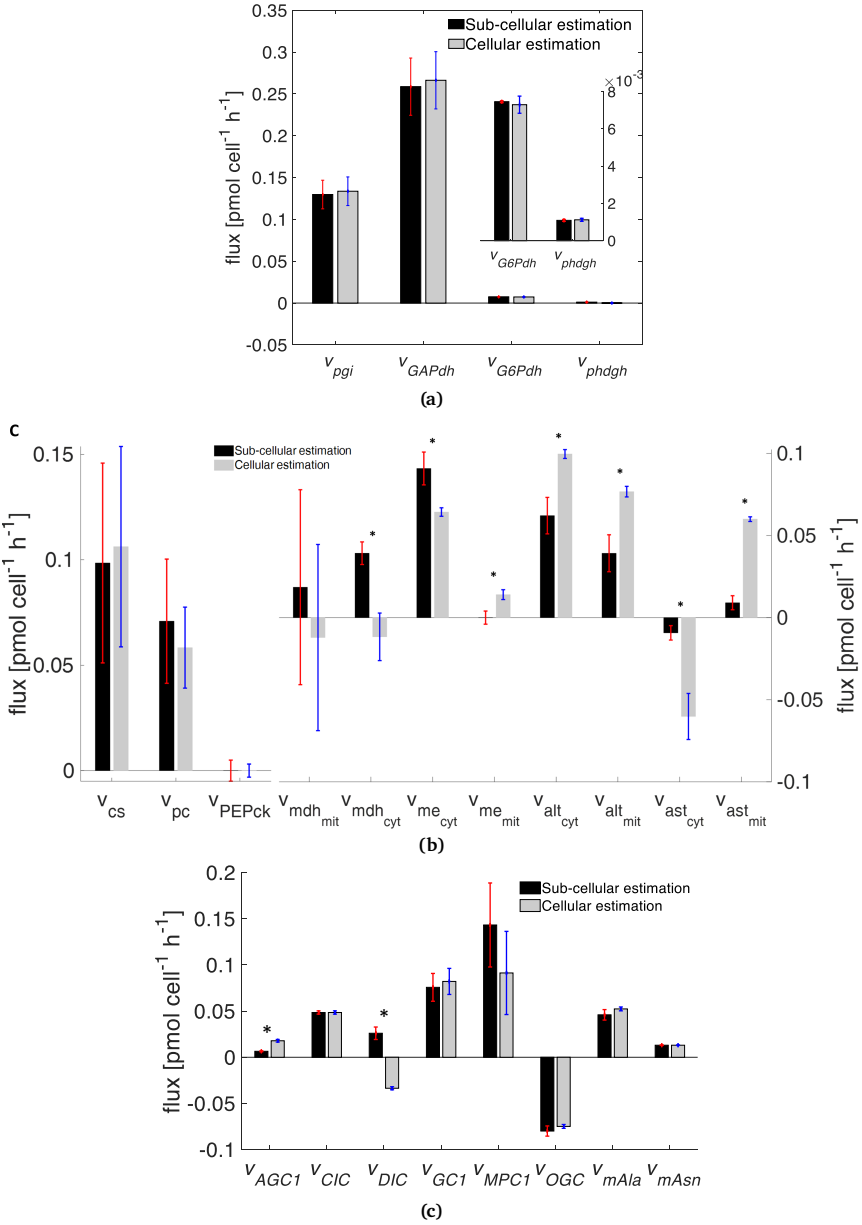

Figure 5.3.: ^{13}C MFA study with and without compartment-specific metabolome data
(a) fluxes of biochemical reactions involving single-compartment metabolites; (b) fluxes of biochemical reactions involving multi-compartment metabolites; and (c) mitochondrial carrier fluxes estimated with compartment-specific and non-compartmented data (* indicates significance $p < 0.05$) [WUH+21]

alanine carrier (v_{mAla}) (Figure 5.3c). Similar to the identification of aspartate amino-transferases, the proper identification of v_{AGC1} depends on the labeling turnover τ_{13C} of Asp in both compartments. Missing compartment-specific measurements lead to the different shuttle fluxes, which are also reflected in the biased flux vast. The same scenario also holds true for the putative alanine carrier (v_{mAla}) and the corresponding reactions (alanine amino-transferases; v_{alt}). Shuttle estimations regarding v_{DIC} and v_{OGC} using non-compartment-specific data contradict flux calculations using compartment-specific information estimation. The sub-cellular labeling information of malate is essential to get accurate flux estimates. Interestingly, the flux estimation of putative asparagine carrier (v_{mAsn}) was not biased by the use of whole-cell labelling data only. This may reflect that vmAsn heavily depends on the measured L-asparagine uptake rate (q_{Asn}) irrespective of the existence of additional subcellular information.

5.2.3.4. Estimated cytosol-mitochondrial fraction (f factor)

Using Equation 5.1, f factors were estimated for each metabolite and compared with the measurements of Junghans and coworkers (Table 5.1). As indicated, all estimated cytosolic fractions (f) were poorly identified with pyruvate, showing the smallest difference of 8.59% only. On average, 59.71% difference was found compared to the real labelling fraction. Notably, the best estimates of pyruvate and asparagine also enabled improved flux values for the corresponding biochemical reactions, e.g. $v_{MPC1/2}$, v_{pdh} for pyruvate, and v_{asns}, v_{mAsn} for asparagine.

Table 5.1.: Complete list of estimated and measured cytosolic fractions of subcellular metabolites used for non-compartmented ^{13}C MFA [WUH+21]

Metabolites	**Cytosolic fraction (f)**		% **differences** (measurement as the reference value)
	Estimated	**Measurement** [JTW+19]	
Mal	0.100	0.829	87.9
Pyr	0.910	0.838	8.59
aKG	0.100	0.714	85.99
Cit	0.995	0.489	103.48
Glu	0.373	0.827	54.90
Ala	0.100	0.840	88.1
Asn	0.717	0.805	10.48
Asp	0.500	0.809	38.20

5.2.3.5. Cellular NADH and NADPH production

Table 5.2 shows a comparison of NADH and NADPH production via compartment-specific analysis and neglection of sub-cellular data. Neglecting sub-cellular data, NADPH production is underestimated by approximately 25%. This reflects the 30% underestimation of cytosolic v_{me} when cellular and not subcellular data are used. In the case of NADH and ATP, the utilization of different datasets disclosed only minor differences. NADH and ATP fluxes were overestimated by 9% and 14% for non-compartmented data, respectively.

Table 5.2.: Comparison of NADH, ATP, and NADPH net production rates in compartment-specific analysis and whole-cell analysis (values presented in pmol·cell^{-1}h^{-1}) [WUH+21]

	NADH	**ATP**	**NADPH**
Compartment-specific	0.55692	0.22752	0.10577
Non-compartmented	0.60815	0.25914	0.07924

5.3. Discussion

This study challenges the information gain when performing ^{13}C MFA with compartment-specific metabolome data compared to exploiting cellular labeling information not distinguishing between cytosol and mitochondria. Figure 5.2 and 5.3 outline the complexity of the interactions. A group of fluxes (v_{pgi}, v_{GAPdh} v_{G6Pdh}, and v_{phdgh}) located in a single compartment (here: cytosol) disclose equal values irrespective of the analytical approach selected. Interestingly, this also holds true for v_{cs}, located in mitochondria, primarily due to poor flux identifiability. Furthermore, v_{pepck} and v_{pc} revealed such high flux variances that no distinction could be found whether cellular or subcellular ^{13}C data were used. Apparently, both reactions depend on cytosolic (OAA_{cyt}) and mitochondrial oxaloacetate (OAA_{mit}). They act at the interphase of the two compartments and rely on proper sub-cellular measurement information (τ_{13C}) for correct identification. Distinct OAA measurements were not available in the current study due to challenging analytical access to the compound. Accordingly, flux estimations might be biased by the quality of OAA pool estimations.

Additionally, some other fluxes should be interpreted with great care, too. This holds particularly true for mitochondrial malate dehydrogenase ($v_{mdh,mit}$)

and the pyruvate carrier $v_{MPC1/2}$. Both disclose large error bars rendering a discrimination between cellular versus subcellular approaches hardly possible (Figure 5.3b and 5.3c). Flux imprecisions reflect the lack of reliable CO_2 evolution rates (q_{CO_2}) and CO_2 labelling profiles.

The whole-cell (cellular) flux estimation failed to estimate the mitochondrial and cytosolic fluxes of the amino-transferases v_{alt} and v_{ast}. This may reflect that those fluxes heavily depend on the compartment-specific labelling information of alanine and aspartate. Not providing this information by using whole-cell labelling data leads to the large discrepancies given in Figure 5.3b.

Almost all mitochondrial carrier fluxes were poorly estimated when using non-compartmented data. Inaccurate estimations of v_{AGC1} and v_{mAla} are also reflected by the results of v_{ast} and v_{alt}. Additionally, the poor estimation of the malate carriers v_{DIC} and v_{OGC} depended on v_{me}. In general, fluxes of transporters and bioreactions heavily relied on the labelling dynamics measured in the related metabolites. Regarding $v_{MPC1/2}$, the reduced shuttle activity based on non-compartmented data reflects the missing malate exported into cytosol (Figure 5.3c).

To check whether the additional use of labelled glutamine [AA13] might have achieved similar subcellular flux resolutions as the compartment-specific analysis, simulations were performed using [U-$^{13}C_5$]-L-glutamine (see Section 5.5.6). Interestingly, without information about compartment-specific metabolomics, cytosolic ^{13}C signals obtained from simulations are pretty similar to those of the whole-cell. This is mainly due to the relatively low information gain with respect to the key mitochondrial metabolites malate and aspartate. Compartment-specific labeling information and turnover of the latter are decisive to resolve activities of mitochondrial transporters.

In general, most of the flux estimations using either non-compartmented or compartmented data led to similar values. Even global cell qualifications, such as rates of total ATP formation and NADH production, were similar. However, two main findings should be considered:

1. Often, cellular analysis achieved similar flux estimations than subcellular studies by fitting measured cytosolic labeling fractions for the sake of estimating pool sizes properly (Table 5.1). In other words, flux optimization algorithms adapted cytosolic and mitochondrial pool sizes to complement missing labeling information. However, the simulated pool size readouts were strongly misleading.

2. Among the fluxes with the largest discrepancies is the cytosolic ME vme. Remarkably, this flux was found to be a promising metabolic engineering target to maximize the formation of heterologous proteins by improved NADPH supply [JTW+19]. Accordingly, exact estimation is a prerequisite for proper strain engineering. Figure 5.4 illustrates that even the result of non-compartment data analysis still fits to the subcellular kinetics published in Junghans and coworkers. Whether or not experimentalists may have identified this enzyme as a metabolic engineering target remains open and is a matter of qualitative discussion rather than quantitative target identification.

To date, the compartment-specific analytical approach of Matuszczyk and coworkers [MTPT15] has shown its suitability for multiple metabolomics studies investigating CHO cells under *in vivo*-like conditions [BJT+19a; BJT+19b; PJTT16; PMT15; VTH+20; VWT+20]. The latter is enabled by fast and standardized metabolism inactivation. Furthermore, data quality essentially relies on the quantitative access to internal standards, such as G6P/F6P (in cytosolic space) and cis-aconitate (in mitochondrion) to correct for mitochondrial leakage. In general, fast metabolic inactivation, standard-

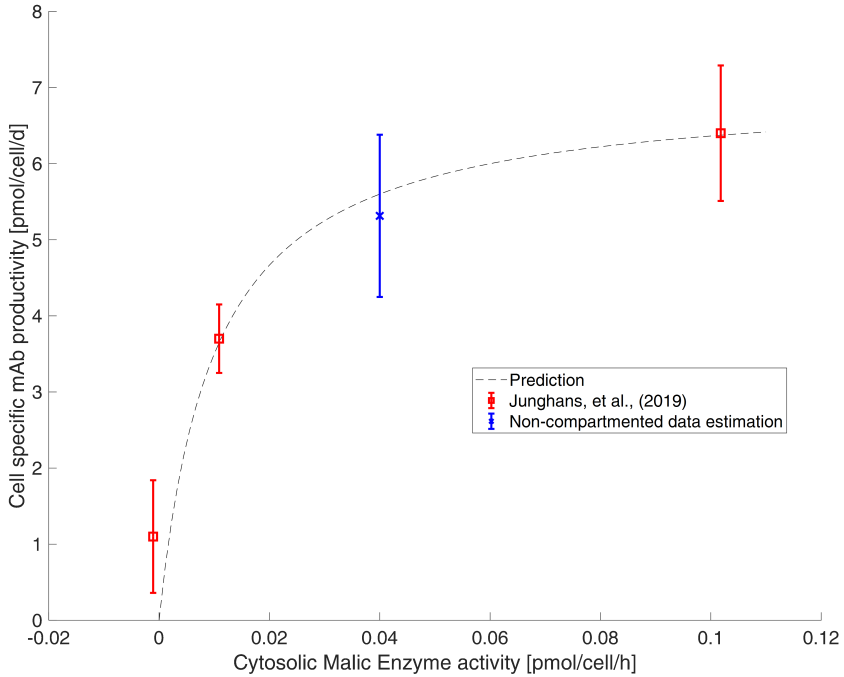

Figure 5.4.: Cell-specific production of monoclonal antibodies in CHO cells [WUH+21]

ized sample processing and use of internal standards are prerequisites for any compartment-specific metabolomics approach that might be used in future applications.

5.4. Conclusion

Investigating the need for using subcellular ^{13}C labeling data, the study revealed that most intracellular fluxes were similar to those derived from non-compartmented labeling information. This also holds true for half of the mitochondrial shuttle fluxes, except for those that immediately rely

on alanine, aspartate and malate labeling dynamics. Furthermore, global properties, such as ATP and NADH formation, were fairly well estimated without subcellular labeling information. Interestingly, key metabolic engineering targets, such as the cytosolic ME flux for NADPH formation, were severely underestimated using cellular data, which may disguise their roles as promising metabolic engineering targets. This underlines the necessity to apply subcellular data for flux estimation, not only to quantify cytosolic/mitochondrial shuttle activities but also to identify metabolic engineering targets and obtain valid values for real pool sizes.

5.5. Supplementary Material

5.5.1. Network Identifiability Analysis

The metabolic network (S) used in this study consists of 61 reactions r and 35 metabolites m. The complete metabolic model is presented in Table 2.5.

The network degree of freedom may be calculated as follow:

$$n_{df} = (dim)(v) - (rank)(S) = 61 - 35 = 26$$

where dim(v) is the number of biochemical reactions in network S; and rank(S) is the number of independent metabolite balances (without redundancy; e.g. conserved moieties).

The degree of freedom (n_{df}) indicates that at least 26 flux rates are required to quantify the intracellular fluxes in the metabolic network S.

Furthermore, calculability analysis [KSG02] was performed to assess how many reactions can be calculated from the input free fluxes. In this case, the

network determinacy is given by the number of identifiable fluxes.

In this study, 18 input fluxes were obtained from extracellular measurements comprising cellular growth, uptake and secretion rates for D-glucose, L-lactate and amino acids. These fluxes are tGln, tGlu, tGlc, tLac, tSer, tAla, tAsp, tAsn, muG6P, muGAP, muP5P, muAcCoA, muSer, muAla, muAsp, muGln, muAsn, and muGlu. Calculability analysis showed that only several intracellular fluxes that can be calculated with the extracellular free fluxes: CIC, acl, asns, gdh, gs, ldh, and mAsn.

In accordance with the degree of freedom, additional 8 fluxes are required to solve the entire metabolic network. Apparently, the 8 fluxes are the intracellular fluxes. The calculability analysis showed that network determinacy (determined case) could be achieved by using a particular set of intracellular fluxes (G6Pdh, phdgh, fGlyco, pepck, alt_c, me_c, me_m, ast_m) and the extracellular free fluxes (see section III for detailed information). These intracellular fluxes will be determined by fitting the ^{13}C enrichment profile of the respective metabolites involved in the biochemical reaction.

5.5.2. Identifiability Analysis Case I

```
% Import metabolic network
S = xlsread('metabolic_model_CHO.xlsx');

flux_label = {'AGC1','CIC','DIC','GC1','MPC1','OGC','acl','adh','alt','altm',...
    'asnsm','ast','astm','csyn','pgi','pfk','fbpa','tpi','gapdh','eno','pkm',...
    'gdh','gs','idh','ldh','mAla','mAsn','mCO2','mdh','mdhc','me','mem','muAcCoA',...
    'muAla','muAsn','muAsp','muG6P','muGAP','muGln','muGlu','muP5P','muSer',...
    'pc','pdh','pepck','G6Pdh','rpi','tkt1','tkt2','phdgh','sds','tAla','tAsn',...
    'tAsp','tCO2','tGlc','tGln','tGlu','tGlyco','tLac','tSer'};

metabolite_label = {'Glum','Asp','Glu','Aspm','Cit','Malm','Citm','Mal','Pyrm',...
    'Pyr','aKG','aKGm','OAA','AcCoA','Asnm','OAAm','AcCoAm','F6P','G6P','FBP',...
    'DHAP','GAP','3PG','PEP','Gln','Lac','Alam','Ala','CO2','S7P','R5P','E4P',...
    'Ser','Asn','CO2m'};

% check identifiability
input_fluxes = [33 34 35 36 37 38 39 40 41 42 52 53 ...
    54 56 57 58 60 61];

unmeasured_fluxes = setdiff( 1:size(S,2), input_fluxes);
Sq = S(:,input_fluxes);
Su = S(:,unmeasured_fluxes);
RNS = null( Su );
k = find( all( [abs(RNS) zeros(size(RNS,1), 2)]' < 1e-6 ) );

% Print result
fprintf( 'Fluxes that can be determined from measurements: \n' )

for i=1:length( k )
    fprintf( '%s\n', flux_label{ unmeasured_fluxes(k(i))} );
end
```

```
Fluxes that can be determined from measurements:
CIC
acl
asnsm
gdh
gs
ldh
mAsn
```

Published with MATLAB® R2018b

5.5.3. Identifiability Analysis Case II

```
% Import metabolic network
S = xlsread('metabolic_model_CHO.xlsx');

flux_label = {'AGC1','CIC','DIC','GC1','MPC1','OGC','acl','adh','alt','altm',...
    'asnsm','ast','astm','csyn','pgi','pfk','fbpa','tpi','gapdh','eno','pkm',...
    'gdh','gs','idh','ldh','mAla','mAsn','mCO2','mdh','mdhc','me','mem','muAcCoA',...
    'muAla','muAsn','muAsp','muG6P','muGAP','muGln','muGlu','muP5P','muSer',...
    'pc','pdh','pepck','G6Pdh','rpi','tkt1','tkt2','phdgh','sds','tAla','tAsn',...
    'tAsp','tCO2','tGlc','tGln','tGlu','tGlyco','tLac','tSer'};

metabolite_label = {'Glum','Asp','Glu','Aspm','Cit','Malm','Citm','Mal','Pyrm',...
    'Pyr','aKG','aKGm','OAA','AcCoA','Asnm','OAAm','AcCoAm','F6P','G6P','FBP',...
    'DHAP','GAP','3PG','PEP','Gln','Lac','Alam','Ala','CO2','S7P','R5P','E4P',...
    'Ser','Asn','CO2m'};

% check identifiability
input_fluxes = [9 13 31 33 34 35 36 37 38 39 40 41 42 43 45 46 50 52 53 ...
    54 56 57 58 59 60 61];

unmeasured_fluxes = setdiff( 1:size(S,2), input_fluxes);
Sq = S(:,input_fluxes);
Su = S(:,unmeasured_fluxes);
RNS = null( Su );
k = find( all( [abs(RNS) zeros(size(RNS,1), 2)]' < 1e-6 ) );

% Print result
fprintf( 'Fluxes that can be determined from measurements: \n' )

for i=1:length( k )
    fprintf( '%s\n', flux_label{ unmeasured_fluxes(k(i))} );
end
```

```
Fluxes that can be determined from measurements:
AGC1
CIC
DIC
GC1
MPC1
OGC
acl
adh
altm
asnsm
ast
csyn
pgi
pfk
fbpa
tpi
gapdh
eno
pkm
gdh
gs
idh
```

```
ldh
mAla
mAsn
mCO2
mdh
mdhc
mem
pdh
rpi
tkt1
tkt2
sds
tCO2
```

Published with MATLAB® R2018b

5.5.4. *In silico* based ^{13}C identifiability analysis (Experimental design)

To check whether the carbon tracer composition (75% [U-$^{13}C_6$]-D-glucose) allows sufficient identifiability of key fluxes (e.g. me_{cyt} identification using ^{13}C Mal_{cyt} enrichment), *in silico* based studies were performed, investigating the impact of different of $v_{me_{cyt}}$ and $\beta_{me_{cyt}}$ (reversibility constant, as explained in the main text) to the Mal_{cyt} enrichment [WNN15]. By assuming real pool sizes measured by Junghans et al [JTW+19] and by applying the planned labeling scenario of 75% [U-$^{13}C_6$]-D-glucose, realistic labeling patterns were created. Simulation results (cytosolic malate enrichment profile) are presented in Figure 5.5. As shown the obtained $v_{me_{cyt}}$ ($0.06-0.12$ pmol cell^{-1} h^{-1}) and $\beta_{me_{cyt}}$ ($1-5$) correspond to a very distinct Mal_{cyt} enrichment.

5.5.5. ^{13}C MFA identifiability analysis

To check whether ^{13}C labeling data (*in vivo*) may be used to identify targeted fluxes, ^{13}C simulations were performed a priori. Furthermore, input fluxes

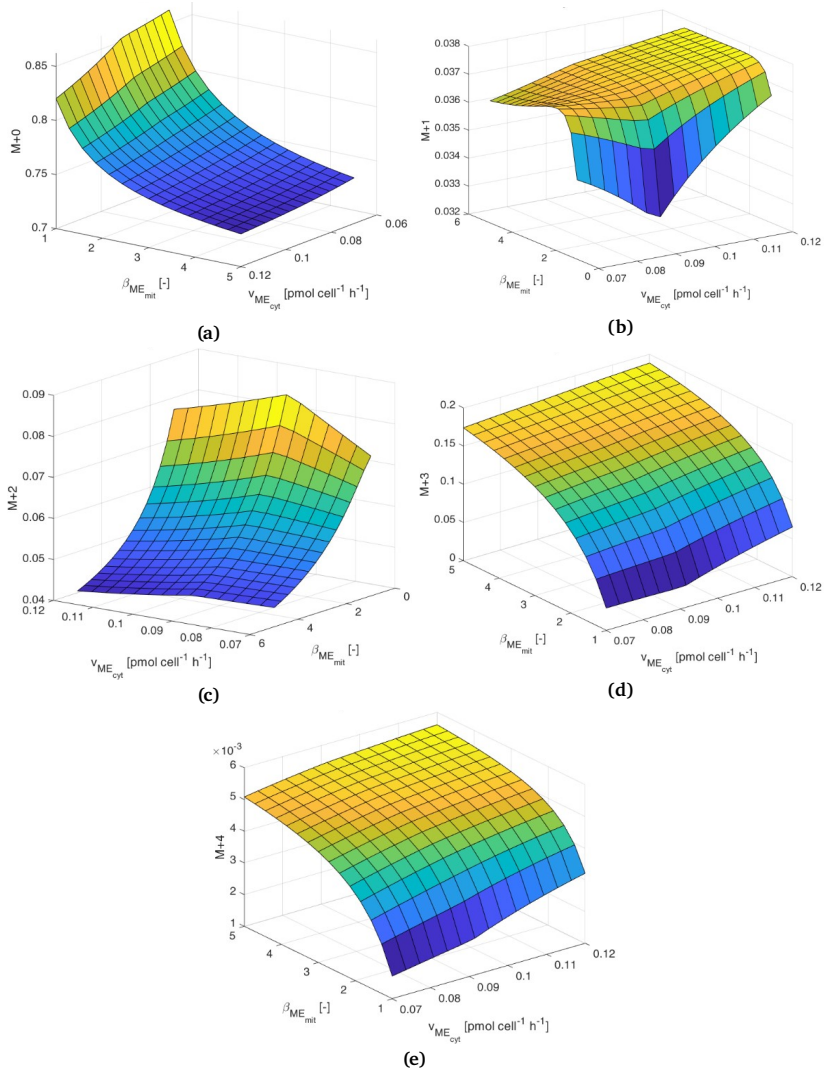

Figure 5.5.: Cytosolic malic enzyme identifiability analysis: cytosolic malate (Mal_{cyt}) enrichment profile simulated using 75% [U-$^{13}C_6$]-D-glucose using various $v_{me_{cyt}}$ ($0.07-0.12$ pmol cell^{-1} h^{-1}) and $\beta_{me_{cyt}}$ ($1-5$): (a) M+0; (b) M+1; (c) M+2 (d) M+3; and (e) M+4 Mal_{cyt} mass-isotopomer species. [WUH+21]

were assumed to be in realistic ranges, too. Figures 5.6 – 5.9 exemplify the good identifiability of intracellular fluxes when performing ^{13}C MFA. For the sake of brevity, only those fluxes are shown that were explicitly discussed in the manuscript. Accordingly, good identifiability is given for cytosolic and mitochondrial malic enzyme (Figure 5.6) and the shuttles AGC, OGC, and DIC (Figure 5.7, 5.8, and 5.9).

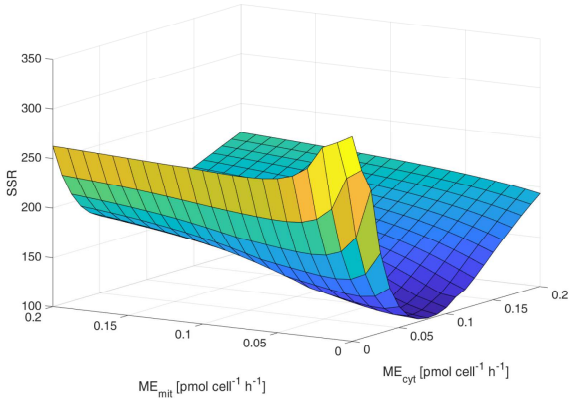

Figure 5.6.: Identifiability analysis of malic enzymes. The figure indicates a global minimum for the cytosolic and mitochondrial malic enzymes activities reported in this study ($v_{me_{cyt}} = 0.091$ pmol cell^{-1} h^{-1} and $v_{me_{mit}} = 0$ pmol cell^{-1} h^{-1}) [WUH+21]

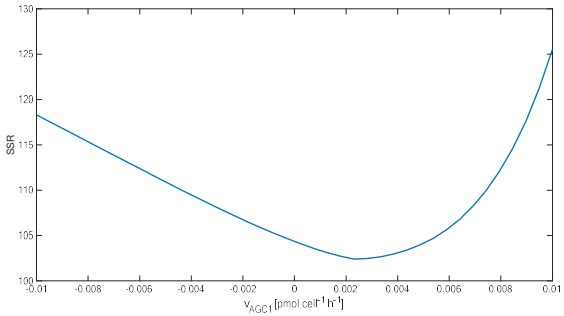

Figure 5.7.: Identifiability analysis of aspartate-glutamate carrier (AGC). The figure indicates a global minimum for the v_{AGC} reported in this study ($v_{AGC} = 0.003$ pmol cell^{-1} h^{-1}) [WUH+21]

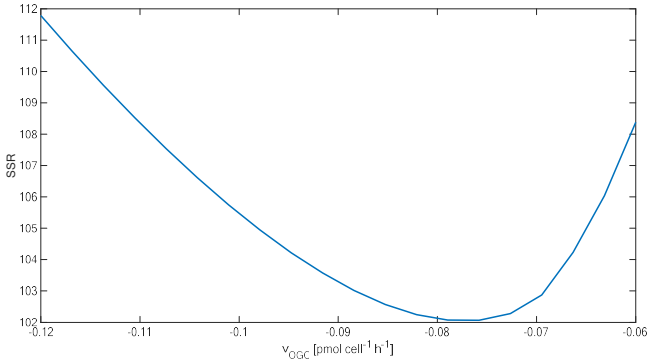

Figure 5.8.: Identifiability analysis of oxo-glutarate-glutamate carrier (OGC). The figure indicates a global minimum for the v_{OGC} reported in this study ($v_{OGC} = -0.0714$ pmol cell^{-1} h^{-1}) [WUH+21]

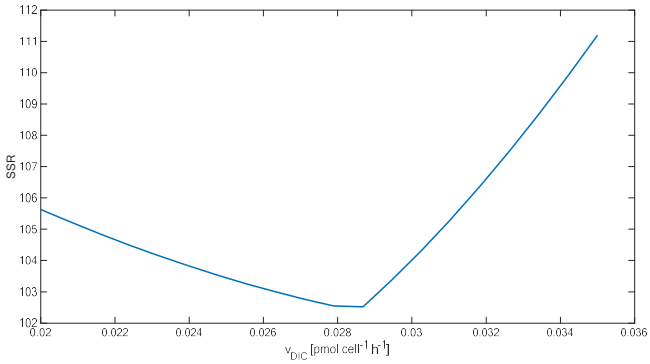

Figure 5.9.: Identifiability analysis of malate carrier (DIC). The figure indicates a global minimum for the v_{DIC} reported in this study ($v_{DIC} = 0.0287$ pmol cell^{-1} h^{-1}) [WUH+21]

5.5.6. Metabolic flux distribution

	Flux ID	Reaction	COMPARTMENT-SPECIFIC				NON-COMPARTMENTED				Welsch Test	
			mean	error prop	UB (95%)	LB (95%)	mean	error prop	UB (95%)	LB (95%)	p	Significance
Extracellular rates	tAla	Ala <-> Ala_ex	0.011	0.0017	0.013	0.009	0.011	0.0017	0.013	0.009		
	tAsn	Asn_ex -> Asn	0.017	0.0000	0.017	0.017	0.017	0.0000	0.017	0.017		
	tAsp	Asp <-> Asp_ex	0.003	0.0010	0.004	0.002	0.003	0.0010	0.004	0.002		
	tCO2	CO2 -> CO2_ex	0.246	0.1529	0.399	0.093	0.269	0.1532	0.422	0.116		
	tGlc	Glc -> G6P	0.112	0.0171	0.129	0.095	0.112	0.0171	0.129	0.095		
	tGln	Gln_ex -> Gln	0.057	0.0104	0.067	0.047	0.057	0.0104	0.067	0.047		
	tGlu	Glu <-> Glu_ex	0.023	0.0094	0.032	0.014	0.023	0.0094	0.032	0.014		
	tLac	Lac <-> Lac_ex	0.134	0.0288	0.163	0.106	0.134	0.0288	0.163	0.106		
	tSer	Ser_ex -> Ser	0.016	0.0050	0.021	0.011	0.016	0.0050	0.021	0.011		
Biomass growth	acl	Cit --> OAA + AcCoA	0.049	0.0018	0.050	0.047	0.049	0.0018	0.050	0.047		
	muAcCoA	AcCoA -> AcCoA_X	0.049	0.0018	0.050	0.047	0.049	0.0018	0.050	0.047		
	muAla	Ala -> Ala_X	0.012	0.0004	0.012	0.011	0.012	0.0004	0.012	0.011		
	muAsn	Asn -> Asn_X	0.006	0.0002	0.006	0.005	0.006	0.0002	0.006	0.005		
	muAsp	Asp -> Asp_X	0.009	0.0003	0.010	0.009	0.009	0.0003	0.010	0.009		
	muG6P	G6P -> G6P_X	0.006	0.0002	0.006	0.005	0.006	0.0002	0.006	0.005		
	muGAP	GAP -> GAP_X	0.002	0.0001	0.002	0.002	0.002	0.0001	0.002	0.002		
	muGln	Gln -> Gln_X	0.006	0.0002	0.007	0.006	0.006	0.0002	0.007	0.006		
	muGlu	Glu -> Glu_X	0.008	0.0003	0.008	0.007	0.008	0.0003	0.008	0.007		
	muP5P	P5P -> P5P_X	0.007	0.0002	0.007	0.006	0.007	0.0002	0.007	0.006		
	muSer	Ser -> Ser_X	0.009	0.0003	0.009	0.008	0.009	0.0003	0.009	0.008		
EMP	fGlyco	Glyco -> G6P	0.016	0.0022	0.020	0.013	0.020	0.0028	0.021	0.017	0.1576	NON-SIG
	pgi	G6P <-> F6P	0.115	0.0173	0.132	0.098	0.119	0.0173	0.136	0.101	0.8018	NON-SIG
	pfk	F6P <-> FbP	0.115	0.0172	0.133	0.098	0.119	0.0173	0.137	0.102	0.8018	NON-SIG
	fbpa	FbP <-> GAP + DHAP	0.115	0.0172	0.133	0.098	0.119	0.0173	0.137	0.102	0.8018	NON-SIG
	tpi	DHAP <-> GAP	0.115	0.0172	0.133	0.098	0.119	0.0173	0.137	0.102	0.8018	NON-SIG
	gapdh	GAP <-> 3PG	0.229	0.0345	0.263	0.194	0.237	0.0347	0.271	0.202	0.8018	NON-SIG
	eno	3PG <-> PEP	0.228	0.0345	0.262	0.193	0.235	0.0347	0.270	0.201	0.8018	NON-SIG
	pkm	PEP -> Pyr	0.228	0.0349	0.262	0.193	0.235	0.0348	0.270	0.200	0.8018	NON-SIG
	ldh	Pyr <-> Lac	0.134	0.0288	0.163	0.106	0.134	0.0288	0.163	0.106	1	NON-SIG
	G6Pdh	G6P -> P5P + CO2	0.007	0.0005	0.008	0.007	0.007	0.0005	0.008	0.007	1	NON-SIG

PPP	tkt1	2*P5P <-> S7P + GAP	0.000	0.0002	0.000	0.000	0.000	0.0002	0.000	0.000	1	NON-SIG
	tald	E4P + P5P <-> F6P + GAP	0.000	0.0002	0.000	0.000	0.000	0.0002	0.000	0.000	1	NON-SIG
	tkt2	S7P + GAP <-> E4P + F6P	0.000	0.0002	0.000	0.000	0.000	0.0002	0.000	0.000	1	NON-SIG
Mitochondrial shuttles	AGC1	Glu + Asp_m --> Glu_m + Asp	0.003	0.0043	0.007	-0.002	-0.048	0.0140	-0.034	-0.062	0.0264	SIG
	CIC	Cit_m + Mal --> Cit + Mal_m	0.049	0.0018	0.050	0.047	0.049	0.0018	0.050	0.047	1	NON-SIG
	DIC	Mal_m <-> Mal	0.029	0.0250	0.054	0.004	-0.035	0.0054	-0.030	-0.041	0.0492	SIG
	GC1	Glu_m <-> Glu	0.054	0.0179	0.072	0.036	0.091	0.0143	0.106	0.077	0.0660	NON-SIG
	MPC1	Pyr --> Pyr_m	0.130	0.0517	0.182	0.078	0.074	0.0457	0.119	0.028	0.252	NON-SIG
	OGC	Mal + aKG_m <-> Mal_m + aKG	-0.071	0.0120	-0.059	-0.083	-0.160	0.0143	-0.146	-0.174	0.0038	SIG
	mAla	Ala <-> Ala_m	0.039	0.0113	0.050	0.028	0.077	0.0032	0.080	0.074	0.0309	SIG
	mAsn	Asn <-> Asn_m	0.012	0.0002	0.012	0.012	0.012	0.0002	0.012	0.012	1	NON-SIG
	mCO2	CO2_m <-> CO2	0.148	0.1545	0.302	-0.007	0.197	0.1533	0.351	0.044	0.7187	NON-SIG
Citric acid	pdh	Pyr_m -> AcCoA_m	0.098	0.0474	0.146	0.051	0.106	0.0475	0.154	0.059	0.8269	NON-SIG
	csyn	AcCoA + OAA -> Cit	0.098	0.0474	0.146	0.051	0.106	0.0475	0.154	0.059	0.8269	NON-SIG
	idh	Cit_m <-> aKG_m + CO2_m	0.050	0.0474	0.097	0.003	0.058	0.0475	0.105	0.010	0.827	NON-SIG
	adh	aKG_m <-> Mal_m + CO2_m	0.070	0.0533	0.123	0.017	0.078	0.0533	0.131	0.025	0.8461	NON-SIG
	mdh	Mal_m <-> OAA_m	0.019	0.0594	0.078	-0.041	-0.012	0.0567	0.045	-0.069	0.1518	NON-SIG
	mdhc	OAA <-> Mal	0.039	0.0069	0.046	0.032	-0.012	0.0145	0.003	-0.026	0.0178	SIG
anaplerotic	pc	Pyr_m <-> OAA_m	0.071	0.0295	0.100	0.041	0.058	0.0192	0.078	0.039	0.5807	NON-SIG
	me	Mal <-> Pyr + CO2	0.091	0.0100	0.101	0.069	0.064	0.0026	0.068	0.062	0.04930	SIG
	mem	Mal_m <-> Pyr_m + CO2_m	0.000	0.0040	0.013	-0.004	0.014	0.0030	0.026	0.011	0.0167	SIG
	pepck	OAA <-> PEP + CO2	0.000	0.0050	0.005	-0.001	0.000	0.0031	0.003	-0.001	1.00000	NON-SIG
Amino acids metabolism	gs	Gln -> Glu	0.051	0.0104	0.061	0.040	0.051	0.0104	0.061	0.040	1	NON-SIG
	gdh	aKG_m <-> Glu_m	-0.003	0.0142	0.011	-0.017	-0.003	0.0142	0.011	-0.017	1	NON-SIG
	phdgh	3PG -> Ser	0.001	0.0001	0.001	0.001	0.001	0.0008	0.002	0.000	0.80950	NON-SIG
	sds	Ser -> Pyr	0.008	0.0050	0.013	0.003	0.008	0.0051	0.013	0.003	0.90768	NON-SIG
	asnsm	Asn_m <-> Asp_m	0.012	0.0002	0.012	0.012	0.012	0.0002	0.012	0.012	1	NON-SIG
	ast	Asp + aKG <-> OAA + Glu	-0.009	0.0044	-0.005	-0.014	-0.060	0.0140	-0.046	-0.074	0.0267	SIG
	astm	Asp_m + aKG_m <-> OAA_m + Glu_m	0.009	0.0043	0.013	0.005	0.060	0.0140	0.074	0.046	0.0264	SIG
	alt	Pyr + Glu <-> Ala + aKG	0.062	0.0111	0.073	0.053	0.100	0.0027	0.102	0.097	0.0296	SIG
	altm	Ala_m + aKG_m <-> Pyr_m + Glu_m	0.039	0.0113	0.050	0.028	0.077	0.0032	0.080	0.074	0.0309	SIG

5.5.7. Simulation when usin [U-$^{13}C_5$]-L-glutamine

Simulation result when using 100% [U-$^{13}C_5$]-L-glutamine as the carbon tracer.

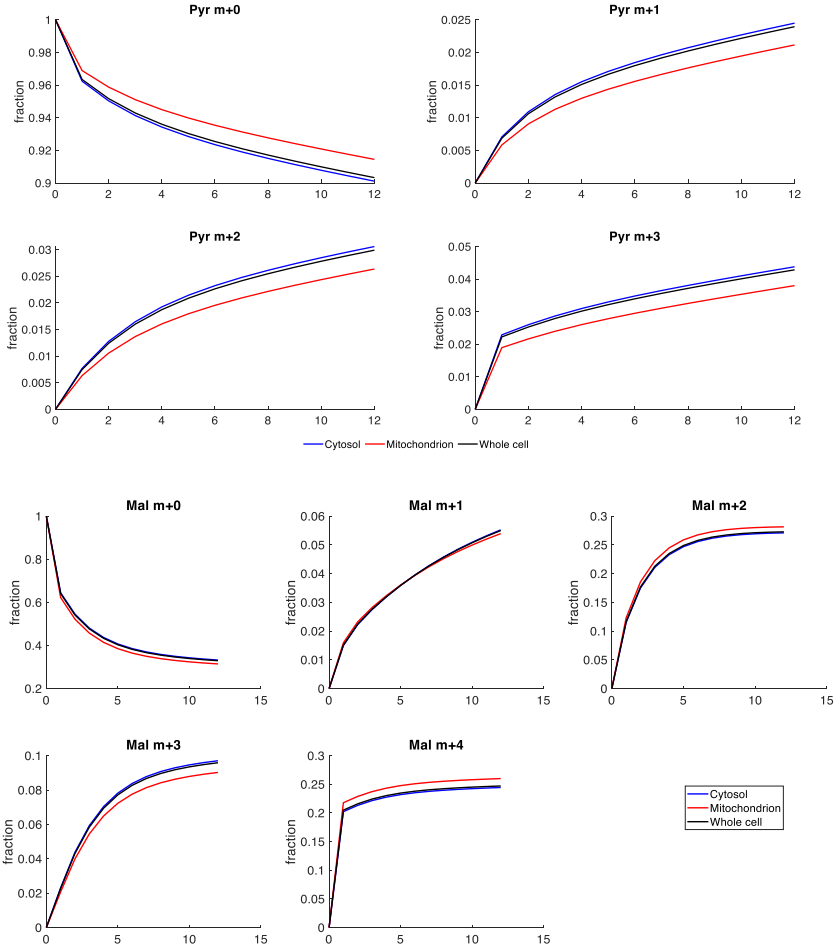

Chapter 6

Compartment-specific ^{13}C metabolic flux analysis reveals boosted NADPH availability coinciding with increased cell-specific productivity for IgG1 producing CHO cells after MTA treatment [1]

Abstract

Increasing cell-specific productivities (CSPs) for the production of heterologous proteins in Chinese hamster ovary (CHO) cells is an omnipresent

[1] This chapter was published as: **Wijaya, A.W.**, Verhagen, N., Teleki, A. & Takors, R. (2021). Compartment-specific ^{13}C metabolic flux analysis reveals boosted NADPH availability coinciding with increased cell-specific productivity for IgG1 producing CHO cells after MTA treatment. *Engineering in life sciences*. **21**(12), 832-847. All experimental work described herein was carried out by Natascha Verhagen. The analytical measurements (metabolomics and ^{13}C profiling) were carried out by Lisa Junghans and Attila Teleki

need in the biopharmaceutical industry. The novel additive 5'-deoxy-5'-(methylthio)adenosine (MTA), a chemical degradation product of S-(5'-adenosyl)-L-methionine (SAM) and intermediate of polyamine biosynthesis, boosts the CSP of IgG1-producing CHO cells by 50%. Compartment-specific ^{13}C flux analysis revealed a fundamental reprogramming of the central metabolism after MTA addition accompanied by cell-cycle arrest and increased cell volumes. Carbon fluxes into the pentose-phosphate pathway increased 22 fold in MTA-treated cells compared to that in non-MTA-treated reference cells. Most likely, cytosolic ATP inhibition of phosphofructokinase mediated the carbon detour. Mitochondrial shuttle activity of the α-ketoglurarate/malate antiporter (OGC) was reversed, reducing cytosolic malate transport. In summary, NADPH supply in MTA-treated cells improved 3 fold compared to that in non-MTA-treated cells, which can be regarded as a major factor for explaining the boosted CSPs.

6.1. Introduction

Biopharmaceutical markets are steadily increasing worldwide; monoclonal antibody production in Chinese hamster ovary (CHO) cells continue to possess the largest share [Wal18]. Product titers improved 100-fold during the last few decades [RDKK15; Wur04]; however, cell-specific productivities (CSPs) have increased only 3–8 fold. Optimization of CSP is a striking demand, envisaging the current need for intensifying bioprocesses and considering continuous production in perfusion processes [BJT+19a; TSM+17; ZWL+13].

However, optimization of CSP requires a detailed understanding of intracellular regulation, which typically requires the concerted application of omics technologies [KBLB13], comprising genome analysis [WH11; XNL+11],

genome-scale modeling [HAH+16], transcript analysis [PJTT16; SBY18], epigenetics [FHF+16; HHP+15], metabolomics [CTH+12], and fluxomics [AA11; JTW+19; TDRY13; TSM+17].

Efforts have been undertaken for enhancing CSP through initiating growth arrest [SB10]. In addition to osmolarity and temperature shifts [FPYW04; PMT15], studies have focused on the addition of effectors such as sodium butyrate [JS08], valeric acid [CKH+16], glycine betaine [AHYS99], and catechin [TAJ+20]. As a common observation, alterations in cell-cycle phases coincided with increase in cell size. Both were anticipated to improve CSP [AECJ92; GKK15]. However, the underlying mechanisms that explain the phenotype remain fragmented. Recently, Verhagen and coworkers demonstrated that cell-cycle arrest could be achieved by exposing CHO cells to the effector 5'-deoxy-5'-(methylthio)adenosine (MTA), which increased CSP by 50% [VTH+20; VZT20].

MTA is a degradation product of the crucial methyl group donor S-adenosylmethionine (SAM) and a by-product of polyamine synthesis [Peg88; WSG82]. MTA is an anticipated effector of the polyamine pathway, DNA synthesis, gene expression control, cell proliferation, lymphocyte activation, tumor development, invasiveness, apoptosis, and signaling pathways [AGM+02; LSD+92; PSDF02; RTF84]. Furthermore, MTA is rapidly metabolized and the end products can be used to replenish adenosine-based nucleotide pools [WSG82]. Recently, Verhagen and coworkers revealed that MTA addition influenced cell size, cell cycle, and transcript levels, ultimately enhancing the IgG1 CSP of CHO-DP12 cells [VTH+20; VZT20]. Additional studies have outlined the dose dependent effect of MTA addition [VZT20]. Notably, MTA addition also lead to prolonged cell viabilities in the tests [VZT20].

After preliminary identification of MTA as a boosting additive28, further studies identified rising CSPs from 5.3 to 9.5 $\mathrm{pg\,cell^{-1}\,d^{-1}}$ after proper MTA

addition, i.e. 0.15 pmol at 50 h [VZT20]. Consequently, IgG1 titers increased from about 120 $mg\,L^{-1}$ to 140 $mg\,L^{-1}$. Hence, not only CSP but also titer improvements were achieved after MTA addition. Encouraged by these observations, this study was performed to identify the underlying metabolic mechanism leading to the production phenotype.

Compartment-specific ^{13}C metabolic flux analysis (^{13}C MFA) was applied to assess the flux changes in the CHO-DP12 culture with and without MTA supplementation. We will outline that the cells undergo significant metabolic reprogramming after MTA exposure. The rise of CSPs will be shown to correlate with increased pentose-phosphate fluxes leading to the hypothesis that the latter should be fine-tuned in hyperproducing cells.

6.2. Results

6.2.1. MTA reduced cellular growth rate while increasing cell volume

During phase A (0–48 h) cells grew under ample nutrient supply with a maximal specific growth rate of 0.705 ± 0.021 d^{-1} while consuming D-glucose, L-asparagine, L-glutamine, and other essential amino acids (Figure 6.1). Metabolic overflow products, such as L-lactate, L-alanine, L-asparagine, and L-glutamate were excreted. After MTA addition during phase B, cellular growth slowed to 0.322 ± 0.003 d^{-1} and recovered after > 60 h. During the first part of phase C, C.I (60–108 h), glucose was steadily consumed. By analogy, MTA was taken up by 0.1772 ± 0.0365 pmol $cell^{-1}$ d^{-1} before depletion (approximately 96 h). In accordance, the cytosolic and mitochondrial MTA levels rose, exceeding REF pool sizes by 170 and 800 times, respectively. Coincidentally, the supplemented cells showed increased L-alanine andL-glutamate secretion compared to the initial phase A. D-glcucose, L-

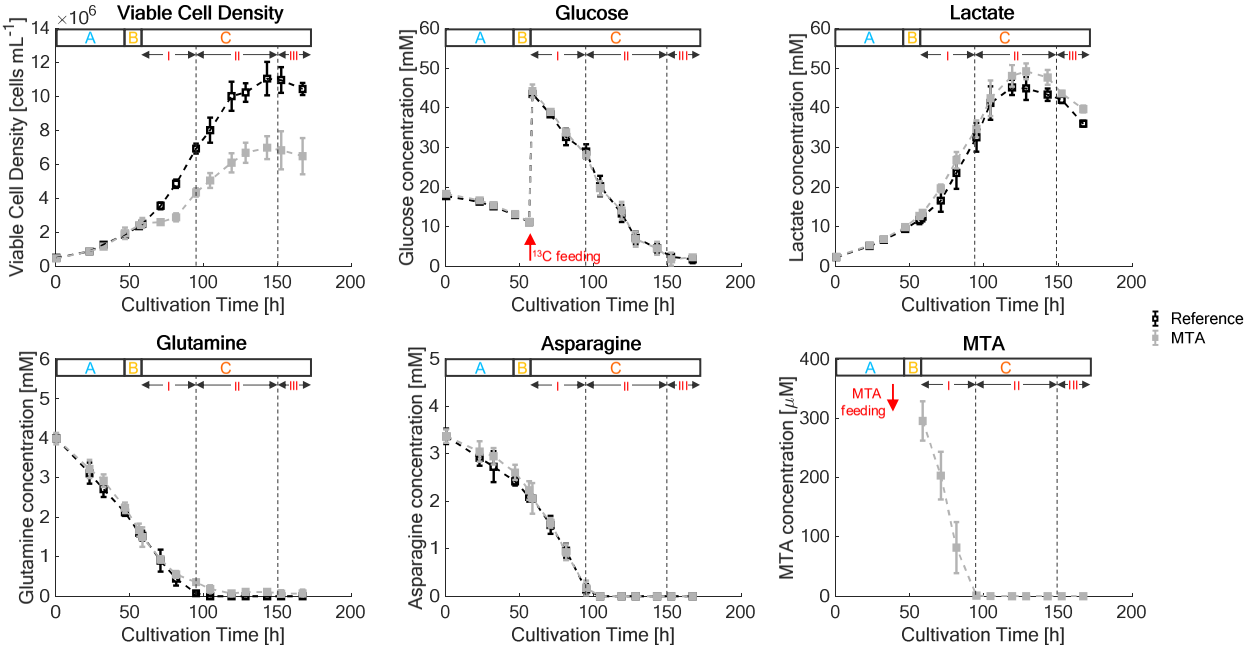

Figure 6.1.: Time course of VCD [cellmL], D-glucose [mM] , L-lactate [mM], L-asparagine [mM], L-glutamine [mM], and 5-deoxy-5-methylthioadenosine (MTA) [M] of the reference cultures (in black) and MTA-supplemented cultures (in grey). MTA was added after phase A (0–48 h), at a final MTA concentration of 250 µM. D-glucose labeling was initiated after phase B (48–60 h). Phase C (60–168 h) is divided into I: overflow; II: N-Limitation; and III: starvation. Error bars indicate the standard deviations for biological duplicates and technical replicates.

asparagine, and L-glutamine were still consumed, whereas L-lactate was secreted. In contrast, reference cultures (without MTA addition) grew with an unaffected high growth rate (0.677 ± 0.031 d^{-1}) (Figure 6.2). After 108 h, L-asparagine was depleted in all cultures. Similarly, L-glutamine depletion occurred in REF, whereas low levels were maintained in MTA-supplemented cells. Accordingly, phase C was divided into C.I (60–108 h) with sufficient L-asparagine and L-glutamine supply, phase C.II with nitrogen limitation (108–144 h), and C. III as strict starvation (> 144 h). In REF, the growth reduced to 0.258 ± 0.039 d^{-1}, reflecting L-glutamine and L-asparagine limitation during C.II. Similar growth trends were observed during phase C.II for MTA-treated cultures, with a growth rate of 0.203 ± 0.012 d^{-1} (Figure 6.2). Both cultures experienced strict starvation during C.III (144–168 h) with maximum VCDs of $(110.55 \pm 9.82) \times 10^5$ cells mL^{-1} for REF and $(69.92 \pm 6.77) \times 10^5$ cells mL^{-1} for MTA-supplemented cells (Figure 6.1).

In addition to the diminished growth rate, MTA addition led to temporary increases in cell volumes. On the basis of the measured cell diameters, the volume of supplemented cells increased by 55% (84 h) and shrank by 31% during phase C.II. In contrast, the cell size of the reference cultures was stable until the end of the cultivation phase C.II. Upon initiating carbon starvation (phase C.III), the cell volumes rose, and the differences leveled out (Figure 6.3a).

The increase in cellular volumes coincided with a change in the cell-cycle distribution after MTA addition (Figure 6.3b). At 84 h, the supplemented cells showed a lower G1-fraction (MTA: $26.02 \pm 0.70\%$; REF: $55.70 \pm 0.26\%$) and higher S-fraction (MTA: $31.32 \pm 1.23\%$; REF: $17.98 \pm 1.71\%$) and G2-fraction (MTA: $43.60 \pm 0.95\%$; REF: $26.88 \pm 1.26\%$). Cells subjected to nitrogen limitation in phase C.II (132 h) exhibited equalization of the cell-cycle phase distribution compared to the reference cultures.

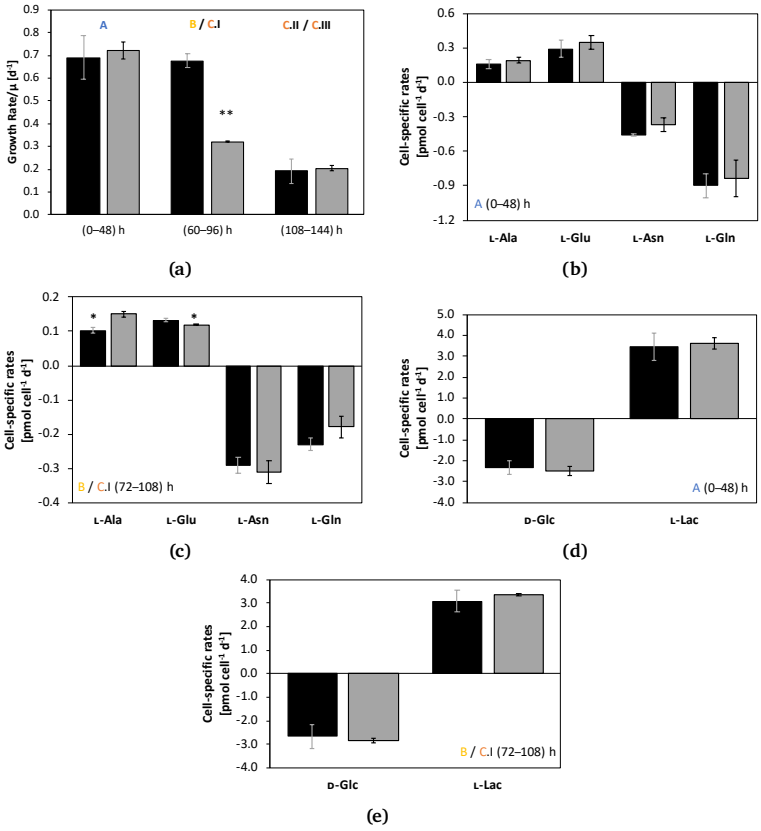

Figure 6.2.: Cellular phenotypes in reference (black) and MTA supplemented (grey) culture (a) Growth rate [d^{-1}]; (b) Cell-specific uptake/secretion rates [in pmol $cell^{-1}$ d^{-1}] for L-glutamine, L-asparagine, L-glutamate, and L-alanine in overflow metabolism before MTA addition (A); and (c) Cell-specific uptake/secretion rates [in pmol $cell^{-1}$ d^{-1}] for L-glutamine, L-asparagine, L-glutamate, and L-alanine in overflow metabolism after MTA addition (B / C.I); (d) Cell-specific uptake/secretion rates [in pmol $cell^{-1}$ d^{-1}] for D-glucose and L-lactate in overflow metabolism before MTA addition (A); (e) Cell-specific uptake/secretion rates [in pmol $cell^{-1}$ d^{-1}] for D-glucose and L-lactate in overflow metabolism after MTA addition (B / C.I). [WVTT21]

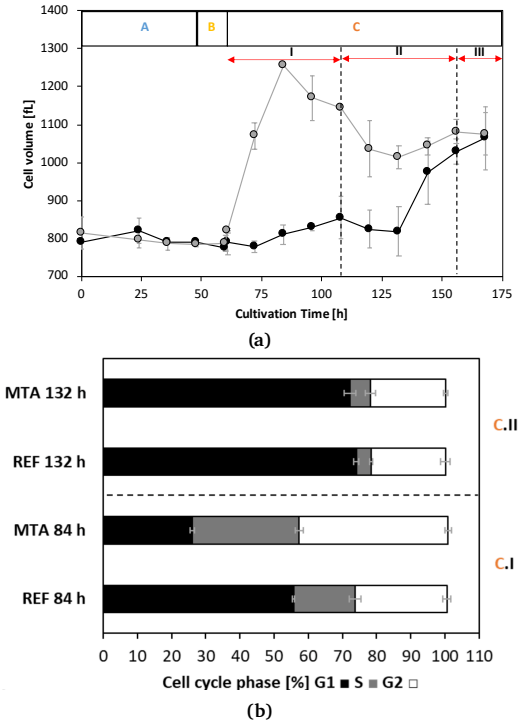

Figure 6.3.: (a) Time course of the cell volume [fL] of MTA-supplemented cells (MTA: grey) and reference cells (REF: black) in the different phases. Cell volume was calculated with the assumption of a spherical cell shape; and (b) Cell-cycle phase distribution [%] of MTA-supplemented cells (MTA) and reference cells (REF) at 84 h (I: Overflow) and 132 h (II: N-limitation). Error bars indicate standard deviations for biological duplicates and technical replicates. [WVTT21]

6.2.2. MTA addition enhanced cell-specific productivity and ATP availability

Figure 6.6 depicts cell-specific (CSP) and cell-volume-specific (CVP) IgG productivities during the exponential growth phase (A) with abundant nutrient supply. The CSP (depicted in Figure 6.4a) exhibited no significant difference before MTA supplementation (e.g., differential CSP at 24 h): REF, 5.01 ± 0.88 pg cell^{-1} d^{-1}; MTA, 5.26 ± 0.83 pg cell^{-1} d^{-1}. Similarly, the

CVP was not significantly different before supplementation (Figure 6.4b). Interestingly, the CSP following MTA supplementation was 170% higher (9.59 ± 1.72 pg cell^{-1} d^{-1}) than that in REF (3.51 ± 1.27 pg cell d^{-1}) during C.I after transient phase B. The subsequent phases C.II and C.III show reduced CSPs for all cultures, which indicates the dominating impact of limited nutrient supply in accordance with previous study [JTW+19]. The CVPs only increased by roughly 95% (MTA: 1.05 ± 0.14 g L^{-1} d^{-1}; REF: 0.54 ± 0.19 g L^{-1} d^{-1}), whereas the CSPs rose by 170%. Thus, CSP improvements mirror the combinatorial effects of elevated cell volumes and metabolic changes. The latter will be investigated through ^{13}C metabolic flux analysis.

Considering the error bars in Figure 6.5a, MTA addition did not change the ATP levels in the mitochondria but significantly increased the ATP content in the cytosol. The latter peaked 12 h after MTA addition before approaching the corresponding levels in REF at the end of C.I (Figure **??**). Notably, the cytosolic ATP trend is in accordance with the CSP profile (Figure 6.4a).

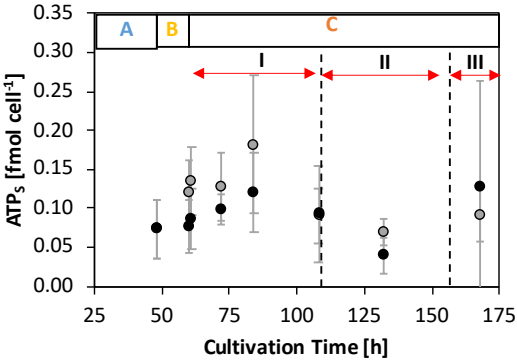

(a)

Figure 6.5.: (a) Time course of the ATP concentrations in the subcellular (mitochondrial, index S) compartment of MTA-supplemented cells (MTA: grey) and reference (REF: black); and (b) Time course of the ATP concentrations in the cytosolic compartment (index C) of MTA-supplemented cells (MTA: grey) and reference cells (REF: black). Error bars represent the standard deviations for biological duplicates and technical replicates. [WVTT21]

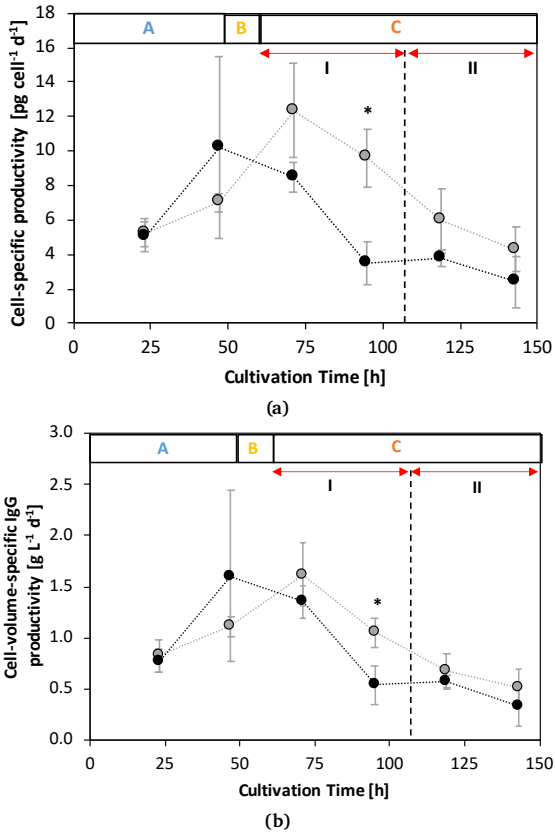

Figure 6.4.: IgG1 productivity (a) cell-specific IgG productivity (CSP) [pg cell^{-1} d^{-1}] and (b) cell-volume-specific IgG productivity (CVP) [g L^{-1} d^{-1}] in different cultivation phases. MTA-supplemented cells (grey) compared to REF cells (black). Error bars indicate standard deviations for biological duplicates and technical replicates. Significance was tested using one-sided t-test. * $p < 0.05$ [WVTT21]

6.2.3. MTA-treated cells detour carbon into the PPP

Isotopically transient ^{13}C MFA was performed to elucidate the impact of MTA addition on central metabolism under ample nutrient supply coinciding with the highest CSPs observed in phase C.I. Figure 6.6a depicts the cytosolic and mitochondrial carbon flux distributions of MTA-supplemented and reference cultures during the exponential growth in phase C.I.

Focusing on the upper glycolysis, the CHO-DP12 reference cultures (Figure 6.6a) showed a metabolic phenotype comparable to that reported by Junghans and coworkers [JTW+19]. Under abundant nutrient supply, approximately 18% of total D-glucose was continuously exchanged with non-labeled endogenous carbon storage (v_{fGlyco}: 0.474 ± 0.109 pmol cell^{-1} d^{-1}). At the same time, a remarkably low fraction of consumed D-glucose (about 4%) was channeled into the oxidative PPP (v_{G6Pdh}: 0.11 ± 0.032 pmol cell^{-1} d^{-1}), which corresponds to the earlier findings [AA11; TDRY13].

In contrast, MTA-supplemented cells exhibited a considerably different flux distribution (Figure 6.6b). The labeling kinetics of G6P indicate significantly reduced carbon exchange with endogenous carbon storage compounds such as glycogen (v_{fGlyco}: 0.02 ± 0.024 pmol cell^{-1} d^{-1}). Instead, approximately 83% of consumed glucose was diverted into the oxidative PPP (v_{G6Pdh}: 2.35 ± 0.17 pmol cell^{-1} d^{-1}). This corresponds to a remarkable rise of 21 fold in the G6Pdh flux in the MTA-supplemented cells compared to that in the G6Pdh flux in the reference culture.

The PPP influx of MTA-supplemented culture exceeded the anabolic ribose 5-phosphate (R5P) requirements, i.e., precursor needs for nucleotide biosynthesis, by a factor of 166. Consequently, approximately 81% of the carbon re-entered glycolysis via fructose 6-phosphate (F6P) and glyceraldehyde 3-phosphate (GAP). Interestingly, lower glycolysis (represented by GAP dehy-

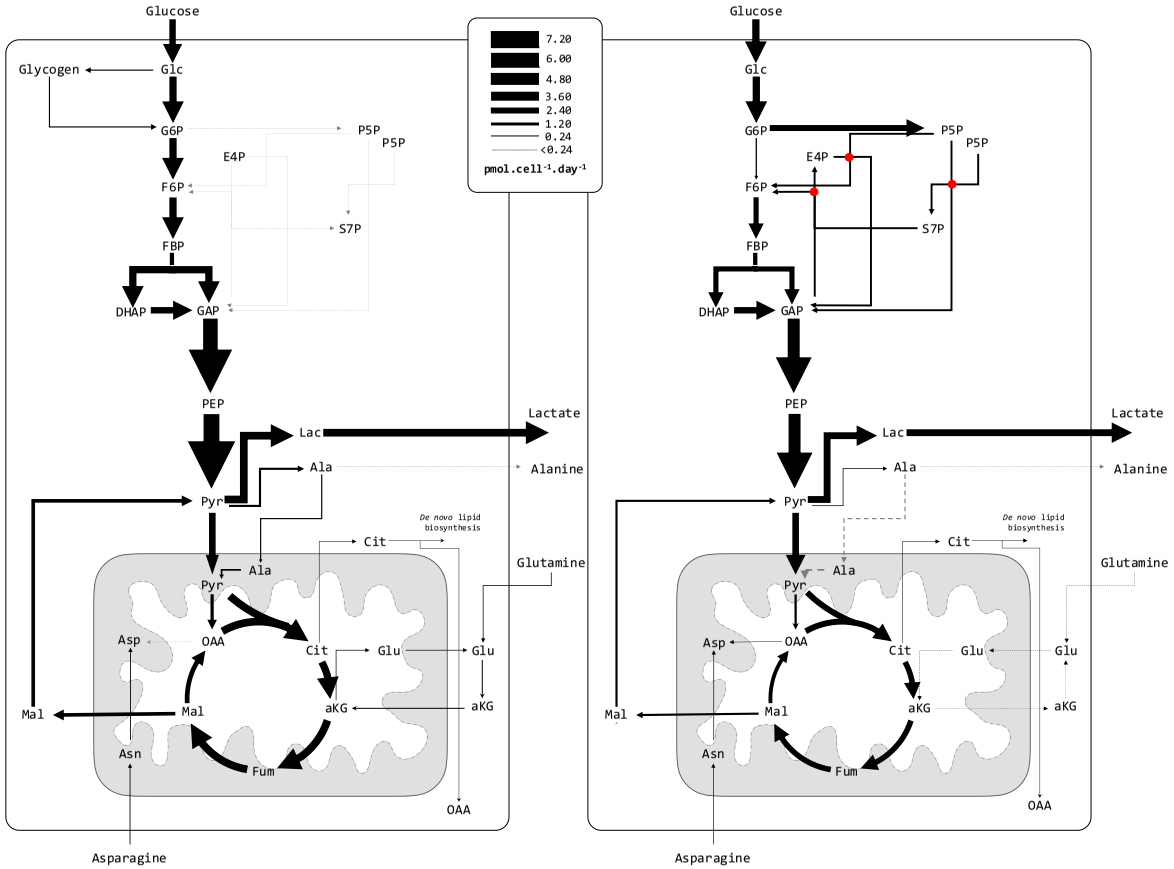

Figure 6.6.: Impact of MTA on the central carbon metabolism of CHO-DP12. (a) Metabolic flux distribution of the reference and MTA-supplemented CHO-DP12 cells. Arrows indicate flux direction, and the thickness of the arrows indicate strength in pmol $\text{cell}^{-1}\,\text{d}^{-1}$. [WVTT21]

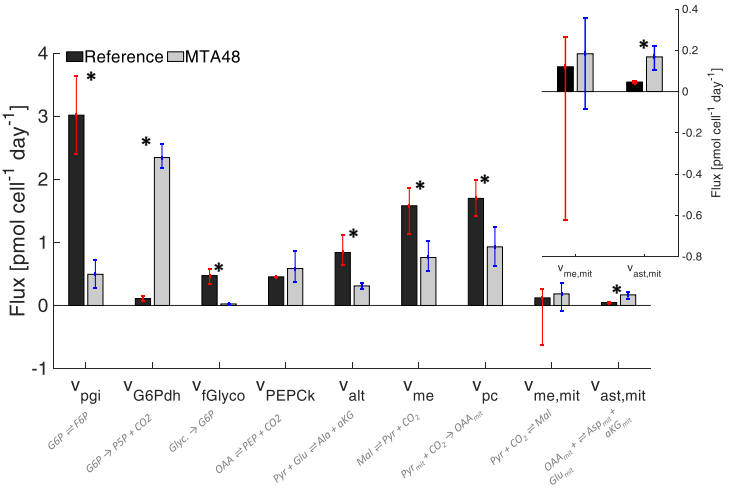

(b)

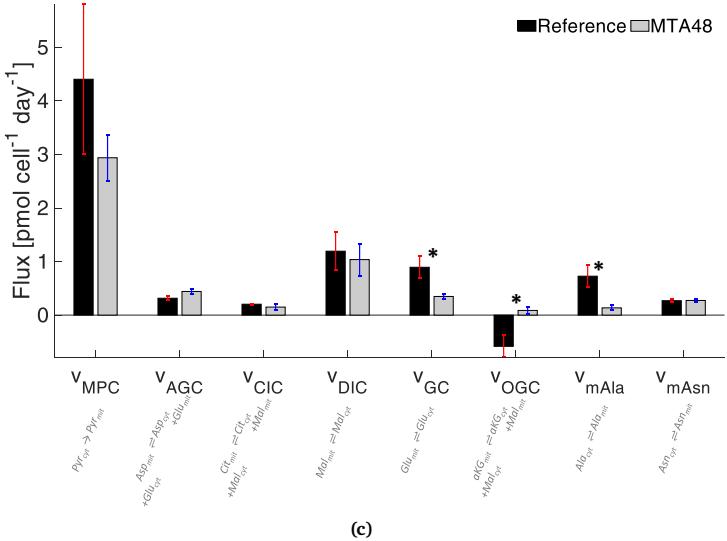

(c)

Figure 6.6.: Impact of MTA on the central carbon metabolism of CHO-DP12. (b) Comparison of key fluxes using abbreviations as follows: phosphoglucose-isomerase (pgi), G6P dehydrogenase (G6Pdh), endogenous glycogen exchange (fGlyco), PEP carboxykinase (PEPCk), alanine amino transferase (alt), malic enzyme (me), pyruvate carboxylase (pc), and aspartate amino transferase (ast); and (c) Comparison of mitochondrial carrier activities: pyruvate/H^+ symporter (MPC), aspartate/glutamate antiporter (AGC), citrate/malate antiporter (CIC), dicarboxylic acid carrier (DIC), glumate carrier (GC), aKG/malate antiporter (OGC), putative alanine carrier (mAla), and putative asparagine carrier (mAsn). * indicates $p < 0.05$. [WVTT21]

drogenase) showed statistically similar fluxes in MTA-supplemented (v_{GAPdh} : 4.87 ± 0.29 pmol cell^{-1} d^{-1}) and reference culture cells (v_{GAPdh} : 6.18 ± 1.24 pmol cell^{-1} d^{-1}).

6.2.4. MTA supplementation reduced net malate export from mitochondria

The compartment-specific ^{13}C MFA revealed the *in vivo* activity of the mitochondrial pyruvate carrier, MPC, and the other solute carriers belonging to the family 2A (SLC25A; see Table 2.4). In the REF culture, the highest mitochondrial carrier activity was observed for the MPC (v_{MPC}: 4.40424 ± 1.4045 pmol cell^{-1} d^{-1}), supporting the earlier study [JTW+19]. The dicarboxylic acid carrier (DIC) and the glutamate carrier (GC) showed the second strongest rates of 0.89 to 1.19 pmol cell^{-1} d^{-1}.

Shuttling activities for malate well described the cellular status [JTW+19]. Previous analysis of malate shuttling revealed that DIC is the key malate carrier in CHO cells. With approximately 1 pmol cell^{-1} d^{-1}, malate export from the mitochondria via DIC was approximately 6-fold higher than malate export via CIC. OGC further supports the export of mitochondrial malate by importing cytosolic α-KG. In total, net malate export occurs from the mitochondria to the cytosol at 1.57 ± 0.41 pmol cell^{-1} d^{-1}, which implies malate-mediated NADPH production in the cytosol [JTW+19].

MTA supplementation fundamentally altered the shuttling activities of GC, OGC, and putative alanine carrier (mAla). Remarkably, OGC transport was reverted, resulting in the export of α-KG to the cytosol and import of malate into the mitochondria. Accordingly, the net malate export to the cytosol was reduced to 0.8 ± 0.31 pmol cell^{-1} d^{-1} due to the MTA supplementation. Additionally, cells exposed to MTA exhibited a reduction in v_{GC} and v_{mAla} to 0.35 ± 0.06 and 0.14 ± 0.05 pmol cell^{-1} d^{-1}, respectively.

6.2.5. Reprogramming of NADPH production strategies while maintaining a similar NADH supply

NADPH is a vital cofactor and crucial redox partner in various cellular reactions, typically anabolic reactions [HV18]. In CHO-DP12, NADPH is produced via oxidative PPP and the cytosolic malic enzyme (me_{cyt}). The latter requires sufficient malate shuttling activity from the mitochondria via the concerted activities of MPC, CIC, and DIC in the citrate–pyruvate shuttle systems. This study identified a relatively high cytosolic malic enzyme flux ($\nu_{me,cyt}$: 1.58 ± 0.28 pmol cell^{-1} d^{-1}) in the reference culture, which is in accordance with the study by Junghans and coworkers [JTW+19]. Notably, fluxes via me_{cyt} were entirely fueled by malate exported from the mitochondria.

In the MTA-supplemented cultures, me_{cyt} activity (0.76 ± 0.21 pmol cell^{-1} d^{-1}) was reduced by 43%, mirroring the reduction of shuttling activities. Consequently, the NADPH supply fundamentally differed between the REF and MTA-treated cells (Figure 6.7). In the reference culture, NADPH supply via cytosolic malic enzyme (me_{cyt}) comprises 88% of the total production compared to 14% in the culture treated with MTA. Despite severe reduction in me_{cyt} activity, the MTA-treated culture produced approximately 3-fold more NADPH than REF through amplification of the NADPH formation via PPP. Notably, PPP-mediated NADPH formation was approximately 4.69 ± 0.34 pmol cell^{-1} d^{-1}, reflecting a 21-fold increase compared to REF. Regarding NADH supply, no statistically significant differences were observed between the REF and MTA-treated cells (Figure 6.7).

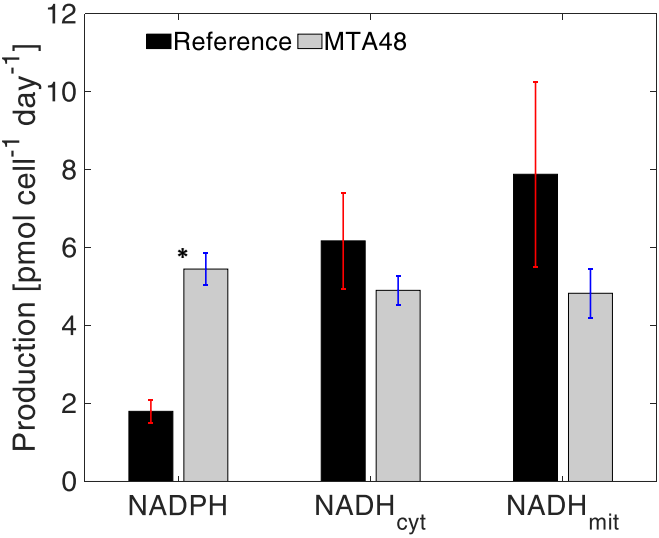

Figure 6.7.: Comparison of NADPH, $NADH_{cyt}$, and $NADH_{mit}$ production in reference culture and MTA-treated culture. * indicates a significant difference ($p < 0.05$). [WVTT21]

6.2.6. Glutamine and alanine metabolism

L-glutamine uptake rate was reduced in the MTA-treated cells (0.16 ± 0.03 pmol cell^{-1} d^{-1}) compared to the reference culture (0.22 ± 0.01 pmol cell^{-1} d^{-1}). Nevertheless, L-glutamine catabolic rates remained similar in both cultures (REF: 0.17 ± 0.01 pmol cell^{-1} d^{-1}; MTA treated: 0.14 ± 0.03 pmol cell^{-1} d^{-1}). In REF, L-glutamine was taken up and initially catabolized in the cytosol via glutaminase (Figure 6.6a). Next, the intermediate product (L-glutamate) was deaminased via cytosolic amino-transferases yielding α-KG, which fueled into the CAC via the Mal/α-KG symporter (OGC). This observation is consistent with the observations of Junghans and coworkers [JTW+19]. Interestingly, cultures treated with MTA showed a variation: cytosolic L-glutamate was imported directly into the mitochondria via AGC, and it did

not require further cytosolic deamination to α-KG.

Cellular secretion of L-alanine was significantly higher in the MTA-supplemented cells than in the REF (Figure 6.2). In contrast, intracellular L-ala formation mirrors cytosolic alanine-aminotransferase (alt_{cyt}) activities $\nu_{alt,cyt}$, which were lower in the MTA-treated cells (0.31 ± 0.05 pmol cell^{-1} d^{-1}) than in REF (0.84 ± 0.20 pmol cell^{-1} d^{-1}).

6.3. Discussion

The addition of MTA and its boosting effect on the CSP in CHO-DP12 cells was first studied by Verhagen and coworkers [VTH+20; VZT20]. MTA plays an essential role in mammalian cell metabolism, especially in polyamine synthesis [Peg88; WSG82]. In this pathway, MTA serves as an intermediate decarboxylation product of SAM to produce spermidine and spermine. High MTA levels are anticipated to inhibit polyamine biosynthesis, finally inducing cell-cycle arrest [Ore03]. Besides, MTA is known to impact gene expression patterns, including apoptosis, cell proliferation in various mammalian cells [AGM+02; RTF84]. In summary, MTA serves as a multi-level regulatory compound that exerts genetic, epigenetic, and metabolic control.

The reduction in spermidine and spermine synthesis after MTA addition is known to induce S-phase arrest in CHO cells [AO00]. This study confirmed the cytostatic effect, as displayed in Figure 6.1. MTA addition significantly reduced the maximum VCD and cell-specific growth rate (Figure 6.2a). Concomitantly, cellular volume increased (Figure 6.3a), cell-cycle distribution changed (Figure 6.3b), and IgG1 CSP (Figure 6.6) increased following MTA addition. Cellular fractions in the S- and G2-phases were temporarily increased 36 h after MTA addition, while the number of cells in G1-phase decreased (Figure 6.3b). The increase in q_{mAb} (Figure 6.6) 48 h after MTA

addition might be attributed to cell-cycle arrest, as previously reported by independent studies [FPYW04; PMT15]. Notably, CSP raise is not limited to a distinct cell-cycle phase.

Moreover, increase in cell volumes [LM00; PDWM17] have been reported to enhance CSP. Although rising cell volumes were observed in our study (Figure 6.3a), comparably low CVPs suggested that post-MTA CSP improvements were not caused by rising cell volumes alone. Indeed, the CVPs of MTA-treated cells remained relatively high until the end when the REF cells showed declining values (Figure 6.6). However, fundamental reorganization of metabolism in arrested cells is supposed to be the key factor explaining rising CSPs [FMB97].

Metabolic rearrangements were studied via ^{13}C labeling analysis. Thus, the approach complements earlier studies by Verhagen and coworkers, which focused on the SAM/MTA interplay and transcriptional responses after MTA feeding [VTH+20; VZT20]. Particularly, compartment-specific flux analysis was applied according to a previously reported protocol [JTW+19] for determining the putative impact of NADPH supply. Moreover, compartment-specific metabolomics essentially enabled flux tracking inside cellular compartments to unravel the putative impact of trans-compartment shuttling activities. Both data are qualified as important information per se.

MTA addition apparently influences the energetic status of the cells, which is reflected by an increase in cytosolic ATP pools (Figure 6.5a). The temporal rise in ATP levels likely inhibits phosphofructokinase (PFK) activity, considering the equally high ATP inhibition constants [FU80; Man63; PL64]. This metabolic inhibition may explain why fluxes through PFK are lower following MTA addition than in the absence of MTA addition in REF (Figure 6.6).

Moreover, Moreadith and Lehninger showed that malic enzyme activity is inhibited by high ATP levels [ML84]. Consequently, enhanced flux into the oxidative PPP is likely to reflect ATP-mediated metabolic inhibition of PFK and malic enzyme. The latter caused a reduction in NADPH formation, which was counterbalanced by an increase in PPP fluxes, ultimately achieving elevated NADPH production (Figure 6.7). The coincidence of metabolic rearrangement and cell-cycle arrest following MTA addition is consistent with the previous findings [VAD+09]. The authors additionally observed a relatively high oxidative PPP activity during the late G1 and S phases, suggesting that more precursors for nucleotide biosynthesis are needed during the S-phase in the cell cycle.

In addition, compartment-specific flux analysis revealed that OGC flux was reversed in MTA-supplemented cultures compared to REF. Whereas OGC exported malate into the cytosol in REF, OGC imported cytosolic malate in MTA-treated cultures. Nevertheless, malate net export into the cytosol continued to be realized via DIC. ν_{DIC} was comparable with that of the reference; however, lack of OGC contribution reduced the net malate export into the cytosol following MTA addition. Consequently, cytosolic malate was adapted to the decrease in cytosolic malic enzyme activity. Notably, the reversion of OGC reverted the flux of the counter ion α-KG. Specifically, instead of importing α-KG in the REF culture, α-KG was exported into the cytosol in the MTA-treated cultures.

In REF, L-glutamine was deaminated via cytosolic glutaminase and glutamate dehydrogenase before importing α-KG into the mitochondria. Because OGC shuttling is reversed, the MTA-treated cells require an alternative pathway to fuel the L-glutamine intermediate into CAC. Nevertheless, L-glutamine was deaminated via cytosolic glutaminase. Next, L-glutamate was imported into the mitochondrion via the amplified activities of the shuttle AGC. Subsequent deamination to α-KG occurred in the mitochondrion. Interestingly, the

potential export of mitochondrial L-glutamate via GC slowed down to ensure sufficient L-glutamate supply inside the mitochondrion.

The compartment-specific ^{13}C MFA additionally revealed that alanine aminotransferase (alt_{mit} and alt_{cyt}) activities were reduced in the MTA-treated culture. As L-glutamate was net imported into the mitochondria, the formation of L-alanine as the amino receptor from L-glutamate in the cytosol was significantly reduced (Figure 6.6). Consequently, less L-alanine was imported into the mitochondria (reduced m_{ala}). Furthermore, the substrate α-KG of alt_{mit} was shuttled out of the mitochondria in exchange with malate and $v_{alt,mit}$ was finally reduced. In essence, the activity of intracellular L-alanine metabolism was lowered, which led to increased L-alanine secretion into the medium.

Both scenarios reflect the changes in L-glutamine metabolism; they are essentially consequences of the rearrangement of glycolytic fluxes following MTA addition. Specifically, the temporal ATP rise was likely to inhibit PFK and cytosolic malic enzyme activities, which resulted in strongly amplified PPP fluxes for improving NADPH formation. Cytosolic malic enzyme lost its dominant role as a key NADPH supplier, which resulted in reduced mitochondrial malate exports and L-glutamine metabolic rearrangements, as described above.

Junghans and coworkers previously outlined the high sensitivity and positive correlation between NADPH supply and CSP for monoclonal antibody formation in CHO cells [JTW+19]. Their compartment-specific metabolome analysis revealed cytosolic malic enzyme as the key NADPH provider in growing cells. Previously, the crucial role of malic enzyme as the major NADPH source was anticipated by Ahn & Antoniewicz [AA11]; and Templeton and coworkers [TDRY13]. Sengupta and coworkers analyzed fluxes in late-stage non-growing CHO and disclosed increasing fluxes into the PPP,

apparently for NADPH formation [SRM11]. Furthermore, Tuttle and coworkers observed a 200-fold increase in G6PDH activity under oxidative stress conditions [TSPB00].

The key reason for the occurrence of fundamental metabolic reprogramming in arrested cells remains open and deserves future studies. However, a beneficial link to heterologous protein formation exists. Flux balance analysis using the simplified metabolic model [VWT+20] considered that the maximum NADPH supply should be supported by high cytosolic malic enzyme flux and high oxidative PPP activity. Interestingly, MTA treatment provides an optimal flux distribution to maximize the NADPH supply. This observation opens the door for bioprocess optimization, including investigation of the impact of serial MTA bolus shots to extend the phase of high-level CSPs.

Alternately, metabolic engineering strategies may focus on redirecting fluxes for the highest NADPH supply. Balsa and coworkers evaluated deletions of G6PDH, ME1, and IDH1 to foster PPP fluxes and NADPH formation [BPB+20]. However, G6PDH deletion resulted in higher oxidative stress, slowed down growth, and even led to cell death. This finding is also in accordance with the previous observations [TSPB00]. Till date, deletions of ME1 or IDH1 have not been reported to induce anticipated NADPH improvements.

6.4. Conclusion

The current study merges recent approaches of compartment-specific metabolomics and non-stationary ^{13}C flux analysis to investigate the impact of MTA addition on monoclonal antibody-producing CHO cells. Complementing the

studies of Verhagen and coworkers[1,2], improvement in CSPs was determined to be tightly linked with cellular arrest and reprogramming of metabolism. MTA addition initiates a cascade of regulatory responses comprising cell proliferation, transcription, and metabolic control, still keeping cell viability on a high level. Most likely, the first is the consequence of MTA-mediated feedback inhibition in polyamine biosynthesis. The resulting accumulation of ATP impairs glycolytic and malic enzyme fluxes, finally enabling significantly enhanced NADPH supply via boosting PPP activity. This knowledge should be exploited via future bioprocess development and metabolic engineering studies for improving the CSP for next-generation CHO hosts. Besides, it may illustrate the close network of cellular responses ranging from cell proliferation to reverting mitochondrial shuttle activities because of MTA addition to a CHO culture.

[1]Verhagen, N., Teleki, A., Heinrich, C., Schilling, M., Unsöld, A., Takors, R. (2020). S-adenosylmethionine and methylthioadenosine boost cellular productivity of antibody forming Chinese Hamster ovary cells. *Biotechnology and Bioengineering*, **117**(11), 3239-3247.

[2]Verhagen, N., Zieringer, J., Takors, R. (2020). Methylthioadenosine (MTA) boosts cell-specific productivity of Chinese hamster ovary cultures: dosage effects on proliferation, cell cycle and gene expression. *FEBS Open bio*, **10**(12), 2791-2804.

Chapter 7

Conclusion & Outlook

7.1. Conclusion

The preceding flux analysis studies in CHO cells have been heavily relied on cellular-derived data. The key studies from the two research group, Antoniewicz lab [AA11] and Young lab [TDRY13; TSM+17], clearly demonstrated the lack of compartment-specificity information. Notably, one fundamental question that remained was the main source of cellular NADPH. It was postulated that the malic enzyme was involved in the said process. This work is based on the development of the method in accessing compartment-specific metabolome data [MTPT15]. The latter demonstrated a distinct metabolic state between cytosol and mitochondria. Therefore, in this thesis, the compartment-specific ^{13}C MFA was developed and applied in studying CHO cells.

The first part of this study aimed to decipher the metabolic phenotypes of

CHO-DP12 cells with the compartment-specific ^{13}C MFA (Junghans et al., 2019). CHO-DP12 growing in ample nutrient conditions demonstrated high metabolic activities. Based on the metabolic flux observation, approximately half of the consumed D-glucose was converted into L-lactate, known as the Warburg effect, which was a rapid way cells could produce ATP inefficiently. Moreover, the lactate production was necessary to replenish the cytosolic NAD^+, which was necessary to metabolize D-glucose.

Proliferating CHO cells also require high amounts of NADPH to support the cellular activities. In this cell line, apparently, the oxidative PPP was not the major NADPH producer as the PPP activity was extremely low. This observation was in accordance with the previous reports that the oxidative PPP of CHO cells has extremely low activity and was not the major NADPH producer. Instead, using the compartment-specific ^{13}C MFA in this study, cytosolic malic enzyme was identified as the major NADPH producer.

The use of time-resolved compartment-specific metabolome data allowed the quantification of compartment-specific metabolic fluxes. Furthermore, *in vivo* mitochondrial shuttle activities (fluxes) were first quantified in this study. During the exponential growth phase, MPC has the highest activities among all carriers, bridging the glycolysis to the TCA cycle. Meanwhile, the malate carrier, DIC, maintained its' activities from growth phase to autophagy by adjusting its' direction according to cellular malate needs.

The study also revealed an alteration in malate shuttling between cytosol and mitochondrion, first observed when L-glutamine was limited. Consequently, cellular production of NADH/NADPH were re-adjusted accordingly. ^{13}C MFA unveiled that malate was shuttled from cytosol to mitochondria, favoring the NADH shuttling and not the NADPH generation. The latter was reported to have a direct correlation with the mAb CSP and was identified as the metabolic engineering target for further optimization.

Digging deeper into the metabolism of CHO DP-12 cells, a unique transhydrogenase-like mechanism was identified. This mechanism was discovered to be responsible in fueling carbon to the cytosolic malic enzyme (major NADPH producer). Even though genomics study has reported the transhydrogenase enzyme (Nicotinamide Nucleotide Transhydrogenase - NNT) in CHO cells. The *in vivo* activity of this enzyme in CHO cells is so far unknown. Here, the compartment-specific ^{13}C MFA identified a transhydrogenase-like mechanism (NADH conversion to NADPH and vice versa) comprising the tight interaction of cytosolic malate dehydrogenase and cytosolic malic enzyme together with the the mitochondrial shuttles (mitochondrial pyruvate carrier - MPC and malate carrier - DIC).

The compartment-specific ^{13}C MFA applied in this study relied on the method to access the sub-cellular metabolome information. This approach requires more laboratory effort to generate sub-cellular metabolome data. Hence, the third study aimed to assess whether the sub-cellular metabolome information has added value to the flux estimation, especially in term of flux accuracy and statistical uncertainty. To summarize, the compartment-specific metabolome information was not required to estimate the cytosolic fluxes involving single compartment metabolites. On the other hand, the estimation of sub-cellular fluxes, isoenzymes, and mitochondrial shuttles requires the compartment-specific information. The latter comprises of shuttles that rely on alanine, aspartate, and malate. Furthermore, the study also demonstrated that sub-cellular information was required to identify properly the key metabolic engineering target in CHO cells. Here, the bias in the cytosolic malic enzyme estimation led to the under estimation of the cellular NADPH, a parameter that influenced the cell-specific protein productivity.

Lastly, the compartment-specific ^{13}C was used to identify the metabolic functionality of a cell culture media additive, namely the 5-Methylthioadenosine (MTA). Apparently, MTA characterization served as a perfect study to show-

case the full capability of the method. Phenotypic-wise, MTA reduced cell growth rate and boost cell-specific IgG productivity by almost 50%. The productivity improvement was most likely due to the reprogramming of metabolism. Here, the ^{13}C MFA served as the most appropriate tool since the metabolic rewiring was reflected by alteration of fluxes. Two key NADPH-producing enzymes, the cytosolic malic enzyme and G6P dehydrogenase, showed a significantly alternation before and after the MTA addition to the culture.

7.2. Outlook

This study provides the first comprehensive assessment of the compartment-specific ^{13}C MFA. The development and application of this technique improved the CHO cells flux estimation, which led to the identification of a new optimization (metabolic engineering) target. Nevertheless, a few questions need to be address in the future.

CHO cells bioprocessing field is currently shifting towards bioprocess intensification, meaning that the use of continuous, small-footprint process is favorable (e.g. perfusion process). Challenges arise in transitioning from the traditional fed-batch processes towards the high-density dynamic perfusion processes, such as the optimization of the perfusion media and bioprocess parameter (e.g. feeding strategy, perfusion control, etc.). Although compartment-specific ^{13}C MFA may serve as a promising tool to aid the development, the current steady-state assumption makes this tool impossible to be applied for a highly dynamic process (e.g. high cell density perfusion process). There have been numerous efforts in quantifying the dynamic metabolic fluxes, especially using the carbon-13. For instance, the use of piece-wise affine functions [SW15] or enzyme kinetic functions [NWN15]

to simulate the labeling dynamics in such system. However, such techniques fell short when it came to the actual metabolic model network (and not the simply toy model). Recently, Quek and coworkers (2020) [QKO+20] managed to quantified the dynamic metabolism fluxes of adipocyte cells using the B-spline fuctions in combination with the Sequencing Batch Reactor (SBR) equations to simulate the metabolome pool changes. Still, the model could not fit the data well.

Furthermore, the current application of ^{13}C MFA is limited to a small metabolic model, which usually focuses on the central carbon metabolism pathway. The combination of the genome-scale model with the compartment-specific ^{13}C MFA would provide an exceptional insight into the cellular metabolism that could assist process and media development. The benefits of using the genome-scale model are as follow:

- the current study only focused on the production of NADPH, which was correctly determined using the central carbon metabolism model. With genome-scale model, the observation could be extended to the NADPH consumption, determining which cellular activities consumed NADPH the most. These information would provide corrective/preventive actions to minimize the NADPH consumption, especially with regard to the oxidative-stress counter activities.

- genome-scale model could shed a light into the glycosylation and fucosylation pathways. These two cellular processes are very important to ensure the product quality (antibody glycans profile). Hence, analyzing the fluxes into these pathways and the effect of any physical parameter and/or media components would certainly be advantageous.

- apart from the commonly known mitochondrial shuttles, genome-scale model would assist in identifying the new putative carriers and the

shuttles that connect cytosol and mitochondria.

The subcellular and mitochondrial shuttles flux distribution allow further *in vivo* studies of the respective enzymes/transporters, for instance, the comprehensive characterization of the *in vivo* enzyme kinetics and its parameter. Hence, the dynamic characterization of the metabolic network could be achieved by the enzyme kinetics modeling. With the emerging of Bioprocess 4.0 and digital twin, the enzyme kinetics will enable further development in hybrid (mechanistic-empirical) modeling for process development or process control.

The media development field is focusing entirely on the application of chemically-defined media. It means, the traditional media that contains serum or animal-derived components (e.g. FBS/FCS) is no longer favorable. In the framework of media development, compartment-specific ^{13}C MFA could be applied with other OMICS, such as transcriptomics and/or proteomics to identify which metabolic pathways were activated/deactivated by the specific serum fraction of interests. This would allow the identification of a novel compound that could do perform a similar task, enabling comparable metabolic behavior when animal-based serum was utilized.

Lastly, this study enabled the NADPH quantification via the metabolic flux analysis. However, this study also fell short in quantifying the putative sinks of NADPH (e.g. biosynthesis, countering oxidative stress). In one of the study, it has been demonstrated that the increase of CSP is likely linked to the boost of intracellular NADPH production (**chapter 6**). Nevertheless, the NADPH boost did not correlate linearly with the CSP improvement. Hence, it is essential to track the fate of the NADPH for further optimization.

Part I.

Paper I

From nutritional wealth to autophagy: *In vivo* metabolic dynamics in the cytosol, mitochondrion and shuttles of IgG producing CHO cells

Lisa Junghans, Attila Teleki, **Andy Wiranata Wijaya** , Max Becker,

Michael Schweikert, & Ralf Takors

Metabolic Engineering 54 (2019) 145–159

Contents lists available at ScienceDirect

Metabolic Engineering

journal homepage: www.elsevier.com/locate/meteng

From nutritional wealth to autophagy: *In vivo* metabolic dynamics in the cytosol, mitochondrion and shuttles of IgG producing CHO cells

Lisa Junghans[a,1], Attila Teleki[a,1], Andy Wiranata Wijaya[a], Max Becker[a], Michael Schweikert[b], Ralf Takors[a,*]

[a] Institute of Biochemical Engineering, University of Stuttgart, Allmandring 31, 70569, Stuttgart, Germany
[b] Institute of Biomaterials and Biomolecular Systems, Department of Biobased Materials, University of Stuttgart, Pfaffenwaldring 57, 70569, Stuttgart, Germany

ARTICLE INFO

Keywords:
In vivo
Mitochondrial fluxes
Cytosolic fluxes
^{13}C isotopic tracer studies
Compartment-specific metabolomics
CHO
Recombinant protein production
Cell line engineering targets

ABSTRACT

To fulfil the optimization needs of current biopharmaceutical processes the knowledge how to improve cell specific productivities is of outmost importance. This requires a detailed understanding of cellular metabolism on a subcellular level inside compartments such as cytosol and mitochondrion. Using IgG1 producing Chinese hamster ovary (CHO) cells, a pioneering protocol for compartment-specific metabolome analysis was applied. Various production-like growth conditions ranging from ample glucose and amino acid supply via moderate to severe nitrogen limitation were investigated in batch cultures. The combined application of quantitative metabolite pool analysis, ^{13}C tracer studies and non-stationary flux calculations revealed that Pyr/H^+ symport (MPC1/2) bore the bulk of the mitochondrial transport under ample nutrient supply. Glutamine limitation induced the concerted adaptation of the bidirectional Mal/aKG (OGC) and the Mal/HPO_4^{2-} antiporter (DIC), even installing completely reversed shuttle fluxes. As a result, NADPH and ATP formation were adjusted to cellular needs unraveling the key role of cytosolic malic enzyme for NADPH production. Highest cell specific IgG1 productivities were closely correlated to a strong mitochondrial malate export according to the anabolic demands. The requirement to install proper NADPH supply for optimizing the production of monoclonal antibodies is clearly outlined. Interestingly, it was observed that mitochondrial citric acid cycle activity was always maintained enabling constant cytosolic adenylate energy charges at physiological levels, even under autophagy conditions.

1. Introduction

The production of biopharmaceuticals such as antibodies is steadily rising (Walsh, 2014; Morrison and Lähteenmäki, 2017) often using Chinese hamster ovary (CHO) cells as producers (Birch and Racher, 2006; Wurm, 2004; Ecker et al., 2015). Currently, research activities are not only driven by increasing market demands but also by the growing number of expiring patents opening the door for cost-minimized production of biosimilars (Mullard, 2012; Gaughan, 2016). Product titers have increased substantially over the past years (Kunert and Reinhart, 2016) predominately reflecting improvements of increasing viable cell densities in fed-batch processes. Interestingly, cell specific productivities did not rise equally still showing typical values of 20–40 pg/cell/day in industrial producers. This observation is particularly important as it mirrors the problem that viable cell densities can be improved by smart process engineering, whereas improvements of cell-specific productivities typically require detailed knowledge of intracellular metabolic control mechanisms. The need of understanding may even increase with the envisaged development of continuous production processes (Hammerschmidt et al., 2014) that demand for optimized operating set points. It has been shown that ATP availabilities positively correlate with cell specific production rates of monoclonal antibodies (Pfizenmaier et al., 2015). However, surprisingly few is known about the *in vivo* interaction of mitochondria, the key spot of respiratory ATP generation, and the cellular metabolism located in the cytosol. Accordingly, this study focuses on the compartment-specific analysis of metabolic fluxes and shuttle transporter activities of IgG1 producing CHO cells under *in vivo* conditions.

Mammalian mitochondria are membrane-bound organelles providing ATP via oxidative reactions linked to chemiosmosis, performing crucial metabolic conversions (DiMauro and Schon, 2003; Kuznetsov and Margreiter, 2009; Scheffler, 2001), and are equipped with a

* Corresponding author.
E-mail address: ralf.takors@ibvt.uni-stuttgart.de (R. Takors).
[1] Equal first authors.

https://doi.org/10.1016/j.ymben.2019.02.005
Received 7 October 2018; Received in revised form 27 January 2019; Accepted 27 February 2019
Available online 28 March 2019

conserved set of 37 genes which are involved in various mitochondrial functions, including respiratory chain, transcription and translation (Gray et al., 1999; Leaver et al., 1983; Logan, 2006; Unseld et al., 1997). They are suspected of playing a key role in apoptotic cell death, which is triggered by the cell's energetic state (Newmeyer and Ferguson-Miller, 2003). Accordingly, the activity of mitochondria is tightly coupled to host cell needs. Transports of metabolites, nucleotides, and cofactors via the inner selective mitochondrial membrane (IMM) are tightly controlled via a set of carrier proteins and ion exchange channels (Palmieri, 2014) finally to install proper bioenergetic conditions and redox states (Kuznetsov and Margreiter, 2009; LaNoue and Williamson, 1971; Palmieri, 2013). Individual facets of the complex shuttle system such as the pyruvate carrier (Vacanti et al., 2014), respiration (Kuznetsov et al., 2008), or particular nucleotides (Imamura et al., 2009) have been studied. Isolated mitochondria (Nargund et al., 2015; Nicolae et al., 2015) or derived metabolic flux maps from whole-cell metabolic measurements that did not experimentally distinguish between cellular compartments have been investigated through alternative approaches (Goudar et al., 2010; Sengupta et al., 2011; Ahn and Antoniewicz, 2011). However, data from compartment resolved *in vivo* metabolomics are key to elucidate real mitochondrial shuttle activities in mammalian cells (Imamura et al., 2009; Matuszczyk et al., 2015; Niklas et al., 2011; Wahrheit et al., 2014).

This contribution builds on recent developments in compartment-specific metabolome quantification (Matuszczyk et al., 2015), extends the approach for ^{13}C labeling analyses, and exploits measurements for ^{13}C metabolic flux analysis (MFA) (Wiechert, 2001; Maier et al., 2008). Accordingly, cytosolic/mitochondrial shuttle activities are quantified *in vivo* investigating different production conditions. As such, the study significantly expands current state-of-the-art technologies by providing *in vivo* time-variant metabolic flux maps based on a broad spectrum of compartment-specific metabolite patterns.

2. Material and methods

2.1. Cell culture conditions and isotope labeling experiment

A IgG1 producing CHO DP-12 cell line (ATCC® CRL-1445™) was grown in suspension in a defined protein-free TC-42 medium (Xell AG) supplemented with 42 mM D-glucose, 6 mM L-glutamine, and 200 nM methothrexate. Precultures were cultivated and scaled up in baffled shake flasks (125–1000 mL, Corning, Inc.) at an initial cell density of 0.4×10^6 cells/mL in a humidified shaking incubator (Infors HT) at 37 °C, 150 rpm, and 5% CO_2. Bioreactor cultivations were performed in a two-fold parallel CellFerm Pro bioreactor system (DASGIP) equipped with pitched blade impellers and a process control system. 3.5 L TC-42 medium supplemented with 20 mM non-labeled [U-^{12}C]- D-glucose were inoculated with an initial cell density of 0.4×10^6 cells/mL. The temperature was set to 37 °C, and the dissolved oxygen (DO) content was controlled using an amperometric electrode (Mettler-Toledo) at 40%. pH was measured with a conventional pH probe (Mettler-Toledo) and maintained at 7.1 using 1 M Na_2CO_3 or CO_2 gassing. The set point for the agitation speed was 150 rpm. After 60.5 h ^{13}C isotopic tracer studies were performed as biological duplicates (n = 2) by the addition of uniformly labeled [U-^{13}C]- D-glucose reaching an extracellular isotopic ratio of 25% [U-^{12}C]- and 75% [U-^{13}C]- D-glucose (Reactor 1 and 3). Additionally, parallel cultivations were supplemented with non-labeled [U-^{12}C]- D-glucose for equal total concentrations (Reactor 2 and 4). Intracellular metabolome samples, samples for viable cell densities and cultivation supernatants were obtained as technical triplicates (n = 3) two times a day.

2.2. Viable cell number and quantification of extracellular titers

Cell growth was monitored by measuring cellular densities and viabilities using an automated counting system (Cedex XS, Roche Innovatis). Titers of D-glucose and L-lactate were measured using an amperometric biosensor system (LaboTRACE, Trace Analytics). Extracellular antibody (IgG1) concentrations were determined by ELISA as described previously (Pfizenmaier et al., 2015). Amino acid titers were quantified on an Agilent 1200 HPLC system equipped with a Zorbax Eclipse Plus C_{18} guard column (Agilent 12.5 × 4.6 mm, 5 µm) and a Zorbax Eclipse Plus C_{18} column (Agilent 250 × 4.6 mm, 5 µm). The bicratic reversed phase (RP) chromatography was based on a pre-column derivatization with *ortho*-phthaldialdehyde (OPA) and fluorenylmethyloxycarbonyl chloride (Fmoc-Cl) with fluorometric detection (λ_{ex} = 230 nm, λ_{em} = 450 nm) (Henderson and Brooks, 2010). Absolute concentrations were obtained by standard-based external calibration using L-ornithine as internal standard.

2.3. Sampling (fast-filtration) and extraction for metabolome analysis

Samples for intracellular metabolome analyses were generated according to a modified and previously published differential fast filtration protocol (Matuszczyk et al., 2015). For the whole cell analyses, defined cell amounts (3×10^7 cells/sample) were directly filtered under vacuum using a boro-silicate glass fiber depth filter with a pore size of 3 µm (Type A/D, 47 mm, Pall) at 30 mbar. The cells were rapidly quenched using 35 mL of an ice-cold washing buffer solution (10 mM KPO_4, 250–290 mOsmol/kg, pH 7.1). Cytosolic depleted cells (mitochondrial fractions) were filtered using the aforementioned Type A/D depth filter combined with a boro-silicate glass fiber surface filter with a pore size of 0.5 µm (Metrigard™, 47 mm, Pall) at 90 mbar. The cells were quenched and partially permeabilized adding 12.5 mL ice-cold washing buffer with digitonin (0.122% wv^{-1}), followed by 43.65 mL regular washing buffer. Afterwards, whole cell and subcellular sample filters (3 technical replicates per time point) were immediately transferred to 120-mL sample cups (Carl Roth), frozen in liquid nitrogen and temporarily stored at −70 °C. Before freezing 21 nmol global internal standards (Nva, KDPG, and MMA) were added to monitor variations during sample preparation.

Whole cell and subcellular samples were extracted by adding 5 mL ice-cold 70% (vv^{-1}) methanol to sample cups, followed by incubation in a cryostat at −20 °C for 90 min. The extraction solutions were separated from incubated filters using a vacuum pump (MZ 2, Vakuubrand). Next, filters and corresponding sample cups were rinsed again with 2 mL of ice-cold 50% (vv^{-1}) methanol. Collected permeates were merged with 0.5 mL of ice-cold chloroform and mixed by vortexing (20 s). The resulting methanol-chloroform solutions were centrifuged at 3200 g at 0 °C for 10 min using a Megafuge 1.0 (Heraeus). The upper aqueous phases (metabolite extracts) were aliquoted (1 mL) in 1.5 mL micro-centrifuge tubes (Eppendorf), evaporated for 110 min at 4 °C (RVC 2.33 IR, Christ), and stored at −70 °C. During extraction and evaporation, sample cups, filters, and micro-centrifuge tubes were precisely weighed after each step for the final calculation of exact extraction volumes.

2.4. Subcellular metabolomics by LC-MS/MS and HPLC-UV

Targeted metabolome studies of endogenous cellular extracts were performed on an Agilent 1200 HPLC system coupled with an Agilent 6410B triple quadrupole mass spectrometer (MS-QQQ) with an electrospray ion source (ESI). System control and MS data acquisition were performed using commercial MassHunter B.05.00 software (Agilent Technologies). MS-grade water and acetonitrile was purchased from VWR and Carl Roth, respectively. Metabolite standards (Sigma-Aldrich) were prepared in MS-grade water and stored at −70 °C. Chromatographic separation of non-derivatized polar metabolites was based on a previously developed bicratic hydrophilic interaction chromatography (HILIC) under alkaline mobile phase conditions (Teleki et al., 2015). Samples were injected onto a Sequant ZIC-pHILIC column (150 × 2.1 mm, 5 µm, Merck Millipore) with guard column

(20 × 2.1 mm, 5 µm, Merck Millipore). Intermediates were detected in the multiple reaction monitoring (MRM) mode using pre-optimized precursor-to-product ion transitions (0.1 u), associated MS/MS parameters and ESI conditions. Non-labeled subcellular metabolite pools were absolutely quantified by isotope dilution mass spectrometry (IDMS) based on the constant addition of uniformly [U-^{13}C]-labeled algal extracts (Vielhauer et al., 2011) as multicomponent internal standard mixes to samples and external calibration matrices. Isotopically labeled metabolite pools after ^{13}C tracer addition were detected separately with enhanced sensitivity in the selected ion monitoring (SIM) mode (0.3 u) and analogues parameters.

The reliable quantification of highly reactive subcellular α-keto acid pools (aKG, Pyr, Gxy, OAA, abbreviations see Table S6) was performed with a newly developed LC-MS/MS protocol. A previously published derivatization strategy based on condensation of keto groups by phenylhydrazine (Zimmermann et al., 2014) was adapted to the requirements of ^{13}C labeling analyses in subcellular endogenous extracts. 5 µL of a freshly prepared phenylhydrazine solution (30 mM) was added to 15 µL of the undiluted extract. The aliquots were spiked with 15 µL of water or defined standard mixes and 2.8 µL α-ketovalerate solution (1 mM) as internal standard. After 1 h incubation at room temperature the reaction was quenched with 0.6 µL 10% (vv^{-1}) formic acid and 21.6 µL acetonitrile. Chromatographic separation of the resulting hydrazine analogues was based on a bicratic reverse phase chromatography (RPLC) under acidic mobile phase conditions. Samples were injected (5 µL) onto a ZORBAX SB-C18 column (150 × 4.6 mm, 5 µm, Agilent Technologies) with a guard column (12.5 × 4.6 mm, 5 µm, Agilent Technologies) maintained at 40 °C. Mobile phases were composed of 0.1% (vv^{-1}) formic acid for eluent A and 0.1% (vv^{-1}) formic acid with 90% (vv^{-1}) acetonitrile for eluent B. Following gradient program with a constant flow rate of 0.3 mL/min was applied: linear gradient from 40% B to 100% B for 27 min, isocratic hold 100% B for 4 min, linear gradient from 100% B to 40% B for 1 min, and isocratic hold of 40% B for 10 min. ESI source parameters were set as follows: nitrogen gas flow rate of 10 L/min at 200 °C, capillary voltages of ± 4.0 kV for both ionization modes, and a nebulizer pressure of 30 psi. Non- and ^{13}C-labeled analytes were detected with pre-optimized transitions and MS/MS parameters (Table S1) in MRM and SIM mode, respectively. Non-labeled subcellular pools were absolutely quantified by a standard quadruple addition of defined amounts of the respective analyte standards directly to the reaction mixtures. Internal calibration curves were prepared with a linear regression ($R^2 > 0.98$) of analyte peak areas normalized by internal standard areas against the spiked concentration levels.

Intracellular concentrations of AMP, ADP, ATP, NAD, and NADP in metabolic extracts were quantified using an Agilent 1200 HPLC system equipped with a Hypersil™ BDS C18 guard column (10 × 4 mm, 5 µm) and a Supercosil LC-18-T column (15 cm × 4.6 mm, 3 µm). The bicratic ion-pair RPLC method is based on UV detection (λ_{abs} = 260 nm) of non-derivatized analytes by a diode array detector (DAD).

2.5. Transmission electron microscopy (TEM)

Samples for analysis of compartment-specific volumes were obtained on day 2.5, 3.5, and 4.6. The cells were fixed in 2.5% (vv^{-1}) glutaraldehyde (EM-grade, Sigma-Aldrich) in sodium-bicarbonate buffer for 1 h. After three washings, the cells were incubated in 1% (wv^{-1}) aqueous osmium-tetroxide solution (EMS, Hatfield) for 1 h and subsequently dehydrated in gradual acetone (30–100%) for 20 min. Next, the cells were embedded in Spurr's resin (Spurr 1969; Polyscience) and cured for 24 h at 60 °C. Ultra-thin sections were cut with a Leica UCT Ultramicrotom equipped with a diamond knife (Diatome) and collected onto 100-mesh copper grids (Agar Scientific). The grids were post-stained with 1% (wv^{-1}) aqueous uranyl acetate solution (Ted Pella) and lead citrate (Carl Roth) (Venable and Coggeshall, 1965) and analyzed under a transmission electron microscope (Tecnai G^2 Sphera, FEI) at 200 kV. TEM images were recorded with EMMENU®-Software (TVIPS) using a 16-megapixel camera (TemCam-F416 [4k × 4k], TVIPS). The images were morphometrically analyzed using ImageJ software and the following criteria: equal distribution of mitochondria using cuts from the center of the cells with significant nuclei and diameters of 9–13 µm. Cytoplasmic volumes were calculated from measurements of mitochondrial, nuclear, and total cell volumes neglecting the remaining organelles (Dewey and Fuhr, 1976).

2.6. ^{13}C metabolic flux analysis (MFA)

The intracellular flux distribution was calculated by analyzing time series of isotopically transient ^{13}C labeling signals in compartment-specific metabolite pools using Insilico Discovery software (Insilico Biotechnology AG; Maier et al., 2008; Schaub et al., 2008). The input for ^{13}C MFA consists of a stoichiometric and carbon transition metabolic model (Table S2), extracellular rates, as well as absolute concentrations and isotopologue distributions of targeted subcellular metabolite pools. The transient ^{13}C courses of the metabolites were analyzed assuming pseudo steady-state pool sizes between two subsequent sampling points to minimize the effect of non-stationary metabolism.

2.6.1. Compartmented metabolic model

^{13}C MFA focused on the central carbon metabolism in CHO-DP12 cells. The overall metabolic model comprised two compartments: the cytosol and the mitochondrion, each consisting of a stoichiometric and a carbon atom transition model. As indicated in Table S2, cellular transporters, the Embden-Meyerhof-Parnas pathway (EMP), the pentose phosphate pathway (PPP), the tricarboxylic acid cycle (TCA), anaplerotic and cataplerotic reactions, and biomass formation were considered with regard to their subcellular location. Accordingly, all fundamental functionalities of the so-called fuelling pathways regarding precursor supply, ATP formation and regeneration of reduction equivalents ($NAD(P)^+$/NAD(P)H) were included. In addition, the TCA cycle does not only act as the source of anabolic precursors and reduction equivalents, it also serves as entry point of some amino acid degradations. Selected reactions of important amino acids (Gln, Glu, Ala, Asn, Asp, Ser) were inserted accordingly. Cellular growth reactions were represented by several sink reactions of amino acids and central carbon metabolites according to the anabolic demands for the biosynthesis of lipids, proteins, RNA, DNA, and carbohydrates reported by Sheikh et al. (2005). A cell density of 122 pg/cell was used to convert the growth rate into a lumped growth flux. Next, depolymerization of storage carbohydrates was assumed to account for the effect of G6P dilution by glycogen. In the final cultivation phase (autophagy), several non-labeled metabolite sources were included to account for protein degradation and to reflect the drastic increase of non-labeled metabolic fractions. Measured ^{13}C labeling distributions were corrected for natural stable isotope abundances (Fernandez et al., 1996) using the MATLAB (The MathWorks, Inc., USA) based *mscorr* function provided in INCA (Young, 2014).

2.6.2. Extracellular production rates

Cell specific extracellular rates reflecting growth $\boldsymbol{\mu}$, substrate conversion and product formation $\pm$ $\boldsymbol{q_i}$ were calculated using viable cell densities $\boldsymbol{C_x}$ and extracellular concentrations $\boldsymbol{C_i}$ as follows:

$$\mu = \frac{\Delta C_X}{\overline{C_X}\Delta t} \quad (1)$$

$$\pm\, q_i = \frac{\Delta C_i}{\overline{C_X}\Delta t} \quad (2)$$

2.6.3. Network degrees of freedom

A metabolic model containing the internal network matrix $\boldsymbol{S}$, the

internal flux vector $\boldsymbol{r}$, the membrane transport vector Γ, the transport flux vector $\mathbf{u}$, the entire network matrix $\boldsymbol{N}$ and flux vector $\boldsymbol{v}$ was formulated as follows:

$$S.\ r + \Gamma.\ u = N.\ v \tag{3}$$

Before performing the flux analysis or parameter estimation, inner and outer degrees of freedom were calculated for each metabolic model. The inner degree of freedom (Equation [5]) was calculated based on a null space analysis of the network matrix by assuming zero transport into/out of the network, whereas the outer degree of freedom (Equation [6]) was calculated by subtracting the inner degree of freedom from the total degrees of freedom (Equation [4]). The outer degree of freedom reflects the number of independent extracellular rates required to solve the system of linear equations, whereas the inner degree of freedom indicates unknown inner fluxes that could be estimated using the ^{13}C labeling data. The Insilico Discovery ^{13}C flux analysis tool only works with determined systems. Therefore, a set of linearly independent extracellular rates and inner fluxes was selected to determine the degrees of freedom of the respective metabolic model.

$$\textit{Total degrees of freedom} = \dim(v) - \textit{rank}(N) \tag{4}$$

$$\textit{Inner degree of freedom} = \dim(r) - \textit{rank}(S) \tag{5}$$

$$\textit{Outer degree of freedom} = \text{Total degrees of freedom} - \text{Inner degree of freedom} \tag{6}$$

2.6.4. Metabolite and isotopomer balancing

To simulate intracellular metabolite time series of ^{13}C enrichments, balancing of each metabolite and each isotopologue is essential. The basic equation of metabolite pool dynamics under steady state conditions is given in equation [7]. Corresponding labeling dynamics can be described by Equation [8]:

$$\frac{dc_i}{dt} = N.\ v \tag{7}$$

$$\frac{d(c_i I_i)}{dt} = \sum_{j=1}^{N}\left[\alpha\left(\bigotimes_{k=1}^{0}\left(\sum_{m=1}^{v_{ij}} IMM_{k\to m}\right)I_k\right)r_j + (1-\alpha)(v_{ij} r_j I_i)\right]$$

With

$$\alpha = \begin{cases} 1, & if\ v_{ij} > 0 \\ 0, & else \end{cases} \tag{8}$$

$\boldsymbol{c_i}$, $\boldsymbol{I_i}$, and $\boldsymbol{I_k}$ denote vectors of intracellular concentrations of metabolites i and the isotopomer distribution vectors for metabolites i and k, respectively. Labeling distribution vectors contain molar ratios that correspond to the fractional amounts of the individual isotopologues. $\mathbf{IMM}_{k\to m}$ is an isotopomer mapping matrix that describes the isotopomer transition from reactant k to product m (Schmidt et al., 1997). v_{ij} equals the stoichiometric coefficient of metabolite i in reaction j, whose molar rate is r_j. The operator ⊗ denotes element-by-element vector multiplication.

2.6.5. Parameter estimation and intracellular flux quantification

Parameter (flux) estimation was achieved by fitting the simulated isotopologue profiles to the measured *in vivo* data and were optimized by minimizing the weighted sum of the squared errors:

$$\min_{\boldsymbol{p}} \Phi = \sum \frac{(x - x_m)^2}{\sigma_x^2} + \sum \frac{(q - q_m)^2}{\sigma_q^2} + \sum \frac{(c - c_m)^2}{\sigma_c^2} \tag{9}$$

$\boldsymbol{x}$, $\boldsymbol{q}$, and $\boldsymbol{c}$ denote isotopologue fractions, estimated free fluxes, and metabolome pool sizes, respectively. $\boldsymbol{\sigma}$ denotes the standard deviation of each measured value. Measured $\boldsymbol{q_m}$ and estimated fluxes $\boldsymbol{p}$ were used to calculate the flux distribution $\boldsymbol{v}$ under specific condition:

$$v = \begin{pmatrix} \boldsymbol{S} \\ \boldsymbol{Q} \end{pmatrix}^{-1} \begin{pmatrix} 0 \\ [\boldsymbol{q_m}\ \ \boldsymbol{p}] \end{pmatrix} \tag{10}$$

2.6.6. Goodness of fit assessment

The goodness of fit of the obtained flux distribution was assessed using the Pearson-Fischer chi-square test (Bolboacă et al., 2011) to determine whether the model reflects the experimental data (extracellular rates, metabolome pool sizes, and isotopologue distributions), properly.

$$\chi^2 = \sum \frac{(O - E)^2}{E} \tag{11}$$

$$df = (n - p) \tag{12}$$

$$\chi^2 \leq \chi^2_{(1-\alpha),\ df} \tag{13}$$

Based on Pearson's chi-square test, the fit of the simulation result and the experimental observations were accepted statistically, based on a 95% confidence interval ($\boldsymbol{\alpha}$ = 0.95). The complete Pearson's chi-square goodness of fit assessment is provided in Table S3.

3. Results

3.1. Experimental conditions for compartment-specific metabolomics

Bioreactor cultivations with CHO DP-12 cells were performed to enable the analysis of shuttle activities under three distinct growth scenarios (Fig. 1B): (I) exponential growth with L-glutamine, L-asparagine, and D-glucose saturation, (II) moderate nitrogen limitation by L-glutamine depletion and L-asparagine and D-glucose saturation, and (III) strong nitrogen limitation without L-glutamine and L-asparagine but with D-glucose saturation. As such, metabolic measurements mirrored the cellular response in the feast-to-famine transition with respect to nitrogen limitation. Resulting growth profiles were clearly determined by the respective extracellular substrate availability. In phase I, the cells grew with a high specific growth rate (0.0246 ± 0.0007 h^{-1}) while substantial amounts of D-glucose, L-glutamine, L-asparagine, and glycine were constantly consumed. The overflow products L-lactate, L-alanine, L-glutamate, and L-aspartate were secreted in abundance. In phase II, L-glutamine was depleted, and the cells grew with a reduced growth rate (0.0202 ± 0.0022 h^{-1}). D-glucose, L-asparagine, and glycine were consumed, whereas L-lactate rather than L-alanine and L-glutamate were excreted. Phase III was characterized by stationary growth and nitrogen limitation as a result of L-asparagine depletion. Beside D-glucose as the main carbon source, much less L-alanine and L-glutamate were consumed during the last phase. However, L-lactate and minor amounts of glycine were still excreted (Fig. S1).

Isotopic tracer studies were performed with biological duplicates (n = 2) by adding uniformly labeled [U-^{13}C]- D-glucose to reach an extracellular isotopic molar ratio of 25% [U-^{12}C]- and 75% [U-^{13}C]- D-glucose on day 2.5 (phase I). Simultaneously, parallel cultivations for absolute quantification of intracellular pools (n = 2) were supplemented with non-labeled [U-^{12}C]- D-glucose to reach equal concentrations (Fig. 1B).

The cultivations were sampled twice per day (from day 1.5 to day 7), and subcellular metabolome analyses were achieved following the differential analysis protocol of Matuszczyk et al. (2015). The method separates the cytosolic fraction from physically intact mitochondria (Fig. 2). Cytosolic depletion and mitochondrial membrane integrity were quantified using G6P, F6P, and cisAco as compartment-specific internal standards (Fig. S2).

To translate non-volumetric concentration measurements (fmol/cell) to compartment-specific pool sizes (mM), mitochondrial volumes were determined via TEM after fixation of cells in glutaraldehyde (Fig. 1D) (Dewey and Fuhr, 1976; Kahle et al., 2015). Interestingly,

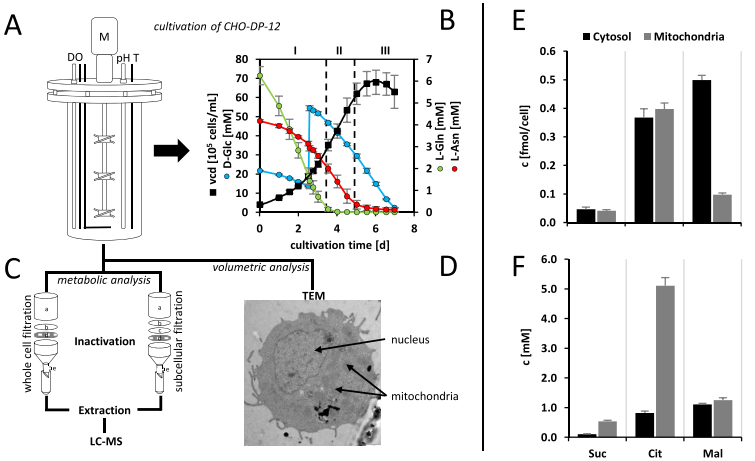

Fig. 1. Experimental setup and validation for whole-cell and subcellular metabolome analyses. **(A)** Bioreactor setup for batch mode. CHO-DP12 cultivations (n = 4) were performed under defined conditions by controlling temperature (37 °C), pH (7.1), dissolved oxygen (40%), agitation (150 rpm), and aeration. **(B)** Time profiles of viable cell density, D-glucose-, L-glutamine-, and L-asparagine titer (n = 4). **(C)** Sample preparation by a differential fast-filtration method: (a) glass funnel, (b) Pall A/D filter, (c) Pall metrigard filter, (d) aluminum filter, and (e) vacuum pump. Metabolite extracts were analyzed by targeted LC-MS/MS. **(D)** Volumetric analysis for the determination of mitochondrial volume fractions using TEM. **(E)** Exemplary non-volumetric subcellular pool sizes [fmol/cell] of succinate, citrate, and malate (n = 4). **(F)** Corrected analogous volumetric concentrations [mM] based on determined compartment-specific volumes (n = 4).

almost constant mitochondrial volume fractions of 9.5 ± 1.65% per cell were obtained irrespective of the process conditions. The mitochondrial volume fraction in CHO cells is smaller than those observed in human hepatocytes and myocardial tissue cells (16–22%) (Alberts et al., 1989; Kahle et al., 2015; O'Brien and Sidell, 2000; Urschel and O'Brien, 2008), but comparable to those in insulin-secreting INS-1E cell lines (6.97 ± 1.09%) (Gerencser et al., 2012). Using the measured cell diameter (11.61 ± 0.17 µm), mitochondrial and cytosolic volumes were estimated as 78 fL and 450 fL, respectively, agreeing well with the findings of Dewey and Fuhr (1976), who studied CHO cells. As indicated in Fig. 1E and F, only compartment-specific adjustments revealed increased pool sizes (for abbreviations see Table S6) of Cit and Suc in the mitochondria, their origin. Mal, which is supposed to be frequently exchanged with the cytosol, showed similar mitochondrial and cytosolic concentrations.

3.2. Subcellular metabolomics during overflow metabolism (phase I)

Phase I was characterized by high uptake rates of the main carbon sources D-glucose and L-glutamine, which led to excretion of overflow metabolites (Altamirano et al., 2000). Of the metabolized D-glucose and L-glutamine, 60% and 50% were found as L-lactate and L-glutamate, respectively (Fig. S1), which is in agreement with the results of previous studies (Ahn and Antoniewicz, 2011; Neermann and Wagner, 1996; Wahrheit et al., 2014). Figs. 3 and 4 depict the time courses of selected intracellular pool sizes representing glycolysis, citric acid cycle (TCA), adenine nucleotides, and amino acids. During phase I, we observed a metabolic steady state for all metabolites that was not affected by the addition of D-glucose on day 2.5 (Fig. 1B). Metabolites of main mitochondrial shuttle systems like Mal, aKG, Glu, and Asp consistently showed similar concentrations in the cytosol and mitochondria. Mitochondrial levels of Cit and Suc were higher than those in the cytosol, underlining that Cit and Suc are predominantly produced in mitochondria (Mycielska et al., 2009; Sun et al., 2010). In contrast, ATP pool sizes were significantly higher in the cytosol, whereas ADP levels were similar in both compartments. These findings may support the notion that most ATP-dependent reactions occur in the cytosol or other compartments rather than in mitochondria (LaNoue and Schoolwerth, 1979) (Fig. S3).

Cellular energetics were studied based on the adenylate energy charge (AEC) and ATP/ADP ratio. During overflow metabolism, the cytosolic AECs were always kept at physiological levels of 0.9 ± 0.02, whereas mitochondrial AECs were significantly below those levels at 0.7 ± 0.02 (Table 1). Similarly, the mitochondrial ATP/ADP ratio (1.3 ± 0.15) was five-fold lower than the cytosolic value (6.3 ± 1.21), which corresponds to findings of Schwenke et al. (1981), who analyzed rat livers and found ratios of 0.9 and 6.9, respectively. Furthermore, equal mitochondrial and cytosolic pool sizes of NAD^+ were measured which conformed to similar studies of neurons (Alano et al., 2007; Stein and Imai, 2012). Further evaluation of the cellular redox state was performed by estimating the NAD^+/NADH ratio (Schafer and Buettner, 2001) following the approach of Taymaz-Nikerel et al. (2009). In essence, NADH-producing and -consuming TCA reactions were assumed to be in steady state and balanced by metabolites transported by the malate-aspartate shuttle. Cytosolic and mitochondrial NAD^+/NADH ratios were estimated to be 215 and 327, respectively (Table 1), indicating small amounts of NADH and excess NAD^+ and reflecting high respiration activity.

3.3. Subcellular metabolomics during glutamine and nitrogen limitation (phase II and III)

Phase II is characterized by limiting L-glutamine supply but ample D-glucose and L-asparagine levels. Interestingly, cellular metabolism managed to maintain almost constant pool sizes of glycolytic metabolites in the cytosol, except for a moderate reduction of G6P and a continuous decrease in subcellular Pyr levels. With the start of nitrogen limitation (phase III), pronounced accumulation of most of glycolytic intermediates was observed; for example, F16bp increased by a factor of 10. Exceptions were G6P and subcellular Pyr pools, which persisted

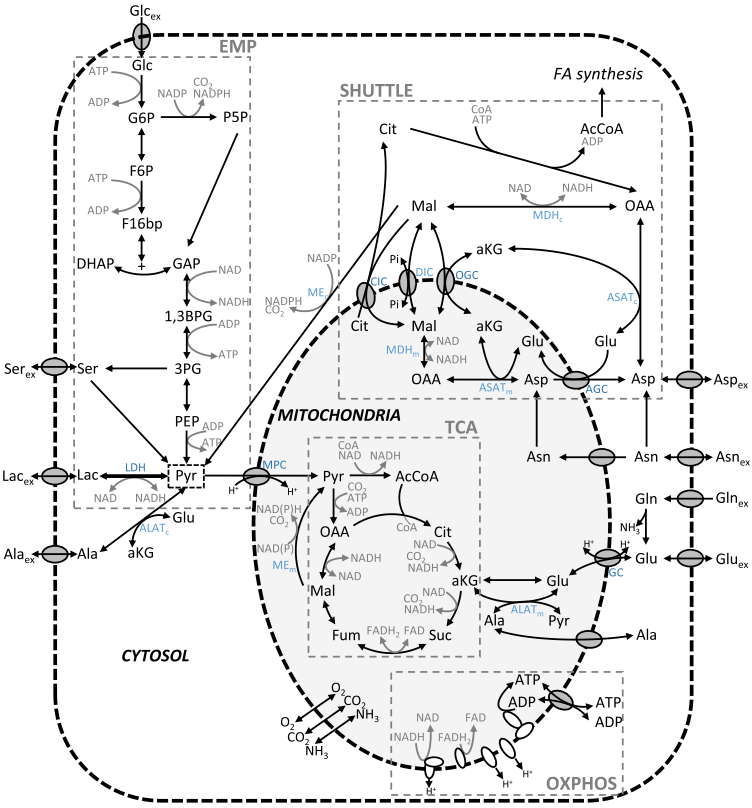

Fig. 2. Schematic illustration of the compartmented central carbon reaction network in CHO-DP12. Subcellular location of key intermediates of central carbon, amino acid, and energy metabolism with regard to mitochondrial shuttle systems and cellular transporters. Lactate dehydrogenase (LDH); cytosolic/mitochondrial malic enzyme ($ME_{c/m}$); malate dehydrogenase ($MDH_{c/m}$); cytosolic/mitochondrial alanine aminotransferase ($ALAT_{c/m}$); cytosolic/mitochondrial aspartate aminotransferase ($ASAT_{c/m}$). See Table S6 for the full names of abbreviated metabolites.

and continued to decrease, respectively (Fig. 3).

In general, pool sizes of TCA metabolites in mitochondria were always found to be larger and more stable than their cytosolic counterparts. The greatest changes in pool sizes in phases II and III were observed for subcellular Cit, Fum, Mal, and aKG, whose levels are tightly coupled with cytosolic exchange via shuttle activities. In phase III, characterized by limited nitrogen, all TCA metabolites were highly diluted in the cytosol. In contrast, accumulation of cytosolic Ser and Ala was observed during phase II and cytosolic Gly and Pro during phase III. Interestingly, the accumulation inverted the concentration ratio from dominant pool sizes in the mitochondria during phase I to dominant cytosolic levels during phases II and III. Moreover, Glu showed steadily decreasing pool sizes in both compartments, whereas subcellular Asp levels demonstrated pool size recovery at the beginning of phase III (Fig. 3 and Fig. S6).

3.4. Metabolic dynamics of the shuttle partners

Fig. 4 depicts the dynamics of mitochondrial/cytosolic shuttle partners, outlining the malate-aspartate shuttle with the antiport partners Glu/H^+-Asp (AGC1/2) and Mal/aKG (OGC) and the pyruvate-citrate shuttle with the antiporter Cit/H^+-Mal (CIC). During the ample growth in phase I, cytosolic and mitochondrial pool ratios of Glu/Asp and Mal/aKG persisted at about 2 and 15, respectively. Mal/Cit ratios remained stable as well, but at ratios of 1.4 in cytosol and 0.2 in the mitochondria. Interestingly, none of the mitochondrial ratios changed with L-glutamine limitation during phase II. However, nitrogen limitation during phase III induced similar trends in both compartments, showing rising Mal/Cit ratios coinciding with falling Glu/Asp ratios.

3.5. Dynamics of nucleotides

Most strikingly, cytosolic AEC was tightly controlled at about 0.9, irrespective of metabolic conditions during phases I–III. In contrast, mitochondrial AEC levels remained at about 0.7 in phases I and II (Table 1) but diminished to 0.56 during phase III. The latter level mirrored the immense rise in AMP in mitochondria during the last period (Fig. 4). Moreover, the cytosolic/mitochondrial NAD^+ ratio was

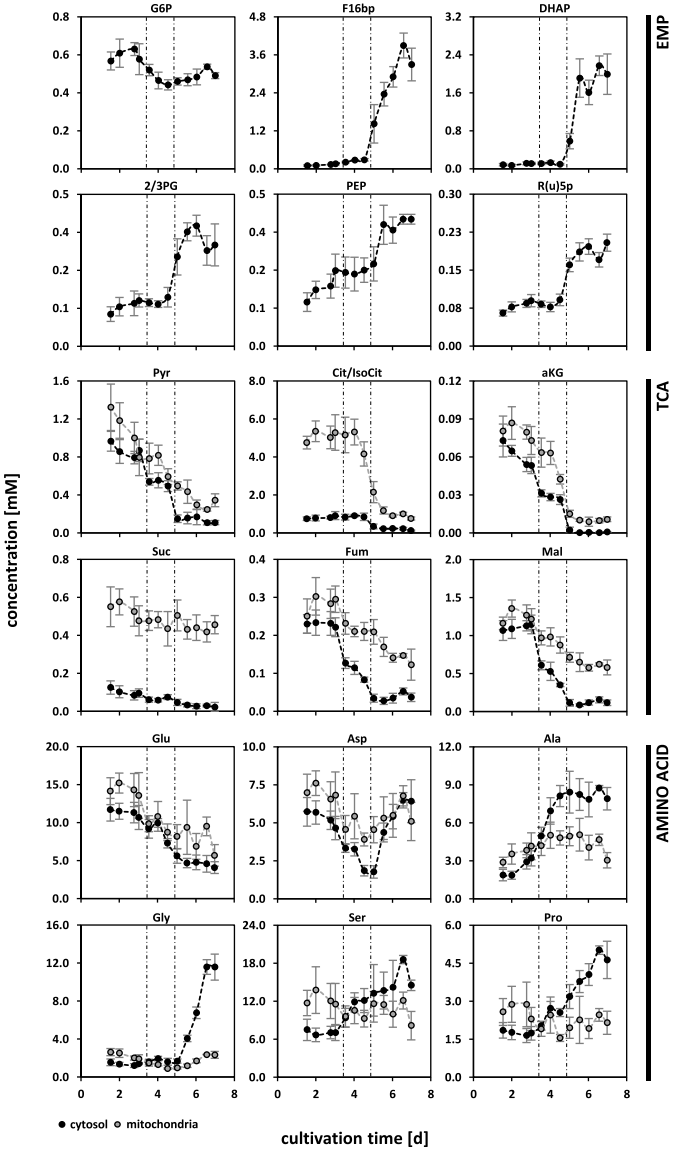

Fig. 3. Subcellular metabolite dynamics during different cultivation phases (I–III). Mean values of depicted subcellular pool concentrations are based on at least two filter replicates and two bioreactor cultivations (n = 4). Errors were calculated using error propagation. Significance of subcellular data sets with partially overlapping error bars were additionally checked by pairwise one-way ANOVA (see supplemental material). Time-variant dynamics are highlighted by connecting lines. See Table S6 for the full names of abbreviated metabolites.

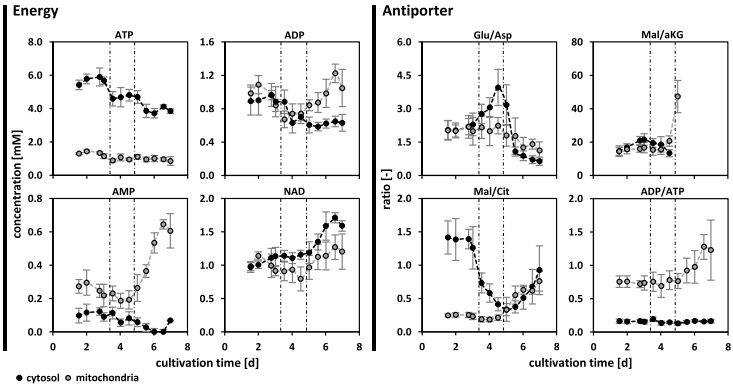

Fig. 4. Subcellular metabolite dynamics and pool ratios during different cultivation phases (I–III). (**A – Energy**) Mean values of depicted subcellular pool concentrations (nucleotides and NAD^+) are based on at least one or two filter replicates and four bioreactor cultivations (n = 6). (**B – Antiporters**) Subcellular pool ratios of mitochondrial shuttle partners. Mean values are based on at least two filter replicates and two bioreactor cultivations (n = 4). Errors were calculated using error propagation. Significance of subcellular data sets with partially overlapping error bars were additionally checked by pairwise one-way ANOVA (see supplemental material). See Table S6 for the full names of abbreviated metabolites.

found to be stable in all phases. In contrast, the equivalent NADH ratio increased from 1.8 to 8.9 (Table 1), hinting to falling transport capacity to translocate cytosolic NADH to mitochondria via the mitochondrial shuttle systems. In agreement, phase II revealed a decrease in the cytosolic NAD^+/NADH ratio from 192 to 89, whereas the mitochondrial ratio increased from 327 to 500.

3.6. Isotopic labeling dynamics

Glycolytic intermediates reached isotopic steady state already by 6 h (first sampling, Fig. 5), revealing the expected 25% non-labeled fraction (m + 0) for all intermediates except for F16bp. During phase II and III, all intermediates showed either a small or large (F16bp) rise in the size of labeling fractions, which hints at changes in metabolic activity as a consequence of nitrogen limitation.

The compartment-specific labeling analysis revealed similar trends for Cit/IsoCit, aKG, Suc, Fum, and Mal. Most strikingly, the expected 25% non-labeled fraction (m + 0), indicating a labeling steady state, was never achieved, neither in phase I nor in phase II. However, phase III apparently induced the inverse effects by equally fueling sources of non-labeled compounds into cytosol and mitochondria. In contrast, cytosolic Pyr pools reached a significantly time-delayed labeling steady state (approximately 60 h after labeling start) but remained in this labeling state even in phase III. Moreover, the labeling dynamics of subcellular Pyr pools differed significantly (Fig. 5).

Fig. 5 illustrates the compartment-specific labeling courses of Ala, Glu, and Asp. Whereas the latter showed a steady reduction in non-labeled Asp fractions, with notable different kinetics in the cytosol and mitochondria. Ala and Glu demonstrated very similar labeling trends in both compartments, characterized by continuous labeling during phases I and II and arrested labeling during phase III. Only Glu reached the expected labeling fraction with the labeled substrate. Additionally, labeling kinetics of mitochondrial Asp and significant amounts of mitochondrial Asn (Fig. 5 and Fig. S6) indicated the presence of an unknown transporter system (m_Asn).

3.7. ^{13}C metabolic flux analysis (MFA)

As indicated in Fig. 6 and Fig. S4, the labeling courses of metabolites were highly dynamic during phases I–III and did not always achieve steady-state labeling patterns. Concomitantly, the turnover rates of individual pools were in the range of minutes, outlining that they went below 1 to 2 orders of magnitude in time compared to the dynamics of pool sizes and labeling patterns. Accordingly, a ^{13}C flux analysis was performed to analyze transient ^{13}C courses of metabolites, assuming pseudo steady-state pool sizes between two subsequent sampling points. Fig. S5 indicates that D-glucose uptake and L-lactate secretion rates were almost equal in phases I and II but that L-glutamine uptake was already negligible in phase II. Additionally, L-lactate secretion was further reducing at the end of phase II and beginning of phase III but

Table 1
Energetic conditions of CHO cells during different cultivation phases (I–III). Mean values are based at least on one to two filter replicates of four bioreactor cultivations (n = 6). Errors were calculated using error propagation. See Table S6 for the full names of abbreviated metabolites.

Ratio	Phase I		Phase II		Phase III	
	Cytosol	Mitochondria	Cytosol	Mitochondria	Cytosol	Mitochondria
AEC	0.9 ± 0.02	0.7 ± 0.02	0.91 ± 0.02	0.69 ± 0.03	0.90 ± 0.01	*0.56* ± 0.06
ATP/ADP	6.3 ± 1.21	1.3 ± 0.15	6.5 ± 1.11	1.4 ± 0.28	6.3 ± 0.80	*0.9* ± 0.22
NAD/NADH*	215 ± 53	327 ± 92	*89* ± 20	*500* ± 157		
ATP_{cyt}/ATP_{mit}	4.4 ± 0.41		4.9 ± 0.78		4.1 ± 0.83	
ADP_{cyt}/ADP_{mit}	0.9 ± 0.19		1.0 ± 0.22		*0.6* ± 0.11	
NAD_{cyt}/NAD_{mit}	1.1 ± 0.15		1.3 ± 0.27		1.3 ± 0.26	
$NADH_{cyt}/NADH_{mit}$*	1.7 ± 0.68		*8.9* ± 3.4			

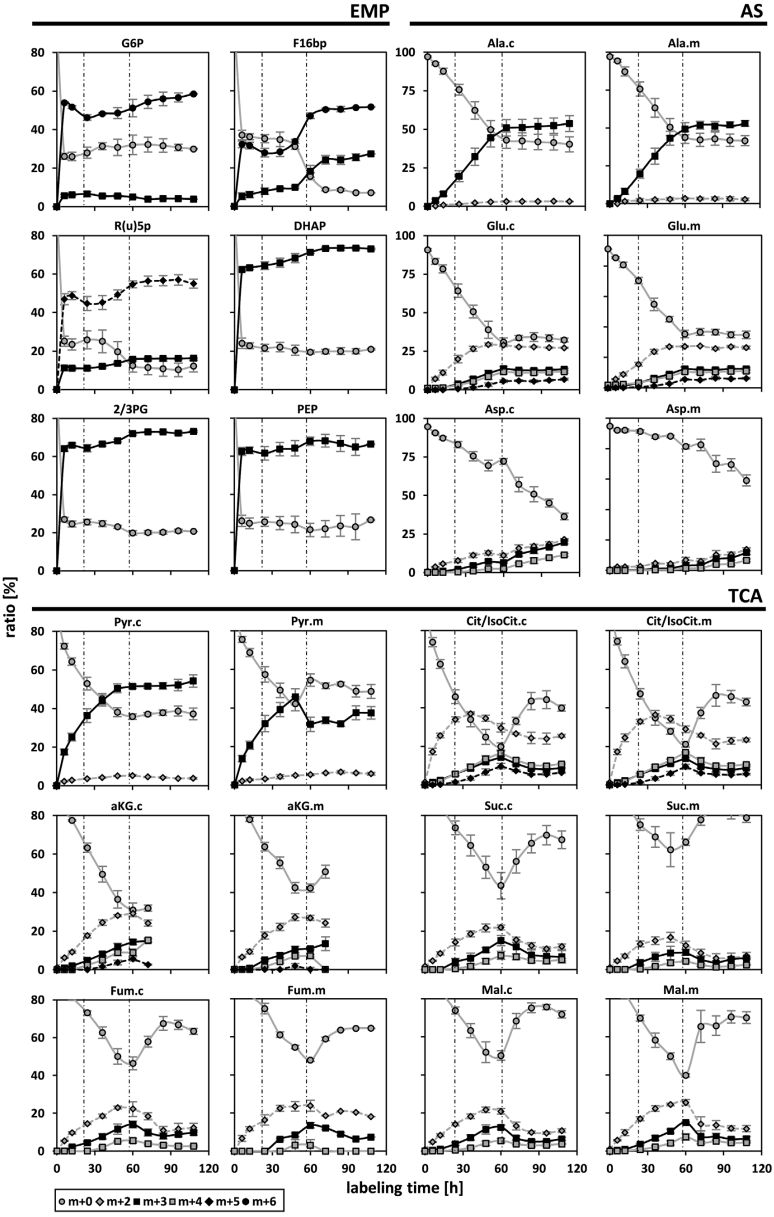

Fig. 5. Subcellular isotopic labeling dynamics of metabolites during different cultivation phases (I–III). Tracer experiments were performed as biological duplicates (n = 2) by the addition of uniformly labeled [U-^{13}C]- D-glucose (2.5 d, phase I) reaching an extracellular composition of 25% [U-^{12}C]- and 75% [U-^{13}C]- D-glucose. Mitochondrial (m) and cytosolic (c) isotopologue fractions (m + x) are listed separately as required. Mean values are based on at least two filter replicates of both [U-^{13}C] supplemented bioreactor cultivations (n = 6). Errors were calculated using standard deviations. See Table S6 for the full names of abbreviated

showed increased rates in the subsequent period. Consequently, four observation windows, I (0–24 h), II (24–48 h), III.1 (48–60 h), and III.2 (60–168 h) were used for ^{13}C flux analysis (Table S4). With this approach, reduced chi-squares (χ^2_{mod}) were calculated as 6.7, 2.06, 1.14, and 8.18 in the modeling phases I, II, III.1, and III.2, respectively. Table S3 indicates a high degree of confidence (95% accuracy) in metabolic flux predictions, because the statistically expected χ^2 values were far greater than the calculated χ^2_{mod} values.

4. Discussion

4.1. Elucidating compartment-specific metabolomics

Systemic analysis necessarily needs to consider transcriptional, translational and post-translational regulation and its coupling to metabolism to gain a comprehensive understanding of cellular regulation and physiology. In this context, compartment-specific metabolomics is key to achieving a spatially resolved understanding of metabolism. To date, FRET-based nucleotide analysis (Imamura et al., 2009) and immunopurification of epitope-tagged mitochondria have facilitated compartment-specific analyses of mammalian cells (Chen et al., 2016). However, such protocols require laborious cell preparations and conditioning, which are likely to interfere with cellular metabolism thereby allowing only snapshots of distinct metabolic conditions. The current approach differs fundamentally because it offers a time series of compartment-specific metabolic data that mirrors the transient aspects of growth physiology without affecting cellular metabolism. Accordingly, metabolic dynamics are unraveled reflecting the time-resolved complex interactions of metabolic adjustment on extracellular stimuli.

Based on preliminary studies of Matuszczyk et al. (2015) and using the current approach, physically intact mitochondria were investigated via differential fast-filtration, and results were qualified with the compartment-specific internal standards cisAco (mitochondrion), G6P, and F6P (cytosol). As indicated in Fig. S2, the markers met the expectations to enable further analyses of the time series.

Compartment-specific metabolite pool calculations demand cytosolic and mitochondrial volume measurements. The common method of using confocal microscopy (Chen et al., 2016; Jakobs, 2006) requires treatment with mitochondrial-specific dyes such as 10-N nonyl-acridine orange (Gallet et al., 1995) or MitoTracker Red 580 (Feng et al., 2005), necessitating incubations that affect the highly dynamic mitochondrial network. To prevent this impact, cells were immediately fixed and analyzed via TEM. The resulting volumetric fractions agreed well with those of former studies in CHO or human INS-1E cell lines (Dewey and Fuhr, 1976; Gerencser et al., 2012) and were remarkably stable across the process phases. The targeted liquid chromatography-tandem mass spectrometry (LC-MS/MS) method of Teleki et al. (2015) enabled a comprehensive and simultaneous quantitative analysis of central carbon, amino acid, and energy metabolism via a single analytical platform with high sensitivity and selectivity. This approach could be expanded to track the labeling of [U-^{13}C]- D-glucose in the cytosolic and mitochondrial compartments. The measured mitochondrial volume fractions led to the accurate and precise determination of compartment-specific volumetric pool sizes and subcellular metabolite distributions, irrespective of the physiological state of the cells. Additionally, a newly developed LC-MS/MS protocol, adapted from previously published quantitative derivatization studies (Zimmermann et al., 2014), enabled reliable analysis of the subcellular pool concentrations of highly reactive α-keto acids (e.g., Pyr).

4.2. Subcellular central metabolism dynamics

Key features of the central metabolism flux dynamics derived from ^{13}C-MFA with four modeling phases (Table S4) are illustrated in Figs. S4 and S5. Flux results are summarized in Fig. 6A. During phases I and II, D-glucose uptake and L-lactate secretion were the highest, with levels of approximately 0.11–0.12 pmol/cell/h and about 0.12–0.13 pmol/cell/h, respectively. The labeling kinetics of glycolysis and pentose phosphate pathway intermediates demanded a consideration of the fueling flux for carbon storage (e.g., glycogen). The assumption of a storage flux fGlyco (Fig. S4) enable a proper fit of the labeling patterns. Accordingly, about 8% of total D-glucose (0.01 pmol/cell/h) was continuously exchanged with non-labeled glycogen, as long as D-glucose was present in excess in phases I, II, and III.1. With an ample D-glucose supply, glycolytic flux is known to be tightly controlled by three key enzymes, hexokinase (HK), phosphofructokinase (PFK) and pyruvate kinase (PK), with HK believed to exert the greatest metabolic control (Mulukutla et al., 2010; Neermann and Wagner, 1996; Wahrheit et al., 2014). Accordingly, allosteric flux control may be exerted by pools of G6P (product of HK), ATP (substrate of HK, substrate and allosteric inhibitor of PFK, and product of PK), ADP and AMP (both activators of PFK), F16bp (product and allosteric inhibitor of PFK), PEP (substrate of PK), NADH (inhibitor of PFK), and Cit (inhibitor of PFK). During phases I and II, all levels of these components persisted along with G6P showing the largest pool size (Fig. 3) based on equally high D-glucose uptake rates. During the same period, oxidative PPP remained constant at 0.0044 pmol/cell/h, which indicates a remarkably low D-glucose uptake fraction (about 4%) (Ahn and Antoniewicz, 2011). Again, this finding agrees with the constant levels of PPP sugars observed (R(u)5p, Fig. 3). Apparently, cellular NADPH demands were met by high malic enzyme (ME) fluxes (Fig. S4) and not by oxidative PPP activity (Templeton et al., 2013; Ahn and Antoniewicz, 2011).

Pyruvate dehydrogenase (PDH) and citrate synthase (CS) converted approximately 0.09 and 0.10 pmol/cell/h during phases I and II, which is the equivalent of about 40% of the consumed D-glucose. At the same time, L-lactate formation occurred at about 0.13 pmol/cell/h, indicating that recognized overflow metabolism (the 'Warburg effect') reduced the incoming glycolytic and anaplerotic fluxes of the cytosolic pyruvate pool by about 29 and 33% during phases I and II. As L-asparagine became limited, metabolic patterns of glycolytic intermediates changed significantly, except for that of G6P (Figs. 3 and 5). D-Glucose uptake and L-lactate secretion rates decreased equally by approximately 25% during phase III.1, which suggested a similar glycolytic flux reduction via PFK. This was apparently the consequence of product inhibition resulting from a ten-fold increase in F16bp levels and decrease in inhibition because of falling cytosolic Cit and ATP levels. Concomitantly, the PPP/glycolysis split ratio increased to about 25% during phase III, accompanied by increasing R(u)5p pool sizes (Figs. 3 and 4). Although the glycolytic changes may still be qualified as moderate, immense flux changes occurred in TCA, as shown by the doubling in the CS flux with nitrogen starvation in phase III.2. Related changes were apparently not induced by glycolysis but by changing Pyr availability, among other parameters.

4.3. Pyruvate, the Link between Glycolysis and TCA

The cytosolic Pyr pool is an important metabolic node connecting glycolysis and the TCA cycle, as well as amino acid and fatty acid metabolism (Vacanti et al., 2014). As depicted in Fig. S4, fluxes via PDH mirrored D-glucose uptake levels well, whereas fluxes via pyruvate carboxylase (PC) revealed steady declines from phases I to III.1. Observations under the ample nutrient conditions of phase I agree well with the findings of Sheikholeslami et al. (2013), which indicated that the majority of Pyr is derived from glycolysis (about 69%), and the remaining from cytosolic ME 1. The mitochondrial Pyr pool fueled the TCA cycle via PDH producing AcCoA and PC producing OAA in approximately equal proportions. Notably, the latter fraction was severely reduced with L-glutamine limitations and even inverse with continued L-asparagine depletion during phase III.2. Concomitantly, anaplerotic fueling fluxes via ME 1 showed a similar reduction, which explained the total loss of subcellular Pyr pools accompanied by the moderately decreased turnover rates (18%) compared to those in phase I (Fig. 3).

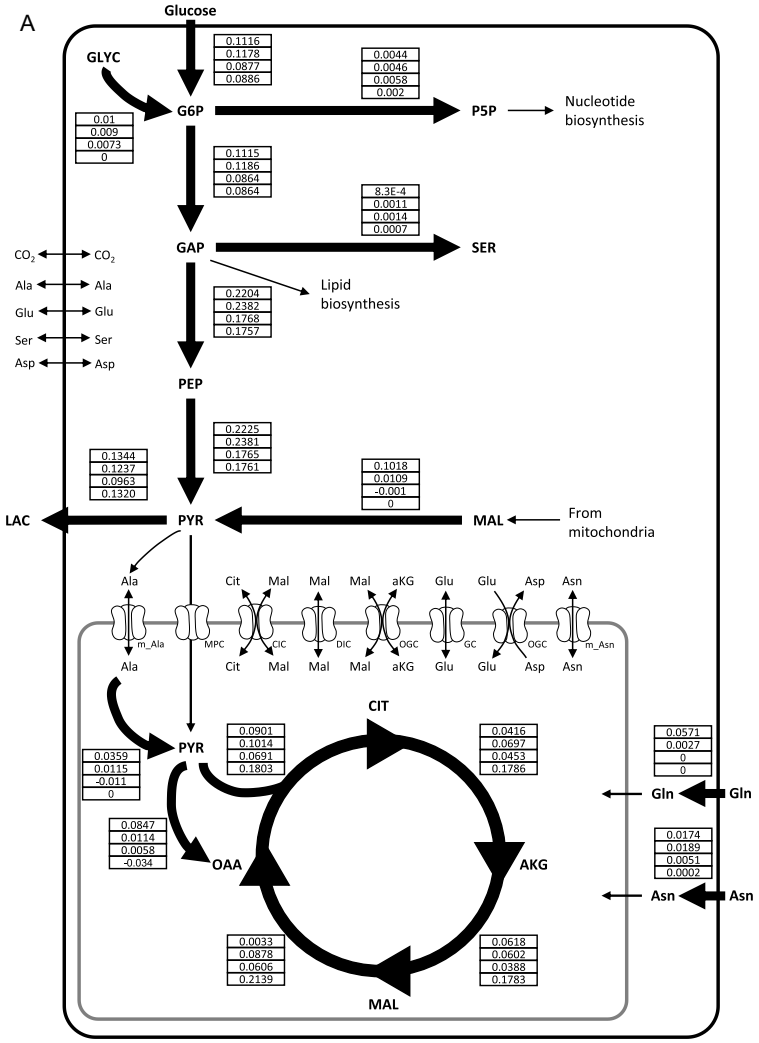

Fig. 6. Flux distributions of reactions and shuttle systems interconnecting the cytosol and mitochondria during different modeling phases (I–III.2). (A) Flux map of the compartmented central carbon metabolism in CHO-DP12. Time-variant intra- and extracellular molar flow rates (arrows) (pmol/cell/h) are depicted in a tabular form for all modeling phases (top-down, I-III.2). **(B)** Simplified map of time-variant (I-III.2) mitochondrial shuttle fluxes comprising transporters and directly associated subcellular metabolite pools. The citrate-pyruvate shuttle system (green) consists of a Pyr/H^+ symporter (*mitochondrial pyruvate carrier*, MPC), Cit/H^+-Mal antiporter (*citrate carrier*, CIC), and Mal/HPO_4^{2-} antiporter (*dicarboxylate carrier*, DIC), as well as three mitochondrial (*pyruvate dehydrogenase*, PDH; *citrate synthase*, *CS*; *pyruvate carboxylase*, PC) and three cytosolic (*citrate lyase*, ACLY; *NADH-dependent malate dehydrogenase*, MDH 1; *NADP-dependent malic enzyme*, ME 1) enzymes. The partially overlapping malate-aspartate shuttle system (blue) consists of a Mal/aKG (*2-oxoglutarate carrier*, OGC) and Glu/H^+-Asp (*aspartate glutamate carrier*, AGC) antiporter, as well as two mitochondrial- and cytosol-specific enzymes (*aspartate transaminase*, ASAT; *malate dehydrogenase*; MDH). The Glu/H^+ symporter (*glutamate carrier*, GC) and two putative mitochondrial carriers (*alanine transporter*, m_Ala; *asparagine transporter*, m_Asn) are additionally depicted. See Table S6 for the full names of abbreviated metabolites. (For interpretation of the references to colour in this figure legend, the reader is referred to the Web version of this article.)

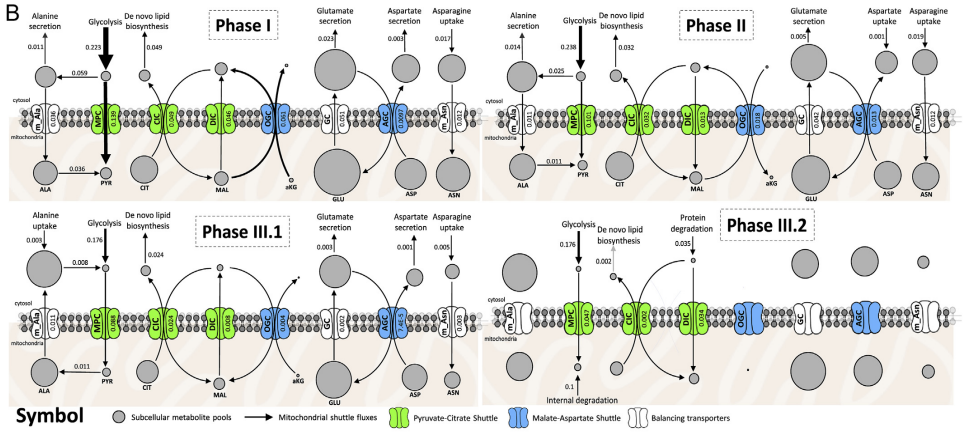

Fig. 6. (*continued*)

Studies on pancreatic beta-cells and liver and kidney cells (Heart et al., 2009; Joseph et al., 2006; Pongratz et al., 2007; Scaduto and Davis, 1986) have indicated that Pyr recycling plays an important role in equilibrating the redox equivalents NADH and NADPH. For example, NADPH formation is achieved via the citrate-pyruvate shuttle, which links phosphate-dependent mitochondrial Mal export (DIC) with NADPH and Pyr formation via cytosolic ME 1. Concomitantly, mitochondrial Cit is exported via the exchange of cytosolic Mal (CIC) and then metabolized to cytosolic Pyr by the enzymes aconitase (ACO1), citrate lyase (ACLY), NADH-dependent malate dehydrogenase (MDH1), and NADP-dependent ME 1 (Ronnebaum et al., 2006) (Figs. 2 and 6). Alternatively, mitochondrial IsoCit is exported via an exchange with cytosolic Mal (CIC) and converted to cytosolic aKG by a NADP-dependent isocitrate dehydrogenase (IDH1). Cytosolic aKG, in turn, can be transported to mitochondria (OGC) and metabolized to Mal via the mitochondrial TCA cycle by the partially overlapping malate-aspartate shuttle (Heart et al., 2009; Luo et al., 2015). Lastly, cytosolic Pyr is imported to mitochondria via an H^+-dependent symport (MPC) and refuels the TCA cycle through PDH, PC, or mitochondrial ME 2/3 (Fig. 2). Obviously, Pyr cycling is tightly linked to mitochondrial shuttle activities, which were further analyzed by exploiting compartment-specific ^{13}C labeling patterns.

4.4. *In vivo* mitochondrial shuttle activities

The *in vivo* dynamics of mitochondrial shuttle systems modeled in phases I–III.2 are depicted in Fig. 6B. With an ample nutrient supply in phase I, the Pyr/H^+ symporter of the citrate-pyruvate shuttle (MPC1/2) bore the brunt of mitochondrial import at 0.139 pmol/cell/h. Notably, this rate was about 30% higher than the D-glucose uptake rate and more than double the rates of the second-best Mal/aKG antiporter (OGC). Referred to the glycolytic influx cytosolic Pyr pools turned over by approximately 43% via fluxes to the mitochondria. Almost equivalent fluxes converted Pyr to Lac via lactate dehydrogenase (LDH), while the rest underwent a cytosolic transaminase reaction to Ala, which partially entered the mitochondria via an unknown importer (m_Ala) based on the ^{13}C labeling analysis (Figs. 5 and 6).

With overflow metabolism (Fig. 6A and B), the Cit/H^+-Mal antiporter (CIC) served as a Cit/H^+ exporter (0.049 pmol/cell/h) driven by the high mitochondrial Cit/Mal ratio (Fig. 4). As a result, cytosolic AcCoA was available as a precursor for fatty acid synthesis (Joseph et al., 2006) and OAA was available for Pyr recycling via MDH and ME 1. Notably, NADPH formation of the citrate-pyruvate shuttle outcompeted synthesis via oxidative PPP by a factor of 12.5 and was responsible for about 1/3 of the Pyr pool turnover (Fig. S4). This finding specifies earlier observations of Templeton et al. (2013) and Ahn and Antoniewicz (2011) suggesting a high malic enzyme activity without compartment specific resolution. Our flux results underscore the abovementioned cellular strategy for NADPH production via cytosolic ME 1 and glycolytic NAD^+ regeneration via cytosolic MDH and LDH during phase I. The dicarboxylate carrier (DIC) served as a Mal exporter (0.046 pmol/cell/h) and met the high demand for cytosolic Mal.

By analogy, the malate-aspartate shuttle predominately operated as a Mal/aKG antiporter (OGC), exporting mitochondrial Mal and outcompeting the amino acid exchange of Glu/Asp (AGC1/2) by a factor of 6. OGC is known as a bidirectional shuttle that is driven by concentration gradients (LaNoue and Schoolwerth, 1979; Lu et al., 2008). Flux directions were confirmed by considering the proportionality between non-equilibrium thermodynamic driving forces (affinity) and shuttle fluxes (Van der Meer et al., 1980) (Table S5). As such, the malate-aspartate shuttle enables high mitochondrial TCA activity by fueling aKG and supports the citrate-pyruvate shuttle for cytosolic NADPH formation and NAD^+ regeneration by achieving a Mal net export of 0.058 pmol/cell/h. Interesting enough, this flux scenario coincided with the highest cell specific IgG1 productivity of about 6.4 ± 0.9 pg/cell/day and an anaplerotic fueling flux via ME 1 of about 0.1 pmol/cell/h (Fig. 7). Apparently, net Mal export and high NADPH formation via cytosolic malic enzyme supported monoclonal antibody formation such that related values outcompeted those of phases II and III manifold. In summary, mitochondrial shuttle systems enabled maximum TCA activity and respiration in parallel with optimum NADH and NADPH supply under ample nutrient conditions. In other words, high shuttle activities ensured that key metabolic and production demands of growing cells were met.

The L-glutamine limitation of phase II (Fig. 6B) diminished overall shuttle activities by about 20–40%, except for those of the Glu/H^+-Asp antiporter (AGC1/2) and glutamate carrier (GC). AGC1/2 links mitochondrial Asp export with cytosolic Glu/H^+ import. GC, in turn, exports Glu/H^+ according to an increasing cytosolic/mitochondrial imbalance (Palmieri, 2008). Cytosolic Glu pools decreased due to the missing L-glutamine influx (Fig. 3). However, mitochondrial Glu uptake by AGC rose by about 34%, indicating that the antiport system is not

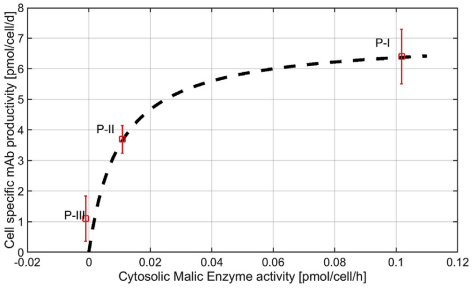

Fig. 7. Comparison of cell specific IgG1 productivities vs. cytosolic malic enzyme activities (fluxes) during different cultivation phases (I–III). The Michaelis-Menten type correlation outlines a maximum productivity $q_{mAB,max}$ of 7 pmol/cell/d and a half-saturation constant K_M = 0.01 pmol/cell/h. Mean values of measured IgG1 titers (P-I to III) are based on four bioreactor cultivations (n = 4). Errors were calculated using standard deviations.

concentration but membrane potential dependent (Dawson, 1979; LaNoue and Williamson, 1971; Meijer and van Dam, 1974). Growth limitation during phase II led to a reduction in anabolic NADPH demands, which in turn severely reduced cytosolic fueling fluxes via MDH and ME 1. The cytosolic/mitochondrial NADH ratio increased from 1.8 to 8.9, coinciding with a sharply reduced mitochondrial Cit/Mal ratio (Fig. 4 and Table 1). Consequently, cytosolic Mal was net reimported (0.027 pmol/cell/h) to translocate cytosolic NADH to mitochondria. This was mainly achieved by a 70% reduction in mitochondrial Mal export via OGC and, interesting enough, by the inversion of DIC, which now served as an importer. Through these means, physiological AECs were further maintained (Table 1). However, flux changes coincided with severely reduced cell specific productivities (Fig. 7).

The L-asparagine limitation and nitrogen starvation in phase III.1 and III.2 (Fig. 6A and B) were reflected in a severe reduction of shuttle transports, in agreement with reduced pool sizes that still showed the highest rates of Pyr import via MPC1/2. However, Mal import decreased further, TCA fluxes declined, and, strikingly, Ala was exported to the cytosol for the first time. Rising amino acid levels (Fig. 3) and diluted labeling patterns of TCA metabolites and amino acids (Fig. 5) suggested that non-labeled carbon sources other than D-glucose, L-glutamine, and L-asparagine must have been supplied. The ^{13}C flux analysis revealed that non-labeled proteinogenic and lipid resources must have been accessed, fueling degradation products for TCA via Suc, Mal, and Fum. In other words, cells initiated an autophagy program to survive extreme nitrogen and starting carbon starvation. Shuttle transporters almost entirely ceased functioning, but TCA metabolism and respiration continued at high level to minimize the drop in ATP (Fig. 4) while glycolytic activity significantly decreased (Fig. S4). Not surprisingly, cell specific productivities were found to be the lowest of the cultivation (Fig. 7).

4.5. Identifying metabolic engineering targets for optimizing IgG1 production

Compartment-specific metabolic flux analysis outlined the positive correlation between cell-specific mAB productivity and cytosolic malic enzyme activity (Fig. 7). Maximum values were achieved under ample carbon and nitrogen supply (phase I) requiring a maximum net Mal export from the mitochondrion into the cytosol to serve NADPH needs for anabolism. Any reduction of nitrogen and/or carbon supply deteriorated the mAB productivity which unravels the apparent demand to install proper substrate supply for achieving maximum product formation rates. Additionally, the Michaelis-Menten type correlation (Fig. 7) outlines that the production potential of the current CHO producer has not been fully exploited, yet. Clearly, $\partial q_{mAB}/\partial v_{ME,cyt}$, i.e. the sensitivity of q_{mAB} with respect to cytosolic malic enzyme fluxes ($v_{ME,cyt}$), is highest under limited nitrogen supply reflecting low undersaturated conditions (phase 2). Apparently, non-metabolic regulation regimes gain importance the better the metabolic precursor, ATP and NADPH supply is. Consequently, research studies should focus on additional impact factors such as protein folding, translocation and secretion once sufficient metabolic precursor supply is ensured.

5. Conclusion

The experimental and analytical approach allowed a time-resolved compartment-specific study of metabolism and shuttle dynamics of CHO cells. Subcellular investigations revealed cellular survival strategies to adapt the cellular metabolism to severely changing nitrogen and carbon availability. Under ample D-glucose and amino acid supply, L-lactate secretion was maximal, as well as activities of the citrate-pyruvate (MPC1/2, DIC, CIC) and malate-aspartate shuttles (OGC, AGC). As a consequence, a well-balanced cytosolic NADH, NADPH, and AcCoA supply, coinciding with high mitochondrial TCA activity, was established. Because most shuttling activities are concentration driven, said activities decreased with limited L-glutamine. However, adaptations were coordinated tightly, as indicated by the interplay between OGC and DIC to ensure a proper supply of malate, also comprising inverted DIC shuttling. Even when the cellular autophagy program was initiated, mitochondrial ATP levels persisted, and Mal exchange and Pyr import into mitochondria continued which assigns key roles of mitochondrial/cytosolic interaction to these metabolites.

In terms of metabolic engineering the findings disclose novel strain engineering perspectives putting proper L-glutamine supply in the focus: The switch from mitochondrial malate net-export to malate net-import coincided with diminishing L-glutamine supply and reduced NADPH formation – and, maybe most important, with a severe reduction of cell specific IgG1 productivities. Given that L-glutamine auxotrophic cells (this study) and cell lines with active glutamine synthase are alternatively used as production hosts, proper L-glutamine supply becomes an optimization goal. This question is further intertwined with product formation kinetics which may show growth coupled or non-growth coupled properties thereby requiring more or less NADPH for growth. In this study, net Mal export from mitochondria to the cytosol, reflecting proper L-glutamine supply, was essential to achieve highest cell specific productivities. Additionally, sufficient respiratory ATP formation should be installed to ensure high cell specific productivities. As a result, L-glutamine supply, NADPH and ATP availability and growth capacities are tightly coupled and affect the product formation kinetics. Additionally, the results show that total productivity control shifts to metabolic engineering targets 'downstream' of precursor supply the better the substrate availability is. Given that current production cells are typically optimized with respect to protein processing the question occurs whether such strains need revisiting of central metabolism to fully exploit the inherent potential. Consequently, detailed systems metabolic engineering studies are needed to enable model-based cell engineering.

Author contributions

L.J. and M.B. designed and conducted the 12/13C experiments.

L.J. and A.T. developed, designed, and conducted compartment-specific 12/13C metabolomics.

L.J. and M.S. conducted the TEM analyses.

A.W.W. and L.J. designed and conducted the 13C MFA experiments.

R.T. supervised the project.

L.J., A.T., A.W.W., and R.T. wrote the manuscript.

Declaration of interests

The authors declare no competing interests.

Acknowledgments

The author would like to acknowledge the Insilico Biotechnology AG team (Klaus Mauch and Waldemar Reusch) and Richard Schäfer for their help in setting up the simulation platform. Parts of the studies presented have been financed by the German Federal Ministry of Education and Research (grant number: 031L0077A, BMBF, Berlin, Germany).

Appendix A. Supplementary data

Supplementary data to this article can be found online at https://doi.org/10.1016/j.ymben.2019.02.005.

References

Ahn, W.S., Antoniewicz, M.R., 2011. Metabolic flux analysis of CHO cells at growth and non-growth phases using isotopic tracers and mass spectrometry. Metab. Eng. 13, 598–609.

Alano, C.C., Tran, A., Tao, R., Ying, W., Karliner, J.S., Swanson, R.A., 2007. Differences among cell types in NAD(+) compartmentalization: a comparison of neurons, astrocytes, and cardiac myocytes. J. Neurosci. Res. 85, 3378–3385.

Alberts, B., Johnson, A., Lewis, J., Raff, M. (Eds.), 1989. Molecular Biology of the Cell. Garland Pub., New York.

Altamirano, C., Paredes, C., Cairó, J.J., Gòdia, F., 2000. Improvement of CHO cell culture medium formulation: simultaneous substitution of glucose and glutamine. Biotechnol. Prog. 16, 69–75.

Birch, J.R., Racher, A.J., 2006. Antibody production. Adv. Drug Deliv. Rev. 58 (5–6), 671–685.

Bolboacă, S.D., Jäntschi, L., Sestraş, A.F., Sestraş, R.E., Pamfil, D.C., 2011. Pearson-Fisher chi-square statistic revisited. Information 2, 528–545.

Chen, W.W., Freinkman, E., Wang, T., Birsoy, K., Sabatini, D.M., 2016. Absolute quantification of matrix metabolites reveals the dynamics of mitochondrial metabolism. Cell 166, 1324–1337.

Dawson, A.G., 1979. Oxidation of cytosolic NADH formed during aerobic metabolism in mammalian cells. Trends Biochem. Sci. 4, 171–176.

Dewey, W.C., Fuhr, M.A., 1976. Quantification of mitochondria during the cell cycle of Chinese hamster cells. Exp. Cell Res. 99, 23–30.

DiMauro, S., Schon, E.A., 2003. Mitochondrial respiratory-chain diseases. N. Engl. J. Med. 348, 2656–2668.

Ecker, D.M., Jones, S.D., Levine, H.L., 2015. The therapeutic monoclonal antibody market. mAbs 7 (1), 9–14.

Feng, J., Lucchinetti, E., Ahuja, P., Pasch, T., Perriard, J.C., Zaugg, M., 2005. Isoflurane postconditioning prevents opening of the mitochondrial permeability transition pore through inhibition of glycogen synthase kinase 3 beta. Anesthesiology 103, 987–995.

Fernandez, C.A., Des Rosiers, C., Previs, S.F., David, F., Brunengraber, H., 1996. Correction of 13C mass isotopomer distributions for natural stable isotope abundance. J. Mass Spectrom. 31, 255–262.

Gallet, P.F., Maftah, A., Petit, J.M., Denis-Gay, M., Julien, R., 1995. Direct cardiolipin assay in yeast using the red fluorescence emission of 10-N-nonyl acridine orange. Eur. J. Biochem. 228, 113–119.

Gerencser, A.A., Chinopoulos, C., Birket, M.J., Jastroch, M., Vitelli, C., Nicholls, D.G., Brand, M.D., 2012. Quantitative measurement of mitochondrial membrane potential in cultured cells: calcium-induced de- and hyperpolarization of neuronal mitochondria. J. Physiol. 590, 2845–2871.

Gaughan, C.L., 2016. The present state of the art in expression, production and characterization of monoclonal antibodies. Mol. Divers. 20 (1), 255–270.

Goudar, C., Biener, R., Boisart, C., Heidemann, R., Piret, J., deGraaf, A., Konstantinov, K., 2010. Metabolic flux analysis of CHO cells in perfusion culture by metabolite balancing and 2D [13C,1H] COSY NMR spectroscopy. Metab. Eng. 12, 138–149.

Gray, M.W., Burger, G., Lang, B.F., 1999. Mitochondrial evolution. Science 283, 1476–1481.

Hammerschmidt, N., Tscheliessnig, A., Sommer, R., Helk, B., Jungbauer, A., 2014. Economics of recombinant antibody production processes at various scales: industry-standard compared to continuous precipitation. Biotechnol. J. 9 (6), 766–775.

Heart, E., Cline, G.W., Collis, L.P., Pongratz, R.L., Gray, J.P., Smith, P.J., 2009. Role for malic enzyme, pyruvate carboxylation, and mitochondrial malate import in glucose-stimulated insulin secretion. Am. J. Physiol. Endocrinol. Metab. 296, E1354–E1362.

Henderson, J.W., Brooks, A., 2010. Improved Amino Acid Methods Using Agilent ZORBAX Eclipse Plus C18 Columns for a Variety of Agilent LC Instrumentation and Separation Goals. Agilent Technologies, Wilmington, DE. http://www.chem.agilent.com/Library/applications/5990-4547EN.pdf.

Imamura, H., Nhat, K.P., Togawa, H., Saito, K., Iino, R., Kato-Yamada, Y., Nagai, T., Noji, H., 2009. Visualization of ATP levels inside single living cells with fluorescence resonance energy transfer-based genetically encoded indicators. Proc. Natl. Acad. Sci. 106, 15651–15656.

Jakobs, S., 2006. High resolution imaging of live mitochondria. Biochim. Biophys. Acta 1763, 561–575.

Joseph, J.W., Jensen, M.V., Ilkayeva, O., Palmieri, F., Alárcon, C., Rhodes, C.J., Newgard, C.B., 2006. The mitochondrial citrate/isocitrate carrier plays a regulatory role in glucose-stimulated insulin secretion. J. Biol. Chem. 281, 35624–35632.

Kahle, M., Schäfer, A., Seelig, A., Schultheiß, J., Wu, M., Aichler, M., Leonhardt, J., Rathkolb, B., Rozman, J., Sarioglu, H., Hauck, S.M., Ueffing, M., Wolf, E., Kastenmueller, G., Adamski, J., Walch, A., Hrabé de Angelis, M., Neschen, S., 2015. High fat diet-induced modifications in membrane lipid and mitochondrial-membrane protein signatures precede the development of hepatic insulin resistance in mice. Mol. Metab. 4, 39–50.

Kuznetsov, A.V., Veksler, V., Gellerich, F.N., Saks, V., Margreiter, R., Kunz, W.S., 2008. Analysis of mitochondrial function in situ in permeabilized muscle fibers, tissues and cells. Nat. Protoc. 3, 965–976.

Kunert, R., Reinhart, D., 2016. Advances in recombinant antibody manufacturing. Appl. Microbiol. Biotechnol. 100 (8), 3451–3461.

Kuznetsov, A.V., Margreiter, R., 2009. Heterogeneity of mitochondria and mitochondrial function within cells as another level of mitochondrial complexity. Int. J. Mol. Sci. 10, 1911–1929.

LaNoue, K.F., Williamson, J.R., 1971. Interrelationships between malate-aspartate shuttle and citric acid cycle in rat heart mitochondria. Metabolism 20, 119–140.

LaNoue, K.F., Schoolwerth, A.C., 1979. Metabolite transport in mitochondria. Annu. Rev. Biochem. 48, 871–922.

Leaver, C.J., Hack, E., Forde, B.G., 1983. Protein synthesis by isolated plant mitochondria. Methods Enzymol. 97, 476–484.

Logan, D.C., 2006. The mitochondrial compartment. J. Exp. Bot. 58, 1225–1243.

Lu, M., Zhou, L., Stanley, W.C., Cabrera, M.E., Saidel, G.M., Yu, X., 2008. Role of the malate-aspartate shuttle on the metabolic response to myocardial ischemia. J. Theor. Biol. 254, 466–475.

Luo, X., Li, R., Yan, L.J., 2015. Roles of pyruvate, NADH, and mitochondrial complex I in redox balance and imbalance in ??-cell function and dysfunction. J. Diabetes Res. 2015, 512618.

Maier, K., Hofmann, U., Reuss, M., Mauch, K., 2008. Identification of metabolic fluxes in hepatic cells from transient 13C-labeling experiments: Part II. Flux estimation. Biotechnol. Bioeng. 100, 355–370.

Matuszczyk, J.C., Teleki, A., Pfizenmaier, J., Takors, R., 2015. Compartment-specific metabolomics for CHO reveals that ATP pools in mitochondria are much lower than in cytosol. Biotechnol. J. 10, 1639–1650.

Meijer, A.J., van Dam, K., 1974. The metabolic significance of anion transport in mitochondria. Biochim. Biophys. Acta 346, 213–244.

Morrison, C., Lähteenmäki, R., 2017. Public biotech in 2016—the numbers. Nat. Biotechnol. 35 (7), 623.

Mullard, A., 2012. Can next-generation antibodies offset biosimilar competition? Nat. Rev. Drug Discov. 11, 426–428.

Mulukutla, B.C., Khan, S., Lange, A., Hu, W.S., 2010. Glucose metabolism in mammalian cell culture: new insights for tweaking vintage pathways. Trends Biotechnol. 28, 476–484.

Mycielska, M.E., Patel, A., Rizaner, N., Mazurek, M.P., Keun, H., Patel, A., Ganapathy, V., Djamgoz, M.B., 2009. Citrate transport and metabolism in mammalian cells: prostate epithelial cells and prostate cancer. Bioessays 31, 10–20.

Nargund, S., Qiu, J., Goudar, C.T., 2015. Elucidating the role of copper in CHO cell energy metabolism using (13)C metabolic flux analysis. Biotechnol. Prog. 31, 1179–1186.

Newmeyer, D.D., Ferguson-Miller, S., 2003. Mitochondria: releasing power for life and unleashing the machineries of death. Cell 112, 481–490.

Neermann, J., Wagner, R., 1996. Comparative analysis of glucose and glutamine metabolism in transformed mammalian cell lines, insect and primary liver cells. J. Cell. Physiol. 166, 152–169.

Nicolae, A., Wahrheit, J., Nonnenmacher, Y., Weyler, C., Heinzle, E., 2015. Identification of active elementary flux modes in mitochondria using selectively permeabilized CHO cells. Metab. Eng. 32, 95–105.

Niklas, J., Sandig, V., Heinzle, E., 2011. Metabolite channeling and compartmentation in the human cell line AGE1.HN determined by 13C labeling experiments and 13C metabolic flux analysis. J. Biosci. Bioeng. 112, 616–623.

O'Brien, K.M., Sidell, B.D., 2000. The interplay among cardiac ultrastructure, metabolism and the expression of oxygen-binding proteins in Antarctic fishes. J. Exp. Biol. 203, 1287–1297.

Palmieri, F., 2008. Diseases caused by defects of mitochondrial carriers: a review. Biochim. Biophys. Acta 1777, 564–578.

Palmieri, F., 2013. The mitochondrial transporter family SLC25: identification, properties and physiopathology. Mol. Aspect. Med. 34, 465–484.

Palmieri, F., 2014. Mitochondrial transporters of the SLC25 family and associated diseases: a review. J. Inherit. Metab. Dis. 37, 565–575.

Pfizenmaier, J., Matuszczyk, J.C., Takors, R., 2015. Changes in intracellular ATP-content of CHO cells as response to hyperosmolality. Biotechnol. Prog. 31 (5), 1212–1216.

Pongratz, R.L., Kibbey, R.G., Shulman, G.I., Cline, G.W., 2007. Cytosolic and mitochondrial malic enzyme isoforms differentially control insulin secretion. J. Biol. Chem. 282, 200–207.

Ronnebaum, S.M., Ilkayeva, O., Burgess, S.C., Joseph, J.W., Lu, D., Stevens, R.D., Becker, T.C., Sherry, A.D., Newgard, C.B., Jensen, M.V., 2006. A Pyruvate cycling pathway involving cytosolic NADP-dependent isocitrate dehydrogenase regulates glucose-stimulated insulin secretion. J. Biol. Chem. 281, 30593–30602.

Scaduto Jr., R.C., Davis, E.J., 1986. The involvement of pyruvate cycling in the metabolism of aspartate and glycerate by the perfused rat kidney. Biochem. J. 237, 691–698.

Schafer, F.Q., Buettner, G.R., 2001. Redox environment of the cell as viewed through the redox state of the glutathione disulfide/glutathione couple. Free Radic. Biol. Med. 30,

1191–1212.
Schaub, J., Mauch, K., Reuss, M., 2008. Metabolic flux analysis in Escherichia coli by integrating isotopic dynamic and isotopic stationary 13C labeling data. Biotechnol. Bioeng. 99, 1170–1185.
Scheffler, I.E., 2001. A century of mitochondrial research: achievements and perspectives. Mitochondrion 1, 3–31.
Schmidt, K., Carlsen, M., Nielsen, J., Villadsen, J., 1997. Modeling isotopomer distributions in biochemical networks using isotopomer mapping matrices. Biotechnol. Bioeng. 55, 831–840.
Schwenke, W.D., Soboll, S., Seitz, H.J., Sies, H., 1981. Mitochondrial and cytosolic ATP/ADP ratios in rat liver in vivo. Biochem. J. 200, 405–408.
Sengupta, N., Rose, S.T., Morgan, J.A., 2011. Metabolic flux analysis of CHO cell metabolism in the late non-growth phase. Biotechnol. Bioeng. 108, 82–92.
Sheikh, K., Förster, J., Nielsen, L.K., 2005. Modeling hybridoma cell metabolism using a generic genome-scale metabolic model of Mus musculus. Biotechnol. Prog. 21, 112–121.
Sheikholeslami, Z., Jolicoeur, M., Henry, O., 2013. Probing the metabolism of an inducible mammalian expression system using extracellular isotopomer analysis. J. Biotechnol. 164, 469–478.
Stein, L.R., Imai, S., 2012. The dynamic regulation of NAD metabolism in mitochondria. Trends Endocrinol. Metabol. 23, 420–428.
Sun, J., Aluvila, S., Kotaria, R., Mayor, J.A., Walters, D.E., Kaplan, R.S., 2010. Mitochondrial and plasma membrane citrate transporters: discovery of selective inhibitors and application to structure/function analysis. Mol. Cell. Pharmacol. 2, 101–110.
Taymaz-Nikerel, H., de Mey, M., Ras, C., ten Pierick, A., Seifar, R.M., van Dam, J.C., Heijnen, J.J., van Gulik, W.M., 2009. Development and application of a differential method for reliable metabolome analysis in Escherichia coli. Anal. Biochem. 386, 9–19.
Teleki, A., Sánchez-Kopper, A., Takors, R., 2015. Alkaline conditions in hydrophilic interaction liquid chromatography for intracellular metabolite quantification using tandem mass spectrometry. Anal. Biochem. 475, 4–13.
Templeton, N., Dean, J., Reddy, P., Young, J.D., 2013. Peak antibody production is associated with increased oxidative metabolism in an industrially relevant fed-batch CHO cell culture. Biotechnol. Bioeng. 110 (7), 2013–2024.
Unseld, M., Marienfeld, J.R., Brandt, P., Brennicke, A., 1997. The mitochondrial genome of Arabidopsis thaliana contains 57 genes in 366,924 nucleotides. Nat. Genet. 15, 57–61.
Urschel, M.R., O'Brien, K.M., 2008. High mitochondrial densities in the hearts of Antarctic icefishes are maintained by an increase in mitochondrial size rather than mitochondrial biogenesis. J. Exp. Biol. 211, 2638–2646.
Vacanti, N.M., Divakaruni, A.S., Green, C.R., Parker, S.J., Henry, R.R., Ciaraldi, T.P., Murphy, A.N., Metallo, C.M., 2014. Regulation of substrate utilization by the mitochondrial pyruvate carrier. Mol. Cell. 56, 425–435.
Van der Meer, R., Westeroff, H.V., Van Dam, K., 1980. Linear relation between rate and thermodynamic force in enzyme-catalyzed reactions. Biochim. Biophys. Acta 591, 488–493.
Venable, J.H., Coggeshall, R., 1965. A simplified lead citrate stain for use in electron microscopy. J. Cell Biol. 25, 407–408.
Vielhauer, O., Zakhartsev, M., Horn, T., Takors, R., Reuss, M., 2011. Simplified absolute metabolite quantification by gas chromatography-isotope dilution mass spectrometry on the basis of commercially available source material. J. Chromatogr. B Analyt. Technol. Biomed. Life. Sci. 879, 3859–3870.
Wahrheit, J., Niklas, J., Heinzle, E., 2014. Metabolic control at the cytosol-mitochondria interface in different growth phases of CHO cells. Metab. Eng. 23, 9–21.
Walsh, G., 2014. Biopharmaceutical benchmarks 2014. Nat. Biotechnol. 32 (10), 992.
Wiechert, W., 2001. 13C metabolic flux analysis. Metab. Eng. 3, 195–206.
Wurm, F.M., 2004. Production of recombinant protein therapeutics in cultivated mammalian cells. Nat. Biotechnol. 22 (11), 1393.
Young, J.D., 2014. INCA: a computational platform for isotopically non-stationary metabolic flux analysis. Bioinformatics 30, 1333–1335.
Zimmermann, M., Sauer, U., Zamboni, N., 2014. Quantification and mass isotopomer profiling of alpha-keto acids in central carbon metabolism. Anal. Chem. 86, 3232–3237.

Paper II

A transhydrogenase-like mechanism in CHO cells comprising concerted cytosolic reaction and mitochondrial shuttling activities

Andy Wiranata Wijaya & Ralf Takors

Biochemical Engineering Journal 170 (2021) 107986

Contents lists available at ScienceDirect

Biochemical Engineering Journal

journal homepage: www.elsevier.com/locate/bej

Short communication

A transhydrogenase-like mechanism in CHO cells comprising concerted cytosolic reaction and mitochondrial shuttling activities

Andy Wiranata Wijaya, Ralf Takors *

Institute of Biochemical Engineering, University of Stuttgart, Stuttgart, Germany

ARTICLE INFO

Keywords:
Chinese hamster ovary
Metabolism
Malate
Mitochondrial shuttle
Transhydrogenase

ABSTRACT

The proper supply and regeneration of reduction equivalents such as NADH and NADPH is of pivotal importance for living cells. Although both, NADH and NADPH, are electron carriers, they serve for different, complementing needs and require well balanced exchange. In Chinese hamster ovary (CHO) cells, the proton translocator 'Nicotinamide Nucleotide Transhydrogenase' (NNT) was annotated recently, but no *in vivo* operational evidence was given, yet. Here, we present another transhydrogenase-like mechanism building on the adaptive interplay of cytosolic malate dehydrogenase (MDH_{cyt}) and cytosolic malic enzyme (ME_{cyt}) with the mitochondrial shuttles citrate carrier (CIC), dicarboxylate carrier (DIC), and mitochondrial pyruvate carrier (MPC). The system is highly flexible using malate and pyruvate as intermediary electron carriers and quickly adapts to current needs. Indications for the existence of the mechanism are found in different monoclonal antibody producing CHO cell lines and under growing and stationary conditions.

1. Introduction

The proper supply and regeneration of reducing equivalents such as NADH and NADPH is pivotal for living cells. Under aerobic conditions, oxidation of NADH is the dominant source of free Gibbs energy. 220 kJ/$mole_{NADH}$ are provided oxidizing NADH to create the thermodynamic driving force for anabolism. Basically, the latter is stored in ATP. On contrary, NADPH serves as an electron donor in anabolic reduction steps. Hence, NADH and NADPH are crucial pyridine nucleotide electron carriers in cellular metabolism, serving completely different; but complementary needs [1].

In mammalian cells, such as Chinese hamster ovary (CHO) cells, the primary NADH sources are found in cytosolic glycolysis and the mitochondrial citric acid cycle. Regeneration of NAD^+ from NADH predominantly occurs via two mechanisms: the cytosolic reduction of pyruvate to lactate via lactate dehydrogenase (LDH) and the fueling of NADH electrons into the electron transport chain of the inner mitochondrial membrane-bound oxidative phosphorylation. Besides, NADPH is oxidized in multiple biosynthetic steps, including the formation of recombinant proteins. The proper supply of NADPH in IgG1 producing cells has been identified as a key metabolic engineering target for optimizing, e.g., monoclonal antibodies production [2]. Anabolic reactions are predominately located outside the mitochondria.

Proliferating cells tend to maintain low NADH/NAD^+ ratios to ensure high glycolytic fluxes [3,4]. Conversely, NADPH/$NADP^+$ ratio remains relatively high to provide sufficient electrons for biosynthetic pathways [5,6]. Mammalian cells may maintain preferred NADH/NAD^+ ratios by controlling lactate dehydrogenase (LDH) activity. By analogy, cytosolic NADPH/$NADP^+$ ratios could be regulated by finetuning activities of the cytosolic, $NADP^+$ dependent enzymes Glucose-6-phosphate dehydrogenase, 6-phosphogluconate dehydrogenase, and malic enzyme [2,7–9].

The proper installation of NADH/NAD^+ and NADPH/$NADP^+$ ratios is crucial for achieving metabolic homeostasis [10]. Whereas the measures mentioned above focus on individual NADH/NAD^+ and NADPH/$NADP^+$ ratios, pro- and eukaryotic cells may use an additional tool: the so-called transhydrogenase enzyme. In essence, cytosolic and membrane-bound enzymatic activities often catalyze the reaction from NADH + $NADP^+$ to NAD^+ + NADPH and *vice versa*, respectively. Recently, Nesci et al. reported the enzyme structure of mitochondrial nicotinamide nucleotide transhydrogenase (NNT) in mammalian cells. [11]. Moreover, a similar proton-translocator encoding cytosolic NNT was annotated in the CHO genome [12]. However, experimental *in vivo*

Abbreviations: CIC, citrate carrier; CHO, Chinese hamster ovary; DIC, dicarboxylate carrier; LDH, lactate dehydrogenase; MDH, malate dehydrogenase; ME, malic enzyme; MPC, mitochondrial pyruvate carrier; NNT, Nicotinamide nucleotide transhydrogenase; PCS, Pyruvate-Citrate Shuttle; PMS, Pyruvate-Malate Shuttle.

* Corresponding author at: Institute of Biochemical Engineering, University of Stuttgart, Allmandring 31, 70569, Stuttgart, Germany.
E-mail address: ralf.takors@ibvt.uni-stuttgart.de (R. Takors).

https://doi.org/10.1016/j.bej.2021.107986
Received 22 October 2020; Received in revised form 1 February 2021; Accepted 2 March 2021
Available online 13 March 2021

evidences of NNT operations in cytosol and mitochondrion are missing, still.

The examples have in common that redox reaction pairs are located in a single compartment. However, eukaryotes offer the possibility to perform oxidation/reduction reactions involving several reaction steps, even crossing membrane barriers, as depicted in Fig. 1. One example may be the so-called pyruvate-citrate shuttle (PCS) comprising the mitochondrial pyruvate carrier (MPC) and the citrate/malate antiporter (CIC). PCS was anticipated to convert NADH into NADPH, utilizing malate as an electron carrier during insulin production [13]. Fig. 1 elucidates that said system might be extended to a trans-compartment transhydrogenase-like function by integrating the pyruvate-malate shuttle (PMS). However, further experimental evidence is missing, still.

Here, we give evidence to another multi-compartment, transhydrogenase-like mechanism building on the adaptive interplay of cytosolic malate dehydrogenase (MDH_{cyt}), cytosolic malic enzyme (ME_{cyt}), and the intermediate electron carriers malate and pyruvate. Whereas pyruvate is always imported into mitochondrion, malate will be shown to be im- or exported depending on the cytosolic needs. Noteworthy, the existence was confirmed under *in vivo* conditions. Conclusions were based on intracellular flux distributions already provided in Junghans et al. (2019) and in Verhagen et al. [2,14]. Said independent studies focused on the two CHO cell lines DP12 and BIBH1 under similar cultivation conditions, supporting the existence of the transhydrogenase-like mechanism in CHO.

2. Materials and methods

2.1. Cell culture

Cell cultivations were performed under similar conditions using two different Chinese hamster ovary cell lines: CHO DP-12 (ATCC® CRL-1445™) and BIBH1 (Boehringer Ingelheim Pharma GmbH & Co. KG, Biberach, Germany). All cells were cultivated using TC-42 medium (Xell AG, Bielefeld, Germany). Four (4) mM L-glutamine and 200 nM of metrotrexate (Sigma-Aldrich, Steinheim, Germany) were supplemented in both experiments. Seed train were performed in a disposable sterile shake flask (Corning, Inc., USA) in a humidified and incubated rotary shaker (Infors HT, Germany) at 37 °C, 150 rpm with 50 mm displacement, and 5% CO2.

CHO DP-12 cultivation was performed by Junghans et al. (2019) using tracer glucose [U-^{13}C]-D-glucose in two bioreactors (n = 2) with pH, temperature and DO control [2]. Whereas BIBH1 cultivation was performed by Verhagen et al. (2020) without using tracer carbon in disposable shake flasks mentioned above with two biological replicates (n = 2) [14]. Details are reported in Junghans et al. (2019) and Verhagen et al. (2020).

2.2. Analytics

During the cultivations, Viable Cell Densities (VCD), exo- and endometabolomes were measured as reported in Junghans et al. (2019) and Verhagen et al. [2,14]. Additionally, changes of intracellular mass isotopomers of about 20 metabolites were monitored using an Agilent 1200 HPLC system coupled with an Agilent 6410B triple quadrupole mass spectrometer with an electrospray ion source (ESI; Agilent Technologies, Waldbronn, Germany). Details of the analytical procedures are given in Junghans et al. (2019) and Verhagen et al. (2020) [2,14].

2.3. Intracellular flux estimation

Isotopically-non-stationary ^{13}C-Metabolic Flux Analysis (^{13}MFA) was used to estimate intracellular flux distributions in CHO DP-12 cells. Details of the metabolic model and the fitting procedure were described in Junghans et al. (2019) [2]. In the case of BIBH1 cell line, FBA was used to predict intracellular flux distributions using measured extracellular rates as additional constraints Verhagen et al. (2020) [14].

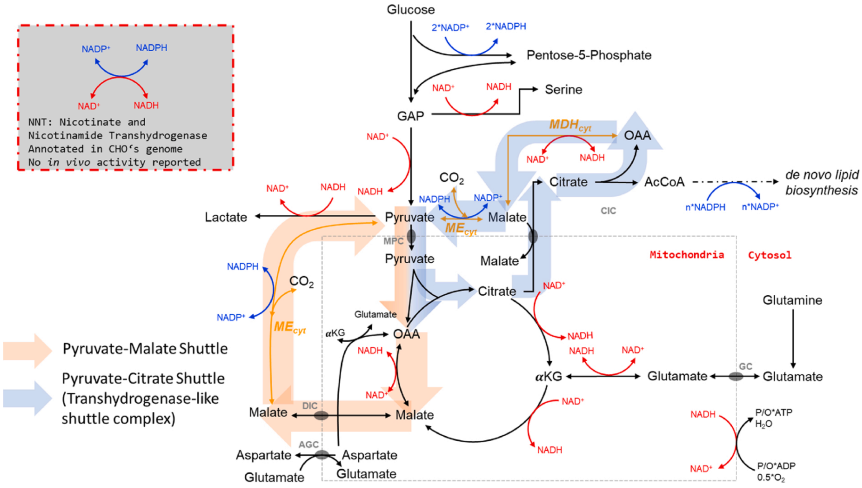

Fig. 1. Primary sources and sinks of NAD(H) and NADP(H) in CHO cells' central carbon metabolism. Malate serves as electron carrier. Orange (Pyruvate-Malate Shuttle): Mitochondrial electrons from oxaloacetate (OAA) and NADH are transferred to cytosolic NADPH via cytosolic malic enzyme (ME_{cyt}). Blue (Pyruvate-Citrate Shuttle): Cytosolic electrons from OAA and NADH are charged on malate via cytosolic malate dehydrogenase (MDH_{cyt}) and translocated to cytosolic NADPH via cytosolic malic enzyme (ME_{cyt}). Consequently, orange Pyruvate-Malate-Shuttle provides trans-compartment transhydrogenase activity. The blue Pyruvate-Citrate-Shuttle provides cytosolic transhydrogenase activity.

2.4. NADH and NADPH generation

NADH generation was calculated by using equation (1)

$$v_{NADH_{cyt},\,prod} = v_{GAPdh} + v_{ldh,rev} + v_{mdh,cyt} \quad (1)$$

$$v_{NADH_{mit},\,prod} = v_{idh} + v_{adh} + v_{mdh,mit} + v_{gdh}$$

Cytosolic NADH generation was calculated with equation (2).

$$v_{NADPH_{cyt},prod} = 2 \times v_{G6Pdh} + v_{me,cyt} \quad (2)$$

3. Results and discussion

Results base on already published data of Junghans et al. (2019) and Verhagen et al. (2020) which were reconsidered for further evaluation [2,14] (see Supplementary Material 2 for complete intracellular flux distribution). Notably, Junghans et al. (2019) performed compartment-specific metabolomics and ^{13}C MFA, which allowed to elucidate mitochondrial shuttle activities *in vivo* via data-driven metabolic flux analysis. The pioneering data are compared with the results of Verhagen et al. (2020), who studied the impact of L-Prolyl-L-Tyrosine (PY) addition on the metabolism of CHO BIBH1. PY amplified the cell-specific glucose uptake rate in the BIBH1 cell line while maintaining the lactate secretion rate. Thus, more carbon was fueled into mitochondria finally yielding different citric acid cycle activities. BIBH1 is an industry based IgG1-producer which demonstrated higher glucose uptake rates and IgG1 cell specific productivity compared to the CHO-DP12 cell line. Accordingly, the two independent data sets reflect similar cultivation conditions but different glycolytic and mitochondrial activities in CHO cells. In this sense, they serve as independent measurements challenging the hypothesis that the interplay of selected mitochondrial shuttle activities provides transhydrogenase-like mechanisms in CHO.

3.1. CHO cells' transhydrogenase-like mechanism

One of the central findings of Junghans et al. (2019) was the identification of the cytosolic malic enzyme (ME_{cyt}) as the primary source of cytosolic NADPH [2]. Notably, related NADPH formation was 12.5-fold higher than NADPH production via the oxidative pentose phosphate pathway in exponentially growing cells. The observation confirmed former hypothesis of Ahn & Antoniewicz (2011) and Templeton et al. (2013), who anticipated that Glucose-6-phosphate dehydrogenase is not the only and dominating source of NADPH [7,15].

Recently, the use of deuterated glucose tracers disclosed the conversion of serine to glycine inside mitochondria by methylene tetrahydrofolate dehydrogenase (MTHFD2/MTHFD2L) as an important mitochondrial source of NADPH [16]. Further evidences for transhydrogenase-like mechanisms were not found although recent findings indicated the existence of active mitochondrial nicotinamide nucleotide transhydrogenase (NNT [11],).

As a further step of data evaluation, we now wondered which electron donors are used to fuel cytosolic NADPH formation via cytosolic malic enzyme. We compared flux patterns of CHO-DP12 and BIBH1 being aware of the different modelling approaches for flux map identification but still wondering about the occurrence of common flux schemes. Interestingly, we found indications for common transhydrogenase-like activities as shown in Fig. 2(a–c)). Reevaluating the measured fluxes, we identified the NADH + $NADP^+$/NAD^++NADPH regeneration scheme depicted in Fig. 2(a–c). Fluxes varied within the observed range as depicted in Fig. 2d. Interesting enough, we observed transhydrogenase-like activity without requiring any distinct

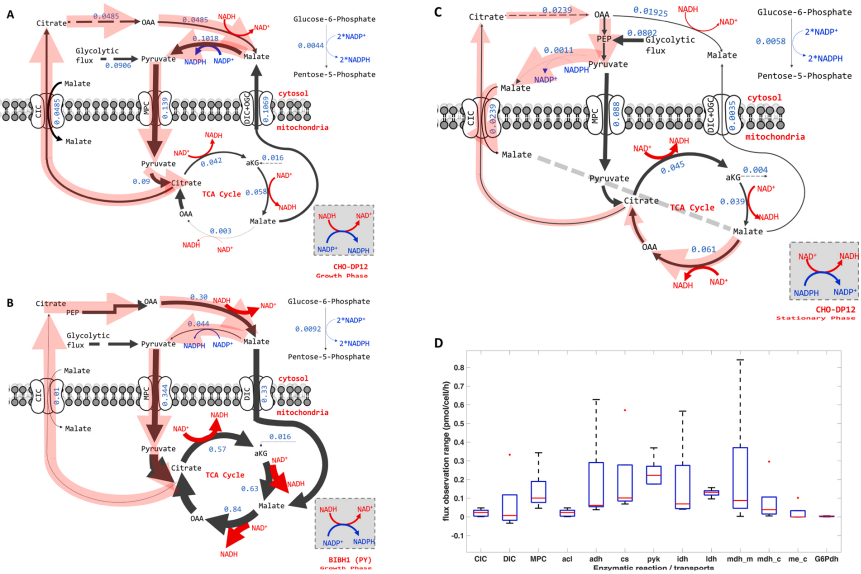

Fig. 2. Transhydrogenase-like mechanisms (highlighted with reddish background) during (A) growth phase of CHO-DP12; (B) growth phase of BIBH1; and (C) stationary phase of CHO-DP12 cells. Each figure indicates flux distribution including mitochondrial shuttles. (D) Observed flux ranges derived from different data sets still supporting the transhydrogenase-like mechanism in two different CHO cell lines (CHO-DP12 and BIBH1). Flux estimates (in pmol $cell^{-1}$ h^{-1}) were derived from experimental duplicates.

transhydrogenase gene such as the annotated NNT.

The two enzymatic protagonists of the transhydrogenase-like mechanism in CHO cells are the MDH_{cyt} and the ME_{cyt}. In brief, MDH_{cyt} catalyzes electron donation by oxidizing NADH to provide the electrons for the reduction of $NADP^+$ in ME_{cyt}. The scenario in Fig. 2a investigating CHO DP12 cells unravels that the majority of NADPH is provided by said mechanism identifying 0.0433 $pmol_{NADPH}$ $cell^{-1}$ h^{-1} via MEcyt and only 0.0044 $pmol_{NADPH}$ $cell^{-1}$ h^{-1} via phosphate pathway. The intermediate electron carrier of cytosolic NADPH formation is malate. Malate was already identified as a key shuttling metabolite during the exponential growth of CHO tightly linking mitochondrial and cytosolic activities via the Malate/Aspartate shuttle [2]. As indicated in Fig. 2a, pyruvate and malate enter the mitochondrion, the first via the mitochondrial pyruvate carrier (MPC) and the second via net interaction of the exporting dicarboxylate shuttle (DIC) and the importing citrate/malate antiporter (CIC). Note that DIC's direction may shift serving as mitochondrial malate exporter in Fig. 2a and as malate importer in Fig. 2b. This underlines the flexibility of the DIC shuttle emphasizing the dual function of malate: Malate export from mitochondrion supports NADPH demands under growth conditions whereas malate import into mitochondrion finally fuels the citric acid cycle. CIC and MPC always function in the same direction importing malate and pyruvate into mitochondrion. Once taken up, both metabolites enter the citric acid cycle, are oxidized to produce NADH which is finally respired to gain ATP. Although malate is net exported into cytosol in Fig. 2a and net imported into mitochondrion in Fig. 2b, predominant cytosolic NADPH formation still happens via ME_{cyt}. Malate and pyruvate serve as intermediate electron carriers in both cases, net importing electrons into mitochondrion predominately via pyruvate using MPC.

Revisiting the data of Verhagen et al. (2020), the same transhydrogenase-type regeneration of NADH + $NADP^+$/ NAD^++NADPH gets obvious, although for opposite needs: Now, the interplay of MDH_{cyt} with ME_{cyt} consumed NADPH which has been produced in the pentose-phosphate pathway. Consequently, malate could be net imported into mitochondrion. CIC mediated malate import outcompeted DIC export. Apparently, the nutrient limiting conditions of scenario in Fig. 2c did not require extraordinary amounts of NADPH for anabolic demands. Instead, there was a higher need for ATP which was fulfilled by oxidizing NADH generated from citric acid cycle activity.

Summarizing, each of the scenarios in Fig. 2a–c gives evidence for the existence of a two-compartment transhydrogenase-like mechanism. The interplay comprises cytosolic MDH_{cyt} and ME_{cyt}, the trans-compartment electron carriers: pyruvate and malate, and the mitochondrial citric acid cycle producing NADH. Reaction and shuttle activities adapt to the current needs of NADPH and NADH which are showcased by the flux maps in Fig. 2a-c. Interesting enough, the common scheme occurs in different cell lines and under different growth conditions covering wide ranges of flux distributions (Fig. 2d). Notably, the wide range of the most flux distribution indicated in Fig. 2d was mainly due to the different experimental setups (bioreactor vs shaking flask), cell lines, conditions, and metabolic states. As an example, high variability of citric acid cycle activities was caused by the PY boost in BIBH1 cell line compared to the reference state of DP12 cell line.

3.2. Transhydrogenase activity in CHO cells

Fig. 3 summarizes compartment-specific production and consumption of NADH and NADPH for the flux scenarios Fig. 2a–c. To be precise: the NADPH producing fluxes via pentose phosphate pathway, cytosolic malic enzyme (ME_{cyt}), and the transhydrogenase-like mechanism are balanced with estimated anabolic demands. Cytosolic and mitochondrial NADH formation and consumption are balanced by analogy considering respiration as gap filling sink (see Fig. 3). During exponential growth, ME_{cyt} fluxes of CHO-DP12 were approximately 0.1 $pmol_{Malate}$ $cell^{-1}$ h^{-1}. 43 % of the produced NADPH originated from the interaction with MDH_{cyt}, i.e., from cytosolic NADH. Considering the entire NADPH formation, including the pentose phosphate pathway, 41 % of total cytosolic NADPH was derived from cytosolic NADH. In the case of BIBH1, the trend was even more pronounced unravelling almost all of the NADPH was supplied from 'transhydrogenase-based' activity. As already outlined in Fig. 2(c), no NADPH was formed via ME_{cyt} under severe nutrient limitation. The related support to NADH formation via reversed ME_{cyt} accounted for less than 1% of total NADH (value too small for indication in Fig. 3).

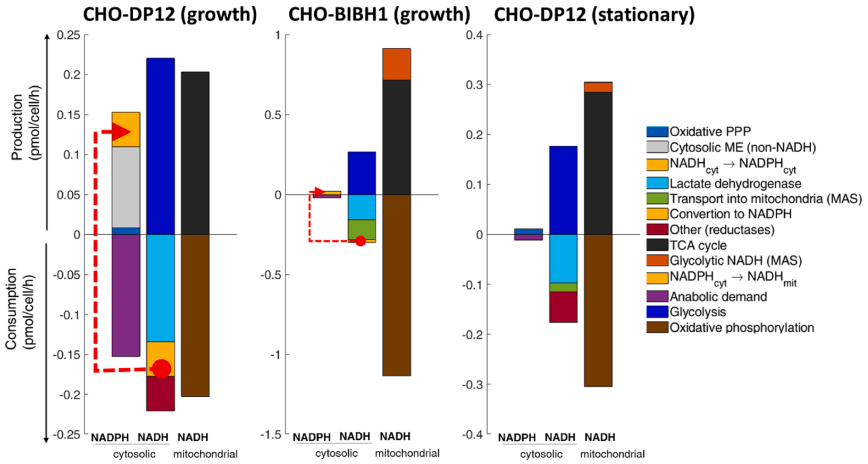

Fig. 3. Production (upper part) and consumption (lower part) of NADPH and NADH assigned to cytosol and mitochondrion and calculated for different cells: CHO-DP12 (left: growing; right: stationary) and CHO-BIBH1 (middle: growing). Different origins and sinks for NADH and NADPH are color encoded as listed in the legend. The dashed red line indicates the electron flows in the transhydrogenase-like mechanism. Fluxes are calculated from independent ^{13}C studies already published as indicated in the text.

3.3. Evaluation of NTT activity by thermodynamic analysis

As operational NNT has not been observed yet in mammalian cell experiments, we wonder why NNT's activity might be very low or even inactive. Revisiting the transhydrogenase's thermodynamic constraint (see Supplementary Material), the thermodynamic equilibrium constant (K'_{eq}) could be estimated for NNT. Comparing the K'eq with the reported *in vivo* NAD/NADH [17] ratios and NADPH/NADP ratios [18], we may conclude that NNT will mostly catalyze the transhydrogenase reaction towards the formation of NADPH. This analysis supports our observation on shuttle-based transhydrogenase with malate as the electron carrier, which majorly converted NADH into NADPH (growth phase). Nevertheless, the native existence of NNT still requires further studies.

4. Concluding remarks

Transhydrogenase activity is often found in pro- and eukaryotic cells to quickly react on changing needs of NADH and NADPH. Genome annotation already anticipates the existence of a said enzyme called NNT in CHO. However, independent ^{13}C flux studies clearly pinpoint to the existence of an additional transhydrogenase-like mechanism comprising the tight interaction of MDH_{cyt} and ME_{cyt} together with the mitochondrial pyruvate carrier (MPC) and malate-dicarboxylate carrier (DIC). The malate carrier (DIC) has shown its high flexibility to adapt to changing needs by even inverting shuttle directions. Accordingly, one may fairly anticipate that the said transhydrogenase mechanism serves as a quick, tactical measure of CHO cells to adapt NADPH needs. It remains somewhat open whether and how NNT further supports electron equilibration for the reduction equivalents. Based on our estimations, NNT is likely to support NADPH formation only. Nevertheless, the question deserves further research activities as proper NADPH may be crucial for maximizing the therapeutic proteins' anabolic formation.

CRediT authorship contribution statement

Andy Wiranata Wijaya: Conceptualization, Methodology, Software, Formal analysis, Investigation, Data curation, Writing - original draft, Visualization. **Ralf Takors:** Conceptualization, Methodology, Writing - review & editing, Supervision, Project administration, Funding acquisition.

Declaration of Competing Interest

The authors declare no financial or commercial conflict of interest.

Acknowledgement

Parts of the studies presented have been financed by the German Federal Ministry of Education and Research (grant number: 031L0077A, BMBF, Berlin, Germany).

Appendix A. Supplementary data

Supplementary material related to this article can be found, in the online version, at doi:https://doi.org/10.1016/j.bej.2021.107986.

References

[1] A.M. Hosios, M.G. Vander Heiden, The redox requirements of proliferating mammalian cells, J. Biol. Chem. 293 (20) (2018) 7490–7498.
[2] L. Junghans, A. Teleki, A.W. Wijaya, M. Becker, M. Schweikert, R. Takors, From nutritional wealth to autophagy: *in vivo* metabolic dynamics in the cytosol, mitochondrion and shuttles of IgG producing CHO cells, Metab. Eng. 54 (2019) 145–159.
[3] J.P. Schwartz, J.V. Passonneau, G.S. Johnson, I. Pastan, The effect of growth conditions on NAD and NADH concentrations and the NAD:NADH ratio in normal and transformed fibroblasts, J. Biol. Chem. 249 (1974) 4138–4143.
[4] Y. Zhao, A. Wang, Y. Zou, N. Su, J. Loscalzo, Y. Yang, In vivo monitoring of cellular energy metabolism using SoNar, a highly responsive sensor for NAD/NADH redox state, Nat. Protoc. 11 (2016) 1345–1359.
[5] R.L. Veech, L.V. Eggleston, H.A. Krebs, The redox state of free nicotinamide-adenine dinucleotide phosphate in the cytoplasm of rat liver, Biochem. J. 115 (1969) 609–619.
[6] N. Pollak, C. Dölle, M. Ziegler, The power to reduce: pyridine nucleotides–small molecules with a multitude of functions, Biochem. J. 402 (2007) 205–218.
[7] W.S. Ahn, M.R. Antoniewicz, Metabolic flux analysis of CHO cells at growth and non-growth phases using isotopic tracers and mass spectrometry, Metab. Eng. 13 (5) (2011) 598–609.
[8] J. Fan, J. Ye, J.J. Kamphorst, T. Shlomi, C.B. Thompson, J.D. Rabinowitz, Quantitative flux analysis reveals folate-dependent NADPH production, Nature 510 (2014) 298–302.
[9] L. Liu, S. Shah, J. Fan, J.O. Park, K.E. Wellen, J.D. Rabinowitz, Malic enzyme tracers reveal hypoxia-induced switch in adipocyte NADPH pathway usage, Nat. Chem. Biol. 12 (2016) 345–352.
[10] S.Y. Lunt, M.G. Vander Heiden, Aerobic glycolysis: meeting the metabolic requirements of cell proliferation, Annu. Rev. Cell Dev. Biol. 27 (2011) 441–464.
[11] S. Nesci, F. Trombetti, A. Pagliarani, Nicotinamide nucleotide transhydrogenase as a sensor of mitochondrial biology, Trends Cell Biol. 30 (1) (2020) 1–3.
[12] H. Hefzi, K.S. Ang, M. Hanscho, A. Bordbar, D. Ruckerbauer, M. Lakshmanan, V. S. Martinez, A consensus genome-scale reconstruction of Chinese hamster ovary cell metabolism, Cell Syst. 3 (5) (2016) 434–443.
[13] F. Palmieri, The mitochondrial transporter family (SLC25): physiological and pathological implications, Pflügers Archiv. 447 (5) (2004) 689–709.
[14] N. Verhagen, A.W. Wijaya, A. Teleki, M. Fadhlullah, A. Unsöld, M. Schilling, R. Takors, Comparison of L-tyrosine containing dipeptides reveals maximum ATP availability for L-prolyl-L-tyrosine in CHO cells, Eng. Life Sci. 20 (9-10) (2020) 384–394.
[15] N. Templeton, J. Dean, P. Reddy, J.D. Young, Peak antibody production is associated with increased oxidative metabolism in an industrially relevant fed-batch CHO cell culture, Biotechnol. Bioeng. 110 (7) (2013) 2013–2024.
[16] C.A. Lewis, S.J. Parker, B.P. Fiske, D. McCloskey, et al., Tracing compartmentalized NADPH metabolism in the cytosol and mitochondria of mammalian cells, Mol. Cell 55 (2) (2014) 253–263.
[17] L.R. Stein, S.I. Imai, The dynamic regulation of NAD metabolism in mitochondria, Trends Endocrinol. Metab. 23 (9) (2012) 420–428.
[18] M. Díaz-Flores, M.A. Ibáñez-Hernández, R.E. Galván, M. Gutiérrez, G. Durán-Reyes, R. Medina-Navarro, L.A. Baiza-Gutman, Glucose-6-phosphate dehydrogenase activity and NADPH/NADP+ ratio in liver and pancreas are dependent on the severity of hyperglycemia in rat, Life Sci. 78 (22) (2006) 2601–2607.

Paper III

Compartment-specific metabolome labeling enables the identification of subcellular fluxes that may serve as promising metabolic engineering targets in CHO cells

Andy Wiranata Wijaya, Andreas Ulmer, Lara Hundsdorfer, Natascha Verhagen,

Attila Teleki, & Ralf Takors

Bioprocess and Biosystems Engineering (2021) 44:2567–2578
https://doi.org/10.1007/s00449-021-02628-1

RESEARCH PAPER

Compartment-specific metabolome labeling enables the identification of subcellular fluxes that may serve as promising metabolic engineering targets in CHO cells

Andy Wiranata Wijaya[1] · Andreas Ulmer[1] · Lara Hundsdorfer[1] · Natascha Verhagen[1] · Attila Teleki[1] · Ralf Takors[1]

Received: 27 April 2021 / Accepted: 27 August 2021 / Published online: 30 September 2021

Abstract
^{13}C labeling data are used to calculate quantitative intracellular flux patterns reflecting in vivo conditions. Given that approaches for compartment-specific metabolomics exist, the benefits they offer compared to conventional non-compartmented ^{13}C flux studies remain to be determined. Using compartment-specific labeling information of IgG1-producing Chinese hamster ovary cells, this study investigated differences of flux patterns exploiting and ignoring metabolic labeling data of cytosol and mitochondria. Although cellular analysis provided good estimates for the majority of intracellular fluxes, half of the mitochondrial transporters, and NADH and ATP balances, severe differences were found for some reactions. Accurate flux estimations of almost all iso-enzymes heavily depended on the sub-cellular labeling information. Furthermore, key discrepancies were found for the mitochondrial carriers v_{AGC1} (Aspartate/Glutamate antiporter), v_{DIC} (Malate/H^+ symporter), and v_{OGC} (α-ketoglutarate/malate antiporter). Special emphasis is given to the flux of cytosolic malic enzyme (v_{ME}): it could not be estimated without the compartment-specific malate labeling information. Interesting enough, cytosolic malic enzyme is an important metabolic engineering target for improving cell-specific IgG1 productivity. Hence, compartment-specific ^{13}C labeling analysis serves as prerequisite for related metabolic engineering studies.

Keywords Compartment-specific · Metabolomics · ^{13}C Metabolic flux analysis · Chinese hamster ovary cells · Eukaryotes · Multi-compartments

Abbreviations

^{13}C MFA	^{13}C metabolic flux analysis
CHO	Chinese hamster ovary
VCD	Viable cell density
PPP	Pentose phosphate pathway
CAC	Citric acid cycle
MID	Mass isotopomer distribution
MPC1/2	Mitochondrial pyruvate carrier
ME	Malic enzyme

Symbols

c_i	pmol L^{-1} Concentration of metabolite i
c_x	cell L^{-1} Viable cell density
dof	[-] Degree of freedom
E	[-] Expected MID measurement data
f_i	[-] Cytosolic fraction of metabolite i
$\mathbf{I}$	[-] Isotopomer distribution vector
$\mathbf{IMM}$	[-] Isotopomer mapping matrices
MID	[-] Mass isotopomer distribution
n	[-] Number of measurement data
O	[-] Observed MID simulation
$\mathbf{p}$	pmol $cell^{-1}$ h^{-1} Vector containing estimated fluxes using mass-isotopomers data
p	[-] Number of fitted parameter
Q_i	pmol L^{-1} h^{-1} Feed-rate of metabolite i
q_i	pmol $cell^{-1}$ h^{-1} Cell-specific rate of exo-metabolite i
$\mathbf{q_m}$	pmol $cell^{-1}$ h^{-1} Vector containing measured extracellular rates
S	[-] Stoichiometric matrix of biochemical network
M	[-] Measurement information matrix

Andy Wiranata Wijaya and Andreas Ulmer were equally contributed for this work (first co-authorship).

✉ Ralf Takors
ralf.takors@ibvt.uni-stuttgart.de

[1] Institute of Biochemical Engineering, University of Stuttgart, Allmandring 31, 70569 Stuttgart, Germany

v_j	pmol cell^{-1} h^{-1} Intracellular flux of biochemical reaction j
v	pmol cell^{-1} h^{-1} Vector containing intracellular metabolic fluxes

Greek symbols

α	[-] Statistical confidence interval
β	[-] Reversibility constant
σ	[-] Measurement standard deviation of MID
Θ	[-] Parameter

Indices

ex	[-] Compartment indication
feed	[-] Feed
in	[-] Compartment indication
i	[-] Compound/metabolite i
j	[-] Biochemical reactions j
meas	[-] Indication for measurement vector
net	[-] Indication for net fluxes
X	[-] Cells/biomass

Introduction

^{13}C metabolic flux analysis (^{13}C MFA) is a key tool for quantitative analysis in systems metabolic engineering. First, applications dealt with prokaryotic cells [1] but the technique was also applied for eukaryotes, such as yeast [2, 3], fungi [4], mammalian [5–8], and plant [9] cells. Among others, prokaryotes and eukaryotes differ in cellular compartmentation, which is particularly important when using ^{13}C MFA. In eukaryotes, compartmentation is essential since each cellular compartment fulfils different functions [10]. Even multi-compartment isozymes exist that serve different purposes. For example, Chinese hamster ovary (CHO) cells comprise cytosolic and mitochondrial malic enzymes (MEs) with different NAD^+ and $NADP^+$ regeneration capacities, thereby fulfilling diverse catabolic and anabolic needs [8].

Metabolic compartmentation must be considered when performing ^{13}C MFA [10]. There are two levels of complexity; on the one hand, subcellular metabolic models should be used to enable proper in silico predictions. On the other hand, in vivo compartment-specific metabolome data should be available to allow data-driven studies. Nicolae et al. and Pfizenmaier & Takors provided evidence for the importance of subcellular stoichiometric models for estimating fluxes in CHO cells [11, 12]. Regarding the latter, Matuszczyk et al. [13] applied compartment-specific metabolomics in CHO outlining that cytosolic ATP pools are considerably larger than their mitochondrial counterparts. Later, Junghans et al. [8] continued investigating mitochondrial and cytosolic metabolic patterns under different cultivation conditions. They found that pool sizes differed between cytosol and mitochondria for all conditions.

Given that subcellular metabolomics are very laborious [8, 13] the question arises what differences may occur if ^{13}C flux analysis is based on whole-cell metabolomics instead of compartment-specific measurements. In other words, whether the additional lab-efforts justify the information gain of subcellular studies.

Alternative approaches such as superimposing the patterns of two independent ^{13}C experiments using labeled glucose and labeled glutamine also aim to decipher subcellular flux distributions [6]. However, they rely on glutamine synthase deficient cells whereas the suggested subcellular metabolomics approach may be universally applicable.

Given that labeling dynamics in metabolite pools expressed by the ^{13}C labeling turn-over (τ_{13C}) are a key information for quantifying fluxes, influencing factors may be considered. Two factors, pool size of metabolite i and net labeling flux j through this pool exist [14]. Either factor may change when a system's analysis shifts from simplifying single to realistic multi-compartment analysis. Differences in τ_{13C} may occur originating from individual pool sizes and fluxes inside the compartments. In theory, the same metabolite in different compartment might present a different labeling dynamic providing that the metabolite turn-over time is different. Thus, resulting on a different labeling dynamics (τ_{13C}).

Exploiting the unique subcellular labeling dataset of Junghans et al. [8] this study investigated whether subcellular labeling information is crucial to obtain the correct compartment-specific flux patterns. Flux distributions considering and ignoring subcellular metabolite labeling were performed using CHO as the showcase. This study investigated whether significant differences exist using whole-cell and compartment-specific metabolic information.

Materials and methods

This study was based on published metabolome and ^{13}C isotopologue data [8]. In particular, the ^{13}C dataset covering the first 24 h was used to focus on the exponential growth phase.

Cell culture and experimental set-up

The CHO DP-12 cell line (ATCC® CRL-1445TM) was cultivated in a suspension with TC-42 medium (Xell AG, Bielefeld, Germany) supplemented with 42 mM D-glucose, 6 mM L-glutamine, and 200 mM methotrexate. Precultures were cultivated in pre-sterilized disposable shake flasks (Corning Inc., NY, USA) with culture volume ranging from 125 mL to 1 L at an initial viable cell density (VCD) of 0.4×10^6 cells/mL in a humidified shaking incubator (Infors HT Minitron,

Infors GmbH, Einsbach, Germany) at 37 °C, 150 rpm, and 5% saturated CO_2.

Bioreactor cultivations were performed in a two-fold parallel CellFerm Pro bioreactor system (DASGIP, Eppendorf, Germany) equipped with pitched blade impellers and a process control system. Bioreactor cultivations were started with a VCD of about 0.4×10^6 cells/mL, temperature was set to 37 °C and agitation to 150 rpm. In addition, the dissolved oxygen content was controlled using an amperometric electrode (Mettler-Toledo Inc., Columbus, OH, USA) at 40%. The pH was measured with a conventional pH probe (Mettler-Toledo Inc., Columbus, OH, USA) and maintained at 7.1 using 1 M Na_2CO_3 or CO_2 gassing. Carbon labeling experiments were performed in the same setup using [U-$^{13}C_6$]-D-glucose as a carbon tracer with an average isotopic ratio of 25% [U-$^{12}C_6$]- and 75% [U-$^{13}C_6$]-D-glucose. Experiments were performed as biological duplicates. In addition to carbon labeling experiments, bioreactor cultivations with [U-$^{12}C_6$]-D-glucose were performed using the same conditions for metabolome profiling.

Extracellular and intracellular analytics

VCD was monitored with a 12 h interval with Cedex XS, an offline cell counting system (Innovatis AG, Bielefeld, Germany). Extracellular D-glucose and L-lactate were monitored offline with LaboTRACE, an amperometric biosensor system (Trace Analytics GmbH, Braunschweig, Germany). Extracellular antibody (IgG1) concentrations were measured using ELISA as reported previously [15]. Extracellular amino acid concentrations were quantified with reversed-phase chromatography (Agilent 1200 Series, Agilent Technologies, Waldbronn, Germany) [8].

Sampling for metabolomics was performed using differential fast filtration [8, 13]. Then, processed samples were analyzed regarding metabolome quantification using an Agilent 1200 HPLC system coupled with an Agilent 6410B (Agilent Technologies, Waldbronn, Germany) triple quadrupole mass spectrometer equipped with an electrospray ion source. Analytical sample preparation and methodology were conducted as reported previously [8, 16].

^{13}C metabolic flux analysis

Isotopic non-stationary ^{13}C MFA was performed in MATLAB 2018a (The MathWorks, Inc., MA, USA). Before performing ^{13}C MFA, measured ^{13}C labeling distributions were corrected for natural stable isotope abundances [17]. Parameter optimization was conducted using MATLAB least square optimization *fmincon* function in combination with *GlobalSearch* and *MultiStart* algorithm in a multi-core computing machine [18]. The first derivative of each isotopomer balance was solved using MATLAB Ordinary Differential Equations *ode15s* solver. The study used the metabolic and carbon-atom transition model in the previous study [8]. Details of the model are indicated in Table S1 (Supplementary Material S1) and are displayed in Fig. 1.

Metabolite balancing

The two-compartment CHO-cell model comprises the stoichiometric matrix S (Supplementary Material S1, Table S1) consisting of m metabolites and n reactions ($m \times n$). The following cell-specific rates [pmol cell^{-1} h^{-1}] were defined: q for cellular uptake and secretion rates, k as inter-compartment transport, and v as compartment-specific reaction. The balance of metabolite i participating in reaction j localized externally, in cytosol, or in mitochondria was described by Eqs. 1 and 2:

$$\frac{d_{c_{i,ex}}}{dt} = Q_{i,\text{feed}} + q_i c_X, \tag{1}$$

$$\frac{d_{c_{i,in}}}{dt} = \left(-q_i - k_i + \sum_{j=1}^{n} v_j \right) \cdot c_x = 0, \tag{2}$$

where c_i denotes the concentration of metabolite i [mol L^{-1}], c_x denotes VCD [cell L^{-1}], t denotes time [h], and $Q_{i,\text{feed}}$ denotes the feed-rate of metabolite i [pmol L^{-1} h^{-1}].

The process model describing the batch cultivation is given in Eq. 1 and allows the estimation of q for metabolite i by time-series analysis of extracellular concentrations c_i. Therefore, the metabolic steady-state was defined as mirrored in the constraint $\frac{d_{c,\text{intracellular}}}{dt} = 0$, which is a prerequisite for ^{13}C flux analysis. Both stationary and non-stationary labeling patterns were analyzed, originating from the metabolic steady-state condition.

Metabolic flux analysis

MFA was performed using the metabolic network S considering the following constraints: (i) pool sizes of cytosolic and mitochondrial metabolites were in a steady-state and (ii) the entire system was (over)-determined because of the ample ^{13}C labeling information. Fluxes were estimated according to:

$$v = \begin{pmatrix} S \\ M \end{pmatrix}^{-1} \begin{pmatrix} 0 \\ [\, q_{\text{meas}} \;\; p \,] \end{pmatrix}, \tag{3}$$

where M is the measurement matrix containing the stoichiometric coefficients of q_{meas} (measured rates [pmol cell^{-1} h^{-1}]) and p contains the estimated fluxes using mass-isotopomer data [pmol cell^{-1} h^{-1}]).

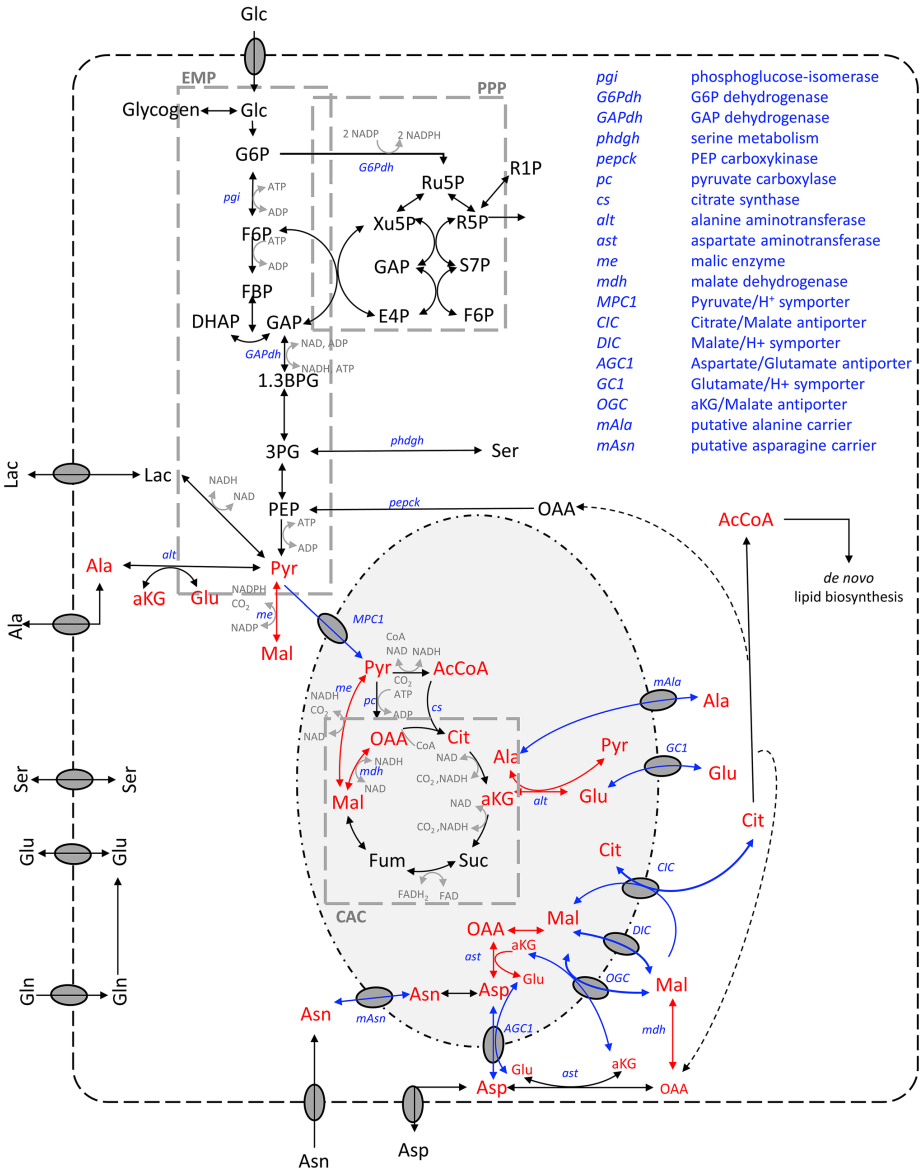

Fig. 1 Metabolic model of CHO cells used in this study (modified figure from Junghans et al. [8]). Arrow coloring indicates the localization of biochemical reactions as follows: black encodes single compartment; red encodes multi-compartments; and blue encodes inter-compartment transporters. In addition, multi-compartment metabolites are indicated in red (color figure online)

Isotopomer balancing and bidirectional reactions

Isotopomer balancing was applied to mathematically describe the incorporation of ^{13}C tracers into intracellular metabolite carbon skeletons [19, 20]. Isotopomer balances for intracellular metabolites are according to Eq. 4:

$$\frac{d(\mathbf{C}_i\mathbf{I}_i)}{dt} = \sum_{j=1}^{N}\left[\alpha\left(\bigotimes_{k=1}^{0}\left(\sum_{m=1}^{n}\mathbf{IMM}_{k\to m}\right)\mathbf{I}_k\right)r_j + (1-\alpha)\left(v_i r_j \mathbf{I}_i\right)\right]$$

with

$$\alpha = \begin{cases} 1, \text{if} v_{ij} > 0 \\ 0, \text{else} \end{cases}, \tag{4}$$

where the isotopomer transition from reactant k to product m is described by $\mathbf{IMM}_{k\to m}$.

Furthermore, Eq. 5 was used to describe labeling dilution by extracellular pools (L-lactate, L-glutamate, L-aspartate, and L-alanine):

$$\frac{d(\mathbf{I}_{i,\text{ex}})}{dt} = \frac{1}{c_{i,\text{ex}}}\left[\overline{c_X}\left(\vec{q}_{i,\text{ex}}\cdot\mathbf{I}_{i,\text{in}} - \overleftarrow{q}_{i,\text{ex}}\cdot\mathbf{I}_{i,\text{ex}}\right) - \frac{dc_{i,\text{ex}}}{dt}\mathbf{I}_{i,\text{ex}}\right]$$

with

$$\begin{aligned} \vec{q}_{i,\text{ex}} &= \beta_i \cdot q^{\text{net}}_{i,\text{ex}} \\ \overleftarrow{q}_{i,\text{ex}} &= \vec{q}_{i,\text{ex}} - q^{\text{net}}_{i,\text{ex}}. \end{aligned} \tag{5}$$

Exchange fluxes were defined for each reversible biochemical reaction [21, 22] according to Eq. 6:

$$\begin{aligned} \vec{v}_j &= \beta_j \cdot v^{\text{net}}_j \\ \overleftarrow{v}_j &= \vec{v}_j - v^{\text{net}}_j. \end{aligned} \tag{6}$$

Parameter estimation and uncertainty

Parameter (flux) estimation was achieved by fitting the simulated mass isotopomer distribution (MID) to the measured in vivo MID as presented in Eq. 7:

$$\min f(\Phi) = \sum\left(\frac{\text{MID}^{\text{sim}}_i - \text{MID}^{\text{exp}}_i}{\sigma_i}\right)^2. \tag{7}$$

Cytosolic and mitochondrial MIDs were defined for subcellular studies. Non-compartmented analysis considered that no subcellular measurements were available. Instead, only entire cell labeling patterns should exist. Consequently, compartment-specific information was merged again, applying Eq. 8:

$$\text{MID}^{\text{comb}}_i = \text{MID}^{\text{cyt}}_i \cdot f + \text{MID}^{\text{mit}}_i \cdot (1-f), \tag{8}$$

where f denotes the molar fraction of metabolite i in the cytosol. During simulations, f was treated as an optimization parameter for those metabolites presented in both compartments; pyruvate, citrate, α-ketoglutarate, malate, alanine, aspartate, asparagine, and glutamine. Accordingly, f serves as an alternate indicator for the importance of considering compartments properly. Furthermore, flux estimation was achieved by fitting the measured non-compartment metabolome data with calculated MID using Eq. 9:

$$\min f(\Phi) = \sum\left(\frac{\text{MID}^{\text{comb}}_i - \text{MID}^{\text{exp}}_i}{\sigma_i}\right)^2. \tag{9}$$

A χ^2 statistical test was used to assess goodness of fit as described in Eq. 10:

$$\begin{aligned} \chi^2 &= \sum\frac{\left(x^{\text{sim}} - x^{\text{exp}}\right)^2}{\sigma^2} \\ dof &= (n-p) \\ \chi^2 &\le \chi^2_{(1-\alpha),dof}. \end{aligned} \tag{10}$$

Parameter uncertainty is essential to evaluate the flux differences including versus excluding compartment-specific data. Conventional parameter uncertainty estimates make use of the local calculation of the Jacobian matrix as a linearized proxy for variance. However, this approach only shows poor performance if a complex and non-linear set of equations should be analyzed, as it is the case in this ^{13}C MFA study. Thus, confidence intervals of each parameter (fluxes) were estimated using the Chi-squared (χ^2) statistics, which works best for non-linear equations as demonstrated by Antoniewicz et al. [23]. The method relies on the assumption that the minimized variance-weighted sum of squared residuals is χ^2 distributed. Thus, the residual difference evaluating the global optimum and fixing one parameter is χ^2 distributed with one degree of freedom.

Statistical analysis

The significant differences between the two analyses were assessed using Welch's t-test for unequal variances [24].

Results

Prior to the ^{13}C MFA studies, a metabolic network model was formulated (Supplementary Material S1). First the structural identifiability and calculability of the network was assessed applying well established methodologies (Supplementary Material S4). Next, the identifiability of distinct

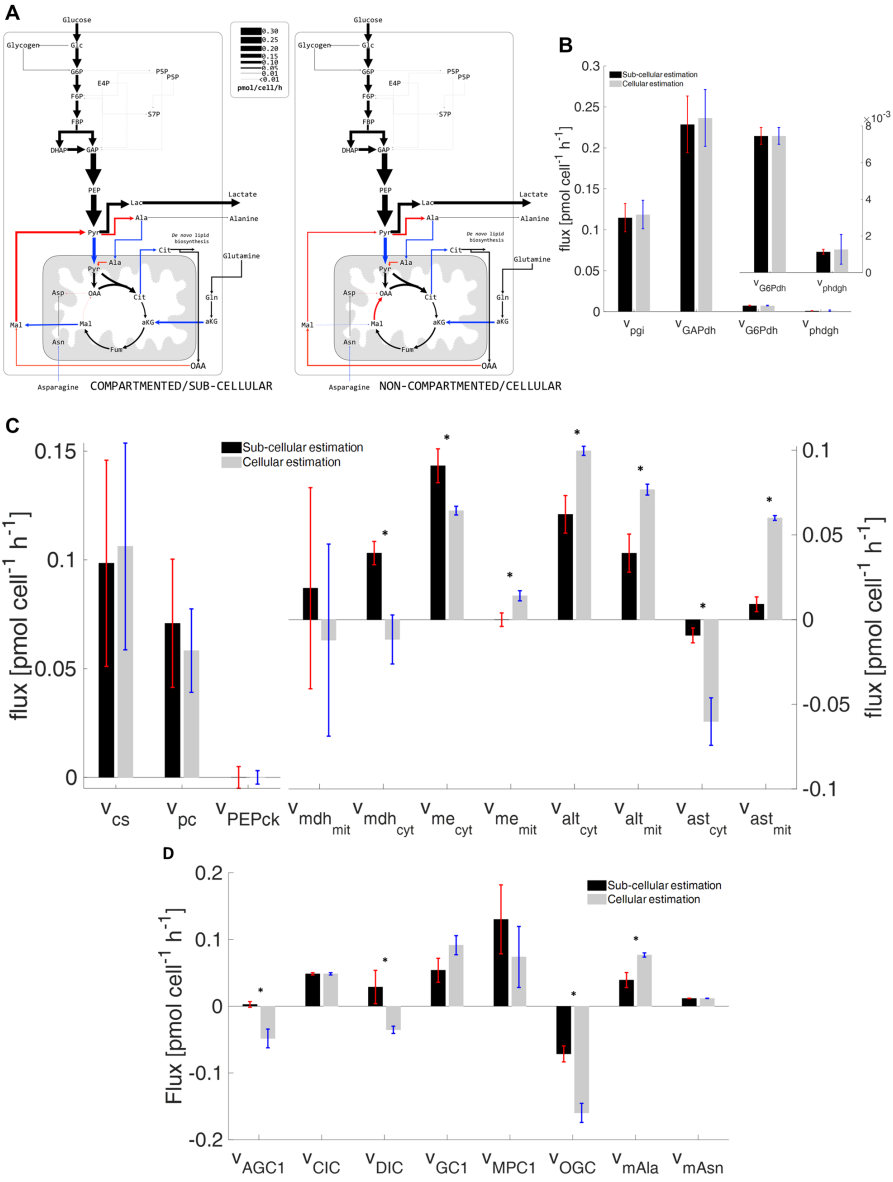
A
Glucose
Glycogen
Glc
G6P
F6P
FBP
DHAP
GAP
PSP
E4P
S7P
PEP
Pyr
Lac
Lactate
Ala
Alanine
De novo lipid biosynthesis
Cit
Glutamine
Asp
OAA
Gln
Mal
aKG
Asn
Fum
Asparagine
COMPARTMENTED/SUB-CELLULAR
NON-COMPARTMENTED/CELLULAR
pmol/cell/h
B
Sub-cellular estimation
Cellular estimation
flux [pmol cell-1 h-1]
vpgi
vGAPdh
vG6Pdh
vphdgh
C
flux [pmol cell-1 h-1]
vcs
vpc
vPEPck
vmdhmit
vmdhcyt
vmecyt
vmemit
valtcyt
valtmit
vastcyt
vastmit
D
Flux [pmol cell-1 h-1]
vAGC1
vCIC
vDIC
vGC1
vMPC1
vOGC
vmAla
vmAsn

◂**Fig. 2** **A** Intracellular flux distribution estimated using compartment-specific (left) and non-compartmented data (right); **B** fluxes of biochemical reactions involving single-compartment metabolites; **C** fluxes of biochemical reactions involving multi-compartment metabolites; and **D** mitochondrial carrier fluxes estimated with compartment-specific and non-compartmented data (* indicates significance $p < 0.05$)

fluxes was checked by simulating intracellular ^{13}C labeling patterns assuming pool sizes measured by Junghans et al. [8]. Results presented in the Supplementary Material S4 indicate the good identifiability of intracellular fluxes which motivated us to continue the study by analyzing real labeling patterns and flux distributions.

In the study by Junghans et al. [8] CHO-DP12 cells were cultivated in a bioreactor to investigate three distinct growth scenarios; (I) exponential growth with no (carbon and nitrogen) limitation; (II) moderate growth with L-glutamine depletion and L-asparagine saturation; and (III) stationary phase with severe nitrogen limitation. However, the current study regarding the impact of subcellular ^{13}C data only covers the exponential growth phase during the first 24 h. This period is typically investigated in vitro because labeling and cultivation conditions can be controlled easily, giving accurate results regarding flux distributions and cell-specific productivities [5, 7]. Furthermore, additional cultivation study data investigating the same cell line and process conditions was used for broadening the data set of subcellular versus cellular ^{13}C metabolomics for flux analysis (see Supplementary Material S6). The summary of all estimated intracellular fluxes is provided in Supplementary Material S2.

Cell growth and carbon labeling studies

During the exponential growth phase, cells grew with $0.025 \pm 0.001\ h^{-1}$. Carbon and nitrogen sources were constantly consumed, and metabolic byproducts were steadily released with constant specific rates (Supplementary Material S1, Table S2). D-Glucose was consumed as a major carbon source while L-glutamine and L-asparagine served as primary nitrogen sources. In addition, the Warburg effect [25] was observed, showing a glucose-to-lactate ratio of 0.93 $mol_{D\text{-}glucose}/mol_{L\text{-}lactate}$. ^{13}C carbon labeling was introduced by the addition of 75% [U-$^{13}C_6$]-D-glucose after 2.5 days, revealing no phenotypic changes, i.e., no alterations of cellular metabolism.

^{13}C metabolic flux analysis using compartment-specific metabolome data

^{13}C MFA was performed using compartment-specific metabolome data reflecting subcellular pools of cytosol and mitochondria together with isotopomer profiles of the said compartments. Flux estimations were performed at least 100 times with randomized input values and rational boundary values for each parameter (Supplementary Material S2). Finally, the chi-square tests achieved 228.87, which served the statistical constraint of 232.92 on a 95% significance level.

Glycolysis and PPP

High glycolytic (0.112 ± 0.017 pmol $cell^{-1}\ h^{-1}$ of hexokinase) and extremely low PPP fluxes (0.008 ± 0.001 pmol $cell^{-1}\ h^{-1}$ of G6P dehydrogenase) were found. The latter accounted for 6.68% of the D-glucose consumed. These observations are in agreement with the findings of Ahn & Antoniewicz [5], who performed ^{13}C MFA in adherent CHO-K1 cells. In addition, approximately 15% (0.016 ± 0.002 pmol $cell^{-1}\ h^{-1}$) of intracellular G6P was continuously in exchange with endogenous glycogen.

In vivo mitochondrial shuttle

Glycolytic carbon fueled into mitochondria via two transport mechanisms; 77% entered via the mitochondrial pyruvate carrier (MPC1/2) and 23% via a putative L-alanine transporter. MPC1/2 showed the highest mitochondrial transport activities while other transporters exchanged compounds for different purposes; (i) mitochondrial citrate carrier (citrate/malate antiporter; 0.049 ± 0.002 pmol $cell^{-1}\ h^{-1}$) served as a citrate exporter to provide cytosolic acetyl-CoA for the de novo lipid biosynthesis pathway; (ii) the malate-aspartate shuttle comprising 2-oxoglutarate carrier (α-ketoglutarate/mal antiporter) and aspartate-glutamate carrier (aspartate/glutamate antiporter), which is often described as an indirect NADH shuttle because imported malate is oxidized to oxaloacetate, releasing NADH, fulfilled a different function; malate was net exported from mitochondria to fuel cytosolic ME.

Cytosolic malic enzyme and NADPH production

NADPH is a key electron donator for anabolic pathways and is essential for monoclonal antibody biosynthesis. Ahn & Antoniewicz, Templeton et al. [5, 7] suggested MEs as key NADPH producers in CHO cells. This hypothesis was further confirmed via compartment-specific flux analysis by Junghans et al. [8]. Cytosolic ME (ME_{cyt}) was identified as

the primary provider serving NADPH needs. Compartment-specific ^{13}C MFA estimated that about 86% of the NADPH requirement was fulfilled by ME_{cyt} (0.09 ± 0.01 pmol cell^{-1} h^{-1}).

^{13}C Metabolic flux analysis using non-compartmented metabolome data

An additional ^{13}C MFA was performed to investigate the importance of distinct sub-cellular information to elucidate proper in vivo subcellular flux patterns. Analyzing the merged data (Eq. 6) via ^{13}C MFA yielded a Chi-squared value of 140.12 on the 95% confidence level, which was accepted as a good fit (with 154.30 as the χ^2 statistical threshold on 95% confidence interval).

This study was performed using the same model consisting of 42 intracellular biochemical reactions. Figure 2A provides the comparison of intracellular flux distributions estimated with (left) and without (right) sub-cellular information (Fig. 2A). The related single-compartment key fluxes and iso-enzymatic rates are depicted as bar plots in Fig. 2B, C. Notably, the term 'iso enzymes' encodes fluxes connecting the same substrates and products but localized in different compartments.

Biochemical reactions localized in a single compartment

Figure 2B, C left shows fluxes of biochemical reactions that exist in one compartment (cytosol or mitochondria) only. Most of them revealed similar results irrespective of whether compartment-specific information was used (black) or not (gray). Figure 2B demonstrates the case the metabolome pools and the respective fluxes were the same for both studies, yielding a similar τ_{13C}. This is also true for citrate synthase v_{CS}, although identifiability was poor. Similar results were observed for cytosolic-based reactions: pyruvate carboxylase (v_{pc}) and PEP carboxykinase (v_{pepck}) (Fig. 2C). These single-compartment reactions possessed the particularity of utilizing the same metabolites but in different compartments (Fig. 1). In this particular case, no statistically sound difference between v_{pc} and v_{pepck} was found, most likely because compartment-specific OAA values lacked.

Iso-enzymatic reactions localized in different compartments

Special emphasis is laid on the so-called iso-enzymatic reactions of Fig. 2C right that catalyze similar conversions in different compartments. The fluxes of malate dehydrogenase (v_{mdh}), ME (v_{me}), aspartate amino-transferases (v_{ast}), and alanine amino-transferases (v_{alt}) are localized in cytosol and mitochondria, respectively. Of the eight iso-enzymes analyzed, seven conversion rates were significantly different. The only exception is the mitochondrial malate dehydrogenase ($v_{mdh,mit}$) which revealed statistical similarity although fluxes even reversed. On contrary, the cytosolic malate dehydrogenase ($v_{mdh,cyt}$) also disclosed flux reversion but with a sound statistical identifiability.

Non-compartmented data were not able to properly reflect real fluxes of the amino-transferases (v_{ast}), namely alanine amino-transferases (v_{alt}) and aspartate amino transferases (v_{ast}). The analysis of whole-cell data resulted in flux overestimation compared to compartment-specific analysis. Notably, the substrate aspartate occurred in cytosol and mitochondria and is a key player of the aspartate-malate shuttle. Moreover, alanine was involved in the co-transport of glycolytic carbon into mitochondria with the MPC1/2. In this case, proper localization and labeling information of the compound is key to estimate fluxes correctly.

In addition, severe bias was observed for fluxes of both malic enzymes (v_{me}) as displayed in Fig. 2C right. By trend, ^{13}C flux estimations using non-compartmented data identified significantly lower (about 30%) cytosolic $v_{me,cyt}$ than the non-compartmented data. Regarding mitochondria, the opposite was found. The finding for v_{me} using non-compartmented data is consistent with the observations of Ahn & Antoniewicz, Templeton et al. [5, 7] who also performed ^{13}C MFA with cellular data. Importantly, cytosolic ME activity via $v_{me,cyt}$ was identified as a key supplier for NADPH needed for IgG production in CHO cells (Junghans et al. [8]).

Mitochondrial metabolite carriers

Comparing shuttle activities using sub-cellular and cellular labeling information reveals significant differences for half of the inter-compartment transporters, namely the aspartate/glutamate antiporter (v_{AGC1}), malate carrier (v_{DIC}), α-ketoglutarate/malate antiporter (v_{OGC}), and the putative alanine carrier (v_{mAla}) (Fig. 2D). Similar to the identification of aspartate amino-transferases, the proper identification of v_{AGC1} depends on the labeling turnover τ_{13C} of Asp in both compartments. Missing compartment-specific measurements lead to the different shuttle fluxes, which are also reflected in the biased flux v_{ast}. The same scenario also holds true for the putative alanine carrier (v_{mAla}) and the corresponding reactions (alanine amino-transferases; v_{alt}). Shuttle estimations regarding v_{DIC} and v_{OGC} using non-compartment-specific data contradict flux calculations using compartment-specific information estimation. The sub-cellular labeling information of malate is essential to get accurate flux estimates. Interestingly, the flux estimation of putative asparagine carrier (v_{mAsn}) was not biased by the use of whole-cell labeling data only. This may reflect that v_{mAsn} heavily depends on the

Table 1 Complete list of estimated and measured cytosolic fractions of subcellular metabolites used for 13C MFA

Metabolites	Cytosolic fraction (*f*)		
	Estimated	Measurement (Junghans et al. [8])	% difference (measurement as the reference value)
Mal	0.100	0.829	87.9
Pyr	0.910	0.838	8.59
aKG	0.100	0.714	85.99
Cit	0.995	0.489	103.48
Glu	0.373	0.827	54.90
Ala	0.100	0.840	88.1
Asn	0.717	0.805	10.48
Asp	0.500	0.809	38.20

measured L-asparagine uptake rate (q_{Asn}) irrespective of the existence of additional subcellular information.

Estimated cytosol–mitochondrial fraction (*f* factor)

Using Eq. 8, *f* factors were estimated for each metabolite and compared with the measurements of Junghans et al. [8] (Table 1). As indicated, all estimated cytosolic fractions (*f*) were poorly identified with pyruvate showing the smallest difference of 8.59% only. On average, 59.71% difference was found compared to the real labeling fraction. Notably, the best estimates of pyruvate and asparagine also enabled improved flux values for the corresponding biochemical reactions, e.g. $v_{MPC1/2}$, v_{pdh} for pyruvate, and v_{asns}, v_{mAsn} for asparagine.

Cellular NADH and NADPH production

Table 2 shows a comparison of NADH and NADPH production via compartment-specific analysis and neglection of sub-cellular data.

Neglecting sub-cellular data, NADPH production is underestimated by approximately 25%. This reflects the 30% underestimation of cytosolic v_{ME} when cellular and not subcellular data are used. In the case of NADH and ATP, the utilization of different datasets disclosed only minor differences. NADH and ATP fluxes were overestimated by 9% and 14% for non-compartmented data, respectively.

Table 2 Comparison of NADH, ATP, and NADPH net production rates in compartment-specific analysis and whole-cell analysis (values presented in pmol cell^{-1} h^{-1})

	NADH	ATP	NADPH
Compartment-specific	0.55692	0.22752	0.10577
Non-compartmented	0.60815	0.25914	0.07924

Challenging the key statements by an additional data set

To investigate whether or not the observed flux characteristics may be specific for the data sets used, additional data of cultivations with the same cell line, cultivation conditions, and analytical tools was used. Figure S6-1:S6-3 (Supplementary Material S6) outlines that very similar key messages are obtained analyzing the new data set: Glycolytic fluxes are fairly similar irrespective whether subcellular or cellular ^{13}C metabolomics is used. On contrary, fluxes for cytosolic malate dehydrogenase and malic enzyme differ statistically significant depending on the granularity of metabolic labeling resolution. The same holds true for shuttle activities such as DIC, GC1, and OGC which is in agreement with the results derived from the other data sets.

Discussion

This study challenges the information gain when performing ^{13}C MFA with compartment-specific metabolome data compared to exploiting cellular labeling information not distinguishing between cytosol and mitochondria.

Figure 2 outlines the complexity of the interactions. A group of fluxes (v_{pgi}, v_{GAPdh} v_{G6Pdh}, and v_{phdgh}) located in a single compartment (here: cytosol) disclose equal values irrespective of the analytical approach selected. Interestingly, this also holds true for v_{cs}, located in mitochondria, primarily due to poor flux identifiability. Furthermore, v_{pepck} and v_{pc} revealed such high flux variances that no distinction could be found whether cellular or subcellular ^{13}C data were used. Apparently, both reactions depend on cytosolic (OAA_{cyt}) and mitochondrial oxaloacetate (OAA_{mit}). They act at the interphase of the two compartments and rely on proper sub-cellular measurement information (τ_{13C}) for correct identification. Distinct OAA measurements were not available in the current study due to challenging analytical access to the compound. Accordingly, flux estimations might be biased by the quality of OAA pool estimations.

In addition, some other fluxes should be interpreted with great care, too. This holds particularly true for mitochondrial malate dehydrogenase ($v_{mdh,mit}$) and the pyruvate carrier v_{MPC1}. Both disclose large error bars rendering a discrimination between cellular versus subcellular approaches hardly possible (Fig. 2C, D). Flux imprecisions reflect the lack of reliable CO_2 evolution rates (q_{CO_2}) and CO_2 labeling profiles.

The whole-cell (cellular) flux estimation failed to estimate the mitochondrial and cytosolic fluxes of the aminotransferases v_{alt} and v_{ast}. This may reflect that those fluxes

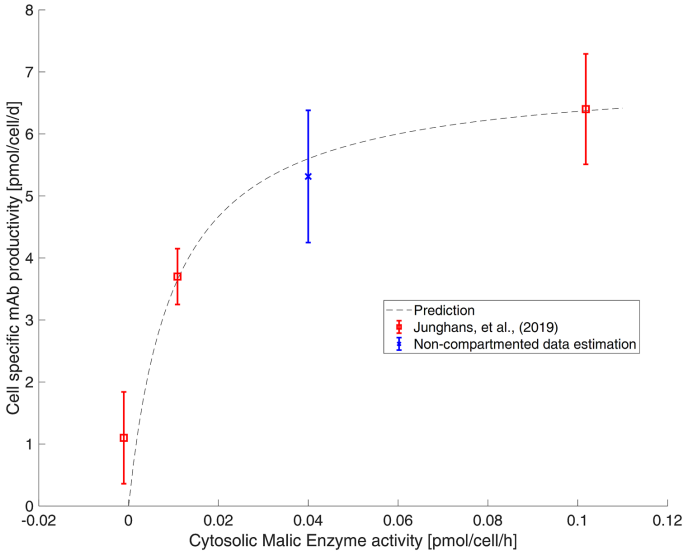

Fig. 3 Cell-specific production of monoclonal antibodies in CHO cells (modified from Junghans et al. [8])

heavily depend on the compartment-specific labeling information of alanine and aspartate. Not providing this information by using whole-cell labeling data leads to the large discrepancies given in Fig. 2C.

Almost all mitochondrial carrier fluxes were poorly estimated when using non-compartmented data. Inaccurate estimations of v_{AGC1} and v_{mAla} are also reflected by the results of v_{ast} and v_{alt}. In addition, the poor estimation of the malate carriers v_{DIC} and v_{OGC} depended on v_{me}. In general, fluxes of transporters and bioreactions heavily relied on the labeling dynamics measured in the related metabolites. Regarding v_{MPC1}, the reduced shuttle activity based on non-compartmented data reflects the missing malate exported into cytosol (Fig. 2D).

To check whether the additional use of labeled glutamine [6] might have achieved similar subcellular flux resolutions as the compartment-specific analysis, simulations were performed using [U-$^{13}C_5$]-L-glutamine (Supplementary Material S3). Interestingly, without information about compartment-specific metabolomics, cytosolic ^{13}C signals obtained from simulations are pretty similar to those of the whole-cell. This is mainly due to the relatively low information gain with respect to the key mitochondrial metabolites malate and aspartate. Compartment-specific labeling information and turnover of the latter are decisive to resolve activities of mitochondrial transporters.

In general, most of the flux estimations using either non-compartmented or compartmented data led to similar values. Even global cell qualifications, such as rates of total ATP formation and NADH production, were similar. However, two main findings should be considered:

1. Often, cellular analysis achieved similar flux estimations as subcellular studies by fitting measured cytosolic labeling fractions for the sake of estimating pool sizes properly (Table 1). In other words, flux optimization algorithms adapted cytosolic and mitochondrial pool sizes to complement missing labeling information. However, the simulated pool size readouts were strongly misleading.
2. Among the fluxes with the largest discrepancies is the cytosolic ME v_{me}. Remarkably, this flux was found to be a promising metabolic engineering target to maximize the formation of heterologous proteins by improved NADPH supply [8]. Accordingly, exact estimation is a prerequisite for proper strain engineering. Figure 3 illustrates that even the result of non-compartment data analysis still fits to the subcellular kinetics published in Junghans et al. [8]. Whether or not experimentalists may have identified this enzyme as a metabolic engineering target remains open and is a matter of qualitative discussion rather than quantitative target identification [8].

To date, the compartment-specific analytical approach has shown its suitability for multiple metabolomic studies

investigating CHO cells under in vivo-like conditions [8, 15, 24–30]. The latter is enabled by fast and standardized metabolism inactivation. Furthermore, data quality essentially relies on the quantitative access to internal standards, such as G6P/F6P (in cytosolic space) and *cis*-aconitate (in mitochondrion) to correct for mitochondrial leakage. In general, fast metabolic inactivation, standardized sample processing and use of internal standards are prerequisites for any compartment-specific metabolomics approach that might be used in future applications.

Conclusions

Investigating the need for using subcellular ^{13}C labeling data, the study revealed that non-compartmented data enabled to identify most fluxes involving single compartment metabolites. Besides, half of the mitochondrial shuttle fluxes and global properties, such as ATP and NADH formation, were fairly well estimated without requiring further subcellular labeling information. However, there is a number of sensitive fluxes that could only be identified properly if compartment-specific pool information was used. Among those were mitochondrial shuttles that rely on alanine, aspartate and malate. Furthermore, key metabolic engineering targets, such as the cytosolic ME flux for NADPH formation, were severely underestimated using (total) cellular data. This may disguise their role as promising metabolic engineering target if non-compartmented pool analysis is performed, only. The finding underlines the necessity to apply subcellular data for flux estimation, not only to quantify cytosolic/mitochondrial shuttle activities but also to identify metabolic engineering targets and obtain valid values for real pool sizes.

Supplementary Information The online version contains supplementary material available at https://doi.org/10.1007/s00449-021-02628-1.

Acknowledgements This work was partially funded by the Bundesministerium für Bildung und Forschung (BMBF, Funding Number 031L0077A and 031B0596B).

Funding Open Access funding enabled and organized by Projekt DEAL.

Declarations

Conflict of interest The authors declare no financial or commercial conflict of interest.

References

1. Wiechert W (2001) ^{13}C metabolic flux analysis. Metab Eng 3(3):195–206
2. Frick O, Wittmann C (2005) Characterization of the metabolic shift between oxidative and fermentative growth in *Saccharomyces cerevisiae* by comparative 13C flux analysis. Microb Cell Fact 4(1):1–16
3. van Winden WA, van Dam JC, Ras C, Kleijn RJ, Vinke JL, van Gulik WM, Heijnen JJ (2005) Metabolic-flux analysis of *Saccharomyces cerevisiae* CEN. PK113–7D based on mass isotopomer measurements of 13C-labeled primary metabolites. FEMS Yeast Res 5(6–7):559–568
4. Zhao Z, Kuijvenhoven K, Ras C, van Gulik WM, Heijnen JJ, Verheijen PJ, van Winden WA (2008) Isotopic non-stationary ^{13}C gluconate tracer method for accurate determination of the pentose phosphate pathway split-ratio in *Penicillium chrysogenum*. Metab Eng 10(3–4):178–186
5. Ahn WS, Antoniewicz MR (2011) Metabolic flux analysis of CHO cells at growth and non-growth phases using isotopic tracers and mass spectrometry. Metab Eng 13(5):598–609
6. Ahn WS, Antoniewicz MR (2013) Parallel labeling experiments with [1,2–^{13}C] glucose and [U-^{13}C] glutamine provide new insights into CHO cell metabolism. Metab Eng 15:34–47
7. Templeton N, Dean J, Reddy P, Young JD (2013) Peak antibody production is associated with increased oxidative metabolism in an industrially relevant fed-batch CHO cell culture. Biotechnol Bioeng 110(7):2013–2024
8. Junghans L, Teleki A, Wijaya AW, Becker M, Schweikert M, Takors R (2019) From nutritional wealth to autophagy: *in vivo* metabolic dynamics in the cytosol, mitochondrion and shuttles of IgG producing CHO cells. Metab Eng 54:145–159
9. Allen DK, Shachar-Hill Y, Ohlrogge JB (2007) Compartment-specific labeling information in ^{13}C metabolic flux analysis of plants. Phytochemistry 68(16–18):2197–2210
10. Ahn WS, Antoniewicz MR (2012) Towards dynamic metabolic flux analysis in CHO cell cultures. Biotechnol J 7(1):61–74. https://doi.org/10.1002/biot.201100052
11. Nicolae A, Wahrheit J, Bahnemann J, Zeng AP, Heinzle E (2014) Non-stationary ^{13}C metabolic flux analysis of Chinese hamster ovary cells in batch culture using extracellular labeling highlights metabolic reversibility and compartmentation. BMC Syst Biol 8(1):50
12. Pfizenmaier J, Takors R (2017) Host organisms: mammalian cells. In: Industrial biotechnology, vol 2. pp 643–671
13. Matuszczyk JC, Teleki A, Pfizenmaier J, Takors R (2015) Compartment-specific metabolomics for CHO reveals that ATP pools in mitochondria are much lower than in cytosol. Biotechnol J 10(10):1639–1650
14. Buescher JM, Antoniewicz MR, Boros LG, Burgess SC, Brunengraber H, Clish CB et al (2015) A roadmap for interpreting ^{13}C metabolite labeling patterns from cells. Curr Opin Biotechnol 34:189–201

15. Pfizenmaier J, Matuszczyk JC, Takors R (2015) Changes in intracellular ATP-content of CHO cells as response to hyperosmolality. Biotechnol Prog 31(5):1212–1216
16. Teleki A, Sánchez-Kopper A, Takors R (2015) Alkaline conditions in hydrophilic interaction liquid chromatography for intracellular metabolite quantification using tandem mass spectrometry. Anal Biochem 475:4–13
17. Fernandez CA, Des Rosiers C, Previs SF, David F, Brunengraber H (1996) Correction of ^{13}C mass isotopomer distributions for natural stable isotope abundance. J Mass Spectrom 31(3):255–262
18. Agnarsson J, Sunde M, Ermilova I (2013) Parallel optimization in MATLAB. Project in Computational Science Report
19. Wiechert W, de Graaf AA (1997) Bidirectional reaction steps in metabolic networks: I. Modeling and simulation of carbon isotope labeling experiments. Biotechnol Bioeng 55(1):101–117
20. Schmidt K, Carlsen M, Nielsen J, Villadsen J (1997) Modeling isotopomer distributions in biochemical networks using isotopomer mapping matrices. Biotechnol Bioeng 55(6):831–840
21. Hofmann U, Maier K, Niebel A, Vacun G, Reuss M, Mauch K (2008) Identification of metabolic fluxes in hepatic cells from transient 13C-labeling experiments: Part I. Experimental observations. Biotechnol Bioeng 100(2):344–354
22. Schaub J, Mauch K, Reuss M (2008) Metabolic flux analysis in *Escherichia coli* by integrating isotopic dynamic and isotopic stationary 13C labeling data. Biotechnol Bioeng 99(5):1170–1185
23. Antoniewicz MR, Kelleher JK, Stephanopoulos G (2006) Determination of confidence intervals of metabolic fluxes estimated from stable isotope measurements. Metab Eng 8(4):324–337
24. Welch BL (1947) The generalization of student's' problem when several different population variances are involved. Biometrika 34(1/2):28–35
25. Warburg O (1956) On the origin of cancer cells. Science 123(3191):309–314
26. Pfizenmaier J, Junghans L, Teleki A, Takors R (2016) Hyperosmotic stimulus study discloses benefits in ATP supply and reveals miRNA/mRNA targets to improve recombinant protein production of CHO cells. Biotechnol J 11(8):1037–1047
27. Becker M, Junghans L, Teleki A, Bechmann J, Takors R (2019) The less the better: how suppressed base addition boosts production of monoclonal antibodies with Chinese Hamster Ovary cells. Front Bioeng Biotechnol 7:76
28. Becker M, Junghans L, Teleki A, Bechmann J, Takors R (2019) Perfusion cultures require optimum respiratory ATP supply to maximize cell-specific and volumetric productivities. Biotechnol Bioeng 116(5):951–960
29. Verhagen N, Wijaya AW, Teleki A, Fadhlullah M, Unsöld A, Schilling M et al (2020) Comparison of L-tyrosine containing dipeptides reveals maximum ATP availability for L-prolyl-L-tyrosine in CHO cells. Eng Life Sci 20(9–10):384–394
30. Verhagen N, Teleki A, Heinrich C, Schilling M, Unsöld A, Takors R (2020) S-adenosylmethionine and methylthioadenosine boost cellular productivities of antibody forming Chinese hamster ovary cells. Biotechnol Bioeng 117(11):3239–3247

Paper IV

Compartment-specific ^{13}C metabolic flux analysis reveals boosted NADPH availability coinciding with increased cell-specific productivity for IgG1 producing CHO cells after MTA treatment.

Andy Wiranata Wijaya, Natascha Verhagen, Attila Teleki, & Ralf Takors

Received: 19 May 2021 | Revised: 5 October 2021 | Accepted: 8 October 2021

DOI: 10.1002/elsc.202100057

Engineering in Life Sciences

RESEARCH ARTICLE

Compartment-specific ^{13}C metabolic flux analysis reveals boosted NADPH availability coinciding with increased cell-specific productivity for IgG1 producing CHO cells after MTA treatment

Andy Wiranata Wijaya | **Natascha Verhagen** | **Attila Teleki** | **Ralf Takors**

Institute of Biochemical Engineering, University of Stuttgart, Stuttgart, Germany

Correspondence
Ralf Takors, University of Stuttgart, Institute of Biochemical Engineering, Allmandring 31, 70563 Stuttgart, Germany.
Email: ralf.takors@ibvt.uni-stuttgart.de

Andy Wiranata Wijaya and Natascha Verhagen contributed equally to this study.

Abstract

Increasing cell-specific productivities (CSPs) for the production of heterologous proteins in Chinese hamster ovary (CHO) cells is an omnipresent need in the biopharmaceutical industry. The novel additive 5′-deoxy-5′-(methylthio)adenosine (MTA), a chemical degradation product of S-(5′-adenosyl)-L-methionine (SAM) and intermediate of polyamine biosynthesis, boosts the CSP of IgG1-producing CHO cells by 50%. Compartment-specific ^{13}C flux analysis revealed a fundamental reprogramming of the central metabolism after MTA addition accompanied by cell-cycle arrest and increased cell volumes. Carbon fluxes into the pentose-phosphate pathway increased 22 fold in MTA-treated cells compared to that in non-MTA-treated reference cells. Most likely, cytosolic ATP inhibition of phosphofructokinase mediated the carbon detour. Mitochondrial shuttle activity of the α-ketoglurarate/malate antiporter (OGC) reversed, reducing cytosolic malate transport. In summary, NADPH supply in MTA-treated cells improved three fold compared to that in non-MTA-treated cells, which can be regarded as a major factor for explaining the boosted CSPs.

KEYWORDS
13C MFA, cell-specific productivity, CHO, MTA, NADPH

1 | INTRODUCTION

Biopharmaceutical markets are steadily increasing worldwide; monoclonal antibody production in Chinese hamster ovary (CHO) cells continues to possess the largest share [1]. Product titers improved 100-fold during the last few decades [2, 3]; however, cell-specific productivities (CSPs) have increased only 38 fold. Optimization of CSP is a striking demand, facing the current need for intensifying bioprocesses and considering continuous production in perfusion processes. [4–6]

However, optimization of CSP requires a detailed understanding of intracellular regulation, which typically

Abbreviations: ^{13}C MFA, ^{13}C Metabolic Flux Analysis; CHO, Chinese Hamster Ovary; MTA, 5′-deoxy-5′-(methylthio)adenosine; VCD, viable cell density

requires the concerted application of omics technologies [7], comprising genome analysis [8, 9], genome-scale modeling [10], transcript analysis [11, 12], epigenetics [13, 14], metabolomics [15], and fluxomics [5, 16-18].

Efforts have been undertaken for enhancing CSP by initiating growth arrest [19]. In addition to osmolarity and temperature shifts [20, 21], studies have focused on the addition of effectors such as sodium butyrate [22], valeric acid [23], glycine betaine [24], and catechin [25]. As a common observation, alterations in cell-cycle phases coincided with increase in cell size. Both were anticipated to improve CSP [26, 27]. However, the underlying mechanisms that explain the phenotype remain fragmented. Recently, Verhagen et al. (2020a,b) [28, 29] demonstrated that cell-cycle arrest could be achieved by exposing CHO cells to the effector 5′-deoxy-5′-(methylthio)adenosine (MTA), which increased CSP by 50%.

MTA is a degradation product of the crucial methyl group donor S-adenosyl-methionine (SAM) and a by-product of polyamine synthesis [30, 31]. MTA is an anticipated effector of the polyamine pathway, DNA synthesis, gene expression control, cell proliferation, lymphocyte activation, tumor development, invasiveness, apoptosis, and signaling pathways [31–35]. Furthermore, MTA is rapidly metabolized and the end products can be used to replenish adenosine-based nucleotide pools [31]. Recently, Verhagen et al. (2020) [28, 29] revealed that MTA addition influenced cell size, cell cycle, and transcript levels, ultimately enhancing the IgG1 CSP of CHO-DP12 cells. Additional studies have outlined the dose dependent effect of MTA addition [29]. Notably, MTA addition also leads to prolonged cell viabilities in the tests [29].

After preliminary identification of MTA as a boosting additive [28], further studies identified rising CSPs from 5.3 to 9.5 pg $cell^{-1}$ day^{-1} after proper MTA addition, i.e. 0.15 pmol at 50 h [29]. Consequently, IgG1 titers increased from about 120 to 140 mg L^{-1}. Hence, not only CSP but also titer improvements were achieved after MTA addition. Encouraged by these observations, this study was performed to identify the underlying metabolic mechanism leading to the production phenotype.

Compartment-specific ^{13}C metabolic flux analysis (^{13}C MFA) was applied to assess the flux changes in the CHO-DP12 culture with and without MTA supplementation. We will outline that the cells undergo significant metabolic reprogramming after MTA exposure. The rise of CSPs will be shown to correlate with increased pentose-phosphate fluxes leading to the hypothesis that the latter should be fine-tuned in hyperproducing cells.

PRACTICAL APPLICATION

Compartment-specific ^{13}C MFA is a tool for investigating cellular metabolism in mammalian cells distinguishing between different compartments such as cytosol and mitochondrion. In this study, we applied ^{13}C MFA based on compartment-specific metabolomics to unravel basic intracellular mechanisms coinciding with boosting cell specific productivities for IgG1 formation. The latter is the consequence of the addition of MTA (5′-deoxy-5′-(methylthio)adenosine) to cell cultures. The technology of compartment-specific ^{13}C MFA could be well applied to investigate similar questions to optimize process and cell performance.

2 | MATERIALS AND METHODS

2.1 | Cell culture conditions and effector and isotopic tracer studies

An IgG1 antibody (anti-IL-8)-producing CHO DP12 cell line (ATCC CRL-1445TM) was adapted to suspension and grown in chemically defined TC-42 medium (Xell AG, Germany). Media were supplemented with 4 mM L-glutamine and 200 nM methotrexate. Precultures were scaled up in shaking flasks (Corning, USA) at 37°C and 150 rpm (50 mm displacement) and under 5% CO_2 with an initial Viable Cell Density (VCD) of 0.5×10^6 cells mL^{-1} in a humidified incubator (Infors HT, Switzerland).

Bioreactor cultivations in batch mode were performed in a four-fold DASGIP parallel bioreactor system DS1500ODSS (Eppendorf, Germany) with a starting volume of 1.2 L supplemented with 20 mM non-labeled [U-$^{12}C_6$] D-glucose (D-glucose) and an initial VCD of 0.4×10^6 cells mL^{-1}. The temperature was set to 37°C, and the pH was maintained at 7.1 with 1 M Na_2CO_3 and CO_2 gassing, which was monitored using a conventional pH probe (Mettler-Toledo, USA). The agitation speed was fixed at 150 rpm, and dissolved oxygen (DO) was controlled at 40% using an amperometric electrode (Mettler-Toledo, USA). After 48 h, effector studies (EFF) were performed as biological duplicates (n = 2) by the addition of 250 μM MTA. Two reactors (n = 2) served as a reference (REF), and an equal volume of sterilized water was added to mimic dilution effects. After 60 h, isotopic tracer studies were performed through addition of ^{13}C-labeled D-glucose,

resulting in an extracellular ratio of 25% [U-$^{12}C_6$]-, 30% [1-$^{13}C_1$]-, and 45% [U-$^{13}C_6$]-D-glucose in all reactors.

2.2 | Quantification of viable cell density and extracellular metabolites

VCD and cellular viability were determined using an automated cell counting system (Cedex XS, Roche Innovatis, Germany) using trypan blue staining. Extracellular concentrations of D-glucose and L-lactate were monitored using an amperometric biosensor system (LaboTRACE, Trace Analytics, Germany). Extracellular antibody concentrations (anti-IL-8 IgG1) were determined using an enzyme-linked immunosorbent assay (ELISA), as described previously [21]. Extracellular MTA was quantified using the method described in Verhagen et al., 2020a [28].

Extracellular amino acid concentrations were measured using an Agilent 1200 HPLC system based on a bicratic reversed phase liquid chromatography (RPLC) method (Agilent Zorbax Eclipse Plus C18 column 250 × 4.6 mm, 5 μm equipped with an Agilent Zorbax Eclipse Plus C18 guard column 12.5 × 4.6 mm, 5 μm) with automated pre-column derivatization and fluorometric detection [36]. We performed absolute quantification using a standard-based external calibration and adapted sample dilutions (1 to 8) with γ-aminobutyric acid (GABA) as an internal standard.

2.3 | Cell size measurement and cell cycle analysis

Cell size was measured in conjuction with the VCD mesaurement using Cedex XS (Roche Innovatis, Germany). The spherical cellular geometry was assumed, and average cellular diameter was obtained as a readout. Cellular volume was calculated based on the spherical volume calculation using the average diameter as the input. Cell cycle analysis was conducted based on the method reported by Verhagen et al., 2020 [28].

2.4 | Fast filtration sampling and extraction for metabolomics

Samples for subcellular metabolome analyses were collected at 48, 60, 61, 72, 84, 108, 132, and 168 h of cultivation time in technical duplicates from each reactor, according to a modified differential fast filtration protocol [18, 37]. Filtered and quenched cells (3×10^7 cells per sample) were extracted directly (whole cell) or after selective permeabilization with digitonin (subcellular fractions), following addition of 5 mL ice-cold 70% v/v methanol (MeOH) to the filters. Additionally, we used L-norvaline and 2-dehydro-3-deoxy-D-gluconate 6-phosphate (KDPG) as internal standards to monitor the stability of the filtration, extraction, and measurement. Filters with captured cells were incubated in sample cups at −20°C for 90 min, and the extraction solutions were subsequently separated using a vacuum pump. The filters and sample cups were rinsed with 2 mL of ice-cold 50% v/v MeOH, and the collected extraction solutions were mixed with 500 μL of ice-cold chloroform and vortexed for 20 s. The emulsion was centrifuged at 3200 × g for 11 min at 4°C. The upper aqueous phase was aliquoted into microcentrifuge tubes (4 × 1 mL), evaporated for 95 min at <20°C (RVC 2.33 IR, Christ), and stored at −70°C. During the entire process, the weights of the sample cups, filters, and micro-centrifuge tubes were tracked to calculate the final extraction volumes.

2.5 | Subcellular metabolomics using LC-MS/MS and HPLC-UV

Subcellular adenosine monophosphate (AMP), adenosine diphosphate (ADP), and adenosine triphosphate (ATP) concentrations in metabolic extracts were determined using an Agilent 1200 HPLC system based on a bicratic ion-pair RPLC method (Hypersil BDS C18 column 15 cm × 4.6 mm, 3 μm equipped with a HypersilTM BDS C18 guard column 10 × 4 mm, 5 μm) and UV light (diode array detector) detection without derivatization [38]. We performed absolute quantification using a standard-based external calibration and selected spikes of reference standard mixes to evaluate the influence of the sample matrices.

Subcellular metabolome studies were performed using an Agilent 1200 HPLC system coupled with an Agilent 6410B triple quadrupole mass spectrometer (MS-QQQ) with an electrospray ion source (ESI). System control, acquisition, and analysis of data were performed using the commercial Mass Hunter B.06.00 software. Endogenous metabolites were separated under alkaline mobile phase conditions (pH 9.2) using bicratic hydrophilic interaction chromatography (HILIC), according to a previously described method [39] with modifications. GABA and α-aminoisobutyric acid (AIBA) were previously added (50 μM) as internal standards and considered for monitoring instrumental fluctuations. Targeted ^{13}C tracer analysis of isotopically labeled metabolite pools was performed in selected ion monitoring (SIM) mode using pre-optimized precursor ion transitions (0.3 u) with adapted MS parameters and ESI conditions [40]. Subcellular metabolite pools were absolutely quantified through a three-fold addition of defined amounts of non-labeled reference standards

(internal calibration). Applied multicomponent standard mixtures were adjusted according to the linear dynamic range of the targeted metabolites and previously estimated concentration levels [41]. Cytosolic depletion and mitochondrial integrity were evaluated using glucose 6-phosphate (G6P), fructose 6-phosphate (F6P), and *cis*-aconitate (*cis*Aco) concentrations (Table S3).

^{13}C mass isotopomer detection of highly reactive α-keto acid pools (αKG, Pyr, Gxy) was performed using a previously established LC-MS protocol [18] using the abovementioned platform. Previously derivatized (phenylhydrazine) metabolite isotopologue pools [42] using α-ketovaleric acid (αKV) were separated under acidic conditions (pH 3) using an RPLC method and were detected in SIM mode with pre-optimized settings. Determination of absolute pool concentrations was performed analogous to the abovementioned strategy.

2.6 | Isotopic non-stationary ^{13}C metabolic flux analysis

For CHO cells, previous studies already outlined the advantages of using isotopically non-stationary ^{13}C MFA for intracellular flux estimation [16–18]. Fluxes were estimated through analyzing the time series of isotopically transient ^{13}C labeling profiles in compartment-specific metabolite pools using MATLAB version 2018a (The MathWorks, Inc., Natick, Massachusetts, USA).

2.7 | Compartment-specific metabolic model

The metabolic network model consisted of two compartments: the cytosol and the mitochondrion, each comprising a stoichiometric and a carbon atom transition model with 36 metabolites and 62 metabolic reactions (see Table S5). A cell density of 122 pg cell^{-1} was assumed according to the previous study [18]. Several sink reactions for amino acids and central carbon metabolites were considered to mimic anabolic demands for the *de novo* synthesis of carbohydrates, proteins, nucleic acids, and lipids [43].

2.8 | Growth, nutrient uptake, and product formation rates

The cell-specific growth rate was estimated using the weighted linear regression of VCDs with related standard deviations based on Equation (1).

$$\frac{dc_X}{dt} = \mu c_X \tag{1}$$

By analogy, cell-specific nutrient uptake and product formation rates were calculated:

$$\frac{dc_i}{dt} = q_i\, c_X \tag{2}$$

Linear regressions were performed in MATLAB and Curve Fitting Toolbox Release 2018a.

2.9 | Metabolite and isotopomer balancing

The balancing of metabolite *i* is described in Equation [3], assuming a (pseudo) steady state for the observation window:

$$\frac{dc_i}{dt} = \mathrm{N} \cdot \mathrm{v} = 0, \tag{3}$$

where $\mathbf{c}_i$ is the concentration vector containing all intracellular metabolites; N is the metabolic network stoichiometry matrix, containing the number of *i* metabolites and *j* reactions; and **v** is the vector containing flux distribution.

Bidirectional fluxes were defined for each of the reversible reactions [44, 45], as described by Equation (4).

$$\vec{v}_j = \beta_j\, v_j^{net} \tag{4}$$

$$\overleftarrow{v}_j = \vec{v}_j - v_j^{net},$$

where β_j is the reversibility factor of reaction j ($\beta_j \geq 1$).

To model transient ^{13}C enrichments, the isotopomers of each metabolite *i* were balanced by Equation (5).

$$\frac{d\left(\mathrm{C}_i \mathrm{I}_i\right)}{dt} = \sum_{j=1}^{N}\left[\alpha\left(\bigotimes_{k=1}^{0}\left(\sum_{m=1}^{n}\mathrm{IMM}_{k\to m}\right)\mathrm{I}_k\right) r_j + (1-\alpha)\left(v_{ij} r_j \mathrm{I}_i\right)\right]$$

with

$$\alpha = \begin{cases} 1, & \text{if } v_{ij} > 0 \\ 0, & \text{else} \end{cases}, \tag{5}$$

where $\boldsymbol{c}_i$, $\boldsymbol{I}_i$, and $\boldsymbol{I}_k$ denote vectors of intracellular concentrations of metabolites i and isotopomer distribution vectors, containing molar ratios that correspond to the fractional amounts of the individual isotopologues for metabolites i and k, respectively. The isotopomer mapping matrix [46] $\mathbf{IMM}_{k\to m}$ describes the isotopomer transition from reactant k (with n number of reactants) to product m. v_{ij} equals the stoichiometric coefficient of metabolite i in reaction j, whose molar rate is r_j. The operator $\otimes$ denotes element-by-element vector multiplication.

Furthermore, isotopomer balancing was considered for extracellular metabolites that were heavily exchanged with intracellular pools [47] (L-lactate, L-alanine, L-glutamate, and L-aspartate), as shown in Equation (6):

$$\frac{d\left(\boldsymbol{I}_{i,ex}\right)}{dt} = \frac{1}{\boldsymbol{C}_{i,ex}}\left[\overline{C_X}\left(\vec{q}_{i_{ex}}\cdot\boldsymbol{I}_{i,in}-\overleftarrow{q}_{i_{ex}}\cdot\boldsymbol{I}_{i,ex}\right)-\frac{dC_{i,ex}}{dt}\boldsymbol{I}_{i,ex}\right]$$

with

$$\vec{q}_{i_{ex}} = \beta_i \cdot q^{net}_{i,ex}$$

$$\overleftarrow{q}_{i_{ex}} = \vec{q}_{i_{ex}} - q^{net}_{i,ex} \tag{6}$$

2.10 | Simulation of ^{13}C labeling experiment

The total set of ordinary differential equations (ODEs), comprising 972 equations, was solved using MATLAB 2018a based on *ode15s*.

2.11 | Parameter estimation and uncertainty

Simulated isotopologue distributions, $\boldsymbol{x}$, were obtained through minimizing the weighted least square sum, subtracting the measured isotopologue values, $\boldsymbol{x}_m$, as indicated in Equation (7). In total, ODEs contain 43 parameters: eight intracellular fluxes and 35 reversibility constants. Parameter fitting was performed using MATLAB 2018a with *fmincon* and *GlobalSearch* and was repeated at least 100 times starting with randomized initiation settings.

$$\min_{p}\Phi = \sum\frac{(\boldsymbol{x}-\boldsymbol{x}_m)^2}{\boldsymbol{\sigma}_x^2}, \tag{7}$$

where $\boldsymbol{x}$ denotes vectors for the isotopologue fractions. $\boldsymbol{\sigma}$ denotes the standard deviation of each measured value.

The goodness of fit of the obtained flux distribution was assessed using the chi-square test to determine whether the model accurately reflects the in vivo data. Statistical acceptance was assigned on the 95% confidence level ($\alpha = 0.05$). The complete flux distribution results is presented in Supplementary Material 2. Furthermore, the simulated mass-isotopomer distribution (MID) is presented in Supporting Information S4.

The measured extracellular rates, $\boldsymbol{q_m}$, and estimated intracellular rates (optimized parameter, $\boldsymbol{p}$) were used to constrain the flux distribution, $\boldsymbol{v}$, as described in Equation (8).

$$\mathrm{v} = \begin{pmatrix}\mathrm{S}\\ \mathrm{M}\end{pmatrix}^{-1}\begin{pmatrix}0\\ [\boldsymbol{q_m} \quad \mathrm{p}]\end{pmatrix}, \tag{8}$$

where $\mathbf{M}$ is the measurement matrix containing all stoichiometric coefficients of $\mathrm{q_m}$ (measured rates [pmol cell^{-1} h^{-1}]) and p (estimated parameter using mass-isotopomer data; as intracellular fluxes [pmol cell^{-1} h^{-1}]).

Parameter uncertainty was assessed using a non-linear algorithm [48]. The method assumes that the sum of squared residual is χ^2 distributed. Thus, the uncertainty of parameter θ was determined when optimizing the said systems with one degree of freedom (χ^2 distributed).

3 | RESULTS

3.1 | MTA reduced cellular growth rate while increasing cell volume

During phase A (0– 48 h) cells grew under ample nutrient supply with a maximal specific growth rate of 0.705 ± 0.021 d^{-1} while consuming D-glucose, L-asparagine, L-glutamine, and other essential amino acids (Figure 1). Metabolic overflow products, such as L-lactate, L-alanine, L-asparagine, and L-glutamate were secreted. After MTA addition during phase B, cellular growth slowed to 0.322 ± 0.003 d^{-1} and recovered after >60 h. During the first part of phase C, C.I (60-108 h), glucose was steadily consumed. By analogy, MTA was taken up with 0.18 ± 0.037 pmol cell^{-1} d^{-1} before depletion (approximately 96 h). In accordance, the cytosolic and mitochondrial MTA levels rose, exceeding REF pool sizes by 170 and 800 times, respectively. Coinciding, the supplemented cells showed increased L-alanine and L-glutamate secretion compared to the initial phase A. D-glucose, L-asparagine, and L-glutamine were still consumed, whereas L-lac was secreted. In contrast, reference cultures (without MTA addition) grew with an unaffected high growth rate (0.677 ± 0.031 d^{-1}) (Figure 2). After 108 h, L-asparagine was

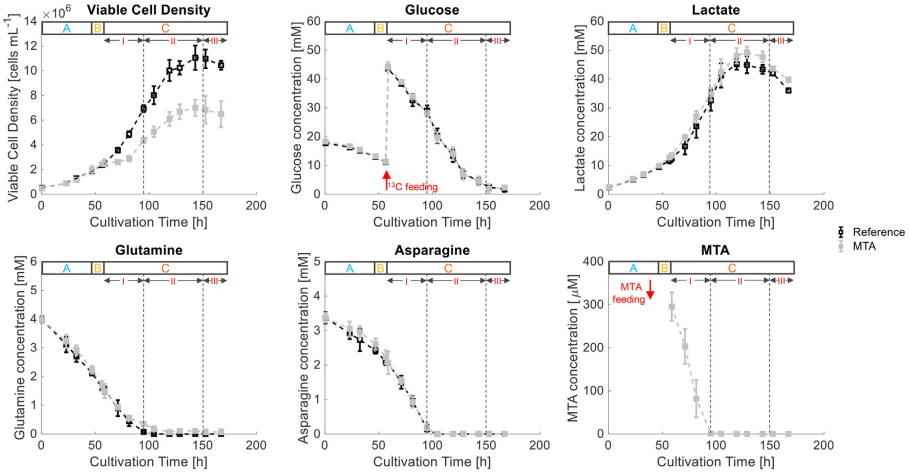

FIGURE 1 Time course of VCD [cells mL^{-1}], D-glucose [mM], L-lactate [mM], L-asparagine [mM], L-glutamine [mM], and 5′-deoxy-5′-methylthioadenosine (MTA) [μM] of the reference cultures (in black) and MTA-supplemented cultures (in grey). MTA was added after phase A (0-48 h), at a final MTA concentration of 250 μM. Glucose labeling was initiated after phase B (48-60 h). Phase C (60-168 h) is divided into I: overflow; II: N-limitation; and III: starvation. Error bars indicate the standard deviations for biological duplicates and technical replicates

depleted in all cultures. Similarly, L-glutamine depletion occurred in REF, whereas low levels were maintained in MTA-supplemented cells. Accordingly, phase C was divided into C.I (60-108 h) with sufficient L-asparagine and L-glutamine supply, phase C.II with L-glutamine and L-asparagine limitations (108-144 h), and C. III as strict starvation (>144 h). For the latter, the simplifying term "nitrogen limitation" will be applied in the manuscript mirroring the important role of L-asparagine and L-glutamine as amino donors. Notably, Junghans et al. (2019) even found evidence for initiated autophagy programs under said condition. In REF, the growth was reduced to 0.258 ± 0.039 d^{-1}, reflecting L-glutamine and L-asparagine limitation during C.II. Similar growth trends were observed during phase C.II for MTA-treated cultures, with a growth rate of 0.203 ± 0.012 d^{-1} (Figure 1). Both cultures experienced strict starvation during C.III (144–168 h) with maximum VCDs of (110.5 ± 9.8) × 10^5 cells mL^{-1} for REF and (69.9 ± 6.8) × 10^5 for MTA-supplemented cells (Figure 1).

In addition to the diminished growth rate, MTA addition led to temporary increases in cell volumes. On the basis of the measured cell diameters, the volume of supplemented cells increased by 55% (84 h) and shrank by 31% during phase C.II. In contrast, the cell size of the reference cultures was stable until the end of the cultivation phase C.II. Upon initiating nitrogen starvation (phase C.III), the cell volumes rose, and the differences leveled out (Figure 3A).

The increase in cellular volumes coincided with a change in the cell-cycle distribution after MTA addition (Figure 3B). At 84 h, the supplemented cells showed a lower G1-fraction (MTA: 26.02 ± 0.70%; REF: 55.70 ± 0.26%) and higher S-fraction (MTA: 31.32 ± 1.23%; REF: 17.98 ± 1.71%) and G2-fraction (MTA: 43.60 ± 0.95%; REF: 26.88 ± 1.26%). Cells subjected to nitrogen limitation in phase C.II (132 h) exhibited equalization of the cell-cycle phase distribution compared to the reference cultures.

3.2 | MTA addition enhanced cell-specific productivity and ATP availability

Figure 4A depicts cell-specific (CSP) and cell-volume-specific (CVP) IgG productivities during the exponential growth phase A with abundant nutrient supply. The CSP exhibited no significant difference before MTA supplementation (e.g., differential CSP at 24 h): REF, 5.01 ± 0.88 pg cell^{-1} d^{-1}; MTA, 5.26 ± 0.83 pg cell^{-1} d^{-1}. Similarly, the CVP was not significantly different before supplementation (Figure 4B). Interestingly, the CSP following MTA supplementation was 170% higher (9.59 ± 1.72 pg cell^{-1} d^{-1}) than that in REF (3.51 ± 1.27 pg cell^{-1} d^{-1}) during C.I

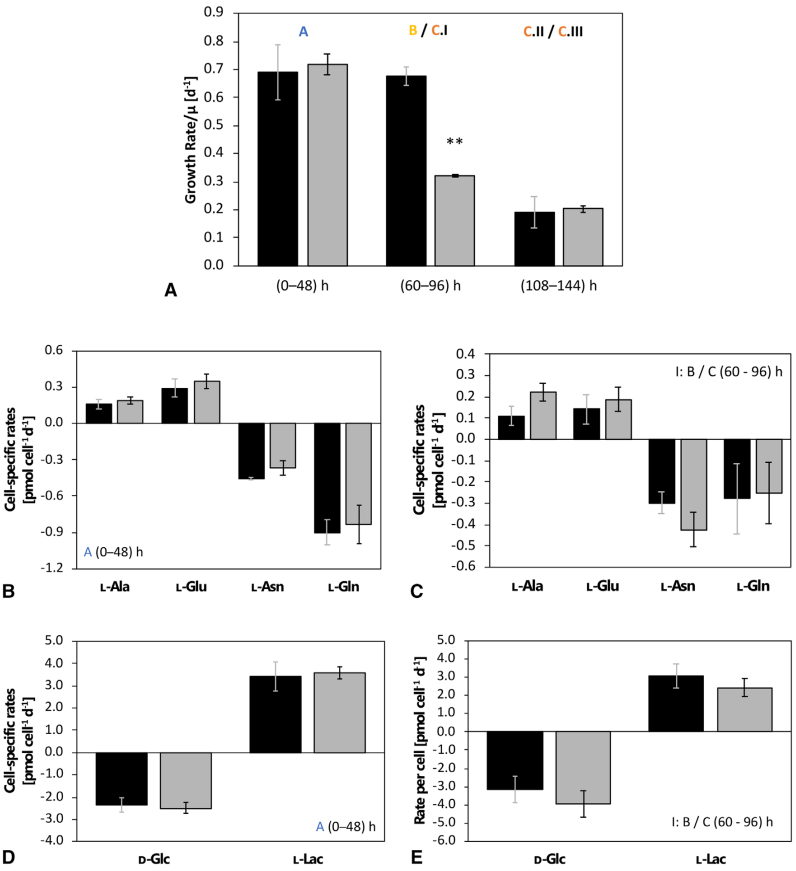

FIGURE 2 A: Growth rate per day [d^{-1}] for the different cultivation phases. B: Cell-specific uptake/secretion rates [pmol $cell^{-1}$ d^{-1}] for L-glutamine (L-Gln), L-asparagine (L-Asn), L-glutamate (L-Glu), and L-alanine (L-Ala) in overflow metabolism before MTA addition (A). C: Cell-specific uptake/secretion rates [pmol $cell^{-1}$ d^{-1}] for L-glutamine (L-Gln), L-asparagine (L-Asn), L-glutamate (L-Glu), and L-alanine (L-Ala) in overflow metabolism after MTA addition (B/C.I). D: Cell-specific uptake/secretion rates [pmol $cell^{-1}$ d^{-1}] for D-glucose (D-Glc) and L-lactate (L-Lac) in overflow metabolism before MTA addition (A). e: Cell-specific uptake/secretion rates [pmol $cell^{-1}$ d^{-1}] for D-glucose (D-Glc) and L-lactate (L-Lac) in overflow metabolism after MTA addition (B/C.I). MTA-supplemented cells (grey) compared to REF (black). MTA was added after phase A (0-48 h) at a final MTA concentration of 250 μM. Glucose labeling was initiated after phase B (48-60 h). Phase C (60-168 h) is divided into I: overflow; II: N-limitation; and III: starvation. Error bars indicate the standard deviations for biological duplicates and technical replicates. Significance was tested using one-sided *t*-test. $^{**}p < 0.01$ $^{*}p < 0.05$

after transient phase B. The subsequent phases C.II and C.III show reduced CSPs for all cultures, which indicates the dominating impact of limited nutrient supply in accordance with previous study [18]. The CVPs only increased by roughly 95% (MTA: 1.05 ± 0.14 g L^{-1} d^{-1}; REF: 0.54 ± 0.19 g L^{-1} d^{-1}), whereas the CSPs rose by 170%. Thus, CSP improvements mirror the combinatorial effects of elevated cell volumes and metabolic changes. The latter will be investigated through ^{13}C metabolic flux analysis.

The cellular energy status was studied on the basis of the ATP concentrations in the cytosolic and mitochondrial compartments (Figure 5).

Considering the error bars in Figure 5A, MTA addition did not change the ATP levels in the mitochondria but

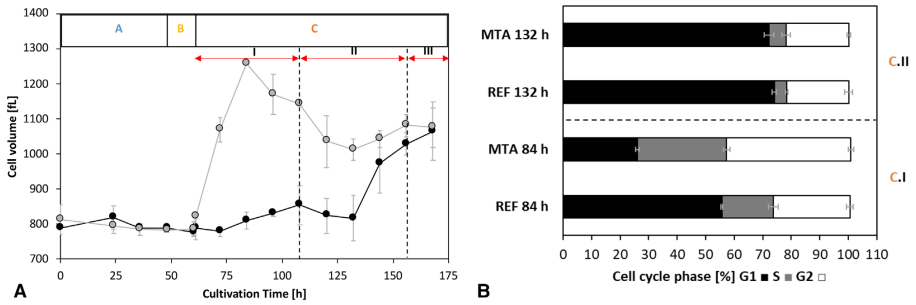

FIGURE 3 A: Time course of the cell volume [fL] of MTA-supplemented cells (MTA: grey) and reference cells (REF: black) in the different phases. Cell volume was calculated with the assumption of a spherical cell shape. B: Cell-cycle phase distribution [%] of MTA-supplemented cells (MTA) and reference cells (REF) at 84 h (I: Overflow) and 132 h (II: N-limitation). MTA was added after phase A (0-48 h) at a final MTA concentration of 250 μM. Glucose labeling was initiated after phase B (48-60 h). Phase C (60-168 h) is divided into I: overflow; II: N-limitation; and III: starvation. Error bars indicate standard deviations for biological duplicates and technical replicates

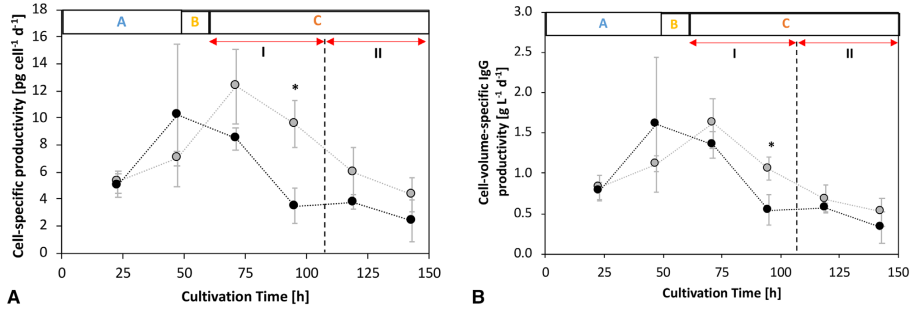

FIGURE 4 Cell-specific IgG productivity (CSP) [pg cell^{-1} d^{-1}] and cell-volume-specific IgG productivity (CVP) [g L^{-1} d^{-1}] regarding the different cultivation phases. A: Differential CSPs over cultivation time. B: Differential CVPs over cultivation time. MTA-supplemented cells (grey) compared to REF cells (black). MTA was added after phase A (0-48 h) at a final MTA concentration of 250 μM. Glucose labeling was initiated after phase B (48-60 h). Phase C (60-168 h) is divided into I: overflow; II: N-limitation; and III: starvation. Error bars indicate standard deviations for biological duplicates and technical replicates. Significance was tested using one-sided *t*-test. *$p < 0.05$

significantly increased the ATP content in the cytosol. The latter peaked 12 h after MTA addition before approaching the corresponding levels in REF at the end of C.I (Figure 5B). Notably, the increase of cytosolic ATP precedes the increase in CSP (Figure 4A).

3.3 | MTA-treated cells detour carbon into the PPP

Isotopically transient ^{13}C MFA was performed to elucidate the impact of MTA addition on central metabolism under ample nutrient supply coinciding with the highest CSPs observed in phase C.I.

Figure 6A depicts the cytosolic and mitochondrial carbon flux distributions of MTA-supplemented and reference cultures during the exponential growth in phase C.I.

Focusing on the upper glycolysis, the CHO-DP12 reference cultures (Figure 6A) showed a metabolic phenotype comparable to that reported by Junghans et al. (2019) [18]. Under abundant nutrient supply, approximately 18% of total D-glucose was continuously exchanged with non-labeled endogenous carbon storage (v_{fGlyco}: 0.474 ± 0.109 pmol cell^{-1} d^{-1}). At the same time, a remarkably

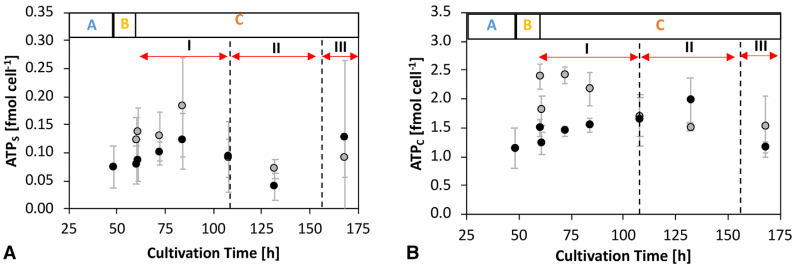

FIGURE 5 A: Time course of the ATP concentrations in the subcellular (mitochondrial, index S) compartment of MTA-supplemented cells (MTA: grey) and reference (REF: black). B: Time course of the ATP concentrations in the cytosolic compartment (index C) of MTA-supplemented cells (MTA: grey) and reference cells (REF: black). MTA was added after phase A (0-48 h) at a final MTA concentration of 250 μM. Glucose labeling was initiated after phase B (48-60 h). Phase C (60-168 h) is divided into I: overflow; II: N-limitation; and III: starvation. Error bars represent the standard deviations for biological duplicates and technical replicates

low fraction of consumed D-glucose (about 4%) was channeled into the oxidative PPP (v_{G6Pdh}: 0.110 ± 0.032 pmol cell^{-1} d^{-1}), which corresponds to the earlier findings [16, 17].

In contrast, MTA-supplemented cells exhibited a considerably different flux distribution (Figure 6B). The labeling kinetics of G6P indicates significantly reduced carbon exchange with endogenous carbon storage compounds such as glycogen (v_{fGlyco}: 0.02 ± 0.024 pmol cell^{-1} d^{-1}). Instead, approximately 83% of consumed glucose was diverted into the oxidative PPP (v_{G6Pdh}: 2.35 ± 0.17 pmol cell^{-1} d^{-1}). This corresponds to a remarkable rise of 21-fold in the G6Pdh flux in the MTA-supplemented cells compared to that in the G6Pdh flux in the reference culture.

The PPP influx of MTA-supplemented culture exceeded the anabolic ribose 5-phosphate (R5P) requirements, i.e., precursor needs for nucleotide biosynthesis, by a factor of 166. Consequently, approximately 81% of the carbon re-entered glycolysis via fructose 6-phosphate (F6P) and glyceraldehyde 3-phosphate (GAP). Interestingly, lower glycolysis (represented by GAP dehydrogenase) showed statistically similar fluxes in MTA-supplemented (v_{GAPdh} : 4.87 ± 0.29 pmol cell^{-1} d^{-1}) and reference culture cells (v_{GAPdh} : 6.18 ± 1.24 pmol cell^{-1} d^{-1}).

3.4 | MTA supplementation reduced net malate export from mitochondria

The compartment-specific ^{13}C MFA revealed the in vivo activity of the mitochondrial pyruvate carrier, MPC, and the other solute carriers belonging to the family 2A (SLC25A; see Figure S1). In the REF culture, the highest mitochondrial carrier activity was observed for the MPC (v_{MPC}: 4.4 ± 1.4 pmol cell^{-1} d^{-1}), supporting the earlier study [18]. The dicarboxylic acid carrier (DIC) and the glutamate carrier (GC) showed the second strongest rates of 0.89 to 1.19 pmol cell^{-1} d^{-1}.

Shuttling activities for malate described the cellular status [18] well. Previous analysis of malate shuttling revealed that DIC is the key malate carrier in CHO cells. With approximately 1 pmol cell^{-1} d^{-1}, malate export from the mitochondria via DIC was approximately six-fold higher than malate export via CIC. OGC further supports the export of mitochondrial malate by importing cytosolic αKG. In total, net malate export occurs from the mitochondria to the cytosol at 1.57 ± 0.41 pmol cell^{-1} d^{-1}, which implies malate-mediated NADPH production in the cytosol [18].

MTA supplementation fundamentally altered the shuttling activities of GC, OGC, and putative alanine carrier (mAla). Remarkably, OGC transport was reverted, resulting in the export of αKG to the cytosol and import of malate into the mitochondria. Accordingly, the net malate export to the cytosol was reduced to 0.80 ± 0.31 pmol cell^{-1} d^{-1} due to the MTA supplementation. Additionally, cells exposed to MTA exhibited a reduction in v_{GC} and v_{mAla} to 0.35 ± 0.06 and 0.14 ± 0.05 pmol cell^{-1} d^{-1}, respectively.

3.5 | Reprogramming of NADPH production strategies while maintaining a similar NADH supply

NADPH is a vital cofactor and crucial redox partner in various cellular reactions, typically anabolic reactions [49]. In CHO-DP12, NADPH is produced via oxidative PPP and the cytosolic malic enzyme (me_{cyt}). The latter requires sufficient malate shuttling activity from the mitochondria

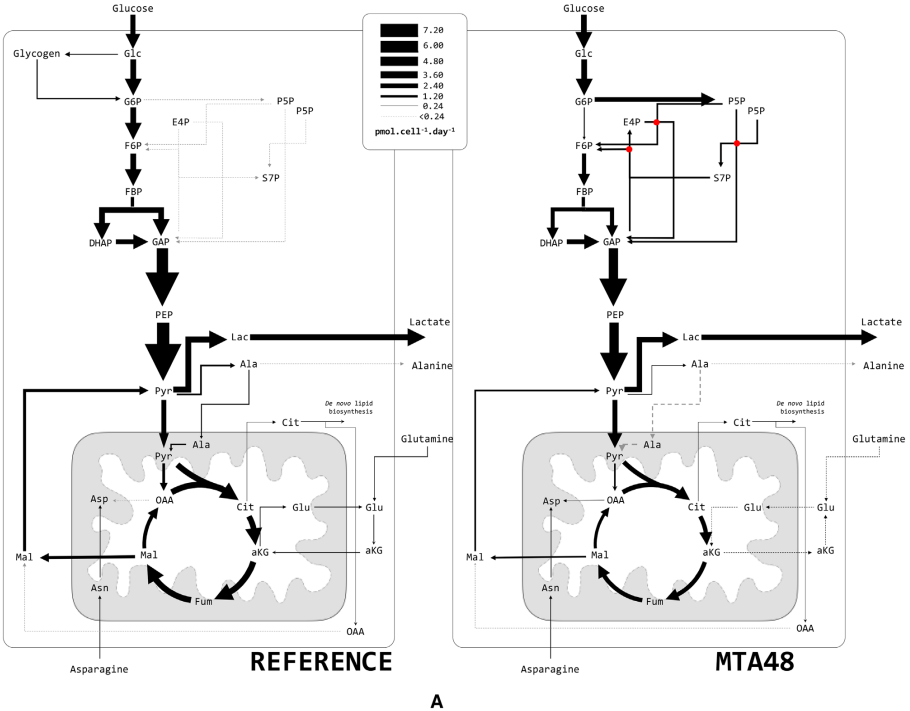

FIGURE 6 A. Metabolic flux distribution of the reference and MTA-supplemented CHO-DP12 cells. Arrows indicate flux direction, and the thickness of the arrows indicate strength in pmol cell^{-1} day^{-1}. B. Comparison of key fluxes using abbreviations as follows: phosphoglucose-isomerase (pgi), G6P dehydrogenase (G6Pdh), endogenous glycogen exchange (fGlyco), PEP carboxykinase (PEPCk), alanine amino transferase (alt), malic enzyme (me), pyruvate carboxylase (pc), and aspartate amino transferase (ast); and C. Comparison of mitochondrial carrier activities: pyruvate/H^+ symporter (MPC), aspartate/glutamate antiporter (AGC), citrate/malate antiporter (CIC), dicarboxylic acid carrier (DIC), glumate carrier (GC), aKG/malate antiporter (OGC), putative alanine carrier (mAla), and putative asparagine carrier (mAsn). *indicates $p < 0.05$

via the concerted activities of MPC, CIC, and DIC in the citrate–pyruvate shuttle systems. This study identified a relatively high cytosolic malic enzyme flux (v_{me_cyt}: 1.58 ± 0.28 pmol cell^{-1} d^{-1}) in the reference culture, which is in accordance with Junghans et al. (2019) [18]. Notably, fluxes via me_{cyt} were entirely fueled by malate exported from the mitochondria.

In the MTA-supplemented cultures, me_{cyt} activity (0.76 ± 0.21 pmol cell^{-1} d^{-1}) was reduced by 43%, mirroring the reduction of shuttling activities. Consequently, the NADPH supply fundamentally differed between the REF and MTA-treated cells (Figure 7). In the reference culture, NADPH supply via cytosolic malic enzyme (me_{cyt}) comprises 88% of the total production compared to 14% in the culture treated with MTA. Despite severe reduction *in* me_{cyt} activity, the MTA-treated culture produced approximately three-fold more NADPH than REF through amplification of the NADPH formation via PPP. Notably, PPP-mediated NADPH formation was approximately 4.69 ± 0.34 pmol cell^{-1} d^{-1}, reflecting a 21-fold increase compared to REF. Regarding NADH supply, no statistically significant differences were observed between the REF and MTA-treated cells (Figure 7).

3.6 | Glutamine and alanine metabolism

L-glutamine uptake rate was reduced in the MTA-treated cells (0.16 ± 0.03 pmol cell^{-1} day^{-1}) compared to the reference culture (0.22 ± 0.01 pmol cell^{-1} day^{-1}). Nevertheless,

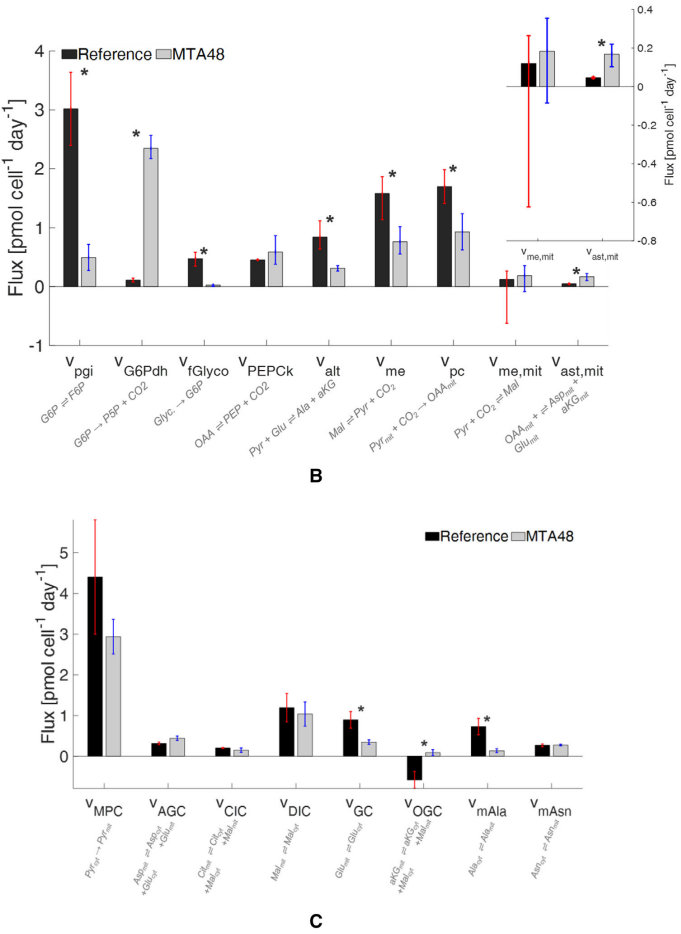

FIGURE 6 Continued

L-glutamine catabolic rates remained similar in both cultures (REF: 0.17 ± 0.01 pmol cell^{-1} day^{-1}; MTA treated: 0.14 ± 0.03 pmol cell^{-1} day^{-1}). In REF, L-glutamine was taken up and initially catabolized in the cytosol via glutaminase (Figure 6A). Next, the intermediate product (L-glutamate) was catabolized via cytosolic amino-transferases yielding αKG, which fueled into the CAC via the Mal/αKG symporter (OGC). This observation is consistent with the observations of Junghans et al. (2019) [18]. Interestingly, cultures treated with MTA showed a variation: cytosolic glutamate was imported directly into the mitochondria via AGC, and it did not require further cytosolic deamination to αKG.

Cellular secretion of L-alanine was significantly higher in the MTA-supplemented cells than in the REF (Figure 2). In contrast, intracellular L-alanine formation mirrors cytosolic alanine-aminotransferase (alt_{cyt}) activities v_{alt_cyt}, which were lower in the MTA-treated cells (0.31 ± 0.05 pmol cell^{-1} day^{-1}) than in REF (0.84 ± 0.20 pmol cell^{-1} day^{-1}).

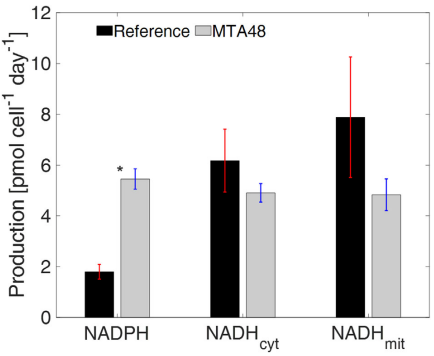

FIGURE 7 Comparison of NADPH, $NADH_{cyt}$, and $NADH_{mit}$ production in reference culture and MTA-treated culture. *Indicates a significant difference ($p < 0.05$)

4 | DISCUSSION

The addition of MTA and its boosting effect on the CSP in CHO-DP12 cells was first studied by Verhagen et al. (2020) [28,29]. MTA plays an essential role in mammalian cell metabolism, especially in polyamine synthesis [30,31]. In this pathway, MTA serves as an intermediate decarboxylation product of SAM to produce spermidine and spermine. High MTA levels are anticipated to inhibit polyamine biosynthesis, finally inducing cell-cycle arrest [50]. Besides, MTA is known to impact gene expression patterns, including apoptosis and cell proliferation in various mammalian cells [32,35]. In summary, MTA serves as a multi-level regulatory compound that exerts genetic, epigenetic, and metabolic control.

The reduction in spermidine and spermine synthesis after MTA addition is known to induce S-phase arrest in CHO cells [51]. This study confirmed the cytostatic effect, as displayed in Figure 1. MTA addition significantly reduced the maximum VCD and cell-specific growth rate (Figure 2A). Concomitantly, cellular volume increased (Figure 3A), cell-cycle distribution changed (Figure 3B), and CSP (q_{mAb}) (Figure 4) increased following MTA addition. Cellular fractions in the S- and G2-phases were temporarily increased 36 h after MTA addition, while the number of cells in G1-phase decreased (Figure 3B). The increase in q_{mAb} (Figure 4) 48 h after MTA addition might be attributed to cell-cycle arrest, as previously reported by independent studies [20,21]. Notably, CSP raise is not limited to a distinct cell-cycle phase.

Moreover, increase in cell volumes [52,53] have been reported to enhance CSP. Although rising cell volumes were observed in our study (Figure 3A), comparably low CVPs suggested that post-MTA CSP improvements were not caused by rising cell volumes alone (Figure 4). Indeed, the CVPs of MTA-treated cells remained significantly higher compared to the REF observation (Figure 4). However, fundamental reorganization of metabolism in arrested cells is supposed to be the key factor explaining rising CSPs [54].

Metabolic rearrangements were studied via ^{13}C labeling analysis. Thus, the approach complements earlier studies by Verhagen et al. (2020) [28,29], which focused on the SAM/MTA interplay and transcriptional responses after MTA feeding. Particularly, compartment-specific flux analysis was applied according to a previously reported protocol [18] for determining the putative impact of NADPH supply. Moreover, compartment-specific metabolomics essentially enabled flux tracking inside cellular compartments to unravel the putative impact of trans-compartment shuttling activities. Both data are qualified as important information per se.

MTA addition apparently influences the energetic status of the cells, which is reflected by an increase in cytosolic ATP pools (Figure 5). We anticipate that anabolic ATP needs are reduced in MTA treated cells as growth rates slowed down. Consequently, ATP pools increased meanwhile. Interestingly, similar observations of ATP rise were made in growth/cell-cycle arrested CHO cells [11]. The temporal rise in ATP levels likely inhibits phosphofructokinase (PFK) activity, considering the equally high ATP inhibition constants [55–57]. This metabolic inhibition may explain why fluxes through PFK are lower following MTA addition compared to REF cultures (Figure 6).

Moreover, Moreadith and Lehninger (1984) showed that malic enzyme activity is inhibited by high ATP levels [58]. Consequently, enhanced flux into the oxidative PPP is likely to reflect ATP-mediated metabolic inhibition of PFK and malic enzyme. The latter caused a reduction in NADPH formation, which was counterbalanced by an increase in PPP fluxes, ultimately achieving elevated NADPH production (Figure 7). The coincidence of metabolic rearrangement and cell-cycle arrest following MTA addition is consistent with the findings of Vizán et al. (2009) [59]. The authors additionally observed a relatively high oxidative PPP activity during the late G1 and S phases, suggesting that more precursors for nucleotide biosynthesis are needed during the S-phase in the cell cycle.

In addition, compartment-specific flux analysis revealed that OGC flux was reversed in MTA-supplemented cultures compared to REF. Whereas OGC exported malate into the cytosol in REF, OGC imported cytosolic malate in MTA-treated cultures. Nevertheless, malate net export into the cytosol continued to be realized via DIC. v_{DIC} was comparable with that of the reference; however, lack of OGC contribution reduced the net malate export into the cytosol

following MTA addition. Consequently, cytosolic malate was adapted to the decrease in cytosolic malic enzyme activity. Notably, the reversion of OGC reverted the flux of the counter ion αKG. Specifically, instead of importing αKG in the REF culture, αKG was exported into the cytosol in the MTA-treated cultures.

In REF, L-glutamine was deaminated via cytosolic glutaminase and glutamate dehydrogenase before importing αKG into the mitochondria. Because OGC shuttling is reversed, the MTA-treated cells require an alternative pathway to fuel the L-glutamine intermediate into CAC. Nevertheless, L-glutamine was deaminated via cytosolic glutaminase. Next, L-glutamate was imported into the mitochondrion via the amplified activities of the shuttle AGC. Subsequent deamination to αKG occurred in the mitochondrion. Interestingly, the potential export of mitochondrial L-glutamate via GC slowed down to ensure sufficient L-glutamate supply inside the mitochondrion.

The compartment-specific ^{13}C MFA additionally revealed that alanine amino-transferase (alt_{mit} and alt_{cyt}) activities were reduced in the MTA-treated culture. As L-glutamate was net imported into the mitochondria, the formation of L-alanine as the amino receptor from L-glutamate in the cytosol was significantly reduced (Figure 6). Consequently, less L-alanine was imported into the mitochondria (reduced m_{ala}). Furthermore, the substrate αKG of alt_{mit} was shuttled out of the mitochondria in exchange with malate and $v_{alt,\mathrm{mit}}$ was finally reduced. In essence, the activity of intracellular L-alanine metabolism was lowered, which led to increased L-alanine secretion into the medium.

Both scenarios reflect the changes in L-glutamine metabolism; they are essentially consequences of the rearrangement of glycolytic fluxes following MTA addition. Specifically, the temporal ATP rise was likely to inhibit PFK and cytosolic malic enzyme activities, which resulted in strongly amplified PPP fluxes for improving NADPH formation. Cytosolic malic enzyme lost its dominant role as a key NADPH supplier, which resulted in reduced mitochondrial malate exports and L-glutamine metabolic rearrangements, as described above.

Junghans et al. (2019) previously outlined the high sensitivity and positive correlation between NADPH supply and CSP for monoclonal antibody formation in CHO cells [18]. Their compartment-specific metabolome analysis revealed cytosolic malic enzyme as the key NADPH provider in growing cells. Previously, the crucial role of malic enzyme as the major NADPH source was anticipated by Ahn and Antoniewicz (2011) and Templeton et al. (2013) [16,17]. Sengupta et al. (2011) analyzed fluxes in late-stage non-growing CHO and disclosed increasing fluxes into the PPP, apparently for NADPH formation [60]. Furthermore, Tuttle et al. (2000) observed a 200-fold increase in G6PDH activity under oxidative stress conditions [61].

The key reason for the occurrence of fundamental metabolic reprogramming in arrested cells remains open and deserves future studies. However, a beneficial link to heterologous protein formation exists. Flux balance analysis using the simplified metabolic model [62] published by Verhagen et al. (2020c) considered that the maximum NADPH supply should be supported by high cytosolic malic enzyme flux and high oxidative PPP activity (Supplementary Material 3). Interestingly, MTA treatment provides an optimal flux distribution to maximize the NADPH supply. This observation opens the door for bioprocess optimization, including investigation of the impact of serial MTA bolus shots to extend the phase of high-level CSPs.

Alternately, metabolic engineering strategies may focus on redirecting fluxes for the highest NADPH supply. Balsa et al. (2020) evaluated deletions of *G6PDH*, *ME1*, and *IDH1* to foster PPP fluxes and NADPH formation [63]. However, *G6PDH* deletion resulted in higher oxidative stress, slowed down growth, and even led to cell death. This finding is in accordance with the observations of Tuttle et al. (2000) [61]. Till date, deletions of *ME1* or *IDH1* have not been reported to induce anticipated NADPH improvements.

5 | CONCLUSIONS

The current study merges recent approaches of compartment-specific metabolomics and non-stationary ^{13}C flux analysis to investigate the impact of MTA addition on monoclonal antibody-producing CHO cells. Complementing the studies of Verhagen et al. (2020), improvement in CSPs was determined to be tightly linked with cellular arrest and reprogramming of metabolism. MTA addition initiates a cascade of regulatory responses comprising cell proliferation, transcription, and metabolic control, still keeping cell viabilities on a high level. Most likely, the first is the consequence of MTA-mediated feedback inhibition in polyamine biosynthesis. The resulting accumulation of ATP impairs glycolytic and malic enzyme fluxes, finally enabling significantly enhanced NADPH supply via boosting PPP activity. This knowledge should be exploited via future bioprocess development and metabolic engineering studies for improving the CSP for next-generation CHO hosts. Besides, it may illustrate the close network of cellular responses ranging from cell proliferation to reverting mitochondrial shuttle activities because of MTA addition to a CHO culture.

Nomenclature

C_x	Viable cell density (VCD) (cell/mL)
C_i	Extracellular concentration of metabolite *i* (mmol/L)
q_i	Extracellular production/consumption rate of *i* (pmol/cell/day)
S	Stoichiometric matrix of the metabolic model ([-])
v_i	Intracellular flux of reaction *j* (pmol/cell/day)
I	metabolite pool size (fmol/cell)
x	simulated mass isotopomer species ([-])
x_m	measured mass isotopomer species ([-])

Greek symbols

μ	cell-specific growth rate (h^{-1})
β_j	flux reversibility constant of reaction *j* ([-])
σ	standard deviation ([-])

ACKNOWLEDGMENTS

The authors gratefully acknowledge funding from the Bundesministerium für Bildung und Forschung (BMBF, DipImpact Project, Funding Number 031L0077A). The authors thank DipImpact project partners supporting this study: Andreas Unsöld (Boehringer Ingelheim Pharma GmbH & Co. KG), Martin Schilling (Evonik Nutrition and Care GmbH), and Christoph Heinrich (Xell AG). Furthermore, the authors thank the research group of Prof. Dr. Noll for providing CHO-DP12 cells.

Open access funding enabled and organized by Projekt DEAL.

CONFLICT OF INTEREST

The authors have declared no conflict of interest.

DATA AVAILABILITY STATEMENT

The datasets supporting the conclusions of this article are included within the article and its additional files.

ORCID

Andy Wiranata Wijaya https://orcid.org/0000-0001-9388-7357

REFERENCES

1. Walsh, G., Biopharmaceutical benchmarks 2018. Nat. Biotechnol. 2018, 36, 1136–1145.
2. Reinhart, D., Damjanovic, L., Kaisermayer, C. and Kunert, R., Benchmarking of commercially available CHO cell culture media for antibody production. Appl. Microbiol. Biotechnol. 2015, 99, 4645–4657.
3. Wurm, F. M., Production of recombinant protein therapeutics in cultivated mammalian cells. Nat Biotechnol. 2004, 22, 1393–1398.
4. Becker, M., Junghans, L., Teleki, A., Bechmann, J. et al., Perfusion cultures require optimum respiratory ATP supply to maximize cell-specific and volumetric productivities. Biotechnol. Bioeng. 2019, 116, 951–960.
5. Templeton, N., Smith, K. D., McAtee-Pereira, A. G., Dorai, H. et al., Application of ^{13}C flux analysis to identify high-productivity CHO metabolic phenotypes. Metab. Eng. 2017, 43, 218–225.
6. Zhang, H., Wang, H., Liu, M., Zhang, T. et al., Rational development of a serum-free medium and fed-batch process for a GS-CHO cell line expressing a recombinant antibody. Cytotechnology 2013, 65, 363–378.
7. Kildegaard, H. F., Baycin-Hizal, D., Lewis, N. E. and Betenbaugh, M. J., The emerging CHO systems biology era: harnessing the 'omics revolution for biotechnology. Curr. Opin. Biotechnol. 2013, 24, 1102–1107.
8. Wurm, F. M. and Hacker, D., First CHO genome. Nat. Biotechnol. 2011, 29, 718–720.
9. Xu, X., Nagarajan, H., Lewis, N., Pan, S. et al., The genomic sequence of the Chinese hamster ovary (CHO)-K1 cell line. Nat. Biotechnol. 2011, 29, 735–741.
10. Hefzi H, Ang KS, Hanscho M, Bordbar, A. et al., A consensus genome-scale reconstruction of Chinese hamster ovary cell metabolism. Cell Syst. 2016, 3, 434-443.
11. Pfizenmaier, J., Junghans, L., Teleki, A. and Takors, R., Hyperosmotic stimulus study discloses benefits in ATP supply and reveals miRNA/mRNA targets to improve recombinant protein production in CHO cells. Biotechnol. J. 2016, 11, 1037–1047.
12. Sha, S., Bhatia, H. and Yoon, S., An RNA-seq-based transcriptomic investigation into productivity and growth variants in Chinese hamster ovary cells. J. Biotechnol. 2018, 271, 37–46.
13. Feichtinger, J., Hernández, I., Fischer, C., Hanscho, M. et al., Comprehensive genome and epigenome characterization of CHO cells in response to evolutionary pressures and over time Biotechnol. Bioeng. 2016, 113, 2241–2253.
14. Harreither E, Hackl M, Pichler J, Shridhar, S. et al., Microarray profiling of preselected CHO host cell subclones identifies gene expression patterns associated with increased production capacity. Biotechnol. J. 2015, 10, 1625–1638.
15. Chong, W.P.K., Thng, S. H., Hiu, A. P., Lee, D. Y. et al., LC-MS-based metabolic characterization of high monoclonal antibody-producing Chinese hamster ovary cells. Biotechnol. Bioeng. 2012, 109, 3103–3111.
16. Ahn, W. S. and Antoniewicz, M. R., Metabolic flux analysis of CHO cells at growth and non-growth phases using isotopic tracers and mass spectrometry. Metab. Eng. 2011, 13, 598–609.
17. Templeton, N., Dean, J., Reddy, P. and Young, J. D., Peak antibody production is associated with increased oxidative metabolism in an industrially relevant fed-batch CHO cell culture. Biotechnol. Bioeng. 2013, 110, 2013–2024.
18. Junghans, L., Teleki, A., Wijaya, A. W., Becker, M. et al., From nutritional wealth to autophagy: *in vivo* metabolic dynamics in the cytosol, mitochondria, and shuttles of IgG-producing CHO cells. Metab. Eng. 2019, 54, 145–159.
19. Sunley, K. and Butler, M., Strategies for the enhancement of recombinant protein production from mammalian cells by growth arrest. Biotechnol. Adv. 2010, 28, 385–394.
20. Fox, S. R., Patel, U. A., Yap, M. G. S. and Wang, D. I. C., Maximizing interferon-γ production by Chinese hamster ovary cells through temperature shift optimization: experimental and modeling. Biotechnol. Bioeng. 2004, 85, 177–184.

21. Pfizenmaier, J., Matuszczyk, J. C. and Takors, R., Changes in intracellular ATP content of CHO cells in response to hyperosmolality. Biotechnol. Prog. 2015, 31, 1212–1216.
22. Jiang, Z. and Sharfstein, S. T., Sodium butyrate stimulates monoclonal antibody over-expression in CHO cells by improving gene accessibility. Biotechnol. Bioeng. 2008, 100, 189–194.
23. Coronel, J., Klausing, S., Heinrich, C., Noll, T. et al., Valeric acid supplementation combined to mild hypothermia increases productivity in CHO cell cultivations. Biochem. Eng. J. 2016, 114, 101–109.
24. Ahn, Y. H., Han, K., Yoon, S. K. and Song, J. Y., Effect of glycine betaine as osmoprotectant on the production of erythropoietin by CHO cells in hyperosmotic serum free media culture. in *Animal Cell Technology*: *Basic & Applied Aspects*, Springer, Dordrecht, 1999. pp. 247–250.
25. Toronjo-Urquiza, L., Acosta-Martin, A. E., James, D. C., Nagy, T. et al., The use of catechins in Chinese hamster ovary cell media for the improvement of monoclonal antibody yields and reduction of acidic species. Biotechnol. Prog. 2020, 36, e2980.
26. Al-Rubeai, M., Emery, A. N., Chalder, S. and Jan, D. C., Specific monoclonal antibody productivity and the cell cycle-comparisons of batch, continuous and perfusion cultures. Cytotechnology 1992, 9, 85–97.
27. Ginzberg, M. B., Kafri, R. and Kirschner, M., Cell biology. On being the right (cell) size. Science 2015, 348, 1245075.
28. Verhagen, N., Teleki, A., Heinrich, C., Schilling, M. et al., S-adenosylmethionine and methylthioadenosine boost cellular productivities of antibody-forming Chinese hamster ovary cells. Biotechnol. Bioeng. 2020a, 117, 3239–3247.
29. Verhagen, N., Zieringer, J. and Takors, R., Methylthioadenosine (MTA) boosts cell-specific productivities of Chinese hamster ovary cultures: dosage effects on proliferation, cell cycle and gene expression. FEBS Open Bio 2020b, 10, 2791–2804.
30. Pegg, A. E., Polyamine metabolism and its importance in neoplastic growth and a target for chemotherapy. Cancer Res. 1988, 48, 759–774. http://www.ncbi.nlm.nih.gov/pubmed/3123052
31. Williams-Ashman, H. G., Seidenfeld, J. and Galletti, P., Trends in the biochemical pharmacology of 5-deoxy-5-methylthioadenosine. Biochem. Pharmacol. 1982, 31, 277–288.
32. Ansorena, E., García-Trevijano, E. R., Martínez-Chantar, M. L., Huang, Z. Z. et al., S-adenosylmethionine and methylthioadenosine are antiapoptotic in cultured rat hepatocytes but proapoptotic in human hepatoma cells. Hepatology 2002, 35, 274–280.
33. Law, R. E., Stimmel, J. B., Damore, M. A., Carter, C. et al., Lipopolysaccharide-induced NF-kappa B activation in mouse 70Z/3 pre-B lymphocytes is inhibited by mevinolin and 5'-methylthioadenosine: roles of protein isoprenylation and carboxyl methylation reactions. Mol. Cell. Biol. 1992, 12, 103–111.
34. Pascale, R. M., Simile, M. M., De Miglio, M. R. and Feo, F., Chemoprevention of hepatocarcinogenesis: S-adenosyl-L-methionine. Alcohol 2002, 27, 193–198.
35. Riscoe, M. K., Tower, P. A. and Ferro, A. J., Mechanism of action of 5-methylthioadenosine in S49 cells. Biochem. Pharmacol. 1984, 33, 3639–3643.
36. Henderson, J. W. and Brooks, A. Improved amino acid methods using Agilent Zorbax Eclipse Plus C18 columns for a variety of Agilent LC instrumentation and separation goals. *Agilent Technologies*, Santa Clara, CA, USA. (2010).
37. Matuszczyk, J. C., Teleki, A., Pfizenmaier, J. and Takors, R., Compartment-specific metabolomics for CHO reveals that ATP pools in mitochondria are much lower than in the cytosol. Biotechnol. J. 2015, 10, 1639–1650.
38. Cserjan-Puschmann, M., Kramer, W., Duerrschmid, E., Striedner, G. et al., Metabolic approaches for the optimisation of recombinant fermentation processes. Applied Microbiol. Biotechnol. 1999, 53, 43–50.
39. Teleki, A., Sánchez-Kopper, A. and Takors, R., Alkaline conditions in hydrophilic interaction liquid chromatography for intracellular metabolite quantification using tandem mass spectrometry. Anal. Biochem. 2015, 475, 4–13.
40. Feith, A., Teleki, A., Graf, M., Favilli, L. et al., HILIC-Enabled ^{13}C metabolomics strategies: comparing quantitative precision and spectral accuracy of QTOF high- and QQQ low-resolution mass spectrometry. Metabolites 2019, 9.
41. Teleki, A., Rahnert, M., Bungart, O., Gann, B. et al., Robust identification of metabolic control for microbial l-methionine production following an easy-to-use puristic approach. Met. Eng. 2017, 41, 159–172.
42. Zimmermann, M., Sauer, U. and Zamboni, N., Quantification and mass isotopomer profiling of α-keto acids in central carbon metabolism. Anal. Chem. 2014, 86, 3232–3237.
43. Sheikh, K., Förster, J. and Nielsen, L. K., Modeling hybridoma cell metabolism using a generic genome-scale metabolic model of *Mus musculus*. Biotechnol. Prog. 2005, 21, 112–121.
44. Schaub, J., Mauch, K. and Reuss, M., Metabolic flux analysis in Escherichia coli by integrating isotopic dynamic and isotopic stationary ^{13}C labeling data. Biotechnol. Bioeng. 2008, 99, 1170–1185.
45. Maier, K., Hofmann, U., Reuss, M. and Mauch, K., Identification of metabolic fluxes in hepatic cells from transient ^{13}C-labeling experiments: Part II. Flux estimation. Biotechnol. Bioeng. 2008, 100, 355–370.
46. Schmidt, K., Carlsen, M., Nielsen, J. and Villadsen, J., Modeling isotopomer distributions in biochemical networks using isotopomer mapping matrices. Biotechnol. Bioeng. 1997, 55, 831–840.
47. Nicolae, A., Wahrheit, J., Bahnemann, J., Zeng, A. P. et al., Non-stationary 13 C metabolic flux analysis of Chinese hamster ovary cells in batch culture using extracellular labeling highlights metabolic reversibility and compartmentation. BMC Syst. Biol. 2014, 8, 50.
48. Antoniewicz, M. R., Kelleher, J. K. and Stephanopoulos, G., Determination of confidence intervals of metabolic fluxes estimated from stable isotope measurements. Met. Eng. 2006, 8, 324–337.
49. Hosios, A. M. and Vander Heiden, M. G., Redox requirements of proliferating mammalian cells. J. Biol. Chem. 2018, 293, 7490–7498.
50. Oredsson, S. M., Polyamine dependence of normal cell-cycle progression. Biochem. Soc. Trans. 2003, 31, 366–370.
51. Alm, K. and Oredsson, S. M., The organization of replicon clusters is not affected by polyamine depletion. J. Struct. Biol. 2000, 131, 1–9.
52. Lloyd, D. and Murray, D. B., Redox cycling of intracellular thiols: state variables for ultradian, cell division cycle, and circadian cycles? in The Redox State and Circadian Rhythms, Springer, Dordrecht, 2000. pp. 85–94.

53. Pan, X., Dalm, C., Wijffels, R. H. and Martens, D. E., Metabolic characterization of a CHO cell size increase phase in fed-batch cultures. Appl. Microbiol. Biotechnol. 2017, 101, 8101–8113.
54. Fussenegger, M., Mazur, X. and Bailey, J. E., A novel cytostatic process enhances the productivity of Chinese hamster ovary cells. Biotechnol. and Bioeng. 1997, 55, 927–939.
55. Furuya, E. and Uyeda, K., Regulation of phosphofructokinase by a new mechanism Activation factor binding to phosphorylated enzyme. J. Biol. Chem. 1980, 255, 11656–11659.
56. Mansour, T. E., Studies on heart phosphofructokinase: purification, inhibition, and activation. J. Biol. Chem. 1963, 238, 22852292.
57. Passonneau, J. V. and Lowry, O. H., Role of phosphofructokinase in metabolic regulation. Adv. Enz. Reg. 1964, 2, 265–274.
58. Moreadith, R. W. and Lehninger, A. L., Purification, kinetic behavior, and regulation of NAD (P)+ malic enzyme in tumor mitochondria. J. Biol. Chem. 1984, 259, 6222–6227.
59. Vizán, P., Alcarraz-Vizán, G., Díaz-Moralli, S., Solovjeva, O. N. et al., Modulation of pentose phosphate pathway during cell cycle progression in the human colon adenocarcinoma cell line HT29. IJC 2009, 124, 2789–2796.
60. Sengupta, N., Rose, S. T. and Morgan, J. A., Metabolic flux analysis of CHO cell metabolism in the late growth phase. Biotechnol. Bioeng. 2011, 108, 82–92.
61. Tuttle, S., Stamato, T., Perez, M. L. and Biaglow, J., Glucose-6-phosphate dehydrogenase and the oxidative pentose phosphate cycle protect cells against apoptosis induced by low doses of ionizing radiation. Radiat. Res. 2000, 153, 781–787.
62. Verhagen, N., Wijaya, A. W., Teleki, A., Fadhlullah, M. et al., Comparison of L-tyrosine-containing dipeptides reveals maximum ATP availability for L-prolyl-L-tyrosine in CHO cells. Eng. Life Sci. 2020c, 20, 384–394.
63. Balsa, E., Perry, E. A., Bennett, C. F., Jedrychowski, M. et al., Defective NADPH production in mitochondrial disease complex I causes inflammation and cell death. Nat. Commun. 2020, 11, 2714.

SUPPORTING INFORMATION

Additional supporting information may be found in the online version of the article at the publisher's website.

How to cite this article: Wijaya, A. W., Verhagen, N., Teleki, A., Takors, R., Compartment-specific C metabolic flux analysis reveals boosted NADPH availability coinciding with increased cell-specific productivity for IgG1 producing CHO cells after MTA treatment. Eng. Life Sci. 2021, 21, 832–847. https://doi.org/10.1002/elsc.202100057

Paper V

Comparison of L-tyrosine containing dipeptides reveals maximum ATP availability for L-prolyl-L-tyrosine in CHO cells

Natascha Verhagen, **Andy Wiranata Wijaya**, Attila Teleki, Muhammad Fadhlullah,

Andreas Unsöld, Martin Schilling, Christoph Heinrich & Ralf Takors

Received: 21 March 2020 | Revised: 10 May 2020 | Accepted: 18 May 2020

DOI: 10.1002/elsc.202000017

Engineering in Life Sciences

RESEARCH ARTICLE

Comparison of L-tyrosine containing dipeptides reveals maximum ATP availability for L-prolyl-L-tyrosine in CHO cells

Natascha Verhagen[1] | **Andy Wiranata Wijaya**[1] | **Attila Teleki**[1] | **Muhammad Fadhlullah**[1] | **Andreas Unsöld**[2] | **Martin Schilling**[3] | **Christoph Heinrich**[4] | **Ralf Takors**[1]

[1] Institute of Biochemical Engineering, University of Stuttgart, Stuttgart, Germany

[2] Boehringer Ingelheim Pharma GmbH & Co. KG, Biberach, Germany

[3] Evonik Nutrition and Care GmbH, Darmstadt, Germany

[4] Xell AG, Bielefeld, Germany

Correspondence
Prof. Dr.-Ing Ralf Takors, University of Stuttgart, Institute of Biochemical Engineering, Allmandring 31, 70563 Stuttgart, Germany.
Email: ralf.takors@ibvt.uni-stuttgart.de

Funding information
Bundesministerium für Bildung und Forschung (BMBF), Grant/Award Number: 031L0077A

Abstract

Increasing markets for biopharmaceuticals, including monoclonal antibodies, have triggered a permanent need for bioprocess optimization. Biochemical engineering approaches often include the optimization of basal and feed media to improve productivities of Chinese hamster ovary (CHO) cell cultures. Often, L-tyrosine is added as dipeptide to deal with its poor solubility at neutral pH. Showcasing IgG1 production with CHO cells, we investigated the supplementation of three L-tyrosine (TYR, Y) containing dipeptides: glycyl-L-tyrosine (GY), L-tyrosyl-L-valine (YV), and L-prolyl-L-tyrosine (PY). While GY and YV led to almost no phenotypic and metabolic differences compared to reference samples, PY significantly amplified TYR uptake thus maximizing related catabolic activity. Consequently, ATP formation was roughly four times higher upon PY application than in reference samples.

KEYWORDS
dipeptides, flux balance analysis, CHO, media optimization, monoclonal antibody

1 | INTRODUCTION

Chinese hamster ovary (CHO) cells are important hosts for recombinant protein production and are the preferred system for monoclonal antibody production [1]. Early bioprocesses relied on the use of animal-derived sera like FBS to meet the growth and productivity needs of those cells [2]. However, the use of such sera is no longer favored because of the inherent risk of viral contamination [3] and typically high lot-to-lot variations, potentially affecting bioprocess performance and product quality [4,5].

Chemically defined (CD) media were introduced about five decades ago and predominately consisted of essential L-amino acids (Eagle's media [6]; F12 media [7]). At a concentration of about 2 mg/mL in water at room temperature and neutral pH, L-tyrosine (TYR) has the lowest solubility of all essential amino acids. Accordingly, only small amounts of TYR can be added to basal and feed media

Abbreviations: CAC, citric acid cycle; CHO, Chinese hamster ovary; EMP, Embden-Meyerhof Parnas; FBA, flux balance analysis; GY, glycyl-L-tyrosine; mAB, monoclonal antibody; MAS, malate-aspartate shuttle; NADH, nicotinamide adenine dinucleotide; PY, L-prolyl-L-tyrosine; REF, reference; TYR, L-tyrosine; VCD, viable cell density; YV, L-tyrosyl-L-valine

to avoid unwanted media precipitation, thereby trying to ensure process stability [5]. Non-wanted TYR insolubility could be prevented by feeding TYR with high pH because the latter greatly increases TYR solubility. However, pH control, salt concentration, and precipitation in the bioreactor are potential problems that can occur with such an approach. A safer and more robust approach is the replacement of single TYR by TYR-containing, chemically defined dipeptides, which can increase solubility up to 250-fold at neutral pH [8].

The industrial performance of CHO cells using specific TYR dipeptides was examined by Kang et al. [5], who demonstrated that substituting free amino acids with L-tyrosyl-L-lysine (YK), L-tyrosyl-L-histidine (LH), L-tyrosyl-L-alanine (YA), and L-tyrosyl-L-valine (YV) decreased secretion of lactate and ammonium by-products. Sánchez-Kopper et al. (2016) [9] showed that dipeptides such as L-alanyl-L-tyrosine (AY), glycyl-L-tyrosine (GY), and L-prolyl-L-tyrosine (PY) are taken up by CHO cells and cleaved intracellularly before entering catabolic and anabolic pathways. Furthermore, recent patents [10] demonstrate industrial interest in protecting the use of TYR-containing dipeptides in feed media.

In this study, we focus on the use of TYR-dipeptides as additional feeding compounds. We investigated the impact of related dipeptides on cellular metabolism. While the potential of TYR-containing dipeptides has been shown by the above studies, little is known about the metabolic consequences resulting from their consumption. Showcasing IgG1 production with CHO cells, our investigation focused on the metabolic impact of dipeptide bolus feeding. We chose GY, YV, and PY as our model dipeptides. Phenotypic tests were complemented by quantitative metabolomics and flux analysis to decipher differences caused by dipeptides compared to cells lacking dipeptides in their feed. Whereas GY and YV did not significantly alter metabolism, PY increased the ATP supply, which represents a promising optimization target for future studies.

PRACTICAL APPLICATION

L-Tyrosine (TYR) is an essential amino acid for mammalian cells and shows poor solubility in cell culture media at neutral pH. Accordingly, TYR-containing dipeptides are commonly used that offer improved cellular supply. Here, we investigate the application of three L-tyrosine containing dipeptides showcasing the production of IgG1 with Chinese hamster ovary (CHO) cells. L-Prolyl-L-tyrosine (PY) caused the highest intracellular ATP availability that is an important property for all experimentalists in this field.

2 | MATERIALS AND METHODS

2.1 | Seed train, shake flask cultivation, and addition of dipeptides

The following dipeptides containing TYR were supplied by Evonik Nutrition and Care GmbH (Darmstadt, Germany): glycyl-L-tyrosine (GY), L-prolyl-L-tyrosine (PY), and L-tyrosyl-L-valine (YV). The IgG1-producing CHO suspension cell line BIBH1 (provided by Boehringer Ingelheim Pharma GmbH & Co. KG, Biberach, Germany) was grown in chemically defined TC-42 medium (Xell AG, Bielefeld, Germany) supplemented with 4 mM L-glutamine (Carl Roth GmbH & Co. KG, Karlsruhe, Germany), 200 nM methotrexate (Sigma–Aldrich, Steinheim, Germany), and 0.1 g/L geneticin (Fisher-Scientific, Schwerte, Germany). Seed train and experiments were performed in pre-sterilized disposable shake flasks (Corning Inc., New York, USA) in a humidified and incubated rotary shaker (Infors HT Minitron, Infors GmbH, Einsbach, Germany) at 37°C, 150 rpm with 50 mm displacement, and 5% CO_2. Stock solutions of TYR-based dipeptides were solved at neutral pH and introduced at the beginning of cultivation (0.05 mM). Furthermore, daily additions (0.05 mmol) of dipeptides were performed from 48 to 120 h of cultivation. In reference cell cultures, sterilized water was used to mimic the additional liquid volume in experimental cultures. Cultivation was performed with biological duplicates in two independent experiments.

2.2 | Extracellular analysis

Samples were taken at least once a day during cultivation. Viable cell density and viability were determined using trypan blue staining and a Cedex XS cell counter (Innovatis AG, Bielefeld, Germany). The extracellular concentrations of D-glucose (D-glc) and L-lactate (L-lac) were determined using a Labotrace automatic analyzer (Trace Analytics GmbH, Braunschweig, Germany). The concentration of produced IgG was determined with an ELISA [11]. All sampling and measurement procedures were performed with three technical replicates. The extracellular concentrations of all proteinogenic amino acids with the exception of L-cysteine were quantified using reversed-phase chromatography (Agilent 1200 Series, Agilent Technologies, Waldbronn, Ger-

many) with a precolumn fluorometric derivatization step using ortho-phthaldiealdehyde (OPA)/9-fluorenylmethyl chloroformate (FMOC) [12,13]. The internal standard γ-aminobutyric acid (GABA) was added to all standard-based external calibration levels and the analyzed samples.

2.3 | Intracellular analysis

For each intracellular sample, 1.6×10^7 cells were harvested, gently centrifuged (10 min, 300 × g, 4°C), washed, and quenched in liquid nitrogen. Washing steps were performed three times using ice-cold isotonic PBS solution to remove all extracellular compounds attached to the cells. Samples were taken after 60, 72, 76, 84, 96, 108, and 120 h of cultivation. Pre-processed cell pellets were stored at −70°C. The intracellular metabolome was extracted from defined pellets using an adapted cold methanol/chloroform extraction method [9]. An ice-cold 1:2 $CHCl_3$:MeOH solution was added to cells followed by ice-cold $CHCl_3$ solution and finally by ice-cold water, with 5 min of vortexing after each addition. Resulting suspensions were incubated for 1 h at 4°C in a rotary overhead-shaker. Phase separation was afterward achieved by centrifugation for 10 min at 3200 × g and 0°C. The upper aqueous phase was separated and stored at −70°C for further analysis. Dipeptide, amino acid, and central metabolite concentrations were determined on an HPLC system (Agilent 1200 Series) coupled with an Agilent 6410B triple quadrupole tandem mass spectrometer (QQQ-MS/MS, Agilent Technologies, Waldbronn, Germany). The LC–MS method was based on a bicratic (two-phase) zwitterionic hydrophilic interaction chromatography (ZIC-pHILIC) under alkaline mobile phase conditions without any derivatization [14,15]. Targeted metabolites were detected with high selectivity with pre-optimized precursor-to-product ion transitions and associated MS/MS settings in multiple reaction monitoring (MRM) mode. Absolute quantifications were performed by adapted standard-based external calibrations with constant addition of global internal standards (50 μM L-norvaline and GABA). Data were analyzed using MassHunter B.06.00 Analysis software.

Intracellular pools of AxP nucleotides were determined using an ion-pair-reversed-phase chromatography method with a HPLC system (Agilent 1200 Series) [16]. Underivatized samples were detected via UV light (diode array detector). Quantifications were performed by external standard calibration and selected samples were spiked with AMP, ADP, and ATP (internal calibration) to evaluate the influence of the sample matrix.

2.4 | Cell-specific rate estimations

Cell-specific rates of changes in extracellular metabolites were used as constraints when performing flux balance analysis (FBA). Cell-specific exo-metabolic rates were estimated from extracellular metabolite concentrations and viable cell density over time. Using Equations 1 and 2 and linear regression, growth rate and specific exo-metabolome uptake and secretion rates were estimated.

$$\frac{dC_X}{dt} = \mu C_x \Rightarrow \ln(C_x) = \mu(t - t_0) + \ln(C_0) \quad (1)$$

$$\frac{dC_i}{dt} = q_i C_x \Rightarrow C_i = \left(\frac{q_i}{\mu}\right) C_x - C_{i,0} \quad (2)$$

2.5 | Flux balance analysis

The metabolic model used in this study is a simplified genome-based model derived from the following sources: KEGG [17], CHOMINE [18], and *Mus musculus* GeM [19]. The detailed metabolic model is presented in Supporting Information S1. This model includes the central carbon metabolic pathway (consisting of the Embden-Meyerhof Parnas [EMP; glycolysis], pentose phosphate pathway [PPP], citric acid cycle [CAC], and anaplerotic reactions), the biosynthesis of essential biomass precursors (fatty acids, steroids, glycogen, and nucleotides), and amino acid catabolism. The biomass composition required to model cell growth uses values reported by Sheikh et al. [20], whereas antibody composition is based on Martens [21]. Dipeptide cleavage occurs intracellularly following findings reported by Sánchez-Kopper et al. [9].

FBA was used to predict the fate of intracellular dipeptides and determine their role in CHO metabolism. FBA was performed using Insilico Discovery (Insilico Biotechnology, Stuttgart, Germany). FBA was carried out during the exponential growth phase, when the highest amount of dipeptide consumption occurs. Multiple assumptions were made for FBA. First, FBA was performed under a metabolic steady state with a constant growth rate and specific rates of change in D-glucose, L-lactate, L-glutamine, and L-asparagine levels. Additionally, the P/O ratio of nicotinamide adenine dinucleotide (NADH) and flavin adenine dinucleotide ($FADH_2$) oxidation was assumed to be 1.5 and 1.2 mol ATP per mol of the nucleotide, respectively. FBA was performed using growth rate and extracellular metabolome uptake/secretion rates as constraints. The objective function of FBA was to maximize the model-predicted growth rate.

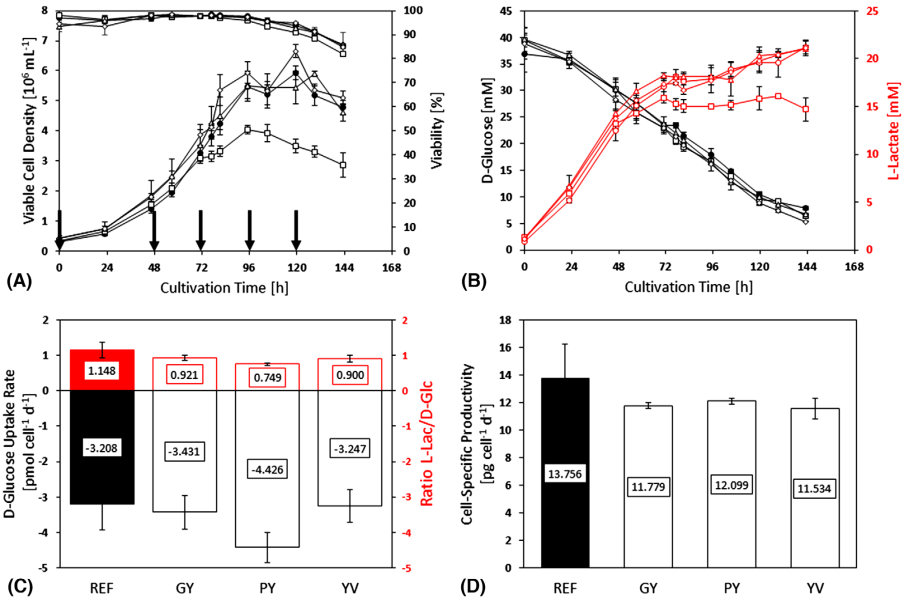

FIGURE 1 (A) Time courses of viable cell density [10^6 cells mL^{-1}] and viability [%] and (B) time courses of extracellular D-glucose (black) and L-lactate (red) concentrations [mM] of dipeptide supplemented cells (GY Δ, PY □, YV ◇) and reference (REF ●). Arrows indicate time points at which dipeptides or water were added. (C) Cell-specific rates of the exponential phase are calculated in [pmol $cell^{-1}$ d^{-1}] for D-glucose consumption (black) and D-glucose-to-L-lactate-ratio (red). (D) Cell-specific productivity [pg $cell^{-1}$ d^{-1}] of dipeptide supplemented cells (GY, PY, YV) and the reference (REF) in the exponential phase. Error bars show standard deviations of biological duplicates

Three simulations were performed for experimental and control cultures (REF, GY, PY, and YV) to obtain the maximum, minimum, and median rate predictions. Maximum (best-case scenario) and minimum predictions were simulated using the maximum or minimum uptake and secretion rates, respectively. For median estimation, maximum and minimum settings were applied as constraints. Upper and lower confidence intervals were calculated using twice the standard error of the predictions (i.e., 95% confidence level).

3 | RESULTS

3.1 | The addition of L-prolyl-L-tyrosine alters cell growth and metabolism

Initially, TYR-containing dipeptides were added to a final concentration of 0.5 mM to cell culture medium used to cultivate CHO BIBH1 cells for IgG1-antibody production. Fresh additions of TYR-containing dipeptides (0.05 mmol) took place after 48, 72, 96, and 120 h of cultivation (indicated by arrows in Figure 1). The addition of L-prolyl-L-tyrosine (PY) significantly reduced viable cell density (VCD), unlike the addition of glycyl-L-tyrosine (GY) and L-tyrosyl-L-valine (YV). Cells receiving regular additions of PY only reached a maximum viable cell density of $(4.030 \pm 0.153) \times 10^6$ cells/mL, which was approximately two-thirds of the viable cell densities of GY, YV, and reference (REF) cultures.

PY addition affected antibody titer (Supporting Information S2, Figure S1) whereas cell-specific antibody productivity was similar for all experimental conditions. Specific D-glucose consumption rates were highest after PY addition during the exponential phase. Furthermore, cells that grew in medium with PY showed reduced L-lactate formation reflected in the low ratio of D-glucose consumption to L-lactate secretion (PY: 0.749 ± 0.030 $mol_{D\text{-}Glucose}/mol_{L\text{-}Lactate}$; REF: 1.148 ± 0.161 $mol_{D\text{-}Glucose}/mol_{L\text{-}Lactate}$; Figure 1).

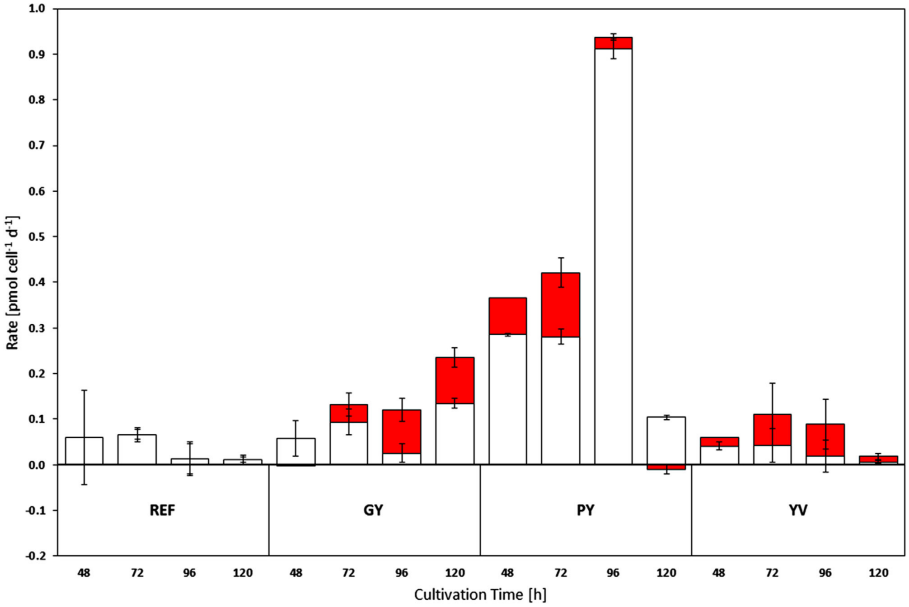

FIGURE 2 TYR uptake and release rates [pmol cell^{-1} d^{-1}] via dipeptides addition compared to reference cultures (REF) after 48, 72, 96, and 120 h of cultivation. Columns indicate the total levels of dipeptide uptake consisting of retained (white) and released (red) parts of TYR. Error bars show standard deviations of biological duplicates

3.2 | Dipeptide uptake depends on composition and causes metabolic changes

Uptake dynamics of TYR at different cultivation time points (48, 72, 96, and 120 h) are displayed in Figure 2. PY addition led to the largest total TYR uptake rates (indicated by the entire columns) and the largest fractions of TYR that remained intracellular (white columns) after 48, 72, and 96 h of cultivation. Remarkably, each addition of a TYR-containing dipeptide increased TYR uptake compared to reference cultures. However, some TYR from the decomposed dipeptide was always secreted (indicated by the red bar).

Small intracellular pools of dipeptides measured in intracellular extracts indicate the uptake of all dipeptides by cells. Intracellular fluctuations reflect extracellular bolus feeding. Repeated dipeptide addition to the medium (48, 72, 96, and 120 h) increased extracellular concentrations and consequently increased intracellular pool sizes of the intact dipeptides thereafter. Besides GY and YV, extracellular PY is depleted at 72 and 96 h demonstrating the faster uptake of PY (Supporting Information S2, Figure S2).

Uptake rates of the essential amino acid L-glutamine were similar in PY (-1.297 ± 0.047 pmol cell^{-1} d^{-1}), GY (-1.243 ± 0.170 pmol cell^{-1} d^{-1}), and REF (-1.373 ± 0.042 pmol cell^{-1} d^{-1}) conditions but differed under YV conditions (-1.028 ± 0.038 pmol cell^{-1} d^{-1}). In contrast, sizes of intracellular L-glutamine pools differed. Compared to REF cultures, YV addition increased the L-glutamine pool while GY addition diminished the L-glutamine pool and PY addition nearly depleted the L-glutamine pool (Figure 3).

As outlined in Figure 2, cells always consumed the surplus of TYR provided by dipeptide addition and retained different fractions of that TYR. The additional TYR provided by PY affected the energetic status of the cells and increased ATP pool sizes beginning from 72 h after cultivation (Figure 4). Simultaneously, AMP pool sizes decreased after dipeptide addition.

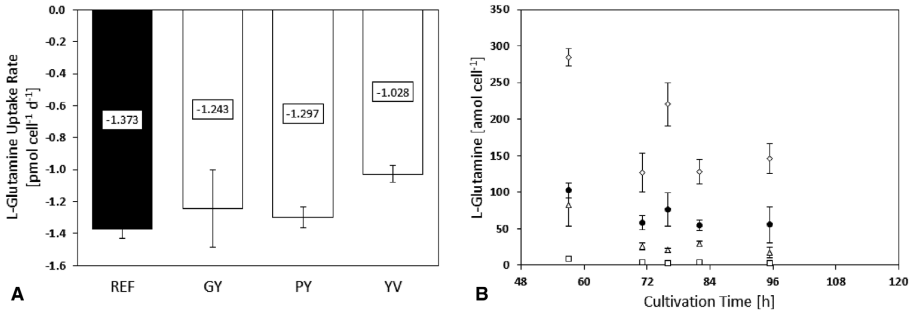

FIGURE 3 L-Glutamine consumption rates [pmol cell^{-1} d^{-1}] (A) and intracellular pool sizes [amol cell^{-1}] (B) of dipeptide-supplemented cells (GY Δ, PY □, YV ◇) and reference cells (REF ●). Negative values indicate an uptake. Error bars show standard deviations of biological duplicates

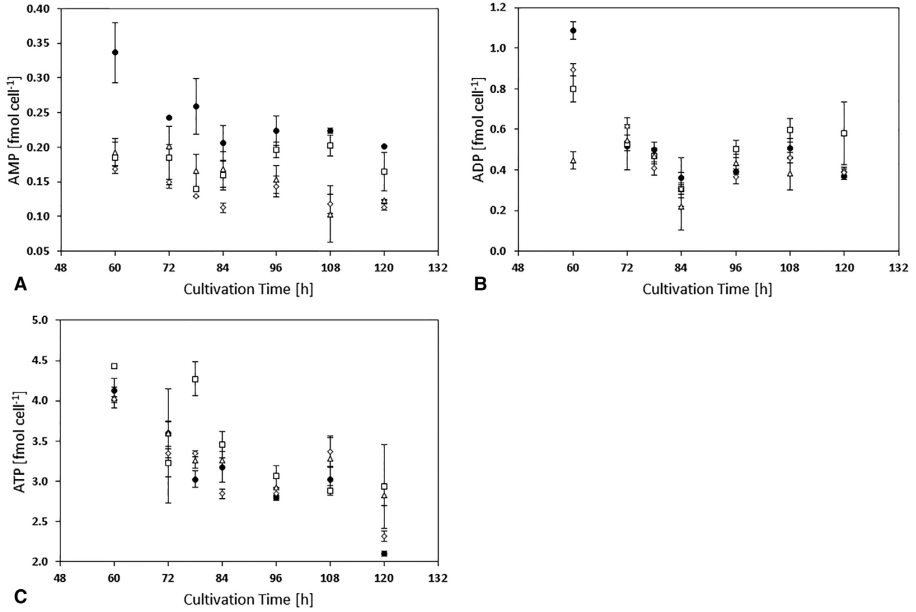

FIGURE 4 Intracellular pools of AMP (A), ADP (B), and ATP (C) [fmol cell^{-1}] of dipeptide supplemented cells (GY Δ, PY □, YV ◇) and reference cells (REF ●). Error bars show standard deviations of biological duplicates

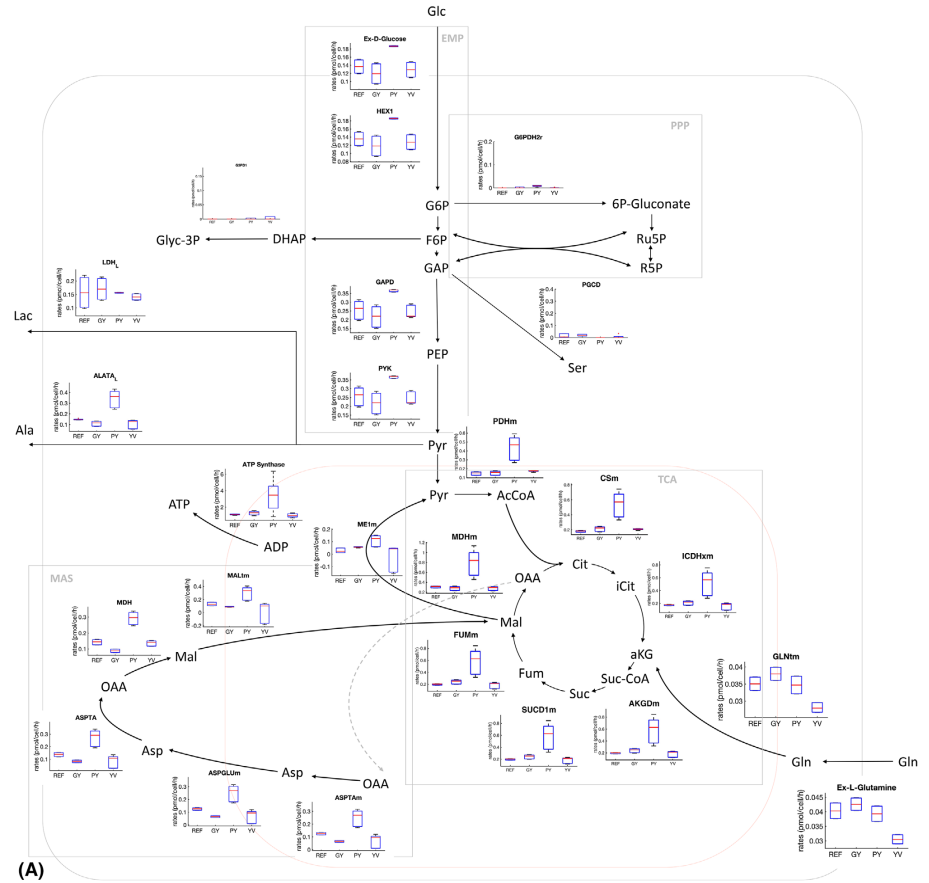

FIGURE 5 (A) Central carbon metabolism flux distribution during exponential growth phase as determined FBA. The boxplot indicates the flux of each reaction with samples arranged in the sequence REF-GY-PY-TY from left to right; (B) Cytosolic NADH production and consumption. Cytosolic NADH is produced predominantly by the EMP pathway. Additionally, NADH/NAD conversion can occur via lactate dehydrogenase (LDH) and/or the malate-aspartate shuttle (MAS). The pie chart indicates fractional amounts, not absolute amounts

3.3 | In silico analysis of the effects of TYR-containing dipeptides on metabolic activities of CHO cells

Figure 5 shows the flux distributions obtained using FBA. FBA was performed during the exponential growth phase (0–96 h of cultivation) where the TYR-containing dipeptides were supplemented to the cultures. Due to the higher D-glucose uptake rate and similar L-lactate secretion rate in PY cultures, it is expected that more glycolytic carbon was channeled to mitochondria in PY cultures compared to other cultures. The fraction of carbon diverted to the PPP, L-serine biosynthesis, and glycerophospholipid biosynthesis is negligible since cellular requirements for purine and glycerophospholipids are low. Moreover, L-serine was also available in the cultivation media.

Accordingly, the estimated citric acid cycle (CAC) flux of PY cultures was about three times higher than in the other cultures.

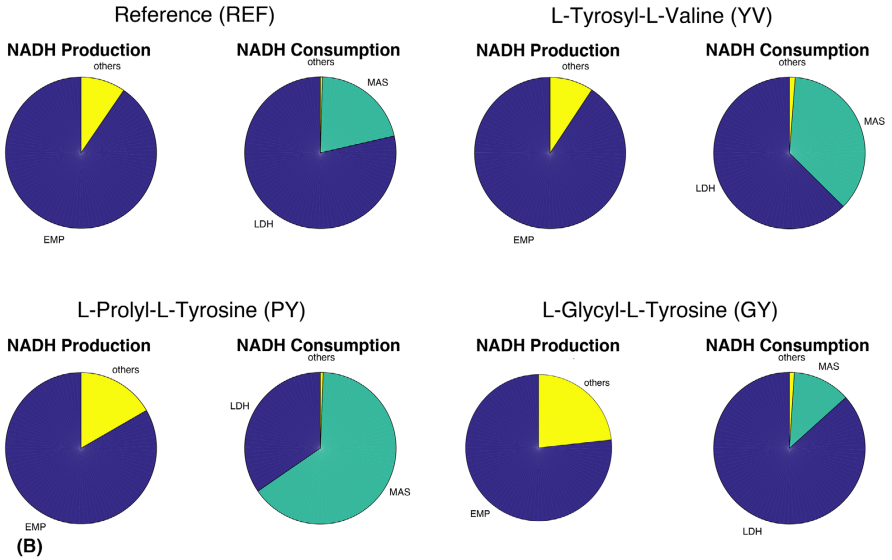

FIGURE 5 Continued

Higher glycolytic flux in PY cultures increased production of cytosolic nicotinamide adenine dinucleotide (NADH). Since the activity of NADH-consuming lactate dehydrogenase was low, NADH was transferred to mitochondria to fuel oxidative phosphorylation. NADH enters mitochondria via the malate–aspartate shuttle (MAS). In our in silico analysis (Figure 5), MAS activity in the PY cultures was 0.29 $pmol_{NADH}$ $cell^{-1}$ h^{-1} and responsible for 65% of cytosolic NADH while MAS activity in REF, YV, and GY cultures yielded 21%, 36%, and 13% cytosolic NADH, respectively. Additionally, FBA predictions revealed that incoming carbon from L-glutamine catabolism did not significantly affect the total CAC flux.

In addition to alleviated D-glucose uptake rates, PY cultures also showed elevated essential amino acid consumption (Supporting Information S2, Figure S3). Considering that cells grew at equal rates in all cultures, the increased amino acid uptake of PY cells is predicted to provide additional ATP. Different dipeptide uptake rates were observed in cultures leading to different fractions of catabolized TYR in FBA calculations (Figure 6). Figure 7 displays the correlation between TYR-containing dipeptide uptake and TYR fraction metabolism in cells. Additionally, a saturating uptake kinetic is observed, hinting at a maximum internal TYR metabolism.

4 | DISCUSSION

Dipeptides are promising supplements for cell culture media in order to compensate for low solubility and stability of individual amino acids. Previous studies have demonstrated that peptide addition may have diverse effects on cellular performance, motivating further tests to elucidate the underlying mechanisms [5,9]. The initial goal of this study was to identify TYR-containing dipeptides that can increase the maximum supply of TYR to cells through cell culture medium. Our experimental findings support the hypothesis that the metabolic effects of TYR depend on the molecular structure of the TYR-containing dipeptide. More specifically, L-prolyl-L-tyrosine (PY) alters cellular metabolism, unlike glycyl-L-tyrosine (GY) and L-tyrosyl-L-valine (YV).

The data support the potential for different uptake mechanisms and kinetics of TYR-containing dipeptides [9]. Moreover, the investigation of intracellular dipeptide pools showed that PY, GY, and YV were taken up as intact dipeptides (Supporting Information S2, Figure S2). Once they entered the cell, the dipeptides were either rapidly degraded, metabolized, or exported. Based on recent CHO genome sequencing and annotation studies, the importers PepT1 and PepT2 may be responsible for dipeptide uptake [18], however, such identification does not yet explain the dipeptide type-dependent differences.

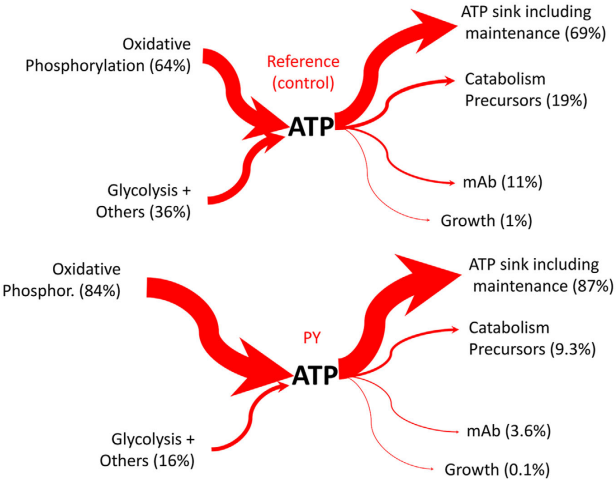

FIGURE 6 ATP flow in reference and PY cultures. The percentage indicates the portion produced or consumed by cellular metabolism

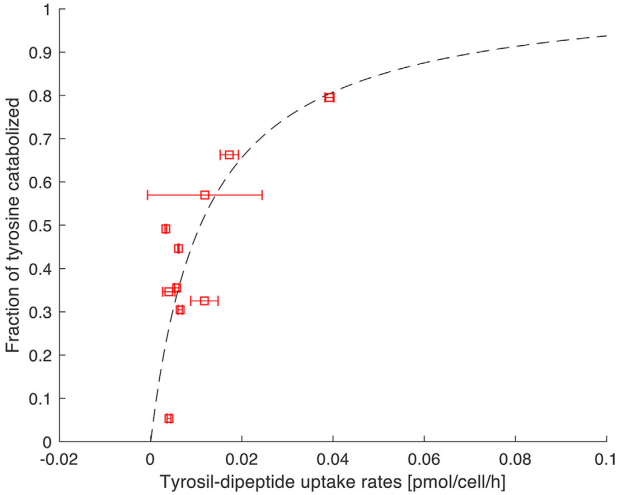

FIGURE 7 The correlation of TYR-containing dipeptides uptake rates with the fraction of TYR metabolized. This correlation forms saturating kinetics indicating that there is a maximal TYR metabolism

PY showed the strongest impact of all tested dipeptides on CHO metabolism and caused decreased growth, increased D-glucose uptake, and reduced overflow metabolism (Figure 1). Moreover, PY supplementation also altered CAC activity, intracellular ATP pools (Figure 4 and 5), and depleted the L-glutamine pool (Figure 3).

The dipeptide PY possibly works as a signal molecule (demonstrated for amino acids by Franek and Sramkova) inducing a reprogramming of the cellular metabolism [22]. An altered intracellular pH (pH_i) may contribute especially to reduced VCD and modified enzyme activities. In this experiment, our data did not encourage a changed pH_i as we observed enhanced D-glc uptake [23]. Additionally, the data set is not sufficient to reveal this effect as intracellular data of L-lac, NH_4^+, and pH_i were not applicable in this setting and were not within the scope of this study.

Nevertheless, addition of PY possibly triggers signaling pathway that contribute to decreased VCD and enhanced ATP formation.

Our FBA results suggest that CAC activity was increased in PY-treated cultures based on relatively low L-lactate formation relative to the D-glucose consumed. Moreover, D-glucose uptake rates of PY-treated cultures were approximately 30% higher compared to other cultures and mitochondrial malate-aspartate shuttle (MAS) activity was tripled in PY cultures compared to the reference (REF) culture. Such phenomenon can be interpreted as cellular responses to increased NADH supply in the cytosol while MAS activity reflects increases in glycolytic activity and reductions in L-lactate formation. MAS, a known indirect transporter of NADH from the cytosol to mitochondria, shuffles excess cytosolic NADH into the mitochondrion to fuel respiration and ATP formation. These metabolic changes resulted in an approximately four times higher ATP formation in PY culture compared to the others.

For our FBA model, only three TYR sinks are possible: (i) TYR utilization for building macromolecules like cellular proteins or mAB, (ii) TYR export, and (iii) TYR catabolism. Interestingly enough, we identified sink (iii) as the dominant fate of TYR, thus TYR was predominately used for ATP formation, beginning with its deamination using α-ketoglutarate (αKG) as amino acceptor. Next, the remaining carbon backbone is converted into fumarate and acetyl-CoA in mitochondria, thus fueling the CAC and supporting respiration. To generate sufficient αKG supply for such scenarios, one of two routes may be engaged, either through quick deamination of L-glutamate, the product of αKG amination, to create a steady-state cycle or the replenishment of αKG by the sequential deamination of L-glutamine. The observation of diminishing levels of intracellular αKG and extracellular L-glutamine pools favors the second scenario. Notably, GY and YV consumption did not result in similar trends of intracellular αKG and extracellular L-glutamine levels compared to PY consumption. Instead, upon GY or YV consumption, L-glutamine pools remained steady or were even elevated and αKG levels showed no decrease.

Becker et al. [24] demonstrated that the cell-specific mAB productivity q_{mAB} rises in D-glucose-limited perfusion cultures when ATP formation via respiration is increased [24]. However, those results are not strictly applicable to our study as our cells were analyzed under D-glucose-saturated conditions. Accordingly, our observations should be compared to those of Bulté et al. [25] who observed increased CAC activity without rising q_{mAB} [25]. Apparently, ATP supply does not limit mAB production under D-glucose-saturating conditions.

Mammalian cells are well known for their high ATP requirements to meet maintenance demands. Killburn et al. [26] estimated this ATP requirement to be larger than 65% of total ATP [26]. Consequently, D-glucose-limited cells, including those in perfusion cultures, may be in an ATP-limited condition such that an additional ATP supply fuels maintenance demands, establishes ion gradients [27] and boosts anabolic mAB formation. In contrast, D-glucose-saturated cells are likely to satisfy ATP maintenance demands, allowing for the use of excess ATP for the formation of recombinant proteins like mAB production. However, such demands are fairly low, only requiring about 11% of total ATP in the reference cultures (Figure 6). As indicated, ATP demands in reference cultures were estimated as 69% of total ATP, in line with the findings of Killburn et al. [26].

5 | CONCLUDING REMARKS

In conclusion, we demonstrated that TYR-containing dipeptides influence CHO cell metabolism in different ways depending on their specific amino acid combination. While the dipeptides glycyl-L-tyrosine (GY) and L-tyrosyl-L-valine (YV) showed minimal impact on cellular metabolism, L-prolyl-L-tyrosine (PY) increased L-glutamine usage and increased ATP availability in the cells. Strictly speaking, the FBA approach cannot distinguish between rising ATP demands for maintenance or improved ATP availability beyond what is required for maintenance. Additional ^{13}C flux studies may help to decipher the maintenance versus excess question experimentally. Our evidence of increased ATP pools in PY cultures favors the presence of improved ATP supply with unchanged maintenance demands. As next step, this exploitation potential could be used to transfer the additional energy into improved product formation. Input parameters like proper D-glucose limitation in combination with different PY feed scenarios should be tested to further optimize production performance.

NOMENCLATURE

C_i [mmol/L]	Extracellular concentration of metabolite *i*
C_x [cell/L]	Viable Cell Density (VCD)
q_i [pmol/cell/h]	Extracellular production/consumption rate of *i*
μ [h^{-1}]	cell-specific growth rate

ACKNOWLEDGMENTS

The authors gratefully acknowledge the funding by the Bundesministerium für Bildung und Forschung (BMBF), (Funding Number 031L0077A).

CONFLICT OF INTEREST

The authors have declared no conflict of interest.

ORCID

Andy Wiranata Wijaya https://orcid.org/0000-0001-9388-7357

REFERENCES

1. Birch, J. R., Racher, A. J. Antibody production. Adv. Drug. Deliv. Rev. 2006, 58, 671–685.
2. Gstraunthaler, G. Alternatives to the use of fetal bovine serum: serum-free cell culture. ALTEX Altern. Anim. Exp. 2003, 20, 275–281.
3. Wessman, S. J., Levings, R. L. Benefits and risks due to animal serum used in cell culture production. Dev. Biol. Stand. 1999, 99, 3–8.
4. van der Valk, J., Brunner, D., De Smet, K., Svenningsen, Å. F. et al. Optimization of chemically defined cell culture media–replacing fetal bovine serum in mammalian in vitro methods. Toxicol. in Vitro 2010, 24, 1053–1063.
5. Kang, S., Mullen, J., Miranda, L. P., Deshpande, R. Utilization of tyrosine-and histidine-containing dipeptides to enhance productivity and culture viability. Biotechnol. Bioeng. 2012, 109, 2286–2294.
6. Eagle, H. The specific amino acid requirements of a mammalian cell (strain L) in tissue culture. J. biol. Chem. 1955, 214, 839–852.
7. Ham, R. G. Clonal growth of mammalian cells in a chemically defined, synthetic medium. PNAS 1965, 53, 288.
8. Fürst, P. Old and new substrates in clinical nutrition. J. Nutr. 1998, 128, 789–796.
9. Sánchez-Kopper, A., Becker, M., Pfizenmaier, J., Kessler, C. et al. Tracking dipeptides at work-uptake and intracellular fate in CHO culture. AMB Express 2016, 6, 48.
10. Barrett and Jacobia (2011) EP 2 561 065 B1. Munich: European Patent Office.
11. Pfizenmaier, J., Matuszczyk, J. C., Takors, R. Changes in intracellular ATP-content of CHO cells as response to hyperosmolality. Biotechnol. Prog. 2015, 31, 1212–1216.
12. Buchholz, J., Schwentner, A., Brunnenkan, B., Gabris, C. et al. Platform engineering of Corynebacterium glutamicum with reduced pyruvate dehydrogenase complex activity for improved production of L-lysine, L-valine, and 2-ketoisovalerate. Appl. Environ. Microbiol. 2013, 79, 5566–5575.
13. Henderson, J. W., Brooks, A. Improved amino acid methods using Agilent ZORBAX Eclipse Plus C18 columns for a variety of Agilent LC instrumentation and separation goals. Agilent Technologies, Santa Clara, CA 2010.
14. Teleki, A., Sánchez-Kopper, A., Takors, R. Alkaline conditions in hydrophilic interaction liquid chromatography for intracellular metabolite quantification using tandem mass spectrometry. Anal. Biochem. 2015, 475, 4–13.
15. Feith, A., Teleki, A., Graf, M., Favilli, L. et al. HILIC-enabled (13)C metabolomics strategies: comparing quantitative precision and spectral accuracy of QTOF High- and QQQ low-resolution mass spectrometry. Metabolites 2019, 9, 63.
16. Cserjan-Puschmann, M., Kramer, W., Duerrschmid, E., Striedner, G. et al. Metabolic approaches for the optimisation of recombinant fermentation processes. Appl. Microbiol. Biotechnol. 1999, 53, 43–50.
17. Kanehisa, M., Goto, S. KEGG: Kyoto encyclopedia of genes and genomes. Nucleic. Acids. Res. 2000, 28, 27–30.
18. Hefzi, H., Ang, K. S., Hanscho, M., Bordbar, A. et al. A consensus genome-scale reconstruction of Chinese hamster ovary cell metabolism. Cell Syst. 2016, 3, 434–443.
19. Quek, L. E., Dietmair, S., Krömer, J. O., Nielsen, L. K. Metabolic flux analysis in mammalian cell culture. Metab. Eng. 2010, 12, 161–171.
20. Sheikh, K., Förster, J., Nielsen, L. K. Modeling hybridoma cell metabolism using a generic genome-scale metabolic model of Mus musculus. Biotechnol. Prog. 2005, 21, 112–121.
21. Martens, D. E. Metabolic flux analysis of mammalian cells. Syst. Biol. 2007, 275–299.
22. Franěk, F., Šrámková, K. Protection of B lymphocyte hybridoma against starvation-induced apoptosis: survival-signal role of some amino acids. Immunol. Lett. 1996, 52, 139–144.
23. Cherlet, M., Marc, A. Intracellular pH monitoring as a tool for the study of hybridoma cell behavior in batch and continuous bioreactor cultures. Biotechnol. Prog. 1998, 14(4), 626–638.
24. Becker, M., Junghans, L., Teleki, A., Bechmann, J. et al. Perfusion cultures require optimum respiratory ATP supply to maximize cell-specific and volumetric productivities. Biotechnol. Bioeng. 2019, 116, 951–960.
25. Bulté, D., Palomares, L. A., Ramírez, O. T., Gómez, C. Overexpression of the mitochondrial pyruvate carrier increases CHO cell and recombinant protein productivity and reduces lactate production. In "Cell Culture Engineering XVI", A. Robinson, PhD, Tulane University R. Venkat, PhD, MedImmune E. Schaefer, ScD, J&J Janssen Eds, ECI Symposium Series, (2018).
26. Kilburn, D. G., Lilly, M. D., Webb, F. C. The energetics of mammalian cell growth. J. Cell Sci. 1969, 4, 645–654.
27. Locasale, J. W., Cantley, L. C. Metabolic flux and the regulation of mammalian cell growth. Cell Metab. 2011, 14, 443–451.

SUPPORTING INFORMATION

Additional supporting information may be found online in the Supporting Information section at the end of the article.

How to cite this article: Verhagen N, Wijaya AW, Teleki A, et al. Comparison of L-tyrosine containing dipeptides reveals maximum ATP availability for L-prolyl-L-tyrosine in CHO cells. *Eng Life Sci*. 2020;20:384–394. https://doi.org/10.1002/elsc.202000017

Appendix A

MATLAB code for the ^{13}C MFA simulation

The code below describes the isotopomer balancing of the metabolites in CHO central carbon metabolism pathway. The code comprises of the definition of biochemical reaction reversibility and isotopomer balancing.

Contents

- ...

```
% Andy Wiranata Wijaya, IBVT (University of Stuttgart)
% Code describing the ODEs for intracellular isotopomers balancing for 13C
% MFA

% reversibility
% Glycolysis

if f.emp1 >= 0
    f.emp1_f = k_emp1 * f.emp1;     f.emp1_b = f.emp1_f - f.emp1;
else
    f.emp1_b = k_emp1 * abs(f.emp1);     f.emp1_f = f.emp1_b - abs(f.emp1);
end

if f.emp2 >= 0
    f.emp2_f = k_emp2 * f.emp2;     f.emp2_b = f.emp2_f - f.emp2;
else
    f.emp2_b = k_emp2 * abs(f.emp2);     f.emp2_f = f.emp2_b - abs(f.emp2);
end

if f.emp3 >= 0
    f.emp3_f = k_emp3 * f.emp3;     f.emp3_b = f.emp3_f - f.emp3;
else
    f.emp3_b = k_emp3 * abs(f.emp3);     f.emp3_f = f.emp3_b - abs(f.emp3);
end

if f.emp31 >= 0
    f.emp31_f = k_emp31 * f.emp31;  f.emp31_b = f.emp31_f - f.emp31;
else
    f.emp31_b = k_emp31 * abs(f.emp31);  f.emp31_f = f.emp31_b - abs(f.emp31);
end

if f.emp4 >= 0
    f.emp4_f = k_emp4 * f.emp4;     f.emp4_b = f.emp4_f - f.emp4;
else
    f.emp4_b = k_emp4 * abs(f.emp4);     f.emp4_f = f.emp4_b - abs(f.emp4);
end

if f.emp5 >= 0
    f.emp5_f = k_emp5 * f.emp5;     f.emp5_b = f.emp5_f - f.emp5;
else
    f.emp5_b = k_emp5 * abs(f.emp5);     f.emp5_f = (f.emp5_b - f.emp5);
end

% PPP
if f.ppp3 >= 0
    f.ppp3_f = k_ppp3 * f.ppp3;     f.ppp3_b = f.ppp3_f - f.ppp3;
else
    f.ppp3_b = k_ppp3 * abs(f.ppp3);     f.ppp3_f = f.ppp3_b - abs(f.ppp3);
end

if f.ppp4 >= 0
    f.ppp4_f = k_ppp4 * f.ppp4;     f.ppp4_b = f.ppp4_f - f.ppp4;
else
    f.ppp4_b = k_ppp4 * abs(f.ppp4);     f.ppp4_f = f.ppp4_b - abs(f.ppp4);
end

if f.ppp5 >= 0
    f.ppp5_f = k_ppp5 * f.ppp5;     f.ppp5_b = f.ppp5_f - f.ppp5;
else
    f.ppp5_b = k_ppp5 * abs(f.ppp5);     f.ppp5_f = f.ppp5_b - abs(f.ppp5);
end

% TCA
if f.idh >= 0
    f.idh_f = k_idh * f.idh;        f.idh_b = f.idh_f - f.idh;
else
    f.idh_b = k_idh * abs(f.idh);        f.idh_f = f.idh_b - abs(f.idh);
end

if f.adh >= 0
    f.adh_f = k_adh * f.adh;        f.adh_b = f.adh_f - f.adh;
else
    f.adh_b = k_adh * abs(f.adh);        f.adh_f = f.adh_b - abs(f.adh);
end

if f.fus >= 0
    f.fus_f = k_fus * f.fus;        f.fus_b = f.fus_f - f.fus;
else
    f.fus_b = k_fus * abs(f.fus);        f.fus_f = f.fus_b - abs(f.fus);
end

if f.mdh >= 0
    f.mdh_f = k_mdh * f.mdh;        f.mdh_b = f.mdh_f - f.mdh;
else
    f.mdh_b = k_mdh * abs(f.mdh);        f.mdh_f = f.mdh_b - abs(f.mdh);
end
```

```
if f.mdhc >= 0
    f.mdhc_f = k_mdhc * f.mdhc;     f.mdhc_b = f.mdhc_f - f.mdhc;
else
    f.mdhc_b = k_mdhc * abs(f.mdhc);     f.mdhc_f = f.mdhc_b - abs(f.mdhc);
end

if f.tGlu >= 0
    f.tGlu_f = k_tGlu * f.tGlu;     f.tGlu_b = f.tGlu_f - f.tGlu;
else
    f.tGlu_b = k_tGlu * abs(f.tGlu);     f.tGlu_f = f.tGlu_b - abs(f.tGlu);
end

if f.tAla >= 0
    f.tAla_f = k_tAla * f.tAla;     f.tAla_b = f.tAla_f - f.tAla;
else
    f.tAla_b = k_tAla * abs(f.tAla);     f.tAla_f = f.tAla_b - abs(f.tAla);
end

if f.tAsp >=0
    f.tAsp_f = k_tAsp * f.tAsp;     f.tAsp_b = f.tAsp_f - f.tAsp;
else
    f.tAsp_b = k_tAsp * abs(f.tAsp);     f.tAsp_f = f.tAsp_b - abs(f.tAsp);
end

if f.GC1 >= 0
    f.GC1_f = k_GC1 * f.GC1;        f.GC1_b = f.GC1_f - f.GC1;
else
    f.GC1_b = k_GC1 * abs(f.GC1);        f.GC1_f = f.GC1_b - abs(f.GC1);
end

if f.ast >= 0
    f.ast_f = k_ast * f.ast;        f.ast_b = f.ast_f - f.ast;
else
    f.ast_b = k_ast * abs(f.ast);        f.ast_f = f.ast_b - abs(f.ast);
end

if f.alt >= 0
    f.alt_f = k_alt * f.alt;        f.alt_b = f.alt_f - f.alt;
else
    f.alt_b = k_alt * abs(f.alt);        f.alt_f = f.alt_b - abs(f.alt);
end

if f.gdh >= 0
    f.gdh_f = k_gdh * f.gdh;        f.gdh_b = f.gdh_f - f.gdh;
else
    f.gdh_b = k_gdh * abs(f.gdh);        f.gdh_f = f.gdh_b - abs(f.gdh);
end

if f.OGC >= 0
    f.OGC_f = k_OGC * f.OGC;        f.OGC_b = f.OGC_f - f.OGC;
else
    f.OGC_b = k_OGC * abs(f.OGC);   f.OGC_f = f.OGC_b - abs(f.OGC);
end

if f.altm >= 0
    f.altm_f = k_altm * f.altm;     f.altm_b = f.altm_f - f.altm;
else
    f.altm_b = k_altm * abs(f.altm);     f.altm_f = f.altm_b - abs(f.altm);
end

if f.astm >= 0
    f.astm_f = k_astm * f.astm;     f.astm_b = f.astm_f - f.astm;
else
    f.astm_b = k_astm * abs(f.astm);  f.astm_f = f.astm_b - abs(f.astm);
end

if f.pepck >= 0
    f.pepck_f = k_pepck * f.pepck;  f.pepck_b = f.pepck_f - f.pepck;
else
   f.pepck_b = k_pepck * abs(f.pepck);  f.pepck_f = f.pepck_b - abs(f.pepck);
end

if f.me >= 0
    f.me_f = k_me * f.me;           f.me_b = f.me_f - f.me;
else
    f.me_b = k_me * abs(f.me);           f.me_f = f.me_b - abs(f.me);
end

if f.mAla >= 0
    f.mAla_f = k_mAla * f.mAla;     f.mAla_b = f.mAla_f - f.mAla;
else
    f.mAla_b = k_mAla * abs(f.mAla);     f.mAla_f = f.mAla_b - abs(f.mAla);
end

if f.mAsn >= 0
    f.mAsn_f = k_mAsn * f.mAsn;     f.mAsn_b = f.mAsn_f - f.mAsn;
else
    f.mAsn_b = k_mAsn * abs(f.mAsn);     f.mAsn_f = f.mAsn_b - abs(f.mAsn);
end

if f.pc >= 0
    f.pc_f = k_pc * f.pc;           f.pc_b = f.pc_f - f.pc;
else
```

```
    f.pc_b = k_pc * abs(f.pc);            f.pc_f = f.pc_b - abs(f.pc);
end

if f.mem >= 0
    f.mem_f = k_mem * f.mem;        f.mem_b = f.mem_f - f.mem;
else
    f.mem_b = k_mem * abs(f.mem);        f.mem_f = f.mem_b - abs(f.mem);
end

if f.DIC >= 0
    f.DIC_f = k_DIC * f.DIC;        f.DIC_b = f.DIC_f - f.DIC;
else
    f.DIC_b = k_DIC * abs(f.DIC);        f.DIC_f = f.DIC_b - abs(f.DIC);
end

if f.asnsm >= 0
    f.asnsm_f = k_asnsm * f.asnsm;  f.asnsm_b = f.asnsm_f - f.asnsm;
else
    f.asnsm_b = k_asnsm * abs(f.asnsm);  f.asnsm_f = f.asnsm_b - abs(f.asnsm);
end

if f.mCO2 >= 0
    f.mCO2_f = k_mCO2 * f.mCO2;     f.mCO2_b = f.mCO2_f - f.mCO2;
else
    f.mCO2_b = k_mCO2 * abs(f.mCO2);     f.mCO2_f = f.mCO2_b - abs(f.mCO2);
end

if f.tLac >= 0
    f.tLac_f = k_tLac * f.tLac;     f.tLac_b = f.tLac_f - f.tLac;
else
    f.tLac_b = k_tLac * abs(f.tLac);     f.tLac_f = f.tLac_b - abs(f.tLac);
end

if f.ldh >= 0
    f.ldh_f = k_ldh * f.ldh;        f.ldh_b = f.ldh_f - f.ldh;
else
    f.ldh_b = k_ldh * abs(f.ldh);        f.ldh_f = f.ldh_b - abs(f.ldh);
end

% isotopomers species definition

x_Gln   = x(1:2^n_Gln);
x_Glu   = x(2^n_Gln+1:2^n_Gln+2^n_Glu);
x_aKGm  = x(2^n_Gln+2^n_Glu+1:2^n_Gln+2^n_Glu+2^n_aKGm);
x_Glum  = x(2^n_Gln+2^n_Glu+2^n_aKGm+1:2^n_Gln+2^n_Glu+2^n_aKGm+2^n_Glum);
x_G6P   = x(2^n_Gln+2^n_Glu+2^n_aKGm+2^n_Glum+1:2^n_Gln+2^n_Glu+2^n_aKGm+2^n_Glum+2^n_G6P);
x_F6P   = x(2^n_Gln+2^n_Glu+2^n_aKGm+2^n_Glum+2^n_G6P+1:2^n_Gln+2^n_Glu+2^n_aKGm+2^n_Glum+2^n_G6P+2^n_F6P);
x_FBP   = x(2^n_Gln+2^n_Glu+2^n_aKGm+2^n_Glum+2^n_G6P+2^n_F6P+1:2^n_Gln+2^n_Glu+2^n_aKGm+2^n_Glum+2^n_G6P+2^n_F6P+2^n_FBP);
x_DHAP  = x(2^n_Gln+2^n_Glu+2^n_aKGm+2^n_Glum+2^n_G6P+2^n_F6P+2^n_FBP+1:2^n_Gln+2^n_Glu+2^n_aKGm+2^n_Glum+2^n_G6P+2^n_F6P+2^n_FBP+2^n_DHAP);
x_GAP   = x(2^n_Gln+2^n_Glu+2^n_aKGm+2^n_Glum+2^n_G6P+2^n_F6P+2^n_FBP+2^n_DHAP+1:2^n_Gln+2^n_Glu+2^n_aKGm+2^n_Glum+2^n_G6P+2^n_F6P+2^n_FBP+2^n_DHAP+2^n_GAP);
x_3PG   = x(2^n_Gln+2^n_Glu+2^n_aKGm+2^n_Glum+2^n_G6P+2^n_F6P+2^n_FBP+2^n_DHAP+2^n_GAP+1:2^n_Gln+2^n_Glu+2^n_aKGm+2^n_Glum+2^n_G6P+2^n_F6P+2^n_FBP+2^n_DHAP+2^n
x_PEP   = x(2^n_Gln+2^n_Glu+2^n_aKGm+2^n_Glum+2^n_G6P+2^n_F6P+2^n_FBP+2^n_DHAP+2^n_GAP+2^n_3PG+1:2^n_Gln+2^n_Glu+2^n_aKGm+2^n_Glum+2^n_G6P+2^n_F6P+2^n_FBP+2^n_
x_Pyr   = x(2^n_Gln+2^n_Glu+2^n_aKGm+2^n_Glum+2^n_G6P+2^n_F6P+2^n_FBP+2^n_DHAP+2^n_GAP+2^n_3PG+2^n_PEP+1:...
    2^n_Gln+2^n_Glu+2^n_aKGm+2^n_Glum+2^n_G6P+2^n_F6P+2^n_FBP+2^n_DHAP+2^n_GAP+2^n_3PG+2^n_PEP+2^n_Pyr);
x_Lac   = x(2^n_Gln+2^n_Glu+2^n_aKGm+2^n_Glum+2^n_G6P+2^n_F6P+2^n_FBP+2^n_DHAP+2^n_GAP+2^n_3PG+2^n_PEP+2^n_Pyr+1:...
    2^n_Gln+2^n_Glu+2^n_aKGm+2^n_Glum+2^n_G6P+2^n_F6P+2^n_FBP+2^n_DHAP+2^n_GAP+2^n_3PG+2^n_PEP+2^n_Pyr+2^n_Lac);
x_P5P   = x(2^n_Gln+2^n_Glu+2^n_aKGm+2^n_Glum+2^n_G6P+2^n_F6P+2^n_FBP+2^n_DHAP+2^n_GAP+2^n_3PG+2^n_PEP+2^n_Pyr+2^n_Lac+1:...
    2^n_Gln+2^n_Glu+2^n_aKGm+2^n_Glum+2^n_G6P+2^n_F6P+2^n_FBP+2^n_DHAP+2^n_GAP+2^n_3PG+2^n_PEP+2^n_Pyr+2^n_Lac+2^n_P5P);
x_S7P   = x(2^n_Gln+2^n_Glu+2^n_aKGm+2^n_Glum+2^n_G6P+2^n_F6P+2^n_FBP+2^n_DHAP+2^n_GAP+2^n_3PG+2^n_PEP+2^n_Pyr+2^n_Lac+2^n_P5P+1:...
    2^n_Gln+2^n_Glu+2^n_aKGm+2^n_Glum+2^n_G6P+2^n_F6P+2^n_FBP+2^n_DHAP+2^n_GAP+2^n_3PG+2^n_PEP+2^n_Pyr+2^n_Lac+2^n_P5P+2^n_S7P);
x_E4P   = x(2^n_Gln+2^n_Glu+2^n_aKGm+2^n_Glum+2^n_G6P+2^n_F6P+2^n_FBP+2^n_DHAP+2^n_GAP+2^n_3PG+2^n_PEP+2^n_Pyr+2^n_Lac+2^n_P5P+2^n_S7P+1:...
    2^n_Gln+2^n_Glu+2^n_aKGm+2^n_Glum+2^n_G6P+2^n_F6P+2^n_FBP+2^n_DHAP+2^n_GAP+2^n_3PG+2^n_PEP+2^n_Pyr+2^n_Lac+2^n_P5P+2^n_S7P+2^n_E4P);
x_Cit   = x(2^n_Gln+2^n_Glu+2^n_aKGm+2^n_Glum+2^n_G6P+2^n_F6P+2^n_FBP+2^n_DHAP+2^n_GAP+2^n_3PG+2^n_PEP+2^n_Pyr+2^n_Lac+2^n_P5P+2^n_S7P+2^n_E4P+1:...
    2^n_Gln+2^n_Glu+2^n_aKGm+2^n_Glum+2^n_G6P+2^n_F6P+2^n_FBP+2^n_DHAP+2^n_GAP+2^n_3PG+2^n_PEP+2^n_Pyr+2^n_Lac+2^n_P5P+2^n_S7P+2^n_E4P+2^n_Cit);
x_OAA   = x(2^n_Gln+2^n_Glu+2^n_aKGm+2^n_Glum+2^n_G6P+2^n_F6P+2^n_FBP+2^n_DHAP+2^n_GAP+2^n_3PG+2^n_PEP+2^n_Pyr+2^n_Lac+2^n_P5P+2^n_S7P+2^n_E4P+2^n_Cit+1:...
    2^n_Gln+2^n_Glu+2^n_aKGm+2^n_Glum+2^n_G6P+2^n_F6P+2^n_FBP+2^n_DHAP+2^n_GAP+2^n_3PG+2^n_PEP+2^n_Pyr+2^n_Lac+2^n_P5P+2^n_S7P+2^n_E4P+2^n_Cit+2^n_OAA);
x_AcCoA = x(2^n_Gln+2^n_Glu+2^n_aKGm+2^n_Glum+2^n_G6P+2^n_F6P+2^n_FBP+2^n_DHAP+2^n_GAP+2^n_3PG+2^n_PEP+2^n_Pyr+2^n_Lac+2^n_P5P+2^n_S7P+2^n_E4P+2^n_Cit+2^n_OAA+
    2^n_Gln+2^n_Glu+2^n_aKGm+2^n_Glum+2^n_G6P+2^n_F6P+2^n_FBP+2^n_DHAP+2^n_GAP+2^n_3PG+2^n_PEP+2^n_Pyr+2^n_Lac+2^n_P5P+2^n_S7P+2^n_E4P+2^n_Cit+2^n_OAA+2^n_AcCo
x_Ser   = x(2^n_Gln+2^n_Glu+2^n_aKGm+2^n_Glum+2^n_G6P+2^n_F6P+2^n_FBP+2^n_DHAP+2^n_GAP+2^n_3PG+2^n_PEP+2^n_Pyr+2^n_Lac+2^n_P5P+2^n_S7P+2^n_E4P+2^n_Cit+2^n_OAA+
    2^n_Gln+2^n_Glu+2^n_aKGm+2^n_Glum+2^n_G6P+2^n_F6P+2^n_FBP+2^n_DHAP+2^n_GAP+2^n_3PG+2^n_PEP+2^n_Pyr+2^n_Lac+2^n_P5P+2^n_S7P+2^n_E4P+2^n_Cit+2^n_OAA+2^n_AcCo
x_Ala   = x(2^n_Gln+2^n_Glu+2^n_aKGm+2^n_Glum+2^n_G6P+2^n_F6P+2^n_FBP+2^n_DHAP+2^n_GAP+2^n_3PG+2^n_PEP+2^n_Pyr+2^n_Lac+2^n_P5P+2^n_S7P+2^n_E4P+2^n_Cit+2^n_OAA+
    2^n_Gln+2^n_Glu+2^n_aKGm+2^n_Glum+2^n_G6P+2^n_F6P+2^n_FBP+2^n_DHAP+2^n_GAP+2^n_3PG+2^n_PEP+2^n_Pyr+2^n_Lac+2^n_P5P+2^n_S7P+2^n_E4P+2^n_Cit+2^n_OAA+2^n_AcCo
x_Asp   = x(2^n_Gln+2^n_Glu+2^n_aKGm+2^n_Glum+2^n_G6P+2^n_F6P+2^n_FBP+2^n_DHAP+2^n_GAP+2^n_3PG+2^n_PEP+2^n_Pyr+2^n_Lac+2^n_P5P+2^n_S7P+2^n_E4P+2^n_Cit+2^n_OAA+
    2^n_Gln+2^n_Glu+2^n_aKGm+2^n_Glum+2^n_G6P+2^n_F6P+2^n_FBP+2^n_DHAP+2^n_GAP+2^n_3PG+2^n_PEP+2^n_Pyr+2^n_Lac+2^n_P5P+2^n_S7P+2^n_E4P+2^n_Cit+2^n_OAA+2^n_AcCo
x_Asn   = x(2^n_Gln+2^n_Glu+2^n_aKGm+2^n_Glum+2^n_G6P+2^n_F6P+2^n_FBP+2^n_DHAP+2^n_GAP+2^n_3PG+2^n_PEP+2^n_Pyr+2^n_Lac+2^n_P5P+2^n_S7P+2^n_E4P+2^n_Cit+2^n_OAA+
    2^n_Gln+2^n_Glu+2^n_aKGm+2^n_Glum+2^n_G6P+2^n_F6P+2^n_FBP+2^n_DHAP+2^n_GAP+2^n_3PG+2^n_PEP+2^n_Pyr+2^n_Lac+2^n_P5P+2^n_S7P+2^n_E4P+2^n_Cit+2^n_OAA+2^n_AcCo
x_Pyrm  = x(2^n_Gln+2^n_Glu+2^n_aKGm+2^n_Glum+2^n_G6P+2^n_F6P+2^n_FBP+2^n_DHAP+2^n_GAP+2^n_3PG+2^n_PEP+2^n_Pyr+2^n_Lac+2^n_P5P+2^n_S7P+2^n_E4P+2^n_Cit+2^n_OAA+
    2^n_Gln+2^n_Glu+2^n_aKGm+2^n_Glum+2^n_G6P+2^n_F6P+2^n_FBP+2^n_DHAP+2^n_GAP+2^n_3PG+2^n_PEP+2^n_Pyr+2^n_Lac+2^n_P5P+2^n_S7P+2^n_E4P+2^n_Cit+2^n_OAA+2^n_AcCo
x_Citm  = x(2^n_Gln+2^n_Glu+2^n_aKGm+2^n_Glum+2^n_G6P+2^n_F6P+2^n_FBP+2^n_DHAP+2^n_GAP+2^n_3PG+2^n_PEP+2^n_Pyr+2^n_Lac+2^n_P5P+2^n_S7P+2^n_E4P+2^n_Cit+2^n_OAA+
    2^n_Gln+2^n_Glu+2^n_aKGm+2^n_Glum+2^n_G6P+2^n_F6P+2^n_FBP+2^n_DHAP+2^n_GAP+2^n_3PG+2^n_PEP+2^n_Pyr+2^n_Lac+2^n_P5P+2^n_S7P+2^n_E4P+2^n_Cit+2^n_OAA+2^n_AcCo
x_Mal   = x(2^n_Gln+2^n_Glu+2^n_aKGm+2^n_Glum+2^n_G6P+2^n_F6P+2^n_FBP+2^n_DHAP+2^n_GAP+2^n_3PG+2^n_PEP+2^n_Pyr+2^n_Lac+2^n_P5P+2^n_S7P+2^n_E4P+2^n_Cit+2^n_OAA+
    2^n_Gln+2^n_Glu+2^n_aKGm+2^n_Glum+2^n_G6P+2^n_F6P+2^n_FBP+2^n_DHAP+2^n_GAP+2^n_3PG+2^n_PEP+2^n_Pyr+2^n_Lac+2^n_P5P+2^n_S7P+2^n_E4P+2^n_Cit+2^n_OAA+2^n_AcCo
x_Malm  = x(2^n_Gln+2^n_Glu+2^n_aKGm+2^n_Glum+2^n_G6P+2^n_F6P+2^n_FBP+2^n_DHAP+2^n_GAP+2^n_3PG+2^n_PEP+2^n_Pyr+2^n_Lac+2^n_P5P+2^n_S7P+2^n_E4P+2^n_Cit+2^n_OAA+
    2^n_Gln+2^n_Glu+2^n_aKGm+2^n_Glum+2^n_G6P+2^n_F6P+2^n_FBP+2^n_DHAP+2^n_GAP+2^n_3PG+2^n_PEP+2^n_Pyr+2^n_Lac+2^n_P5P+2^n_S7P+2^n_E4P+2^n_Cit+2^n_OAA+2^n_AcCo
x_aKG   = x(2^n_Gln+2^n_Glu+2^n_aKGm+2^n_Glum+2^n_G6P+2^n_F6P+2^n_FBP+2^n_DHAP+2^n_GAP+2^n_3PG+2^n_PEP+2^n_Pyr+2^n_Lac+2^n_P5P+2^n_S7P+2^n_E4P+2^n_Cit+2^n_OAA+
    2^n_Gln+2^n_Glu+2^n_aKGm+2^n_Glum+2^n_G6P+2^n_F6P+2^n_FBP+2^n_DHAP+2^n_GAP+2^n_3PG+2^n_PEP+2^n_Pyr+2^n_Lac+2^n_P5P+2^n_S7P+2^n_E4P+2^n_Cit+2^n_OAA+2^n_AcCo
x_Aspm  = x(2^n_Gln+2^n_Glu+2^n_aKGm+2^n_Glum+2^n_G6P+2^n_F6P+2^n_FBP+2^n_DHAP+2^n_GAP+2^n_3PG+2^n_PEP+2^n_Pyr+2^n_Lac+2^n_P5P+2^n_S7P+2^n_E4P+2^n_Cit+2^n_OAA+
    2^n_Gln+2^n_Glu+2^n_aKGm+2^n_Glum+2^n_G6P+2^n_F6P+2^n_FBP+2^n_DHAP+2^n_GAP+2^n_3PG+2^n_PEP+2^n_Pyr+2^n_Lac+2^n_P5P+2^n_S7P+2^n_E4P+2^n_Cit+2^n_OAA+2^n_AcCo
x_Alam  = x(2^n_Gln+2^n_Glu+2^n_aKGm+2^n_Glum+2^n_G6P+2^n_F6P+2^n_FBP+2^n_DHAP+2^n_GAP+2^n_3PG+2^n_PEP+2^n_Pyr+2^n_Lac+2^n_P5P+2^n_S7P+2^n_E4P+2^n_Cit+2^n_OAA+
    2^n_Gln+2^n_Glu+2^n_aKGm+2^n_Glum+2^n_G6P+2^n_F6P+2^n_FBP+2^n_DHAP+2^n_GAP+2^n_3PG+2^n_PEP+2^n_Pyr+2^n_Lac+2^n_P5P+2^n_S7P+2^n_E4P+2^n_Cit+2^n_OAA+2^n_AcCo
x_Asnm  = x(2^n_Gln+2^n_Glu+2^n_aKGm+2^n_Glum+2^n_G6P+2^n_F6P+2^n_FBP+2^n_DHAP+2^n_GAP+2^n_3PG+2^n_PEP+2^n_Pyr+2^n_Lac+2^n_P5P+2^n_S7P+2^n_E4P+2^n_Cit+2^n_OAA+
    2^n_Gln+2^n_Glu+2^n_aKGm+2^n_Glum+2^n_G6P+2^n_F6P+2^n_FBP+2^n_DHAP+2^n_GAP+2^n_3PG+2^n_PEP+2^n_Pyr+2^n_Lac+2^n_P5P+2^n_S7P+2^n_E4P+2^n_Cit+2^n_OAA+2^n_AcCo
x_AcCoAm = x( 2^n_Gln+2^n_Glu+2^n_aKGm+2^n_Glum+2^n_G6P+2^n_F6P+2^n_FBP+2^n_DHAP+2^n_GAP+2^n_3PG+2^n_PEP+2^n_Pyr+2^n_Lac+2^n_P5P+2^n_S7P+2^n_E4P+2^n_Cit+2^n_OA
```

```
     2^n_Gln+2^n_Glu+2^n_aKGm+2^n_Glum+2^n_G6P+2^n_F6P+2^n_FBP+2^n_DHAP+2^n_GAP+2^n_3PG+2^n_PEP+2^n_Pyr+2^n_Lac+2^n_P5P+2^n_S7P+2^n_E4P+2^n_Cit+2^n_OAA+2^n_AcC
x_OAAm  = x(2^n_Gln+2^n_Glu+2^n_aKGm+2^n_Glum+2^n_G6P+2^n_F6P+2^n_FBP+2^n_DHAP+2^n_GAP+2^n_3PG+2^n_PEP+2^n_Pyr+2^n_Lac+2^n_P5P+2^n_S7P+2^n_E4P+2^n_Cit+2^n_OAA+
    2^n_Gln+2^n_Glu+2^n_aKGm+2^n_Glum+2^n_G6P+2^n_F6P+2^n_FBP+2^n_DHAP+2^n_GAP+2^n_3PG+2^n_PEP+2^n_Pyr+2^n_Lac+2^n_P5P+2^n_S7P+2^n_E4P+2^n_Cit+2^n_OAA+2^n_AcCo
x_CO2   = x(2^n_Gln+2^n_Glu+2^n_aKGm+2^n_Glum+2^n_G6P+2^n_F6P+2^n_FBP+2^n_DHAP+2^n_GAP+2^n_3PG+2^n_PEP+2^n_Pyr+2^n_Lac+2^n_P5P+2^n_S7P+2^n_E4P+2^n_Cit+2^n_OAA+
    2^n_Gln+2^n_Glu+2^n_aKGm+2^n_Glum+2^n_G6P+2^n_F6P+2^n_FBP+2^n_DHAP+2^n_GAP+2^n_3PG+2^n_PEP+2^n_Pyr+2^n_Lac+2^n_P5P+2^n_S7P+2^n_E4P+2^n_Cit+2^n_OAA+2^n_AcCo
x_CO2m  = x(2^n_Gln+2^n_Glu+2^n_aKGm+2^n_Glum+2^n_G6P+2^n_F6P+2^n_FBP+2^n_DHAP+2^n_GAP+2^n_3PG+2^n_PEP+2^n_Pyr+2^n_Lac+2^n_P5P+2^n_S7P+2^n_E4P+2^n_Cit+2^n_OAA+
    2^n_Gln+2^n_Glu+2^n_aKGm+2^n_Glum+2^n_G6P+2^n_F6P+2^n_FBP+2^n_DHAP+2^n_GAP+2^n_3PG+2^n_PEP+2^n_Pyr+2^n_Lac+2^n_P5P+2^n_S7P+2^n_E4P+2^n_Cit+2^n_OAA+2^n_AcCo

x_Glu_ex = x(2^n_Gln+2^n_Glu+2^n_aKGm+2^n_Glum+2^n_G6P+2^n_F6P+2^n_FBP+2^n_DHAP+2^n_GAP+2^n_3PG+2^n_PEP+2^n_Pyr+2^n_Lac+2^n_P5P+2^n_S7P+2^n_E4P+2^n_Cit+2^n_OAA
       2^n_Gln+2^n_Glu+2^n_aKGm+2^n_Glum+2^n_G6P+2^n_F6P+2^n_FBP+2^n_DHAP+2^n_GAP+2^n_3PG+2^n_PEP+2^n_Pyr+2^n_Lac+2^n_P5P+2^n_S7P+2^n_E4P+2^n_Cit+2^n_OAA+2^n_
x_Lac_ex = x(2^n_Gln+2^n_Glu+2^n_aKGm+2^n_Glum+2^n_G6P+2^n_F6P+2^n_FBP+2^n_DHAP+2^n_GAP+2^n_3PG+2^n_PEP+2^n_Pyr+2^n_Lac+2^n_P5P+2^n_S7P+2^n_E4P+2^n_Cit+2^n_OAA
    2^n_Gln+2^n_Glu+2^n_aKGm+2^n_Glum+2^n_G6P+2^n_F6P+2^n_FBP+2^n_DHAP+2^n_GAP+2^n_3PG+2^n_PEP+2^n_Pyr+2^n_Lac+2^n_P5P+2^n_S7P+2^n_E4P+2^n_Cit+2^n_OAA+2^n_AcCo
x_Ala_ex = x(2^n_Gln+2^n_Glu+2^n_aKGm+2^n_Glum+2^n_G6P+2^n_F6P+2^n_FBP+2^n_DHAP+2^n_GAP+2^n_3PG+2^n_PEP+2^n_Pyr+2^n_Lac+2^n_P5P+2^n_S7P+2^n_E4P+2^n_Cit+2^n_OAA
       2^n_Gln+2^n_Glu+2^n_aKGm+2^n_Glum+2^n_G6P+2^n_F6P+2^n_FBP+2^n_DHAP+2^n_GAP+2^n_3PG+2^n_PEP+2^n_Pyr+2^n_Lac+2^n_P5P+2^n_S7P+2^n_E4P+2^n_Cit+2^n_OAA+2^n_
x_Asp_ex = x(2^n_Gln+2^n_Glu+2^n_aKGm+2^n_Glum+2^n_G6P+2^n_F6P+2^n_FBP+2^n_DHAP+2^n_GAP+2^n_3PG+2^n_PEP+2^n_Pyr+2^n_Lac+2^n_P5P+2^n_S7P+2^n_E4P+2^n_Cit+2^n_OAA
    2^n_Gln+2^n_Glu+2^n_aKGm+2^n_Glum+2^n_G6P+2^n_F6P+2^n_FBP+2^n_DHAP+2^n_GAP+2^n_3PG+2^n_PEP+2^n_Pyr+2^n_Lac+2^n_P5P+2^n_S7P+2^n_E4P+2^n_Cit+2^n_OAA+2^n_AcCo

x_Fumm = x(2^n_Gln+2^n_Glu+2^n_aKGm+2^n_Glum+2^n_G6P+2^n_F6P+2^n_FBP+2^n_DHAP+2^n_GAP+2^n_3PG+2^n_PEP+2^n_Pyr+2^n_Lac+2^n_P5P+2^n_S7P+2^n_E4P+2^n_Cit+2^n_OAA+2
    2^n_Gln+2^n_Glu+2^n_aKGm+2^n_Glum+2^n_G6P+2^n_F6P+2^n_FBP+2^n_DHAP+2^n_GAP+2^n_3PG+2^n_PEP+2^n_Pyr+2^n_Lac+2^n_P5P+2^n_S7P+2^n_E4P+2^n_Cit+2^n_OAA+2^n_AcCo

% ODE functions

% Gln (final)
d_Gln = zeros(2^n_Gln,1);
for i = 1:length(d_Gln)
    d_Gln(i)= (f.tGln*x_Gln_ex(i) - ((f.gs + f.muGln)*x_Gln(i)))/V_Gln;
end

% Glu (final)
d_Glu = zeros(2^n_Glu,1);
for i = 1:length(d_Glu)
    d_Glu(i) = (f.gs*x_Gln(i) + f.GC1_f*x_Glum(i) + ...
        (f.alt_b + f.ast_f)*x_aKG(i) - ((f.tGlu+f.muGlu+f.GC1_b+f.AGC1+f.alt_f+f.ast_b)*...
        x_Glu(i)))/V_Glu;
end

% aKG_m
d_aKGm = zeros(2^n_aKGm,1);
Malm_indexing = [1, 9, 5, 13, 3, 11, 7, 15, 2, 10, 6, 14, 4, 12, 8, 16];
j = 1;  % CO2m indexing
k = 1;  % Malm indexing
for i = 1:length(d_aKGm)
    d_aKGm(i)=(x_Glum(i)*(f.altm_b + f.astm_b + f.gdh_f) + x_aKG(i)*f.OGC_b + (x_Citm(i)+x_Citm(i+32))*f.idh_f + ...
        0.5*x_CO2m(j)*x_Fumm(k)*f.adh_b + 0.5*x_CO2m(j)*x_Fumm(Malm_indexing(k))*f.adh_b ...
        - ((f.gdh_b+f.OGC_f+f.idh_b+f.adh_f+f.altm_f+f.astm_f)*x_aKGm(i)))/V_aKGm;

    if j == 2
        j = 1;
        k = k+1;
    else
        j = j+1;
    end

end

% Glu_m
d_Glum = zeros(2^n_Glum,1);
for i = 1:length(d_Glum)
    d_Glum(i) = (x_aKGm(i)*(f.gdh_b+f.altm_f+f.astm_f) + x_Glu(i)*(f.GC1_b+f.AGC1) - ...
        ((f.gdh_f+f.GC1_f+f.altm_b+f.astm_b)*x_Glum(i)))/V_Glum;
end

% G6P
d_G6P = zeros(2^n_G6P,1);
for i = 1:length(d_G6P)
    d_G6P(i)=(x_Glc_ex(i)*f.tGlc + x_Glyco_ex(i)*f.tGlyco + x_F6P(i)*f.emp1_b -...
        ((f.emp1_f+f.ppp1+f.muG6P)*x_G6P(i)))/V_G6P;
end

% F6P
d_F6P = zeros(2^n_F6P,1);
j = 1;  % indexing for E4P
k = 1;  % indexing for P5P
l = 1;  % indexign for GAP
m = 1;  % indexing for S7P
for i = 1:length(d_F6P)
    d_F6P(i)=(x_G6P(i)*f.emp1_f + x_FBP(i)*f.emp2_b +...
        (x_E4P(j)*(x_P5P(k)+x_P5P(k+4)+x_P5P(k+8)+x_P5P(k+12)+x_P5P(k+16)+x_P5P(k+20)+x_P5P(k+24)+x_P5P(k+28)))*f.ppp4_f+...
        (x_GAP(l)*(x_S7P(m)+x_S7P(m+8)+x_S7P(m+16)+x_S7P(m+24)+x_S7P(m+32)+x_S7P(m+40)+x_S7P(m+48)+x_S7P(m+56)+x_S7P(m+64)+...
        x_S7P(m+72)+x_S7P(m+80)+x_S7P(m+88)+x_S7P(m+96)+x_S7P(m+104)+x_S7P(m+112)+x_S7P(m+120)))*f.ppp5_f-...
        ((f.emp1_b+f.emp2_f+f.ppp4_b+f.ppp5_b)*x_F6P(i)))/V_F6P;

    if k == 4
        j = j+1;
        k = 1;
    else
        k = k+1;
    end

    if m == 8
        l = l+1;
        m = 1;
    else
```

```
        m = m+1;
    end
end

% FBP
d_FBP = zeros(2^n_FBP,1);
j = 1;  % DHAP indexing
k = 1;  % GAP indexng
DHAP_indexing = [1, 5, 3, 7, 2, 6, 4, 8];
for i = 1:length(d_FBP)
    d_FBP(i) = (x_F6P(i)*f.emp2_f + (x_DHAP(DHAP_indexing(j))*x_GAP(k))*f.emp3_b - ((f.emp2_b+f.emp3_f)*x_FBP(i)))/V_FBP;

    if j == 8
        j = 1;
        k = k+1;
    else
        j = j+1;
    end
end

% DHAP
d_DHAP = zeros(2^n_DHAP,1);
for i = 1:length(d_DHAP)
    d_DHAP(i)= ((x_FBP(DHAP_indexing(i))+x_FBP(DHAP_indexing(i)+8)+x_FBP(DHAP_indexing(i)+16)+x_FBP(DHAP_indexing(i)+24)+...
        x_FBP(DHAP_indexing(i)+32)+x_FBP(DHAP_indexing(i)+40)+x_FBP(DHAP_indexing(i)+48)+x_FBP(DHAP_indexing(i)+56))*f.emp3_f+...
        x_GAP(i)*f.emp31_b - ((f.emp3_b+f.emp31_f)*x_DHAP(i)))/V_DHAP;
end

% GAP
d_GAP = zeros(2^n_GAP,1);
j = 1;  % FBP indexing
k = 1;  % P5P indexing
for i = 1:length(d_GAP)
    d_GAP(i) = ((x_FBP(j)+x_FBP(j+1)+x_FBP(j+2)+x_FBP(j+3)+x_FBP(j+4)+x_FBP(j+5)+x_FBP(j+6)+x_FBP(j+7))*f.emp3_f+...
        x_DHAP(i)*f.emp31_f + x_3PG(i)*f.emp4_b + (x_P5P(k)+x_P5P(k+1)+x_P5P(k+2)+x_P5P(k+3))*(f.ppp3_f+f.ppp4_f)+...
        (x_F6P(j)+x_F6P(j+1)+x_F6P(j+2)+x_F6P(j+3)+x_F6P(j+4)+x_F6P(j+5)+x_F6P(j+6)+x_F6P(j+7))*f.ppp5_b - ...
        ((f.emp3_b+f.emp31_b+f.emp4_f+f.ppp3_b+f.ppp4_b+f.ppp5_f+f.muGAP)*x_GAP(i)))/V_GAP;

    j = j+8;
    k = k+4;
end

% 3PG
d_3PG = zeros(2^n_3PG,1);
for i = 1:length(d_3PG)
    d_3PG(i) = (x_GAP(i)*f.emp4_f + x_PEP(i)*f.emp5_b -((f.emp4_b+f.emp5_f+f.ser1)*x_3PG(i)))/V_3PG;
end

% PEP (checked2)
d_PEP = zeros(2^n_PEP,1);
for i = 1:length(d_PEP)
    d_PEP(i) = (x_3PG(i)*f.emp5_f + (x_OAA(i)+x_OAA(i+8))*f.pepck_f-((f.emp5_b+f.emp6+f.pepck_b)*x_PEP(i)))/V_PEP;
end


% Pyr
d_Pyr = zeros(2^n_Pyr,1);
for i = 1:length(d_Pyr)
    d_Pyr(i) = (x_PEP(i)*f.emp6 + x_Lac(i)*f.ldh_b + (x_Mal(i)+x_Mal(i+8))*f.me_f + x_Ser(i)*f.ser2 + x_Ala(i)*f.alt_b-...
        ((f.ldh_f+f.MPC1+f.me_b+f.alt_f)*x_Pyr(i)))/V_Pyr;
end

% Lac
% modification: tLac from reversible into irreversible
d_Lac = zeros(2^n_Lac,1);
for i = 1:length(d_Lac)
    d_Lac(i) = (x_Pyr(i)*f.ldh_f + f.tLac_b*x_Lac_ex(i) - ((f.ldh_b+f.tLac_f)*x_Lac(i)))/V_Lac;
end

% P5P
d_P5P = zeros(2^n_P5P,1);
j = 1;  % G6P indexing
k = 1;  % S7P indexing
l = 1;  % F6- and S7P (2) indexing
m = 1;  % GAP indexing
for i = 1:length(d_P5P)
    d_P5P(i) = ((x_G6P(j)+x_G6P(j+1))*f.ppp1 + (x_S7P(k)+x_S7P(k+1)+x_S7P(k+2)+x_S7P(k+3))*f.ppp3_b + ...
        ((x_S7P(l)+x_S7P(l+4)+x_S7P(l+8)+x_S7P(l+12)+x_S7P(l+16)+x_S7P(l+20)+x_S7P(l+24)+x_S7P(l+28)+x_S7P(l+32)+...
        x_S7P(l+36)+x_S7P(l+40)+x_S7P(l+44)+x_S7P(l+48)+x_S7P(l+52)+x_S7P(l+56)+x_S7P(l+60)+x_S7P(l+64)+x_S7P(l+68)+...
        x_S7P(l+72)+x_S7P(l+76)+x_S7P(l+80)+x_S7P(l+84)+x_S7P(l+88)+x_S7P(l+92)+x_S7P(l+96)+x_S7P(l+100)+x_S7P(l+104)+...
        x_S7P(l+108)+x_S7P(l+112)+x_S7P(l+116)+x_S7P(l+120)+x_S7P(l+124))*x_GAP(m))*f.ppp3_b + ((x_F6P(l)+x_F6P(l+4)+x_F6P(l+8)+...
        x_F6P(l+12)+x_F6P(l+16)+x_F6P(l+20)+x_F6P(l+24)+x_F6P(l+28)+x_F6P(l+32)+x_F6P(l+36)+x_F6P(l+40)+x_F6P(l+44)+x_F6P(l+48)+...
        x_F6P(l+52)+x_F6P(l+56)+x_F6P(l+60))*x_GAP(m))*f.ppp4_b -((f.muP5P+2*f.ppp3_f+f.ppp4_f)*x_P5P(i)))/V_P5P;

    if l == 4
        l = 1;
        m = m+1;
    else
        l = l+1;
    end

    j = j+2;
    k = k+4;
```

```
end

% S7P
d_S7P = zeros(2^n_S7P,1);
j = 1;  % P5P indexing
k = 1;  % P5P (2) indexing
l = 1;  % F6P indexing
m = 1;  % E4P indexing
for i = 1:length(d_S7P)
    d_S7P(i) = ((x_P5P(j)+x_P5P(j+4)+x_P5P(j+8)+x_P5P(j+12)+x_P5P(j+16)+x_P5P(j+20)+x_P5P(j+24)+x_P5P(j+28))*x_P5P(k)*f.ppp3_f+...
        (x_F6P(l)+x_F6P(l+8)+x_F6P(l+16)+x_F6P(l+24)+x_F6P(l+32)+x_F6P(l+40)+x_F6P(l+48)+x_F6P(l+56))*x_E4P(m)*f.ppp5_b-...
        ((f.ppp3_b+f.ppp5_f) * x_S7P(i)))/V_S7P;

    if j == 4
        j = 1;
        k = k+1;
    else
        j = j+1;
    end

    if l == 8
        l = 1;
        m = m+1;
    else
        l = l+1;
    end
end

% E4P
d_E4P = zeros(2^n_E4P,1);
j = 1;  % F6P indexing
k = 1;  % S7P indexing
for i = 1:length(d_E4P)
    d_E4P(i) = ((x_F6P(j)+x_F6P(j+1)+x_F6P(j+2)+x_F6P(j+3))*f.ppp4_b + ...
        (x_S7P(k)+x_S7P(k+1)+x_S7P(k+2)+x_S7P(k+3)+x_S7P(k+4)+x_S7P(k+5)+x_S7P(k+6)+x_S7P(k+7))*f.ppp5_f -...
        (f.ppp4_f+f.ppp5_b)*x_E4P(i))/V_E4P;

    j = j+4;
    k = k+8;
end

% Cit
d_Cit = zeros(2^n_Cit,1);
for i = 1:length(d_Cit)
    d_Cit(i) = (x_Citm(i)*f.CIC -(f.acl*x_Cit(i)))/V_Cit;
end

% OAA
d_OAA = zeros(2^n_OAA,1);
j = 1;
k = 1;
l = 1;  % CO2 indexing
m = 1;  % PEP indexing
Mal_index = [1, 9, 5, 13, 3, 11, 7, 15, 2, 10, 6, 14, 4, 12, 8, 16];
Cit_index_odd = [1, 5, 3, 7, 2, 6, 4, 8];
Cit_index_even = [33, 37, 35, 39, 34, 38, 36, 40];
for i = 1:length(d_OAA)
    if mod(i,2) == 0
        d_OAA(i) = ((x_Cit(Cit_index_even(j))+x_Cit(Cit_index_even(j)+8)+x_Cit(Cit_index_even(j)+16)+x_Cit(Cit_index_even(j)+24))*f.acl + ((x_CO2(l))*(x_PEP(m)
            0.5*x_Mal(i)*f.mdhc_b + 0.5*x_Mal(Mal_index(i))*f.mdhc_b + x_Asp(i)*f.ast_f - ((f.pepck_f+f.mdhc_f+f.ast_b)*x_OAA(i)))/V_OAA;

        if i == 8
           l = l+1;
           m = 1;
        else
            m = m+1;
        end

        j = j+1;
    else
        d_OAA(i) = ((x_Cit(Cit_index_odd(k))+x_Cit(Cit_index_odd(k)+8)+x_Cit(Cit_index_odd(k)+16)+x_Cit(Cit_index_odd(k)+24))*f.acl+((x_CO2(l))*(x_PEP(m)))*f.p
            0.5*x_Mal(i)*f.mdhc_b + 0.5*x_Mal(Mal_index(i))*f.mdhc_b + x_Asp(i)*f.ast_f - ((f.pepck_f+f.mdhc_f+f.ast_b)*x_OAA(i)))/V_OAA;

        if i == 8
            l = l+1;
            m = 1;
        else
            m = m+1;
        end

        k = k+1;
    end
end

% AcCoA
d_AcCoA = zeros(2^n_AcCoA,1);
j = 1;
for i = 1:length(d_AcCoA)
    d_AcCoA(i) = ((x_Cit(j)+x_Cit(j+1)+x_Cit(j+2)+x_Cit(j+3)+x_Cit(j+4)+x_Cit(j+5)+x_Cit(j+6)+x_Cit(j+7)+x_Cit(j+32)+...
        x_Cit(j+33)+x_Cit(j+34)+x_Cit(j+35)+x_Cit(j+36)+x_Cit(j+37)+x_Cit(j+38)+x_Cit(j+39))*f.acl -...
        (f.muAcCoA * x_AcCoA(i)))/V_AcCoA;

    if i == 1
```

```
        j = 17;
    elseif i ==2
        j = 9;
    elseif i ==3
        j = 25;
    end
end

% Ser
d_Ser = zeros(2^n_Ser,1);
for i = 1:length(d_Ser)
    d_Ser(i) = (x_Ser_ex(i)*f.tSer + x_3PG(i)*f.ser1 - ((f.muSer+f.ser2)*x_Ser(i)))/V_Ser;
end

% Ala
d_Ala = zeros(2^n_Ala,1);
for i = 1:length(d_Ala)
    d_Ala(i) = (x_Alam(i)*f.mAla_b + x_Ala_ex(i)*f.tAla_b + x_Pyr(i)*f.alt_f - ((f.muAla+f.mAla_f+f.tAla_f+f.alt_b)*x_Ala(i)))/V_Ala;
end

% Asp
d_Asp = zeros(2^n_Asp,1);
for i = 1:length(d_Asp)
    d_Asp(i) = (x_Aspm(i)*f.AGC1 + x_Asp_ex(i)*f.tAsp_b +x_OAA(i)*f.ast_b - ((f.muAsp+f.tAsp_f+f.ast_f)*x_Asp(i)))/V_Asp;
end

% Asn
d_Asn = zeros(2^n_Asn,1);
for i = 1:length(d_Asn)
    d_Asn(i) = (x_Asnm(i)*f.mAsn_b + x_Asn_ex(i)*f.tAsn - ((f.muAsn+f.mAsn_f)*x_Asn(i)))/V_Asn;
end

% Pyr_m
d_Pyrm = zeros(2^n_Pyrm,1);
for i = 1:length(d_Pyrm)
    d_Pyrm(i) = (x_Pyr(i)*f.MPC1 + (x_OAAm(i)+x_OAAm(i+8))*f.pc_b + (x_Malm(i)+x_Malm(i+8))*f.mem_f + x_Alam(i)*f.altm_f -...
        ((f.pdh+f.pc_f+f.mem_b+f.altm_b)*x_Pyrm(i)))/V_Pyrm;
end

% Cit_m
d_Citm = zeros(2^n_Citm,1);
OAA_indexing_odd = [1, 9, 5, 13, 3, 11, 7, 15];
OAA_indexing_even = [2, 10, 6, 14, 4, 12, 8, 16];
AcCoA_indexing = [1, 3, 2, 4, 1, 3, 2, 4];
j = 1;  % OAAm
k = 1;  % AcCoA
for i = 1:length(d_Citm)
    if i < 33
        d_Citm(i) = ((x_OAAm(OAA_indexing_odd(j))*x_AcCoA(AcCoA_indexing(k)))*f.csyn + x_aKGm(i)*x_CO2m(1)*f.idh_b -((f.CIC+f.idh_f)*x_Citm(i)))/V_Citm;

        if j == 8
            j = 1;
            k = k+1;
        else
            j = j+1;
        end

    else
        d_Citm(i) = ((x_OAAm(OAA_indexing_even(j))*x_AcCoA(AcCoA_indexing(k)))*f.csyn + x_aKGm(i-32)*x_CO2m(2)*f.idh_b -((f.CIC+f.idh_f)*x_Citm(i)))/V_Citm;

        if j == 8
            j = 1;
            k = k+1;
        else
            j = j+1;
        end
    end
end

% Mal
d_Mal = zeros(2^n_Mal,1);
j = 1;  % Pyr indexing
k = 1;  % CO2 indexing
for i = 1:length(d_Mal)
    d_Mal(i) = ((f.DIC_f+f.OGC_b)*x_Malm(i) + x_Pyr(j)*x_CO2(k)*f.me_b + 0.5*x_OAA(i)*f.mdhc_f +...
        0.5*x_OAA(Mal_index(i))*f.mdhc_f - ((f.CIC+f.DIC_b+f.OGC_f+f.me_f+f.mdhc_b)*x_Mal(i)))/V_Mal;
    if j == 8
        j = 1;
        k = k+1;
    else
        j = j+1;
    end
end

% Mal_m
d_Malm = zeros(2^n_Malm,1);
aKG_indexing = [1, 17, 9, 25, 5, 21, 13, 29, 3, 19, 11, 27, 7, 23, 15, 31];
j = 1;  % Mal indexing
k = 1;  % Pyr indexing
l = 1;  % CO2 indexing
for i = 1:length(d_Malm)
    d_Malm(i) = (x_Mal(i)*(f.CIC+f.DIC_b+f.OGC_f) + 0.5*(x_Fumm(i))*f.fus_f + 0.5*x_Fumm(Mal_index(i))*f.fus_f +...
        0.5*(x_OAAm(i))*f.mdh_b + 0.5*x_OAAm(Mal_index(i))*f.mdh_b + ...
```

```
        x_Pyrm(k)*x_CO2m(l)*f.mem_b - ((f.DIC_f+f.OGC_b+f.fus_b+f.mdh_f+f.mem_f)*x_Malm(i)))/V_Malm;
    j = j+2;

    if k == 8
        k = 1;
        l = l+1;
    else
        k = k+1;
    end
end

% aKG
d_aKG = zeros(2^n_aKG,1);
for i = 1:length(d_aKG)
    d_aKG(i) = (x_aKGm(i)*f.OGC_f + x_Glu(i)*(f.alt_f+f.ast_b) - ((f.OGC_b+f.alt_b+f.ast_f)*x_aKG(i)))/V_aKG;
end

% Asp_m
d_Aspm = zeros(2^n_Aspm,1);
for i = 1:length(d_Aspm)
    d_Aspm(i) = (x_OAAm(i)*f.astm_b + x_Asnm(i)*f.asnsm_f - ((f.AGC1+f.astm_f+f.asnsm_b)*x_Aspm(i)))/V_Aspm;
end

% Ala_m
d_Alam = zeros(2^n_Alam,1);
for i = 1:length(d_Alam)
    d_Alam(i) = (x_Ala(i)*f.mAla_f + x_Pyrm(i)*f.altm_b- ((f.mAla_b+f.altm_f)*x_Ala(i)))/V_Alam;
end

% Asn_m
d_Asnm = zeros(2^n_Asnm,1);
for i = 1:length(d_Asnm)
    d_Asnm(i) = (x_Asn(i)*f.mAsn_f + x_Aspm(i)*f.asnsm_b-((f.mAsn_b+f.asnsm_f)*x_Asnm(i)))/V_Asnm;
end

% AcCoA_m
d_AcCoAm = zeros(2^n_AcCoAm,1);
for i = 1:length(d_AcCoAm)
    d_AcCoAm(i) = ((x_Pyrm(i)+x_Pyrm(i+4))*f.pdh - f.csyn*x_AcCoAm(i))/V_AcCoAm;
end

% OAA_m
d_OAAm = zeros(2^n_OAAm,1);
Mal_index = [1, 9, 5, 13, 3, 11, 7, 15, 2, 10, 6, 14, 4, 12, 8, 16];
j = 1;  % Pyr indexing
k = 1;  % CO2 indexing
for i = 1:length(d_OAAm)
    d_OAAm(i) = (0.5*x_Malm(i)*f.mdh_f + 0.5*x_Malm(Mal_index(i))*f.mdh_f + x_Pyrm(j)*x_CO2m(k)*f.pc_f + x_Aspm(i)*f.astm_f-...
        ((f.csyn+f.mdh_b+f.pc_b+f.astm_b)*x_OAAm(i)))/V_OAAm;

    if j == 8
        j = 1;
        k = k+1;
    else
        j = j+1;
    end
end

% CO2
d_CO2 = zeros(2^n_CO2,1);
d_CO2m = zeros(2^n_CO2m,1);
j = 1;
k = 1;
for i = 1:length(d_CO2)
    d_CO2(i) = (x_CO2m(i)*f.mCO2_f  + ...
        (x_Mal(j)+x_Mal(j+1)+x_Mal(j+2)+x_Mal(j+3)+x_Mal(j+4)+x_Mal(j+5)+x_Mal(j+6)+x_Mal(j+7))*f.me_f + ...
        (x_OAA(j)+x_OAA(j+1)+x_OAA(j+2)+x_OAA(j+3)+x_OAA(j+4)+x_OAA(j+5)+x_OAA(j+6)+x_OAA(j+7))*f.pepck_f + ...
        (x_G6P(i)+x_G6P(i+2)+x_G6P(i+4)+x_G6P(i+6)+x_G6P(i+8)+x_G6P(i+10)+x_G6P(i+12)+...
        x_G6P(i+14)+x_G6P(i+16)+x_G6P(i+18)+x_G6P(i+20)+x_G6P(i+22)+x_G6P(i+24)+x_G6P(i+26)+x_G6P(i+28)+x_G6P(i+30)+...
        x_G6P(i+32)+x_G6P(i+34)+x_G6P(i+36)+x_G6P(i+38)+x_G6P(i+40)+x_G6P(i+42)+x_G6P(i+44)+x_G6P(i+46)+x_G6P(i+48)+...
        x_G6P(i+50)+x_G6P(i+52)+x_G6P(i+54)+x_G6P(i+56)+x_G6P(i+58)+x_G6P(i+60)+x_G6P(i+62))*f.ppp1 ...
        - ((f.tCO2+f.pepck_b+f.me_b+f.mCO2_b)*x_CO2(i)))/V_CO2;

    d_CO2m(i) = ((x_aKGm(i)+x_aKGm(i+2)+x_aKGm(i+4)+x_aKGm(i+6)+x_aKGm(i+8)+x_aKGm(i+10)+x_aKGm(i+12)+x_aKGm(i+14)+x_aKGm(i+16)+...
        x_aKGm(i+18)+x_aKGm(i+20)+x_aKGm(i+22)+x_aKGm(i+24)+x_aKGm(i+26)+x_aKGm(i+28)+x_aKGm(i+30))*f.adh_f + ...
        (x_Citm(k)+x_Citm(k+1)+x_Citm(k+2)+x_Citm(k+3)+x_Citm(k+4)+x_Citm(k+5)+x_Citm(k+6)+x_Citm(k+7)+x_Citm(k+8)+...
        x_Citm(k+9)+x_Citm(k+10)+x_Citm(k+11)+x_Citm(k+12)+x_Citm(k+13)+x_Citm(k+14)+x_Citm(k+15)+x_Citm(k+16)+x_Citm(k+17)+...
        x_Citm(k+18)+x_Citm(k+19)+x_Citm(k+20)+x_Citm(k+21)+x_Citm(k+22)+x_Citm(k+23)+x_Citm(k+24)+x_Citm(k+25)+x_Citm(k+26)+...
        x_Citm(k+27)+x_Citm(k+28)+x_Citm(k+29)+x_Citm(k+30)+x_Citm(k+31))*f.idh_f + ...
        x_CO2(i)*f.mCO2_b + ...
        (x_Malm(j)+x_Malm(j+1)+x_Malm(j+2)+x_Malm(j+3)+x_Malm(j+4)+x_Malm(j+5)+x_Malm(j+6)+x_Malm(j+7))*f.mem_f + ...
        (x_Pyrm(i)+x_Pyrm(i+2)+x_Pyrm(i+4)+x_Pyrm(i+6))*f.pdh + ...
        (x_OAAm(j)+x_OAAm(j+1)+x_OAAm(j+2)+x_OAAm(j+3)+x_OAAm(j+4)+x_OAAm(j+5)+x_OAAm(j+6)+x_OAAm(j+7))*f.pc_b ...
        - ((f.idh_b+f.adh_b+f.pc_f+f.mem_b+f.mCO2_f)*x_CO2m(i)))/V_CO2m;

    j = j+8;
    k = k+32;
end

% Glu_ex
d_Glu_ex = zeros(2^n_Glu,1);
for i = 1:length(d_Glu_ex)
%     d_Glu_ex(i) = (f.tGlu_f*x_Glu(i) - (f.tGlu_b+f.tGlu)*x_Glu_ex(i))/V_Glu_ex;
```

```
    d_Glu_ex(i) = (X_c*(f.tGlu_f*x_Glu(i) - f.tGlu_b*x_Glu_ex(i)) - f.tGlu*x_Glu_ex(i))/V_Glu_ex;
end

% Lac_ex
d_Lac_ex = zeros(2^n_Lac,1);
for i = 1:length(d_Lac_ex)

        d_Lac_ex(i) = (X_c*(f.tLac_f*x_Lac(i) - f.tLac_b*x_Lac_ex(i)) - f.tLac*x_Lac_ex(i))/V_Lac_ex;
end

% Ala_ex
d_Ala_ex = zeros(2^n_Ala,1);
for i = 1:length(d_Ala_ex)
    d_Ala_ex(i) = (X_c*(f.tAla_f*x_Ala(i) - f.tAla_b*x_Ala_ex(i)) - f.tAla*x_Ala_ex(i))/V_Ala_ex;
end

% Asp_ex
d_Asp_ex = zeros(2^n_Asp,1);
for i = 1:length(d_Asp_ex)
    d_Asp_ex(i) = (X_c*(f.tAsp_f*x_Asp(i) - f.tAsp_b*x_Asp_ex(i)) - f.tAsp*x_Asp_ex(i))/V_Asp_ex;
end

% Fumm
d_Fumm = zeros(2^n_Fum,1);
j = 1;
for i = 1:length(d_Fumm)
    d_Fumm(i) = (0.5*(x_aKGm(j)+x_aKGm(j+1))*f.adh_f + 0.5*(x_aKGm(aKG_indexing(i))+x_aKGm(aKG_indexing(i)+1))*f.adh_f + ...
        0.5*(x_Malm(i))*f.fus_b + 0.5*x_Malm(Mal_index(i))*f.fus_b- ...
        (f.adh_b+f.fus_f) * x_Fumm(i))/V_Fumm;
    j = j+2;
end
```

...

```
d_Gln(1) = 0-sum(d_Gln(2:end,1));
d_Glu(1) = 0-sum(d_Glu(2:end,1));
d_aKGm(1) = 0-sum(d_aKGm(2:end,1));
d_Glum(1) = 0-sum(d_Glum(2:end,1));
d_G6P(1) = 0-sum(d_G6P(2:end,1));
d_F6P(1) = 0-sum(d_F6P(2:end,1));
d_FBP(1) = 0-sum(d_FBP(2:end,1));
d_DHAP(1) = 0-sum(d_DHAP(2:end,1));
d_GAP(1) = 0-sum(d_GAP(2:end,1));
d_3PG(1) = 0-sum(d_3PG(2:end,1));
d_PEP(1) = 0-sum(d_PEP(2:end,1));
d_Pyr(1) = 0-sum(d_Pyr(2:end,1));
d_Lac(1) = 0-sum(d_Lac(2:end,1));
d_P5P(1) = 0-sum(d_P5P(2:end,1));
d_S7P(1) = 0-sum(d_S7P(2:end,1));
d_E4P(1) = 0-sum(d_E4P(2:end,1));
d_Cit(1) = 0-sum(d_Cit(2:end,1));
d_OAA(1) = 0-sum(d_OAA(2:end,1));
d_AcCoA(1) = 0-sum(d_AcCoA(2:end,1));
d_Ser(1) = 0-sum(d_Ser(2:end,1));
d_Ala(1) = 0-sum(d_Ala(2:end,1));
d_Asp(1) = 0-sum(d_Asp(2:end,1));
d_Asn(1) = 0-sum(d_Asn(2:end,1));
d_Pyrm(1) = 0-sum(d_Pyrm(2:end,1));
d_Citm(1) = 0-sum(d_Citm(2:end,1));
d_Mal(1) = 0-sum(d_Mal(2:end,1));
d_Malm(1) = 0-sum(d_Malm(2:end,1));
d_aKG(1) = 0-sum(d_aKG(2:end,1));
d_Aspm(1) = 0-sum(d_Aspm(2:end,1));
d_Alam(1) = 0-sum(d_Alam(2:end,1));
d_Asnm(1) = 0-sum(d_Asnm(2:end,1));
d_AcCoAm(1) = 0-sum(d_AcCoAm(2:end,1));
d_OAAm(1) = 0-sum(d_OAAm(2:end,1));
d_CO2(1) = 0-sum(d_CO2(2:end,1));
d_CO2m(1) = 0-sum(d_CO2m(2:end,1));
d_Glu_ex(1) = 0-sum(d_Glu_ex(2:end,1));
d_Lac_ex(1) = 0-sum(d_Lac_ex(2:end,1));
d_Ala_ex(1) = 0-sum(d_Ala_ex(2:end,1));
d_Asp_ex(1) = 0-sum(d_Asp_ex(2:end,1));
d_Fumm(1) = 0-sum(d_Fumm(2:end,1));

dx = [d_Gln; d_Glu; d_aKGm; d_Glum; d_G6P; d_F6P; d_FBP; d_DHAP; d_GAP; d_3PG; d_PEP; d_Pyr; d_Lac; d_P5P; d_S7P; d_E4P;...
    d_Cit; d_OAA; d_AcCoA; d_Ser; d_Ala; d_Asp; d_Asn; d_Pyrm; d_Citm; d_Mal; d_Malm; d_aKG; d_Aspm; d_Alam; d_Asnm; d_AcCoAm; ...
    d_OAAm; d_CO2; d_CO2m; d_Glu_ex; d_Lac_ex; d_Ala_ex; d_Asp_ex; d_Fumm];
```

Published with MATLAB® R2022b

Bibliography

[AA11] W. S. Ahn, M. R. Antoniewicz. “Metabolic flux analysis of CHO cells at growth and non-growth phases using isotopic tracers and mass spectrometry.” In: *Metabolic engineering* 13.5 (2011), pp. 598–609 (cit. on pp. 38, 45, 47, 59, 70, 72, 88, 96, 97, 113, 116, 128, 132–134, 138, 161, 169, 178, 181).

[AA12] W. S. Ahn, M. R. Antoniewicz. “Towards dynamic metabolic flux analysis in CHO cell cultures.” In: *Biotechnology journal* 7.1 (2012), pp. 61–74 (cit. on pp. 47, 58, 128, 129).

[AA13] W. S. Ahn, M. R. Antoniewicz. “Parallel labeling experiments with [1,2-^{13}C] glucose and [U-^{13}C] glutamine provide new insights into CHO cell metabolism.” In: *Metabolic engineering* 15 (2013), pp. 34–47 (cit. on pp. 88, 129, 143).

[AECJ92] M. Al-Rubeai, A. Emery, S. Chalder, D. Jan. “Specific monoclonal antibody productivity and the cell cycle-comparisons of batch, continuous and perfusion cultures.” In: *Cytotechnology* 9.1-3 (1992), pp. 85–97 (cit. on p. 161).

[AGM+02] E. Ansorena, E. R. Garcıa-Trevijano, M. L. Martınez-Chantar, Z.-Z. Huang, L. Chen, J. M. Mato, M. Iraburu, S. C. Lu, M. A. Avila. “S-adenosylmethionine and methylthioadenosine are antiapoptotic in cultured rat hepatocytes but proapoptotic in human hepatoma cells.” In: *Hepatology* 35.2 (2002), pp. 274–280 (cit. on pp. 161, 175).

[AHYS99] Y.-H. Ahn, K. Han, S. K. Yoon, J.-Y. Song. “Effect of glycine betaine as osmoprotectant on the production of erythropoietin by CHO cells in hyperosmotic serum free media culture.” In: *Animal Cell Technology: Basic & Applied Aspects*. Springer, 1999, pp. 247–250 (cit. on p. 161).

[AKS06] M. R. Antoniewicz, J. K. Kelleher, G. Stephanopoulos. “Determination of confidence intervals of metabolic fluxes estimated from stable isotope measurements.” In: *Metabolic Engineering* 8.4 (2006), pp. 324–337 (cit. on p. 77).

[Ant15] M. R. Antoniewicz. “Methods and advances in metabolic flux analysis: a mini-review.” In: *Journal of industrial microbiology & biotechnology* 42.3 (2015), pp. 317–325 (cit. on p. 56).

[AO00] K. Alm, S. M. Oredsson. “The organization of replicon clusters is not affected by polyamine depletion.” In: *Journal of structural biology* 131.1 (2000), pp. 1–9 (cit. on p. 175).

[ASO07] D. K. Allen, Y. Shachar-Hill, J. B. Ohlrogge. “Compartment-specific labeling information in ^{13}C metabolic flux analysis of plants.” In: *Phytochemistry* 68.16-18 (2007), pp. 2197–2210 (cit. on p. 128).

[ASR98] C. L. Atanassov, N. Seiler, G. Rebel. “Reduction of ammonia formation in cell cultures by L-alanyl-L-glutamine requires optimization of the dipeptide concentration.” In: *Journal of biotechnology* 62.2 (1998), pp. 159–162 (cit. on p. 54).

[BAB+15] J. M. Buescher, M. R. Antoniewicz, L. G. Boros, S. C. Burgess, H. Brunengraber, C. B. Clish, R. J. DeBerardinis, O. Feron, C. Frezza, B. Ghesquiere, et al. “A roadmap for interpreting ^{13}C metabolite labeling patterns from cells.” In: *Current opinion in biotechnology* 34 (2015), pp. 189–201 (cit. on p. 130).

[BHR+11] J. Becker, M. Hackl, O. Rupp, T. Jakobi, J. Schneider, R. Szczepanowski, T. Bekel, N. Borth, A. Goesmann, J. Grillari, et al. “Unraveling the Chinese hamster ovary cell line transcriptome by next-generation sequencing.” In: *Journal of biotechnology* 156.3 (2011), pp. 227–235 (cit. on p. 38).

[BJS+11] S. D. Bolboacă, L. Jäntschi, A. F. Sestraş, R. E. Sestraş, D. C. Pamfil. "Pearson-Fisher chi-square statistic revisited." In: *Information* 2.3 (2011), pp. 528–545 (cit. on p. 77).

[BJT+19a] M. Becker, L. Junghans, A. Teleki, J. Bechmann, R. Takors. "Perfusion cultures require optimum respiratory ATP supply to maximize cell-specific and volumetric productivities." In: *Biotechnology and bioengineering* 116.5 (2019), pp. 951–960 (cit. on pp. 144, 160).

[BJT+19b] M. Becker, L. Junghans, A. Teleki, J. Bechmann, R. Takors. "The less the better: How suppressed base addition boosts production of monoclonal antibodies with Chinese Hamster Ovary cells." In: *Frontiers in bioengineering and biotechnology* 7 (2019), p. 76 (cit. on p. 144).

[BKP21] K. Braasch, M. Kryworuchko, J. M. Piret. "Autophagy-inducing peptide increases CHO cell monoclonal antibody production in batch and fed-batch cultures." In: *Biotechnology and Bioengineering* 118.5 (2021), pp. 1876–1883 (cit. on p. 40).

[Bor20] P. Borst. "The malate–aspartate shuttle (Borst cycle): How it started and developed into a major metabolic pathway." In: *IUBMB life* 72.11 (2020), pp. 2241–2259 (cit. on p. 44).

[BPB+20] E. Balsa, E. A. Perry, C. F. Bennett, M. Jedrychowski, S. P. Gygi, J. G. Doench, P. Puigserver. "Defective NADPH production in mitochondrial disease complex I causes inflammation and cell death." In: *Nature communications* 11.1 (2020), pp. 1–12 (cit. on p. 179).

[BPP+20] D. B. Bulté, L. A. Palomares, C. G. Parra, J. A. Martınez, M. A. Contreras, L. G. Noriega, O. T. Ramırez. "Overexpression of the mitochondrial pyruvate carrier reduces lactate production and increases recombinant protein productivity in CHO cells." In: *Biotechnology and Bioengineering* 117.9 (2020), pp. 2633–2647 (cit. on p. 43).

[BR06] J. R. Birch, A. J. Racher. "Antibody production." In: *Advanced drug delivery reviews* 58.5-6 (2006), pp. 671–685 (cit. on p. 86).

[BS79] J. E. Bottenstein, G. H. Sato. “Growth of a rat neuroblastoma cell line in serum-free supplemented medium.” In: *Proceedings of the National Academy of Sciences* 76.1 (1979), pp. 514–517 (cit. on p. 53).

[BTC+12] D. Baycin-Hizal, D. L. Tabb, R. Chaerkady, L. Chen, N. E. Lewis, H. Nagarajan, V. Sarkaria, A. Kumar, D. Wolozny, J. Colao, et al. “Proteomic analysis of Chinese hamster ovary cells.” In: *Journal of proteome research* 11.11 (2012), pp. 5265–5276 (cit. on p. 38).

[But05] M. Butler. “Animal cell cultures: recent achievements and perspectives in the production of biopharmaceuticals.” In: *Applied Microbiology and Biotechnology* 68.3 (Aug. 2005), pp. 283–291 (cit. on p. 52).

[BVM+03] C. C. Burteau, F. R. Verhoeye, J. F. Molsl, J.-S. Ballez, S. N. Agathos, Y.-J. Schneider. “Fortification of a protein-free cell culture medium with plant peptones improves cultivation and productivity of an interferon-γ-producing CHO cell line.” In: *In Vitro Cellular & Developmental Biology-Animal* 39.7 (2003), pp. 291–296 (cit. on p. 40).

[CB94] A. Christie, M. Butler. “Glutamine-based dipeptides are utilized in mammalian cell culture by extracellular hydrolysis catalyzed by a specific peptidase.” In: *Journal of biotechnology* 37.3 (1994), pp. 277–290 (cit. on p. 55).

[CKH+16] J. Coronel, S. Klausing, C. Heinrich, T. Noll, A. Figueredo-Cardero, L. R. Castilho. “Valeric acid supplementation combined to mild hypothermia increases productivity in CHO cell cultivations.” In: *Biochemical Engineering Journal* 114 (2016), pp. 101–109 (cit. on p. 161).

[CN00] B. Christensen, J. Nielsen. “Metabolic network analysis of Penicillium chrysogenum using ^{13}C-labeled glucose.” In: *Biotechnology and Bioengineering* 68.6 (2000), pp. 652–659 (cit. on p. 44).

[CTH+12] W. P. K. Chong, S. H. Thng, A. P. Hiu, D.-Y. Lee, E. C. Y. Chan, Y. S. Ho. “LC-MS-based metabolic characterization of high monoclonal antibody-producing Chinese hamster ovary cells.” In: *Biotechnology and bioengineering* 109.12 (2012), pp. 3103–3111 (cit. on p. 161).

[CWG18] C. Chen, H. E. Wong, C. T. Goudar. “Upstream process intensification and continuous manufacturing.” In: *Current opinion in chemical engineering* 22 (2018), pp. 191–198 (cit. on p. 36).

[DEM+03] A. Drysch, M. El Massaoudi, C. Mack, R. Takors, A. de Graaf, H. Sahm. “Production process monitoring by serial mapping of microbial carbon flux distributions using a novel Sensor Reactor approach: II—^{13}C-labeling-based metabolic flux analysis and L-lysine production.” In: *Metabolic engineering* 5.2 (2003), pp. 96–107 (cit. on p. 44).

[DEM+16] J. Dumont, D. Euwart, B. Mei, S. Estes, R. Kshirsagar. “Human cell lines for biopharmaceutical manufacturing: history, status, and future perspectives.” In: *Critical reviews in biotechnology* 36.6 (2016), pp. 1110–1122 (cit. on p. 36).

[DS03] S. DiMauro, E. A. Schon. “Mitochondrial respiratory-chain diseases.” In: *New England Journal of Medicine* 348.26 (2003), pp. 2656–2668 (cit. on p. 87).

[DW11] M. De Jesus, F. M. Wurm. “Manufacturing recombinant proteins in kg-ton quantities using animal cells in bioreactors.” In: *European Journal of Pharmaceutics and Biopharmaceutics* 78.2 (2011), pp. 184–188 (cit. on p. 37).

[Eag55] H. Eagle. “The specific amino acid requirements of a mammalian cell (strain L) in tissue culture.” In: *Journal of Biological Chemistry* 214 (1955), pp. 839–852 (cit. on pp. 40, 52, 53).

[EJL15] D. M. Ecker, S. D. Jones, H. L. Levine. “The therapeutic monoclonal antibody market.” In: *MAbs*. Vol. 7. 1. Taylor & Francis. 2015, pp. 9–14 (cit. on p. 86).

[EP93] K. S. Emmerson, J. M. Phang. “Hydrolysis of proline dipeptides completely fulfills the proline requirement in a proline-auxotrophic Chinese hamster ovary cell line.” In: *The Journal of nutrition* 123.5 (1993), pp. 909–914 (cit. on p. 55).

[FHF+16] J. Feichtinger, I. Hernández, C. Fischer, M. Hanscho, N. Auer, M. Hackl, V. Jadhav, M. Baumann, P. M. Krempl, C. Schmidl, et al. “Comprehensive genome and epigenome characterization of CHO cells in response to evolutionary pressures and over time.” In: *Biotechnology and bioengineering* 113.10 (2016), pp. 2241–2253 (cit. on p. 161).

[FMB97] M. Fussenegger, X. Mazur, J. E. Bailey. “A novel cytostatic process enhances the productivity of Chinese hamster ovary cells.” In: *Biotechnology and bioengineering* 55.6 (1997), pp. 927–939 (cit. on p. 176).

[FPS59] H. W. Fisher, T. T. Puck, G. Sato. “Molecular Growth Requirements of Single Mammalian Cells.” In: *Journal of Experimental Medicine* 109.6 (1959) (cit. on p. 52).

[FPYW04] S. R. Fox, U. A. Patel, M. G. Yap, D. I. Wang. “Maximizing interferon-γ production by chinese hamster ovary cells through temperature shift optimization: Experimental and modeling: Experimental and modeling.” In: *Biotechnology and bioengineering* 85.2 (2004), pp. 177–184 (cit. on pp. 161, 176).

[FSCP00] S. Farfari, V. Schulz, B. Corkey, M. Prentki. “Glucose-regulated anaplerosis and cataplerosis in pancreatic beta-cells: possible implication of a pyruvate/citrate shuttle in insulin secretion.” In: *Diabetes* 49.5 (2000), pp. 718–726 (cit. on p. 65).

[FTC+06] B. Farges-Haddani, B. Tessier, S. Chenu, I. Chevalot, C. Harscoat, I. Marc, J. Goergen, A. Marc. “Peptide fractions of rapeseed hydrolysates as an alternative to animal proteins in CHO cell culture media.” In: *Process Biochemistry* 41.11 (2006), pp. 2297–2304 (cit. on p. 40).

[FU80] E. Furuya, K. Uyeda. “Regulation of phosphofructokinase by a new mechanism. An activation factor binding to phosphorylated enzyme.” In: *Journal of Biological Chemistry* 255.24 (1980), pp. 11656–11659 (cit. on p. 176).

[Für98] P. Fürst. “Old and new substrates in clinical nutrition.” In: *The Journal of nutrition* 128.5 (1998), pp. 789–796 (cit. on p. 54).

[FW05] O. Frick, C. Wittmann. “Characterization of the metabolic shift between oxidative and fermentative growth in *Saccharomyces cerevisiae* by comparative ^{13}C flux analysis.” In: *Microbial cell factories* 4.1 (2005), pp. 1–16 (cit. on p. 128).

[FYK+14] J. Fan, J. Ye, J. J. Kamphorst, T. Shlomi, C. B. Thompson, J. D. Rabinowitz. “Quantitative flux analysis reveals folate-dependent NADPH production.” In: *Nature* 510.7504 (2014), pp. 298–302 (cit. on p. 113).

[Gau16] C. L. Gaughan. “The present state of the art in expression, production and characterization of monoclonal antibodies.” In: *Molecular diversity* 20.1 (2016), pp. 255–270 (cit. on p. 86).

[GBB+10a] C. Goudar, R. Biener, C. Boisart, R. Heidemann, J. Piret, A. de Graaf, K. Konstantinov. “Metabolic flux analysis of CHO cells in perfusion culture by metabolite balancing and 2D [^{13}C, ^{1}H] COSY NMR spectroscopy.” In: *Metabolic engineering* 12.2 (2010), pp. 138–149 (cit. on p. 88).

[GBB+10b] C. Goudar, R. Biener, C. Boisart, R. Heidemann, C. Zhang, A. de Graaf, J. Piret, K. Konstantinov. “Characterizing Physiology and Metabolism of High-Density CHO Cell Perfusion Cultures Using 2D-NMR Spectroscopy.” In: *Cells and Culture*. Springer, 2010, pp. 349–357 (cit. on p. 38).

[GBL99] M. W. Gray, G. Burger, B. F. Lang. “Mitochondrial evolution.” In: *Science* 283.5407 (1999), pp. 1476–1481 (cit. on p. 87).

[GHJ13] A. Ghorbaniaghdam, O. Henry, M. Jolicoeur. “A kinetic-metabolic model based on cell energetic state: study of CHO cell behavior under Na-butyrate stimulation.” In: *Bioprocess and biosystems engineering* 36.4 (2013), pp. 469–487 (cit. on p. 38).

[GKK15] M. B. Ginzberg, R. Kafri, M. Kirschner. “On being the right (cell) size.” In: *Science* 348.6236 (2015) (cit. on p. 161).

[GM76] D. Gospodarowicz, J. S. Moran. “Growth factors in mammalian cell culture.” In: *Annual review of biochemistry* 45.1 (1976), pp. 531–558 (cit. on p. 54).

[GMA+07] C. Guay, S. M. Madiraju, A. Aumais, É. Joly, M. Prentki. “A role for ATP-citrate lyase, malic enzyme, and pyruvate/citrate cycling in glucose-induced insulin secretion.” In: *Journal of Biological Chemistry* 282.49 (2007), pp. 35657–35665 (cit. on p. 65).

[GMG85] F. Gasser, P. Mulsant, M. Gillois. “Long-term multiplication of the Chinese hamster ovary (CHO) cell line in a serum-free medium.” In: *In Vitro Cellular amp; Developmental Biology* 21.10 (Oct. 1985), pp. 588–592 (cit. on pp. 52, 53).

[HAH+16] H. Hefzi, K. S. Ang, M. Hanscho, A. Bordbar, D. Ruckerbauer, M. Lakshmanan, C. A. Orellana, D. Baycin-Hizal, Y. Huang, D. Ley, et al. “A consensus genome-scale reconstruction of Chinese hamster ovary cell metabolism.” In: *Cell systems* 3.5 (2016), pp. 434–443 (cit. on pp. 39, 42, 43, 59, 62, 65, 99, 113, 161).

[Ham65] R. G. Ham. “Clonal growth of mammalian cells in a chemically defined, synthetic medium.” In: *Proceedings of the National Academy of Sciences of the United States of America* 53.2 (1965), p. 288 (cit. on pp. 52, 53).

[HCY10] J. K. Hong, S. M. Cho, S. K. Yoon. “Substitution of glutamine by glutamate enhances production and galactosylation of recombinant IgG in Chinese hamster ovary cells.” In: *Applied Microbiology and Biotechnology* 88.4 (Oct. 2010), pp. 869–876. URL: http://link.springer.com/10.1007/s00253-010-2790-1 (cit. on p. 53).

[HGY+13] Z. Hu, D. Guo, S. S. Yip, D. Zhan, S. Misaghi, J. C. Joly, B. R. Snedecor, A. Y. Shen. “Chinese hamster ovary K1 host cell enables stable cell line development for antibody molecules which are difficult to express in DUXB11-derived dihydrofolate reductase deficient host cell.” In: *Biotechnology progress* 29.4 (2013), pp. 980–985 (cit. on p. 37).

[HH77] W. G. Hamilton, R. G. Ham. “Clonal growth of chinese hamster cell lines in protein-free media.” In: *In vitro* 13.9 (Sept. 1977), pp. 537–547. URL: http://link.springer.com/10.1007/BF02627849 (cit. on pp. 52, 53).

[HHP+15] E. Harreither, M. Hackl, J. Pichler, S. Shridhar, N. Auer, P. P. Łabaj, M. Scheideler, M. Karbiener, J. Grillari, D. P. Kreil, et al. “Microarray profiling of preselected CHO host cell subclones identifies gene expression patterns associated with in-creased production capacity.” In: *Biotechnology journal* 10.10 (2015), pp. 1625–1638 (cit. on p. 161).

[HM90] J. L. Hamlin, C. Ma. “The mammalian dihydrofolate reductase locus.” In: *Biochimica et Biophysica Acta (BBA)-Gene Structure and Expression* 1087.2 (1990), pp. 107–125 (cit. on p. 51).

[HMG07] E. P. Huang, C. P. Marquis, P. P. Gray. “Development of Super-CHO protein-free medium based on a statistical design.” In: *Journal of Chemical Technology & Biotechnology* 82.5 (May 2007), pp. 431–441 (cit. on p. 53).

[HS76] I. Hayashi, G. H. Sato. “Replacement of serum by hormones permits growth of cells in a defined medium.” In: *Nature* 259.5539 (1976), pp. 132–134 (cit. on p. 53).

[HTS+14] N. Hammerschmidt, A. Tscheliessnig, R. Sommer, B. Helk, A. Jungbauer. “Economics of recombinant antibody production processes at various scales: Industry-standard compared to continuous precipitation.” In: *Biotechnology journal* 9.6 (2014), pp. 766–775 (cit. on p. 87).

[HTY+92] J.-i. Hata, T. Tamura, S. Yokoshima, S. Yamashita, S. Kabeno, K. Matsumoto, K. Onodera. “Chemically defined medium for the production of biologically active substances of CHO cells.” In: *Cytotechnology* 10.1 (1992), pp. 9–14. URL: http://dx.doi.org/10.1007/BF00376095%20http://link.springer.com/10.1007/BF00376095 (cit. on pp. 52, 53).

[HV18] A. M. Hosios, M. G. Vander Heiden. “The redox requirements of proliferating mammalian cells.” In: *Journal of Biological Chemistry* 293.20 (2018), pp. 7490–7498 (cit. on pp. 59, 96, 112, 173).

[HZQ+00] R. Heidemann, C. Zhang, H. Qi, J. Larrick Rule, C. Rozales, S. Park, S. Chuppa, M. Ray, J. Michaels, K. Konstantinov, et al. “The use of peptones as medium additives for the production of a recombinant therapeutic protein in high density perfusion cultures of mammalian cells.” In: *Cytotechnology* 32.2 (2000), pp. 157–167 (cit. on p. 53).

[INT+09] H. Imamura, K. P. H. Nhat, H. Togawa, K. Saito, R. Iino, Y. Kato-Yamada, T. Nagai, H. Noji. “Visualization of ATP levels inside single living cells with fluorescence resonance energy transfer-based genetically encoded indicators.” In: *Proceedings of the National Academy of Sciences* 106.37 (2009), pp. 15651–15656 (cit. on pp. 87, 88).

[ITT+10] Y. Imamoto, H. Tanaka, K. Takahashi, Y. Konno, T. Suzawa. “Advantage of Alagln as an Additive to Cell Culture Medium.” In: *Basic and Applied Aspects*. Dordrecht: Springer Netherlands, 2010, pp. 65–71. URL: http://www.springerlink.com/index/10.1007/978-90-481-3892-0%7B%5C_%7D11 (cit. on p. 53).

[JS08] Z. Jiang, S. T. Sharfstein. “Sodium butyrate stimulates monoclonal antibody over-expression in CHO cells by improving gene accessibility.” In: *Biotechnology and bioengineering* 100.1 (2008), pp. 189–194 (cit. on p. 161).

[JTW+19] L. Junghans, A. Teleki, A. W. Wijaya, M. Becker, M. Schweikert, R. Takors. “From nutritional wealth to autophagy: In vivo metabolic dynamics in the cytosol, mitochondrion and shuttles of IgG producing CHO cells.” In: *Metabolic engineering* 54 (2019), pp. 145–159 (cit. on pp. 39, 45, 47, 62, 66, 70, 74, 89, 90, 92, 94, 100, 101, 105, 107, 112, 113, 115, 116, 119, 129, 130, 132, 134, 138, 141, 144, 150, 161, 167, 169, 172–174, 176, 178).

[JWHY+07] K. P. Jayapal, K. F. Wlaschin, W. Hu, M. G. Yap, et al. “Recombinant protein therapeutics from CHO cells-20 years and counting.” In: *Chemical engineering progress* 103.10 (2007), p. 40 (cit. on p. 36).

[KBLB13] H. F. Kildegaard, D. Baycin-Hizal, N. E. Lewis, M. J. Betenbaugh. “The emerging CHO systems biology era: harnessing the ‘omics revolution

for biotechnology." In: *Current opinion in biotechnology* 24.6 (2013), pp. 1102–1107 (cit. on pp. 37, 44, 160).

[Kel09] B. Kelley. "Industrialization of mAb production technology: the bioprocessing industry at a crossroads." In: *MAbs*. Vol. 1. 5. Taylor & Francis. 2009, pp. 443–452 (cit. on p. 36).

[Kit02] H. Kitano. "Systems biology: a brief overview." In: *science* 295.5560 (2002), pp. 1662–1664 (cit. on p. 37).

[KKK+15a] S. Kishishita, S. Katayama, K. Kodaira, Y. Takagi, H. Matsuda, H. Okamoto, S. Takuma, C. Hirashima, H. Aoyagi. "Optimization of chemically defined feed media for monoclonal antibody production in Chinese hamster ovary cells." In: *Journal of bioscience and bioengineering* 120.1 (2015), pp. 78–84 (cit. on p. 37).

[KKK+15b] S. Kishishita, S. Katayama, K. Kodaira, Y. Takagi, H. Matsuda, H. Okamoto, S. Takuma, C. Hirashima, H. Aoyagi. "Optimization of chemically defined feed media for monoclonal antibody production in Chinese hamster ovary cells." In: *Journal of Bioscience and Bioengineering* 120.1 (2015), pp. 78–84 (cit. on p. 54).

[KM09] A. V. Kuznetsov, R. Margreiter. "Heterogeneity of mitochondria and mitochondrial function within cells as another level of mitochondrial complexity." In: *International journal of molecular sciences* 10.4 (2009), pp. 1911–1929 (cit. on p. 87).

[KMMD12] S. Kang, J. Mullen, L. P. Miranda, R. Deshpande. "Utilization of tyrosine- and histidine-containing dipeptides to enhance productivity and culture viability." In: *Biotechnology and bioengineering* 109.9 (2012), pp. 2286–2294 (cit. on pp. 54, 55).

[KOT+05] S. Kuwae, T. Ohda, H. Tamashima, H. Miki, K. Kobayashi. "Development of a fed-batch culture process for enhanced production of recombinant human antithrombin by Chinese hamster ovary cells." In: *Journal of bioscience and bioengineering* 100.5 (2005), pp. 502–510 (cit. on p. 37).

[KR16] R. Kunert, D. Reinhart. “Advances in recombinant antibody manufacturing.” In: *Applied microbiology and biotechnology* 100.8 (2016), pp. 3451–3461 (cit. on pp. 37, 86).

[KR95] M. J. Keen, N. T. Rapson. “Development of a serum-free culture medium for the large scale production of recombinant protein from a Chinese hamster ovary cell line.” In: *Cytotechnology* 17.3 (1995), pp. 153–163. URL: http://link.springer.com/10.1007/BF00749653 (cit. on p. 53).

[Kre07] M. T. A. P. Kresnowati. “Stimulus response methodology for quantitative model development of central carbon metabolism in *Saccharomyces cerevisiae*.” In: (2007) (cit. on p. 45).

[KSG02] S. Klamt, S. Schuster, E. D. Gilles. “Calculability analysis in underdetermined metabolic networks illustrated by a model of the central metabolism in purple nonsulfur bacteria.” In: *Biotechnology and Bioengineering* 77.7 (2002), pp. 734–751 (cit. on pp. 69, 146).

[KVG+08] A. V. Kuznetsov, V. Veksler, F. N. Gellerich, V. Saks, R. Margreiter, W. S. Kunz. “Analysis of mitochondrial function in situ in permeabilized muscle fibers, tissues and cells.” In: *Nature protocols* 3.6 (2008), p. 965 (cit. on p. 87).

[LHF83] C. Leaver, E. Hack, B. Forde. “[43] Protein synthesis by isolated plant mitochondria.” In: *Methods in enzymology* 97 (1983), pp. 476–484 (cit. on p. 87).

[LM00] D. Lloyd, D. B. Murray. “Redox cycling of intracellular thiols: state variables for ultradian, cell division cycle and circadian cycles?” In: *The Redox State and Circadian Rhythms*. Springer, 2000, pp. 85–94 (cit. on p. 176).

[Log06] D. C. Logan. “The mitochondrial compartment.” In: *Journal of experimental botany* 57.6 (2006), pp. 1225–1243 (cit. on p. 87).

[LPF+14] C. A. Lewis, S. J. Parker, B. P. Fiske, D. McCloskey, D. Y. Gui, C. R. Green, N. I. Vokes, A. M. Feist, M. G. Vander Heiden, C. M. Metallo. "Tracing compartmentalized NADPH metabolism in the cytosol and mitochondria of mammalian cells." In: *Molecular cell* 55.2 (2014), pp. 253–263 (cit. on p. 116).

[LSA10] F. Li, A. Shen, A. Amanullah. "Cell culture processes in monoclonal antibody production." In: *Pharmaceutical Sciences Encyclopedia: Drug Discovery, Development, and Manufacturing* (2010), pp. 1–38 (cit. on p. 37).

[LSD+92] R. Law, J. Stimmel, M. Damore, C. Carter, S. Clarke, R. Wall. "Lipopolysaccharide-induced NF-kappa B activation in mouse 70Z/3 pre-B lymphocytes is inhibited by mevinolin and 5'-methylthioadenosine: roles of protein isoprenylation and carboxyl methylation reactions." In: *Molecular and cellular biology* 12.1 (1992), pp. 103–111 (cit. on p. 161).

[LSF+16] L. Liu, S. Shah, J. Fan, J. O. Park, K. E. Wellen, J. D. Rabinowitz. "Malic enzyme tracers reveal hypoxia-induced switch in adipocyte NADPH pathway usage." In: *Nature chemical biology* 12.5 (2016), pp. 345–352 (cit. on p. 113).

[LV11] S. Y. Lunt, M. G. Vander Heiden. "Aerobic glycolysis: meeting the metabolic requirements of cell proliferation." In: *Annual review of cell and developmental biology* 27 (2011), pp. 441–464 (cit. on pp. 59, 60, 113).

[LW71] K. F. LaNoue, J. R. Williamson. "Interrelationships between malate-aspartate shuttle and citric acid cycle in rat heart mitochondria." In: *Metabolism* 20.2 (1971), pp. 119–140 (cit. on p. 87).

[Mac82] M. J. MacDonald. "Evidence for the malate aspartate shuttle in pancreatic islets." In: *Archives of biochemistry and biophysics* 213.2 (1982), pp. 643–649 (cit. on pp. 44, 63).

[Mac95] M. J. MacDonald. "Feasibility of a Mitochondrial Pyruvate Malate Shuttle in Pancreatic Islets: Further Implication of Cytosolic NADPH

in Insulin Secretion ().” In: *Journal of Biological Chemistry* 270.34 (1995), pp. 20051–20058 (cit. on p. 65).

[Man63] T. E. Mansour. “Studies on heart phosphofructokinase: purification, inhibition, and activation.” In: *Journal of Biological Chemistry* 238.7 (1963), pp. 2285–2292 (cit. on p. 176).

[MBB+18] M. Madigan, K. Bender, D. Buckley, W. Sattley, D. Stahl. “Brock Biology of Microorganisms, 15th Global edition.” In: *Boston, US: Benjamin Cummins* (2018) (cit. on p. 58).

[MBHW11] M. Matasci, L. Baldi, D. L. Hacker, F. M. Wurm. “The PiggyBac transposon enhances the frequency of CHO stable cell line generation and yields recombinant lines with superior productivity and stability.” In: *Biotechnology and bioengineering* 108.9 (2011), pp. 2141–2150 (cit. on p. 37).

[MEO+09] N. Ma, J. Ellet, C. Okediadi, P. Hermes, E. McCormick, S. Casnocha. “A single nutrient feed supports both chemically defined NS0 and CHO fed-batch processes: Improved productivity and lactate metabolism.” In: *Biotechnology Progress* 25.5 (Sept. 2009), pp. 1353–1363 (cit. on pp. 52, 53).

[MHRM08] K. Maier, U. Hofmann, M. Reuss, K. Mauch. “Identification of metabolic fluxes in hepatic cells from transient ^{13}C-labeling experiments: Part II. Flux estimation.” In: *Biotechnology and Bioengineering* 100.2 (June 2008), pp. 355–370. URL: http://doi.wiley.com/10.1002/bit.21746 (cit. on pp. 72, 88).

[MKK+17] B. C. Mulukutla, J. Kale, T. Kalomeris, M. Jacobs, G. W. Hiller. “Identification and control of novel growth inhibitors in fed-batch cultures of Chinese hamster ovary cells.” In: *Biotechnology and bioengineering* 114.8 (2017), pp. 1779–1790 (cit. on p. 37).

[ML17] C. Morrison, R. Lähteenmäki. “Public biotech in 2016—the numbers.” In: *Nature biotechnology* 35.7 (2017), pp. 623–629 (cit. on p. 86).

[ML84] R. Moreadith, A. L. Lehninger. “Purification, kinetic behavior, and regulation of NAD (P)+ malic enzyme of tumor mitochondria.” In: *Journal of Biological Chemistry* 259.10 (1984), pp. 6222–6227 (cit. on p. 177).

[MS87] E. A. Madden, B. Storrie. “The preparative isolation of mitochondria from Chinese hamster ovary cells.” In: *Analytical biochemistry* 163.2 (1987), pp. 350–357 (cit. on pp. 37, 99).

[MTPT15] J.-C. Matuszczyk, A. Teleki, J. Pfizenmaier, R. Takors. “Compartment-specific metabolomics for CHO reveals that ATP pools in mitochondria are much lower than in cytosol.” In: *Biotechnology Journal* 10.10 (2015), pp. 1639–1650 (cit. on pp. 39, 47, 48, 88, 90, 129, 144, 181).

[Mul12] A. Mullard. “Can next-generation antibodies offset biosimilar competition?” In: *Nature Reviews Drug Discovery* 11.6 (2012), p. 426 (cit. on p. 86).

[MWHY18] A. G. McAtee Pereira, J. L. Walther, M. Hollenbach, J. D. Young. “^{13}C flux analysis reveals that rebalancing medium amino acid composition can reduce ammonia production while preserving central carbon metabolism of CHO cell cultures.” In: *Biotechnology journal* 13.10 (2018), p. 1700518 (cit. on pp. 40, 54).

[MWS87] E. A. Madden, J. B. Wirt, B. Storrie. “Purification and characterization of lysosomes from Chinese hamster ovary cells.” In: *Archives of biochemistry and biophysics* 257.1 (1987), pp. 27–38 (cit. on p. 38).

[NBF+99] G. B. Nyberg, R. R. Balcarcel, B. D. Follstad, G. Stephanopoulos, D. I. C. Wang. “Metabolism of peptide amino acids by Chinese hamster ovary cells grown in a complex medium.” In: *Biotechnology and Bioengineering* 62.3 (Feb. 1999), pp. 324–335 (cit. on pp. 38, 44, 46, 54).

[NF03] D. D. Newmeyer, S. Ferguson-Miller. “Mitochondria: releasing power for life and unleashing the machineries of death.” In: *Cell* 112.4 (2003), pp. 481–490 (cit. on p. 87).

[NQG15] S. Nargund, J. Qiu, C. T. Goudar. “Elucidating the role of copper in CHO cell energy metabolism using ^{13}C metabolic flux analysis.” In: *Biotechnology progress* 31.5 (2015), pp. 1179–1186 (cit. on p. 87).

[NSH11] J. Niklas, V. Sandig, E. Heinzle. “Metabolite channeling and compartmentation in the human cell line AGE1. HN determined by ^{13}C labeling experiments and ^{13}C metabolic flux analysis.” In: *Journal of bioscience and bioengineering* (2011) (cit. on p. 88).

[NTP20] S. Nesci, F. Trombetti, A. Pagliarani. “Nicotinamide nucleotide transhydrogenase as a sensor of mitochondrial biology.” In: *Trends in cell biology* 30.1 (2020), pp. 1–3 (cit. on pp. 113, 116).

[NWB+14] A. Nicolae, J. Wahrheit, J. Bahnemann, A.-P. Zeng, E. Heinzle. “Non-stationary ^{13}C metabolic flux analysis of Chinese hamster ovary cells in batch culture using extracellular labeling highlights metabolic reversibility and compartmentation.” In: *BMC systems biology* 8.1 (2014), p. 50 (cit. on pp. 46, 47, 58, 129).

[NWN+15] A. Nicolae, J. Wahrheit, Y. Nonnenmacher, C. Weyler, E. Heinzle. “Identification of active elementary flux modes in mitochondria using selectively permeabilized CHO cells.” In: *Metabolic engineering* 32 (2015), pp. 95–105 (cit. on pp. 39, 47, 87, 99).

[NWN15] S. Niedenführ, W. Wiechert, K. Nöh. “How to measure metabolic fluxes: a taxonomic guide for 13C fluxomics.” In: *Current opinion in biotechnology* 34 (2015), pp. 82–90 (cit. on p. 184).

[Ore03] S. Oredsson. “Polyamine dependence of normal cell-cycle progression.” In: *Biochemical Society Transactions* 31.2 (2003), pp. 366–370 (cit. on p. 175).

[Pal04] F. Palmieri. “The mitochondrial transporter family (SLC25): physiological and pathological implications.” In: *Pflügers Archiv* 447.5 (2004), pp. 689–709 (cit. on pp. 42–44, 62, 64, 87, 114).

[Pal06] B. Ø. Palsson. *Systems biology: properties of reconstructed networks*. Cambridge university press, 2006 (cit. on pp. 57, 67).

[Pal13] F. Palmieri. “The mitochondrial transporter family SLC25: identification, properties and physiopathology.” In: *Molecular aspects of medicine* 34.2-3 (2013), pp. 465–484 (cit. on pp. 43, 87).

[PDWM17] X. Pan, C. Dalm, R. H. Wijffels, D. E. Martens. “Metabolic characterization of a CHO cell size increase phase in fed-batch cultures.” In: *Applied microbiology and biotechnology* 101.22 (2017), pp. 8101–8113 (cit. on p. 176).

[PDZ07] N. Pollak, C. Dölle, M. Ziegler. “The power to reduce: pyridine nucleotides–small molecules with a multitude of functions.” In: *Biochemical Journal* 402.2 (2007), pp. 205–218 (cit. on p. 113).

[Peg88] A. E. Pegg. “Polyamine metabolism and its importance in neoplastic growth and as a target for chemotherapy.” In: *Cancer research* 48.4 (1988), pp. 759–774 (cit. on pp. 161, 175).

[PHB22] J. U. Park, H.-J. Han, J. Y. Baik. “Energy metabolism in Chinese hamster ovary (CHO) cells: Productivity and beyond.” In: *Korean Journal of Chemical Engineering* (2022), pp. 1–10 (cit. on p. 43).

[PJTT16] J. Pfizenmaier, L. Junghans, A. Teleki, R. Takors. “Hyperosmotic stimulus study discloses benefits in ATP supply and reveals miRNA/mRNA targets to improve recombinant protein production of CHO cells.” In: *Biotechnology journal* 11.8 (2016), pp. 1037–1047 (cit. on pp. 144, 161).

[PL64] J. V. Passonneau, O. H. Lowry. “The role of phosphofructokinase in metabolic regulation.” In: *Advances in enzyme regulation* 2 (1964), pp. 265–274 (cit. on p. 176).

[PM85] E. T. Papoutsakis, C. L. Meyer. “Equations and calculations of product yields and preferred pathways for butanediol and mixed-acid fermentations.” In: *Biotechnology and bioengineering* 27.1 (1985), pp. 50–66 (cit. on p. 44).

[PMT15] J. Pfizenmaier, J.-C. Matuszczyk, R. Takors. “Changes in intracellular ATP-content of CHO cells as response to hyperosmolality.” In: *Biotechnology progress* 31.5 (2015), pp. 1212–1216 (cit. on pp. 87, 144, 161, 176).

[PSD+17] X. Pan, M. Streefland, C. Dalm, R. H. Wijffels, D. E. Martens. “Selection of chemically defined media for CHO cell fed-batch culture processes.” In: *Cytotechnology* 69.1 (2017), pp. 39–56 (cit. on p. 37).

[PSDF02] R. M. Pascale, M. M. Simile, M. R. De Miglio, F. Feo. “Chemoprevention of hepatocarcinogenesis: S-adenosyl-L-methionine.” In: *Alcohol* 27.3 (2002), pp. 193–198 (cit. on p. 161).

[PT17] J. Pfizenmaier, R. Takors. “Host Organisms: Mammalian Cells.” In: *Industrial Biotechnology: Microorganisms* 2 (2017), pp. 643–671 (cit. on pp. 46, 47, 58, 129).

[Puc85] T. T. Puck. “Consideration of measurements and calculations involved in assessment of the effects of human exposure to low doses of ionizing radiation and other mutagens.” In: *Letters in Mathematical Physics* 10.2-3 (1985), pp. 225–230 (cit. on p. 51).

[QKO+20] L.-E. Quek, J. R. Krycer, S. Ohno, K. Yugi, D. J. Fazakerley, R. Scalzo, S. D. Elkington, Z. Dai, A. Hirayama, S. Ikeda, et al. “Dynamic 13C flux analysis captures the reorganization of adipocyte glucose metabolism in response to insulin.” In: *Iscience* 23.2 (2020), p. 100855 (cit. on p. 185).

[RDKK15] D. Reinhart, L. Damjanovic, C. Kaisermayer, R. Kunert. “Benchmarking of commercially available CHO cell culture media for antibody production.” In: *Applied Microbiology and Biotechnology* 99.11 (2015), pp. 4645–4657. URL: https://doi.org/10.1007/s00253-015-6514-4 (cit. on p. 160).

[ROH+88] E. Roth, G. Ollenschlager, G. Hamilton, A. Simmel, K. Langer, W. Fekl, R. Jakesz. “Influence of two glutamine-containing dipeptides on growth of mammalian cells.” In: *In vitro cellular & developmental biology* 24.7 (1988), pp. 696–698 (cit. on p. 54).

[RTF84] M. K. Riscoe, P. A. Tower, A. J. Ferro. “Mechanism of action of 5’-methylthioadenosine in S49 cells.” In: *Biochemical pharmacology* 33.22 (1984), pp. 3639–3643 (cit. on pp. 161, 175).

[SAB+00] D.-K. Song, Y.-H. Ahn, J. H. Bae, W. K. Park, Y.-S. Hong, W.-K. Ho, Y. E. Earm. “Evidence of enhancement of malate-aspartate shuttle activity in β cells of streptozotocin-induced non—insulin-dependent diabetic rats.” In: *Metabolism* 49.1 (2000), pp. 92–96 (cit. on p. 44).

[SB10] K. Sunley, M. Butler. “Strategies for the enhancement of recombinant protein production from mammalian cells by growth arrest.” In: *Biotechnology advances* 28.3 (2010), pp. 385–394 (cit. on p. 161).

[SBP+16] A. Sánchez-Kopper, M. Becker, J. Pfizenmaier, C. Kessler, A. Karau, R. Takors. “Tracking dipeptides at work-uptake and intracellular fate in CHO culture.” In: *AMB Express* 6.1 (Dec. 2016), p. 48 (cit. on pp. 54–56).

[SBY18] S. Sha, H. Bhatia, S. Yoon. “An RNA-seq based transcriptomic investigation into the productivity and growth variants with Chinese hamster ovary cells.” In: *Journal of biotechnology* 271 (2018), pp. 37–46 (cit. on p. 161).

[Sch01] I. E. Scheffler. “A century of mitochondrial research: achievements and perspectives.” In: *Mitochondrion* 1.1 (2001), pp. 3–31 (cit. on p. 87).

[SCM+11] C. A. Sellick, A. S. Croxford, A. R. Maqsood, G. Stephens, H. V. Westerhoff, R. Goodacre, A. J. Dickson. “Metabolite profiling of recombinant CHO cells: designing tailored feeding regimes that enhance recombinant antibody production.” In: *Biotechnology and bioengineering* 108.12 (2011), pp. 3025–3031 (cit. on p. 38).

[SCNV97] K. Schmidt, M. Carlsen, J. Nielsen, J. Villadsen. “Modeling isotopomer distributions in biochemical networks using isotopomer mapping matrices.” In: *Biotechnology and Bioengineering* 55.6 (Sept. 1997), pp. 831–840 (cit. on p. 74).

[SFN05] K. Sheikh, J. Förster, L. K. Nielsen. “Modeling hybridoma cell metabolism using a generic genome-scale metabolic model of Mus musculus.” In: *Biotechnology progress* 21.1 (2005), pp. 112–121 (cit. on p. 61).

[SJH13] Z. Sheikholeslami, M. Jolicoeur, O. Henry. “Probing the metabolism of an inducible mammalian expression system using extracellular isotopomer analysis.” In: *Journal of biotechnology* 164.4 (2013), pp. 469–478 (cit. on p. 97).

[SMR08] J. Schaub, K. Mauch, M. Reuss. “Metabolic flux analysis in Escherichia coli by integrating isotopic dynamic and isotopic stationary ^{13}C labeling data.” In: *Biotechnology and bioengineering* 99.5 (2008), pp. 1170–1185 (cit. on pp. 45, 72).

[SPJP74] J. P. Schwartz, J. V. Passonneau, G. S. Johnson, I. Pastan. “The effect of growth conditions on NAD^+ and NADH concentrations and the NAD+: NADH ratio in normal and transformed fibroblasts.” In: *Journal of Biological Chemistry* 249.13 (1974), pp. 4138–4143 (cit. on p. 113).

[SRM11] N. Sengupta, S. T. Rose, J. A. Morgan. “Metabolic flux analysis of CHO cell metabolism in the late non-growth phase.” In: *Biotechnology and bioengineering* 108.1 (2011), pp. 82–92 (cit. on pp. 38, 88, 179).

[SSB+18] G. Stolfa, M. T. Smonskey, R. Boniface, A.-B. Hachmann, P. Gulde, A. D. Joshi, A. P. Pierce, S. J. Jacobia, A. Campbell. “CHO-omics review: The impact of current and emerging technologies on chinese hamster ovary based bioproduction.” In: *Biotechnology journal* 13.3 (2018), p. 1700227 (cit. on p. 37).

[SW15] R. Schumacher, S. A. Wahl. “Effective estimation of dynamic metabolic fluxes using 13C labeling and piecewise affine approximation: from theory to practical applicability.” In: *Metabolites* 5.4 (2015), pp. 697–719 (cit. on p. 184).

[TAJ+20] L. Toronjo-Urquiza, A. E. Acosta-Martin, D. C. James, T. Nagy, R. J. Falconer. “The use of catechins in Chinese hamster ovary cell media for the improvement of monoclonal antibody yields and a reduction of

acidic species." In: *Biotechnology progress* 36.4 (2020), e2980 (cit. on p. 161).

[TDRY13] N. Templeton, J. Dean, P. Reddy, J. D. Young. "Peak antibody production is associated with increased oxidative metabolism in an industrially relevant fed-batch CHO cell culture." In: *Biotechnology and bioengineering* 110.7 (2013), pp. 2013–2024 (cit. on pp. 38, 45, 47, 59, 72, 96, 97, 116, 132, 134, 138, 161, 169, 178, 181).

[TP58] J. H. Tjio, T. T. Puck. "Genetics of somatic mammalian cells: II. Chromosomal constitution of cells in tissue culture." In: *The Journal of experimental medicine* 108.2 (1958), p. 259 (cit. on pp. 35, 37, 51).

[TSM+17] N. Templeton, K. D. Smith, A. G. McAtee-Pereira, H. Dorai, M. J. Betenbaugh, S. E. Lang, J. D. Young. "Application of ^{13}C flux analysis to identify high-productivity CHO metabolic phenotypes." In: *Metabolic engineering* 43 (2017), pp. 218–225 (cit. on pp. 39, 47, 160, 161, 181).

[TSPB00] S. Tuttle, T. Stamato, M. L. Perez, J. Biaglow. "Glucose-6-phosphate Dehydrogenase and the Oxidative Pentose Phosphate Cycle Protect Cellsagainst Apoptosis Induced by Low Doses of Ionizing Radiation." In: *Radiation research* 153.6 (2000), pp. 781–787 (cit. on p. 179).

[UMBB97] M. Unseld, J. R. Marienfeld, P. Brandt, A. Brennicke. "The mitochondrial genome of Arabidopsis thaliana contains 57 genes in 366,924 nucleotides." In: *Nature genetics* 15.1 (1997), pp. 57–61 (cit. on p. 87).

[VAD+09] P. Vizán, G. Alcarraz-Vizán, S. Dıaz-Moralli, O. N. Solovjeva, W. M. Frederiks, M. Cascante. "Modulation of pentose phosphate pathway during cell cycle progression in human colon adenocarcinoma cell line HT29." In: *International journal of cancer* 124.12 (2009), pp. 2789–2796 (cit. on p. 177).

[VBD+10] J. van der Valk, D. Brunner, K. De Smet, Å. Fex Svenningsen, P. Honegger, L. Knudsen, T. Lindl, J. Noraberg, A. Price, M. Scarino, G. Gstraunthaler. "Optimization of chemically defined cell culture media – Replacing fetal bovine serum in mammalian in vitro methods." In: *Tox-*

icology in Vitro 24.4 (June 2010), pp. 1053–1063. URL: http://linkinghub.elsevier.com/retrieve/pii/S0887233310000809 (cit. on p. 52).

[VDG+14] N. M. Vacanti, A. S. Divakaruni, C. R. Green, S. J. Parker, R. R. Henry, T. P. Ciaraldi, A. N. Murphy, C. M. Metallo. "Regulation of substrate utilization by the mitochondrial pyruvate carrier." In: *Molecular cell* 56.3 (2014), pp. 425–435 (cit. on p. 87).

[VEK69] R. Veech, L. Eggleston, H. Krebs. "The redox state of free nicotinamide–adenine dinucleotide phosphate in the cytoplasm of rat liver." In: *Biochemical Journal* 115.4 (1969), pp. 609–619 (cit. on p. 113).

[VHH+94] R. Van der Heijden, J. Heijnen, C. Hellinga, B. Romein, K. C. A. Luyben. "Linear constraint relations in biochemical reaction systems: I. Classification of the calculability and the balanceability of conversion rates." In: *Biotechnology and Bioengineering* 43.1 (1994), pp. 3–10 (cit. on p. 68).

[VP94] A. Varma, B. O. Palsson. "Metabolic flux balancing: basic concepts, scientific and practical use." In: *Bio/technology* 12.10 (1994), pp. 994–998 (cit. on pp. 44, 45, 68).

[VTH+20] N. Verhagen, A. Teleki, C. Heinrich, M. Schilling, A. Unsöld, R. Takors. "S-adenosylmethionine and methylthioadenosine boost cellular productivities of antibody forming Chinese Hamster ovary cells." In: *Biotechnology and Bioengineering* 117.11 (2020), pp. 3239–3247 (cit. on pp. 144, 161, 175, 176).

[VWT+20] N. Verhagen, A. W. Wijaya, A. Teleki, M. Fadhlullah, A. Unsöld, M. Schilling, C. Heinrich, R. Takors. "Comparison of L-tyrosine containing dipeptides reveals maximum ATP availability for L-prolyl-L-tyrosine in CHO cells." In: *Engineering in life sciences* 20.9-10 (2020), pp. 384–394 (cit. on pp. 115, 119, 144, 179).

[VZT20] N. Verhagen, J. Zieringer, R. Takors. "Methylthioadenosine (MTA) boosts cell-specific productivities of Chinese hamster ovary cultures: dosage effects on proliferation, cell cycle and gene expression." In:

FEBS Open bio 10.12 (2020), pp. 2791–2804 (cit. on pp. 161, 162, 175, 176).

[Wal14] G. Walsh. "Biopharmaceutical benchmarks 2014." In: *Nature biotechnology* 32.10 (2014), pp. 992–1000 (cit. on pp. 35, 86).

[Wal18] G. Walsh. "Biopharmaceutical benchmarks 2018." In: *Nature Biotechnology* 36.12 (2018), pp. 1136–1145 (cit. on pp. 36, 160).

[War56] O. Warburg. "On the origin of cancer cells." In: *Science* 123.3191 (1956), pp. 309–314 (cit. on pp. 90, 133).

[WDR+05] W. A. van Winden, J. C. van Dam, C. Ras, R. J. Kleijn, J. L. Vinke, W. M. van Gulik, J. J. Heijnen. "Metabolic-flux analysis of Saccharomyces cerevisiae CEN. PK113-7D based on mass isotopomer measurements of ^{13}C-labeled primary metabolites." In: *FEMS yeast research* 5.6-7 (2005), pp. 559–568 (cit. on p. 128).

[WG97] W. Wiechert, A. A. de Graaf. "Bidirectional reaction steps in metabolic networks: I. Modeling and simulation of carbon isotope labeling experiments." In: *Biotechnology and bioengineering* 55.1 (1997), pp. 101–117 (cit. on p. 72).

[WH11] F. M. Wurm, D. Hacker. "First CHO genome." In: *Nature Biotechnology* 29.8 (2011), pp. 718–720 (cit. on p. 160).

[Wie01] W. Wiechert. "^{13}C metabolic flux analysis." In: *Metabolic engineering* 3.3 (2001), pp. 195–206 (cit. on pp. 44, 45, 128).

[WL99] S. J. Wessman, R. L. Levings. "Benefits and risks due to animal serum used in cell culture production." In: *Developments in biological standardization* 99 (1999), pp. 3–8 (cit. on p. 52).

[WNH14] J. Wahrheit, J. Niklas, E. Heinzle. "Metabolic control at the cytosol-mitochondria interface in different growth phases of CHO cells." In: *Metabolic Engineering* 23 (2014), pp. 9–21 (cit. on p. 88).

[WNN15] W. Wiechert, S. Niedenführ, K. Nöh. "A Primer to ^{13}C metabolic flux analysis." In: *Fundamental Bioengineering* (2015), pp. 97–142 (cit. on pp. 71, 73, 150).

[WSG82] H. G. Williams-Ashman, J. Seidenfeld, P. Galletti. “Trends in the biochemical pharmacology of 5-deoxy-5-methylthioadenosine.” In: *Biochemical pharmacology* 31.3 (1982), pp. 277–288 (cit. on pp. 161, 175).

[WT21] A. W. Wijaya, R. Takors. “A transhydrogenase-like mechanism in CHO cells comprising concerted cytosolic reaction and mitochondrial shuttling activities.” In: *Biochemical Engineering Journal* 170 (2021), p. 107986 (cit. on pp. 114, 117, 118, 121).

[WUH+21] A. W. Wijaya, A. Ulmer, L. Hundsdorfer, N. Verhagen, A. Teleki, R. Takors. “Compartment-specific metabolome labeling enables the identification of subcellular fluxes that may serve as promising metabolic engineering targets in CHO cells.” In: *Bioprocess and biosystems engineering* 44.12 (2021), pp. 2567–2578 (cit. on pp. 47, 56, 131, 136, 139, 141, 142, 145, 151–154).

[Wur04] F. M. Wurm. “Production of recombinant protein therapeutics in cultivated mammalian cells.” In: *Nature biotechnology* 22.11 (2004), pp. 1393–1398 (cit. on pp. 37, 86, 160).

[WVTT21] A. W. Wijaya, N. Verhagen, A. Teleki, R. Takors. “Compartment-specific ^{13}C metabolic flux analysis reveals boosted NADPH availability coinciding with increased cell-specific productivity for IgG1 producing CHO cells after MTA treatment.” In: *Engineering in life sciences* 21.12 (2021), pp. 832–847 (cit. on pp. 165–168, 170, 171, 174).

[WW01] W. Wiechert, M. Wurzel. “Metabolic isotopomer labeling systems: Part I: global dynamic behavior.” In: *Mathematical biosciences* 169.2 (2001), pp. 173–205 (cit. on p. 88).

[WW17] F. M. Wurm, M. J. Wurm. “Cloning of CHO cells, productivity and genetic stability—a discussion.” In: *Processes* 5.2 (2017), p. 20 (cit. on pp. 35, 37, 51).

[XGJC17] S. Xu, J. Gavin, R. Jiang, H. Chen. “Bioreactor productivity and media cost comparison for different intensified cell culture processes.” In: *Biotechnology progress* 33.4 (2017), pp. 867–878 (cit. on p. 36).

[XKK+11] Z. Xing, B. Kenty, I. Koyrakh, M. Borys, S.-H. Pan, Z. J. Li. “Optimizing amino acid composition of CHO cell culture media for a fusion protein production.” In: *Process Biochemistry* 46.7 (2011), pp. 1423–1429 (cit. on p. 54).

[XNL+11] X. Xu, H. Nagarajan, N. E. Lewis, S. Pan, Z. Cai, X. Liu, W. Chen, M. Xie, W. Wang, S. Hammond, et al. “The genomic sequence of the Chinese hamster ovary (CHO)-K1 cell line.” In: *Nature biotechnology* 29.8 (2011), p. 735 (cit. on pp. 38, 62, 160).

[YMK+16] W. C. Yang, D. F. Minkler, R. Kshirsagar, T. Ryll, Y.-M. Huang. “Concentrated fed-batch cell culture increases manufacturing capacity without additional volumetric capacity.” In: *Journal of biotechnology* 217 (2016), pp. 1–11 (cit. on p. 36).

[ZKR+08] Z. Zhao, K. Kuijvenhoven, C. Ras, W. M. van Gulik, J. J. Heijnen, P. J. Verheijen, W. A. van Winden. “Isotopic non-stationary ^{13}C gluconate tracer method for accurate determination of the pentose phosphate pathway split-ratio in Penicillium chrysogenum.” In: *Metabolic Engineering* 10.3-4 (2008), pp. 178–186 (cit. on p. 128).

[ZR05] J. Zhang, D. Robinson. “Development of Animal-free, Protein-Free and Chemically-Defined Media for NS0 Cell Culture.” In: *Cytotechnology* 48.1-3 (June 2005), pp. 59–74. URL: http://link.springer.com/10.1007/s10616-005-3563-z (cit. on p. 53).

[ZWL+13] H. Zhang, H. Wang, M. Liu, T. Zhang, J. Zhang, X. Wang, W. Xiang. “Rational development of a serum-free medium and fed-batch process for a GS-CHO cell line expressing recombinant antibody.” In: *Cytotechnology* 65.3 (2013), pp. 363–378 (cit. on p. 160).

[ZWZ+16] Y. Zhao, A. Wang, Y. Zou, N. Su, J. Loscalzo, Y. Yang. “*In vivo* monitoring of cellular energy metabolism using SoNar, a highly responsive sensor for NAD^+/NADH redox state.” In: *Nature protocols* 11.8 (2016), p. 1345 (cit. on p. 113).